BIDGE Publications

Measurement, Analysis and Manufacturing for Engineering Systems

Editor: Doç. Dr. Murat MAKARACI

ISBN: 978-625-6707-24-5

Page Layout: Gözde YÜCEL
1st Edition:
Publication Date: 25.12.2023
BIDGE Publications,

Certificate No: 71374

www.bidgeyayinlari.com.tr - bidgeyayinlari@gmail.com

Krc Bilişim Ticaret ve Organizasyon Ltd. Şti.
Güzeltepe Mahallesi Abidin Daver Sokak Sefer Apartmanı No: 7/9 Çankaya / Ankara

Contents

CHAPTER I

Optimizing Operations: The Power of Energy Management Systems in Companies

Ali Kemal ÇAKIR[1]

1. Introduction

Energy; It has entered every aspect of our lives and has become an essential element in our lives. Our energy consumption is increasing rapidly due to the increasing population, the increase in people's living standards and the use of technological devices at every stage of our lives [1].

There is a parallel increase in the production sector along with consumption. Rapid increases, especially in the manufacturing sector, have further increased the importance of energy.

[1] Doç. Dr., Adnan Menderes University, Aydın Vocational School, Machine and Metal Technology Department, AYDIN

In an era where sustainability and efficiency are paramount, companies are increasingly turning to innovative solutions to manage their energy consumption. One such solution gaining prominence is the implementation of Energy Management Systems (EMS). These systems offer businesses a comprehensive approach to monitor, control, and optimize their energy usage, leading to cost savings, environmental benefits, and improved operational efficiency.

In today's dynamic business landscape, energy management has emerged as a critical factor for success. Companies across industries are increasingly recognizing the need to optimize their energy consumption, not only to reduce costs and enhance profitability but also to minimize their environmental impact. Energy management systems (EMS) have emerged as powerful tools to address these challenges, empowering businesses to achieve sustainable energy efficiency.

Energy Management System is gaining importance in terms of correct management of energy resources, as the trend towards environmentally friendly energy sources begins and the cost of access to energy increases. Providing the needed energy at lower costs, continuously, in high quality and cleanly, and planning its use in an environmentally friendly manner is very important for businesses [2]. In this regard, it is very important for companies to understand the energy management system correctly.

1.1. Understanding Energy Management Systems

An Energy Management System is a sophisticated tool designed to track, analyze, and manage energy consumption within an organization. It integrates with existing infrastructure to collect real-time data on energy usage, enabling businesses to make informed decisions about their energy consumption patterns. It is necessary to know the requirements of the energy management system well. The Basic Components of the Energy Management System are:

1.1.1. Data Acquisition and Monitoring

- EMS utilizes advanced metering and sensor technologies to collect real-time data on energy consumption.
- Smart meters, sensors, and sub-metering devices are deployed across various departments and facilities to provide a granular view of energy usage.

1.1.2. Data Analysis and Reporting

- The collected data is analyzed to identify patterns, trends, and areas of inefficiency.
- Comprehensive reports and analytics provide valuable insights into energy usage, helping companies make informed decisions.

1.1.3. Control Systems

- EMS often integrates with a company's existing control systems to enable automated adjustments based on real-time data.
- This may include optimizing HVAC systems, lighting, and other equipment to reduce energy consumption during non-peak hours.

1.1.4. Forecasting and Planning

- Advanced EMS solutions use predictive modelling to forecast future energy needs.
- This allows companies to plan for peak demand periods, optimize resource allocation, and negotiate favourable energy supply contracts.

Benefits of Implementing Energy Management Systems:

1.1.5. Cost Savings

- By identifying and eliminating energy waste, companies can significantly reduce operational costs.
- Peak demand management and load shedding strategies help avoid expensive energy peaks.

1.1.6. Environmental Impact

- Reduced energy consumption translates to a smaller carbon footprint [3].
- Companies can align with sustainability goals and contribute to a greener, more environmentally responsible image.

1.1.7. Operational Efficiency

- EMS provides real-time insights into energy usage patterns, allowing for proactive management and optimization of operations.
- Predictive maintenance based on energy data helps prevent downtime and extends the life of equipment.

1.1.8. Regulatory Compliance

- Many regions have stringent regulations regarding energy consumption and emissions.
- Implementing an EMS ensures compliance with these regulations, avoiding penalties and fostering a positive relationship with regulatory bodies.

1.1.9. Improved Corporate Social Responsibility (CSR)

Companies that actively manage and reduce their energy consumption demonstrate a commitment to CSR, which can positively impact brand reputation. There are various difficulties in the establishment and operability of the energy management system.

1.2. Challenges and Considerations

While the benefits of Energy Management Systems are evident, companies must navigate challenges such as initial implementation costs, employee training, and potential resistance to change. However, the long-term advantages and positive impact on the bottom line often outweigh these challenges. These;

1.2.1. Initial Investment

These;

- Companies may hesitate due to the perceived high initial costs of implementing an Energy Management System.
- However, it's essential to recognize that the long-term savings in operational costs often outweigh the upfront investment.

1.2.2. Employee Training and Change Management

These;

- Introducing a new system requires employees to adapt to changes in their workflows.
- Providing comprehensive training programs and emphasizing the benefits of the system can ease the transition.

1.2.3. Integration with Existing Infrastructure

The functionality of the energy management system goes parallel with its Integration with the Existing Infrastructure. These;

- Compatibility with existing technologies and infrastructure can be a concern.
- Choosing a flexible EMS that integrates seamlessly with current systems minimizes disruption during implementation.

Large companies such as Walmart and Intel have greatly reduced their carbon footprints thanks to the energy management

system. Walmart has successfully implemented an Energy Management System across its global operations. Through efficient lighting, HVAC controls, and data-driven insights, Walmart has achieved substantial energy savings and reduced its carbon footprint. Intel's commitment to sustainability is evident through its implementation of EMS. By optimizing energy usage in its manufacturing processes, Intel has not only saved costs but also garnered recognition for its environmental stewardship. Also, Dow Chemical has implemented EMS to optimize energy usage across its manufacturing plants, saving over $1 billion annually.

2. The Future of Energy Management Systems:

As technology continues to advance, the future of Energy Management Systems promises even greater efficiency and sustainability. Here are some anticipated developments.

2.1. Artificial Intelligence (AI) Integration

AI algorithms will enhance the predictive capabilities of EMS, allowing for more accurate forecasting and proactive energy management.

2.2. Blockchain for Energy Trading

Blockchain technology could facilitate transparent and secure energy transactions between businesses, enabling a decentralized energy market.

2.3. Internet of Things (IoT) Connectivity

Increased connectivity between devices through IoT will enable a more comprehensive and interconnected approach to energy management.

2.4. Addressing Specific Industries

2.4. 1. Manufacturing Sector

For manufacturing companies, where energy-intensive processes are the norm, EMS provides precise control over machinery and equipment. Real-time monitoring helps identify bottlenecks and inefficiencies, leading to optimized production schedules and reduced energy waste.

2.4.2. Commercial Buildings

In the commercial real estate sector, EMS is instrumental in managing lighting, heating, ventilation, and air conditioning (HVAC) systems. Building automation through EMS ensures that energy consumption aligns with occupancy patterns, reducing unnecessary energy use during vacant periods.

2.4.3. Information Technology (IT) Industry

Data Centers, integral to the IT industry, are notorious for their high energy consumption. EMS helps IT companies manage and optimize server loads, cooling systems, and lighting, resulting in significant energy savings.

2.5. Global Trends and Policies

2.5.1. Renewable Energy Integration

Many countries are investing heavily in renewable energy sources. EMS facilitates the seamless integration of renewable energy into the grid by balancing supply and demand.

2.5.2. Government Incentives

Governments worldwide are offering incentives and subsidies for companies adopting energy-efficient practices, including the implementation of EMS. Taking advantage of these incentives can further offset initial costs for businesses.

2.6. Looking Ahead: Challenges and Opportunities

2.6.1. Cybersecurity Concerns

As EMS becomes more interconnected, cybersecurity becomes a critical consideration. Companies must invest in robust cybersecurity measures to protect sensitive energy data.

2.6.2. Scalability

As businesses grow, the scalability of EMS becomes crucial. Choosing a system that can adapt to the evolving needs and size of the company ensures long-term viability.

2.6.3. Consumer and Investor Expectations

Consumers and investors increasingly favor companies with strong environmental and social responsibility initiatives. Having an EMS in place not only meets regulatory requirements but also aligns with the growing demand for sustainable business practices. Overcoming obstacles such as advances in technology, audience diversity, and maintaining online reputation requires constant vigilance. But the potential rewards (brand awareness, market expansion, and customer engagement) are unparalleled [4]. These strategies help you communicate your vision of a sustainable future and invite stakeholders to participate in that vision. In this context, companies that include energy management in their vision will be lucky in the future.

3. Energy Management System and Standardization

An Energy Management System (EMS) is a comprehensive framework designed to monitor, control, and optimize energy consumption within an organization or facility [6]. The primary goal of an EMS is to enhance energy efficiency, reduce costs, and minimize environmental impact by systematically managing energy resources. Key components of an EMS typically include energy data monitoring, performance analysis, goal setting, and continuous

improvement strategies. Standardization in the context of energy management refers to the development and implementation of uniform guidelines, specifications, and protocols that ensure consistency and compatibility across different energy management systems. Standardization plays a crucial role in promoting interoperability, fostering best practices, and facilitating a common language for energy management globally. Standardized frameworks, such as ISO 50001, provide a structured approach for organizations to establish, implement, maintain, and improve their energy management systems.

An Energy Management System is a holistic approach to strategically handle energy consumption, while standardization ensures a common and interoperable foundation for effective energy management practices across diverse industries and geographical regions. These initiatives collectively contribute to sustainability, cost savings, and environmental responsibility in the use of energy resources.

3.1. ISO 50001 Standard and The Advantages of ISO 50001 Standard in Companies

The ISO 50001 standard, which focuses on energy management, has evolved over the years to address the growing importance of sustainable practices and energy efficiency in organizations.

ISO 50001 was first introduced in June 2011 by the International Organization for Standardization (ISO). Its development was influenced by other management system standards, such as ISO 9001 for quality management and ISO 14001 for environmental management. ISO 50001 was designed to provide organizations with a systematic and structured approach to managing energy. The standard introduced a framework for establishing policies, identifying energy consumption patterns, setting objectives, and implementing processes to continually improve energy performance. Following its initial release, ISO 50001 gained

widespread acceptance globally. Organizations across various industries recognized the importance of implementing effective energy management systems to reduce costs, enhance efficiency, and meet environmental sustainability goals.

In 2018, ISO 50001 underwent a revision to align with the High-Level Structure (HLS) common to all ISO management system standards [5]. This alignment aimed to facilitate integration with other management systems, such as those for quality and environmental management, streamlining processes for organizations seeking multiple certifications. ISO 50001 was designed to integrate seamlessly with other ISO standards, allowing organizations to combine their efforts in energy management with quality, environmental, and occupational health, and safety management systems. This integration supports a holistic approach to organizational performance. One of the key principles of ISO 50001 is the emphasis on continual improvement. The standard follows the Plan-Do-Check-Act (PDCA) cycle, encouraging organizations to regularly assess their energy performance, identify areas for improvement, and implement measures to enhance efficiency over time. This cycle is a systematic approach to continuous improvement in energy management. Here's a brief summary of each phase of the PUKO cycle:

- **Plan (P):** In this phase, organizations identify and analyze energy aspects, set energy objectives and targets, and establish action plans to achieve these goals. This involves understanding the organization's energy context, legal and other requirements, and determining significant energy uses.
- **Do (U):** The implementation phase involves putting the energy management plans into action. This includes training personnel, establishing communication processes, and implementing operational controls to ensure that activities align with the organization's energy policy and objectives. Monitoring and measuring energy performance also occur during this phase.

- **Check (K):** This phase involves monitoring, measurement, analysis, and evaluation of energy performance against the objectives and targets set in the planning phase. It includes regular energy reviews and assessments to ensure that the organization is on track and compliance with the standard.
- **Act (O):** The final phase involves taking actions to continually improve energy performance. Based on the results of monitoring and evaluation, organizations identify opportunities for improvement, implement corrective actions, and update the energy management system accordingly. This phase ensures that the organization learns from its experiences and strives for ongoing energy efficiency.

By following the PUKO cycle, organizations can establish a robust energy management framework that aligns with ISO 50001 standards, leading to sustained improvements in energy performance and contributing to environmental sustainability and cost-effectiveness.

ISO 50001 has gained recognition as a valuable tool for organizations seeking to demonstrate their commitment to energy efficiency and sustainability. Its global impact extends to various sectors, including manufacturing, services, and public administration, contributing to a more energy-conscious and environmentally responsible business landscape. As of the latest available information, ISO 50001 continues to play a crucial role in guiding organizations toward sustainable energy practices. Its relevance is expected to grow as businesses globally prioritize environmental responsibility and governments enact regulations to promote energy efficiency.

In an era where environmental sustainability and energy efficiency have become paramount concerns, companies worldwide are increasingly turning to international standards to streamline their operations. One such standard that stands out is ISO 50001, an Energy Management System (EnMS) designed to help organizations improve their energy performance and reduce their environmental

impact. Using the ISO 50001 standard has many advantages for companies. These advantages;

- One of the primary benefits of ISO 50001 is its focus on enhancing energy performance. The standard provides a systematic approach to developing and implementing energy management policies, identifying energy consumption patterns, and establishing objectives to continually improve energy efficiency. By doing so, companies can optimize their energy usage, leading to cost savings and reduced environmental impact.
- Implementing ISO 50001 can lead to significant cost savings by identifying areas of energy waste and inefficiency. Through the establishment of energy performance indicators and regular monitoring, companies can pinpoint opportunities for improvement, implement energy-saving measures, and ultimately reduce operational costs. This not only contributes to a more sustainable business model but also enhances overall operational efficiency.
- In an increasingly regulated business environment, companies face a growing number of energy-related compliance requirements. ISO 50001 provides a framework that aligns with various international and regional regulations, making it easier for companies to navigate complex legal landscapes. Compliance with ISO 50001 can serve as a strategic advantage by demonstrating a commitment to sustainability and responsible energy management.
- Consumers are becoming more environmentally conscious, and stakeholders are placing greater emphasis on corporate responsibility. Adopting ISO 50001 demonstrates a company's commitment to sustainability and environmental stewardship. This commitment can enhance the company's reputation, attract environmentally conscious customers, and foster

positive relationships with investors, suppliers, and other stakeholders.

- ISO 50001 encourages employee involvement in the energy management process. By raising awareness about energy efficiency and involving employees in identifying and implementing energy-saving measures, companies can foster a culture of sustainability. Engaged employees are more likely to contribute innovative ideas and demonstrate a sense of responsibility, leading to increased productivity and overall job satisfaction.
- ISO 50001 follows the Plan-Do-Check-Act (PDCA) cycle, providing a framework for continual improvement. This cyclical process ensures that companies not only establish effective energy management systems but also continually assess and enhance their performance. The commitment to ongoing improvement aligns with the evolving nature of energy management practices and positions companies to adapt to future challenges and opportunities.

ISO 50001 is a valuable tool for companies looking to boost energy efficiency, reduce operational costs, and enhance their sustainability efforts. By adopting this international standard, organizations can not only comply with regulatory requirements but also gain a competitive edge in the market by showcasing their commitment to responsible energy management. As businesses worldwide seek ways to align with global sustainability goals, ISO 50001 stands out as a comprehensive and effective solution.

4. Conclusion

In an era where the global community is collectively addressing environmental challenges, Energy Management Systems emerge as a beacon of hope for companies seeking to balance economic growth with environmental responsibility. The integration of EMS is not just a technological upgrade; it represents a paradigm shift in how businesses perceive and manage their energy footprint.

As companies worldwide embrace these systems, the path to a sustainable and resilient future becomes clearer, one optimized energy decision at a time. In a world where sustainability and efficiency are integral to success, Energy Management Systems are becoming indispensable tools for businesses. The ability to monitor, analyze, and control energy usage empowers companies to make informed decisions, reduce costs, and contribute to a more sustainable future. As technology continues to advance, the role of Energy Management Systems in shaping the future of corporate sustainability will undoubtedly become even more significant. Companies that embrace these systems today are not only securing their bottom line but also paving the way for a greener and more efficient tomorrow.

In conclusion, the adoption of Energy Management Systems in companies marks a pivotal step toward achieving sustainability, cost-effectiveness, and operational efficiency. While challenges exist, the long-term benefits, both in terms of cost savings and environmental impact, make the integration of EMS a wise investment for forward-thinking organizations. As the world grapples with the consequences of climate change and strives for a more sustainable future, the role of companies in managing their energy consumption responsibly cannot be overstated. Energy Management Systems not only position businesses as leaders in corporate responsibility but also contribute significantly to global efforts to create a more sustainable and resilient world.

References

X: [1] İNCEKARA, Ç., Ö. ISO 50001 Energy Management System Application in Industrial Sector with Fuzzy Logic, Research Article, AKU J. Sci. Eng. 20 (2020) 065301 (991-1013), DOI: 10.35414/akufemubid.819645.

[2] Anonyms-a, Enerji Yönetim Sistemi, https://www.konzek.com/blog/enerji-yonetim-sistemi, (In Turkish), (Accessed: 09/10/2023).

[3] Anonyms-b, How You Can Cut Energy Costs Through the Inflation Reduction Act, Forme Solar, https://formesolar.com/cut-energy-costs-through-inflation-reduction-act/, (Accessed: 16/10/2023).

[4] Anonyms,-c Harnessing the Power of Digital: Effective Online Strategies for Clean Energy Businesses, https://underconstructionpage.com/harnessing-the-power-of-digital-effective-online-strategies-for-clean-energy-businesses/, (Accessed: 13/11/2023).

[5] Alper, M.P. Enhancing Proficiency Testing: Exploring the Innovations in ISO/IEC 17043:2023. *MAPAN* (2023). https://doi.org/10.1007/s12647-023-00684-4.

[6] Anonyms-d, Market Research Report, https://www.imarcgroup.com/us-energy-management-system-market, (Accessed: 23/11/2023).

CHAPTER II

Measurement Techniques for Nonlinear Optical Effects in Engineering Applications

Ferit ARTKIN[1]

Introduction

There is a great deal of interest in discovering materials having significant yet fast nonlinearities. As a result, this database requires expansion. Throughout the book section, methods for determining nonlinear coefficients are described. This interest, which is largely motivated The look for materials for applications such as sensor protection and all-optical switching results in two categories: nonlinear absorption (NLA) and nonlinear refraction (NLR). In many situations, the database for nonlinear optical characteristics of materials, particularly organic materials, is insufficient for establishing trends to guide synthesis efforts.

[1] Lect.Dr., Kocaeli University, Hereke Asimkocabiyik Vocational School, Department of Machinery and Metal Technologies, Machinery Programme

Organic nonlinear optics offers numerous exciting opportunities for basic study as well as real-world applications. Similar to other high-tech industries microelectronics and genetic engineering are two examples. Technical and scientific advances are likely to interact fundamentally in a way that promotes improvements in the other. Nonlinear optical phenomena, for example, are increasingly being used in optical and laser technology.

Methods for Studying of Optical Nonlinearity of Materials Applications

Certain methodologies are used in practice to explore one or more nonlinear effects. One of these methodologies, Z-scan methods, is particularly well suited for the simultaneous investigation of two nonlinear phenomena, nonlinear absorption and nonlinear refraction, both of which are related to material dielectric permeability. This technique has been updated in two ways: open aperture Z-scan is used to examine optical nonlinear absorption, and closed aperture Z-scan is used to study material nonlinear refraction.

- Degenerate Four Wave Mixing, DFWM: Used to measure the amplitude of a third order nonlinear response.
- Third Harmonic Generation: Only used to measure third order nonlinearity.
- Z-Scan: Used to determine the magnitude and sign of third order nonlinearity.
- Electro-absorption method: This approach is used to study third order nonlinearity dispersion.
- Time-Resolved Optical Kerr Effect and Transient Absorption Techniques: These techniques are used to present photophysical processes that determine nonlinearity.

A z-scan measurement is used in nonlinear optics to determine the nonlinear index n_2 Kerr nonlinearity and the nonlinear absorption coefficient using the "open" and "closed" approaches,

respectively. Because nonlinear absorption might impact nonlinear index measurement, the open approach is commonly used in conjunction with closed technique to correct the computed value (Artkin F., 2014).

Degenerate Four Wave Mixing (DFWM)

Essentially, the physical explanation of degenerate four-wave mixing is comparable to that of harmonic generation, also known as frequency mixing. The distinction here is that three spatially distinct waves of fields E1(ω,t), E2(ω,t), and E3(ω,t) at the same frequency ω interact to produce a fourth wave, E4(ω,t), in an alternate direction of transmission, yet at the same frequency.

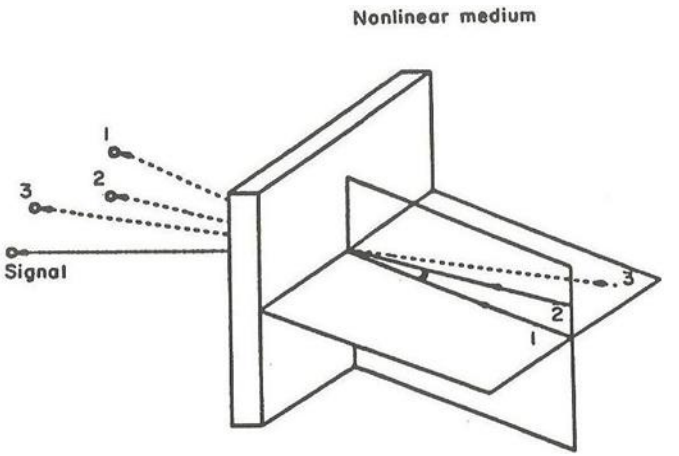

Figure 1. The illustration shows beams for degenerate four-wave mixing in the forward-wave setups.

The lightwave intensity variation along the propagation distance is negligible on the scale of light wavelength, and negligible pump beam depletion. The phase-matching condition $k_1 + k_2 + k_3 + k_4 = 0$ is likewise yielded by the wave equation, just like in the case of harmonic creation. Various beam geometries have been employed in degenerate four-wave mixing (DFWM) applications. Figures 1 and 2 show off the two common geometries. The forward-wave geometry configuration is depicted in Figure 1, where the incident

beams (E1, E2, and E3) are all traveling moving in the same way from right to left. It also displays the output beam's (signal's) phase-matched direction. In Figure 2, a backward-wave geometry is depicted. The forward and backward beams, Ef and Eb, are represented by beams E1 and E2, respectively, while the probe beam, Ep, is represented by beam E3, which is incident at a tiny angle θ with respect to E1. Since kf = - kb in this geometry, ks = kp would be necessary for the phase-matching requirement. Stated differently, in Figure 2, the phase-matched signal will be generated counterpropagating to the probe beam.

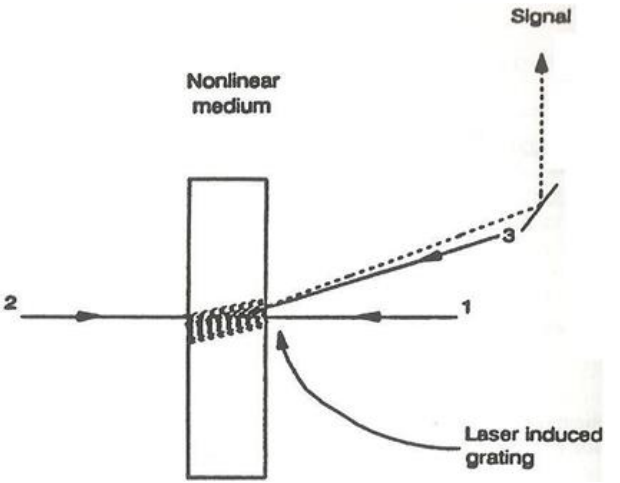

Figure 2. Diagrams showing the four beams in the backward-wave configuration for combining degenerate four waves.

Optical phase conjugation and the reverse wave geometry technique of DFWM are interchangeable (Fisher, R.A., 1983). They create a phase conjugate mirror, is taken into consideration in this respect. When a probe beam impacted on it, it can exchange energy with the other beams but is reflected back to retrace itself. The conjugate of the probe beam Ip is known as the signal Is. As a result, beam Is reconstructs any phase distortion experienced by the probing beam Ip. Dynamic holography with great contrast may be achieved with this approach. The effectiveness of the DFWM process is

commonly expressed in terms of nonlinear reflectivity R = Is/Ip in the phase-conjugation image. The following expression for the reflectivity R results from solving wave equation 1 (Yariv, A., 1978). Under the assumptions of a weak probe beam field Ep, minimal pump beam depletion, and uniform pump amplitude along the probe beam's interaction path length:

$$R = \tan^2(k|E_f E_b|l) \quad (1)$$

The overall appearance of a laser-induced grating may also be utilized to grasp the DFWM process cognitively (Eichler, H., et al., 1986). In this case, intensity modulation is caused by the relationship between a material's two coherent beams. Because a nonlinear medium's intensity changes its refractive index, the result is index modulation, This is just a diffraction grating. When the real component of the refractive index of a material with a complicated refractive index is changed, a phase grating is created (Fayer, M. D., 1982). The refractive index's imaginary component is present when changed, an amplitude grating is created. In the event of a DFWM with a reverse wave form, each two-beam pair generates three distinct gratings, However, only two of these gratings are present, provide phase-matched conjugate signals (Shen, Y.R., 1984).

Third Harmonic Generation (THG)

When the phase velocities of the fundamental and third-harmonic waves are the same. Fundamental and third-harmonic wave phase velocities, however, differ due to dispersion in the refractive indices (i.e., $n_{3\omega}$ and n_{ω} are, generally, different). As a result, $I_{3\omega}$ experiences damped oscillations for phase mismatch finite values, reducing based on its worth at $\Delta k = 0$.

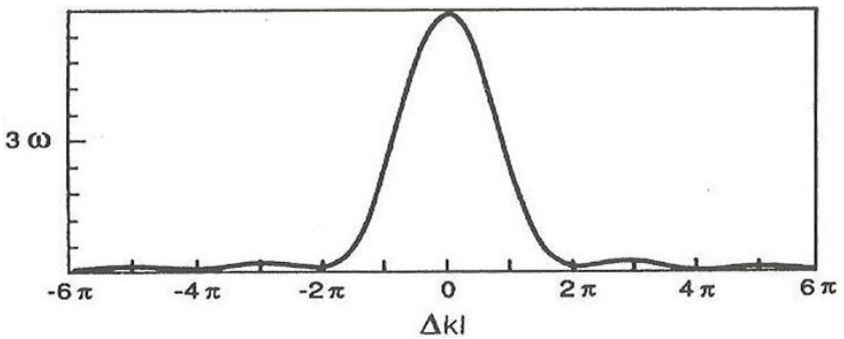

Figure 3. Plotting the third-harmonic intensity, $I_{3\omega}$, for every unit, Δk, as a function of Δkl.

$\Delta k_{1/2}$, the whole value of $I_{3\omega}$, is a helpful measure for an acceptable wave-vector mismatch in a medium that allows a significant amount of third-harmonic production. The value of this quantity is (Reintjes, J F., 1984).

$$\Delta k_{1/2} = 5.6/\, l \qquad (2)$$

The intrinsic birefringence of anisotropic media, such birefringent crystals, able could be applied for phase matching, as is the case for effective second-harmonic production. For instance, one can decide on a propagation direction for which where amazing and ordinary rays are denoted by the letters e and o. However, owing to the fundamental and third harmonic waves have radically different frequency values and there is inadequate birefringence, it is extremely difficult to accomplish

$$ne(3\omega) = no(\omega) \qquad (3)$$

Phase matching for the practical generation of third harmonics in a crystal. To the best of our knowledge. As far as we know, no crystal has been shown to exhibit phase-matched third-harmonic generation.

Dispersion effects on refractive index prevent phase matching in pure isotropic media, such as liquids, gases, or amorphous polymers. Nonetheless, combining two isotropic media

A and B (such as two gases) might theoretically result in phase matching (Reintjes, J F., 1984). So that

$$n_A(\omega) + n_B(\omega) = n_A(3\omega) + n_B(3\omega) \quad (4)$$

As a result of the normal dispersion relation, $n(\omega) < n(3\omega)$. In order for equation 4 to hold, one of the materials must compensate for $n_B(\omega) < n_B(3\omega)$ and display anomalous dispersion, which characterizes the condition $n_A(\omega) > n_A(3\omega)$. Alkali metal vapors have been known to exhibit this kind of anomalous dispersion (Reintjes, J F., 1984), (Bloom, D. M., 1975).

If phase-matching is not present, the interaction length can be changed to maximize third-harmonic generation. When the interaction length is altered, either by translating a wedge-shaped sample or rotating the sample as in the Maker fringe approach, the harmonic intensity oscillates for a fixed value of Δk. The coherence length Ic is given by (Reintjes, J F., 1984) as follows:

$$I_c = \pi/\Delta k \quad (5)$$

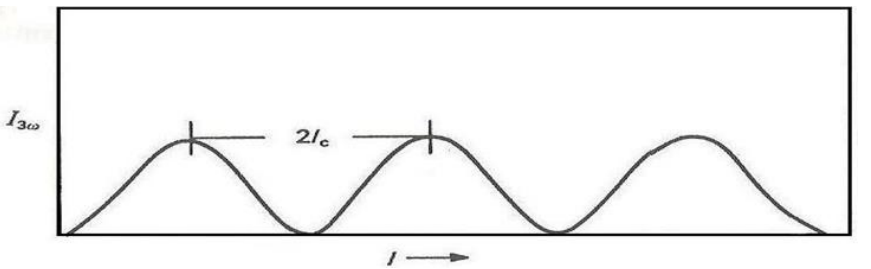

Figure 4. To alter the route length l, the wedge fringe pattern for the third-harmonic signal $I_{3\omega}$ which is acquired as a sample, is translated.

A fringing curve describes the oscillatory behavior of $I_{3\omega}$ when the interaction duration is varied. When a wedge-shaped sample is translated, the interaction length changes, resulting in the wedge fringe pattern seen in Figure 4. Harmonic creation, or, more broadly, frequency mixing, is a coherent process as there's a clear

correlation between the phase of the input waves and the out wave generated at the new frequency.

Z-Scan

The Z-scan technique has become a standard for isolating the nonlinear variations in absorbance and index and has been rapidly embraced by the nonlinear optics community. Generally speaking, Any nonlinear optical method that alters the absorption coefficient and/or refractive index can be detected using a Z-scan approach making it impossible to identify the underlying physical processes that are present (Paras N. Prasad., et al., 1991).

A nonlinear sample causes a change in the overall refractive index that is proportional to both the nonlinear refractive index of the material and the beam intensity as it passes through it. This leads to the following modification in the most basic scenario, when there are just third-order nonlinearities:

$$n = n_0 + n_2 I \quad (6)$$

In this case, I represents the excitation intensity, The linear refractive index is denoted by n_0, the third-order nonlinear refractive index by n_2, and the overall refractive index is represented by n. When a lens is applied to a Gaussian incoming beam, the intensity profile of the beam will cause a nonlinear refractive index change in the profile of the beam. Consequently, a refractive index lens is being produced in the nonlinear medium by the beam propagation.

Sheik Bahae et al.'s (M. Sheik-Bahae et al., 1990) transmission Z-scan technique is a simple and accurate single beam methodology for detecting the amount and sign of the real and imaginary components of third order nonlinear susceptibility.

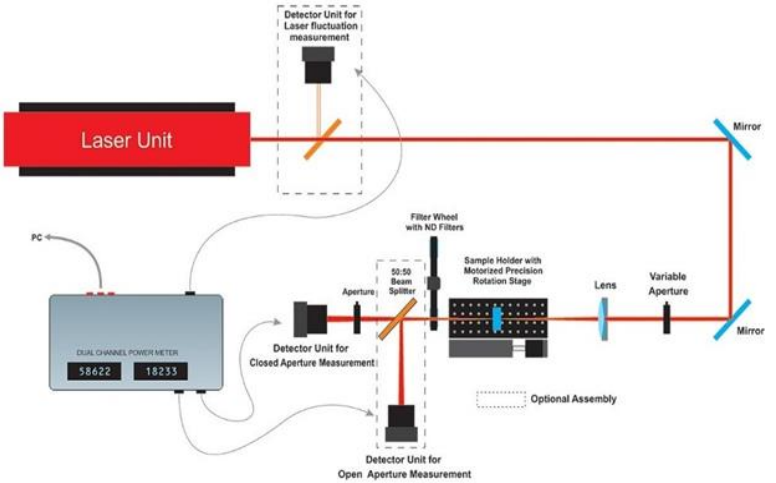

Figure 5. Experimental Z-scan setup (holmarc.com, 2023).

The foundation a lens's focal plane (the focusing lens L1 in Figure 5). A detector positioned behind the sample in the far field with an aperture in front of it (closed aperture Z-scan) tracks the refractive index lens effect as the sample moves. As a result, the sample's varying focusing/defocusing caused by the light-induced lens is assessed. The focusing lens, the translation stage, the three primary components are the detector, the detector, and the detector of the experimental setup for transmission Z-scan investigations, which is shown in Figure 5.

Electro-absorption Method (EA)

An effective method for examining a material's third-order nonlinear optical susceptibility $\chi^{(3)}$ dispersion is electro-absorption (EA) spectroscopy. It modifies a material's absorption spectra by applying an electric field, revealing details about alterations in the material's optical and electronic structure.

The electrons in the material interact with this electric field. This is noticed as a shift in the transmitted light's intensity at various wavelengths. The EA spectrum is useful for figuring out the

distribution of $\chi^{(3)}$ over a variety of wavelengths. The third-order nonlinearity dispersion of many different materials, such as organic semiconductors, polymers, nanomaterials, and quantum dots, has been extensively studied using the EA approach. New materials with improved nonlinear optical characteristics for use in optical communications, lasers, and other technologies can be developed using the data gathered from EA experiments.

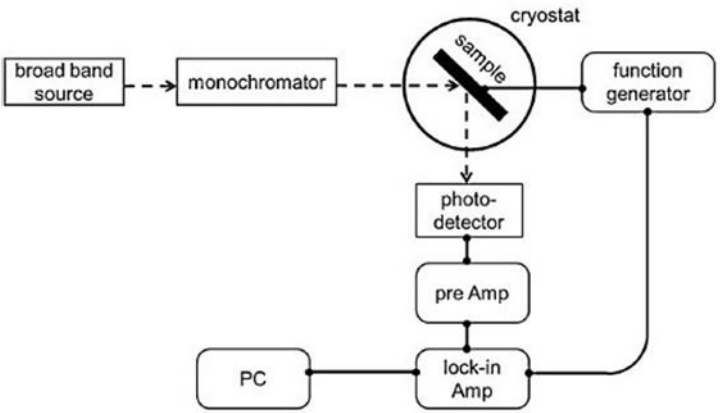

Figure 6. Diagram showing the Electro Absorption (EA) spectroscopic setup (Lai T.H., et al. 2013).

The EA spectrum is frequently analyzed using the Kramers-Kronig relations. It measured absorption change, these relations help distinguish the real and imaginary components of $\chi(3)$. Additional nonlinear optical characteristics, such as the nonlinear susceptibility of second order $\chi^{(2)}$, can also be studied using the EA approach. The EA approach comes in a variety of forms, each having pros and cons of its own. Photocurrent spectroscopy (PCS), differential electro-absorption (DEA), and linear electro-absorption (LEA) are a few popular versions.

To sum up, the electro-absorption technique is a useful instrument for researching the dispersion of materials with third-order nonlinearity. It gives researchers a way to quantify the alterations in electronic structure and optical characteristics brought

about by the utilization of an applied electric field, important information for creating novel materials with improved nonlinear optical functions **(**Lai T.H., et al., 2013; Loukos, P., et al., 2014).

Time-Resolved Optical Kerr Effect and Transient Absorption Techniques

Transient absorption (TA) and time-resolved optical Kerr effect (OKE) are two effective methods for examining the ultrafast dynamics of materials, especially in condensed phases. These methods provide complementary insights into molecular interactions, structural alterations, and excited state dynamics. In isotropic materials, A third-order nonlinear optical phenomenon is the OKE. The material becomes optically anisotropic upon contact with power laser sources, leading to a transient birefringence. The laser pulse's electric field produces the atoms in the material to distort their electron clouds, which results in a transient dipole moment and birefringence.

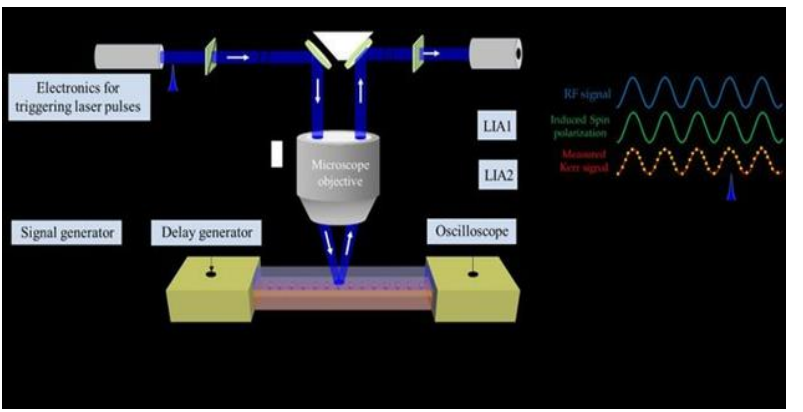

Figure 7. Transverse magneto-optical Kerr effect measurements with time resolution (TR-TMOKE) experimental configuration (Auvray F., et al., 2018).

OKE has a number of benefits. High temporal resolution: femtosecond timeframe dynamics may be measured. Non-invasive: No modifications or changes are required to the sample. Sensitive to

a variety of phenomena: It may examine structural alterations, vibrational motion, and changes in electronic structure. Also, OKE has some restrictions: Restricted spectral range: It usually extends only to the near-infrared spectrum. Indirect measurement: It excited state dynamics, more analysis is necessary as the refractive index variation affects the signal that is captured.

Using transient absorption spectroscopy, one may quantify a material's change in After being stimulated by a laser pulse, absorption occurs. The creation of excited states and environment cause this shift in absorption. TA measurements consist of: Pump pulse: The material is energized and excited states a femtosecond laser pulse produces. Probe pulse: The excited state population is examined by a weaker probe pulse that. Measuring the change in absorption: OKE and TA are two effective methods for examining the ultrafast dynamics of substances. Which method you chose to use will rely on the specific facts you are looking for.

In several instances, the combined use of OKE and TA yields a thorough understanding of a material's ultrafast dynamics. For instance, While OKE certain excited state species may be tracked using TA (Hosung, K., et al. 2021).

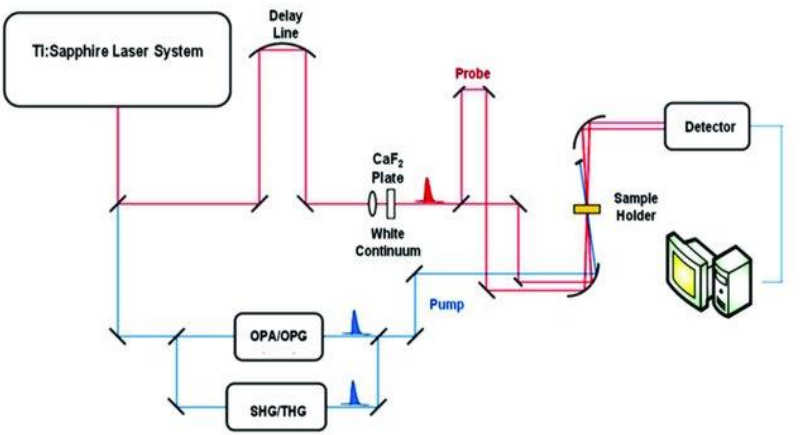

Figure 8. Diagram showing the general setup for Transient Absorption Spectroscopy (TAS) (Patrizi B., 2020).

Conclusion

Exciting opportunities arise from nonlinear optical phenomena for a variety of sophisticated technologies, from innovative materials with specialized features to all-optical signal processing. Precisely quantifying these impacts is essential to comprehending their fundamental physics and maximizing their utilization.

This review examined many methods that are often used to quantify nonlinear optical characteristics. It particular impact being researched, as well as required degree of precision and sensitivity. A straightforward and sensitive technique for figuring out optical coefficients, such as nonlinear refraction and nonlinear absorption, is the Z scan approach. Because of the ease of use and low cost of execute, it is extensively employed. In conclusion, precise and dependable measuring methods are crucial in the study of nonlinear optics. It is essential for researchers to comprehend their particular requirements and to successfully explore and make use of the intriguing phenomenon of nonlinear optics. This evaluation has focused mostly on third-order nonlinear effects. Higher-order nonlinearity measurement techniques are also available and under development. Aside from performance, other considerations that may impact the measuring technique choice include equipment availability, cost, and complexity. The limits can be measured are continually being pushed by developments in laser technology and apparatus, As a result, more complicated and sensitive measurement techniques have emerged.

Acknowledge

This study serves as the foundation for my doctoral studies at Sofia Technical University. This research was improved for my doctoral work. A portion of the material and data utilized in this piece came from the PhD research Computer-aided Z-Scan Testing Apparatus Integrated Apparatus Integrated into Servo Motor and PLC for Investigation of Non-linear Materials' Permeability. I would

want to express my gratitude to Associate Prof. Dr. Ivanka Kalimanova of the Technical University of Sofia, and Prof. Dr. Fevzi Necati Ecevit of Gebze Technical University.

REFERENCES

Artkin F., (2014), PhD Thesis, Computer Aided Z-Scan Testing Apparatus Integrated into Servo Motor and PLC for Investigation of Non-Linear Ma- terials' Permeability, Technical University Of Sofia.

Auvray F., Puebla J., Xu M., Rana B., Hashizume D.,, Otani Y., Spin Accumulation at Nonmagnetic Interface Induced by Direct Rashba–Edelstein Effect, Journal of Materials Science: Materials in Electronics (2018) 29: 15664-15670 https://doi.org/10.1007/s10854-018-9162-5.

Bloom, D. M., G. W. Bekkers, J. F. Young, and S.E. Harris, Appl. Phys. Lett. 26, 687 (1975a).

Bloom, D. M., J. F. Young, and S.E. Harris, Appl. Phys. Lett. 27, 360 (1975b).

Eichler, H., P. Gunther, and D. W. Pohl, Laser Induced Dynamic Gratings, Springer-Verlag, Berlin, (1986).

Fayer, M. D., Annu. Rev. Phys. Chem. 33, 63 (1982).

Fisher, R.A. (Ed.), Optical Phase Conjugation, Academic, New York, (1983).

Hosung Ki, Seungjoo Choi, Jungmin Kim, Eun Hyuk Choi, Seonggon Lee, Yunbeom Lee, Kihwan Yoon, Chi Woo Ahn, Doo-Sik Ahn, Jae Hyuk Lee, Jaeku Park, Intae Eom, Minseok Kim, Sae Hwan Chun, Joonghan Kim, Hyotcherl Ihee, and Jeongho Kim, Optical Kerr Effect of Liquid Acetonitrile Probed by Femtosecond Time-Resolved X-ray Liquidography, *J. Am. Chem. Soc*. (2021), 143, 35, 14261–14273, https://doi.org/10.1021/jacs.1c06088.

https://holmarc.com/z_scan_system.php, Accessed 2 December 2023.

Lai T.H., Tsang S.W., Manders J.R., Chen S., So F., Properties of Interlayer for Organicphotovoltaics, Materials Today, Volume 16, Number 11, (2013), 424-432.

Loukos, P., Papagiannouli, I., Bourlinos, A. B., Zboril, R., Couris, S., Third-Order Nonlinear Optical Response and Optical Limiting of Colloidal Carbon Dots. Opt. Express (2014), 22, 12013-12027.

M. Sheik-Bahae et al., "High-sensitivity, single-beam n_2 measurements", Opt. Lett. 14 (17), 955 (1989).

M. Sheik-Bahae et al., "Sensitive measurement of optical nonlinearities using a single beam", IEEE J. Quantum Electron. 26, 760, (1990).

Paras N. Prasad, David J. Williams, Introduction to Nonlinear Optical Effects in Molecules and Polymers John Willey & Sons Inc., U.S., (1991), ISBN: 978-0-471-51562-3.

Patrizi B., Cozza C., Pietropaolo A., Fogg P., Cumis M.S., Synergistic Approach of Ultrafast Spectroscopy and Molecular Simulations in the Characterization of Intramolecular Charge Transfer in Push-Pull Molecules, (2020), Molecules MDPI 25(2):430, DOI: 10.3390/molecules25020430.

Reintjes, J F., Nonlinear Optical Parametric Process in Liquids and Gases, Academic, New York, (1984).

Shen, Y.R., The Principles of Nonlinear Optics, Wiley, New York, Chap. 2, (1984).

Yariv, A., IEEE J. Quantum Electron. QE-14, 650, (1978).

CHAPTER III

Properties And Use Of Ultra High Molecular Weight Polyethylene (Uhmwpe) Materials In The Ballistic Field

Kubilay HAN[1]
Ömer ÇERLEK[2]
Muahmmed Asım KESERCİOĞLU[3]

Introduction

In the 1950s, Ultra High Molecular Weight Polyethylene (UHMWPE), developed by a German company, began to take the form of fibers towards the end of the 1990s. UHMWPE is a type of polyethylene with a density ranging from 0.930 to 0.935 g/cm3 and a molecular weight ranging from 2 to 6 million. UHMWPE is a special variant of thermoplastic polyethylene and is also referred to

[1] M.Sc., Sakarya University of Applied Sciences, kubilayhan@subu.edu.tr
[2] M.Sc., Sakarya University of Applied Sciences, omercerlek@subu.edu.tr
[3] M.Sc., Sakarya University of Applied Sciences, mkesercioglu@subu.edu.tr

as High Modulus Polyethylene (HMPE). This material is characterized by extremely long molecular chains, typically extending up to 3.5 to 7.5 million atomic weight units. The extended chain structure strengthens interactions between molecules, providing the material with exceptional impact resistance and hardness. Thanks to its long chain structure, UHMWPE is one of the thermoplastic materials with the highest impact resistance and hardness (Wei and Benson, 2011; Han et al., 2023).

The structural analysis of UHMWPE indicates a limited distance between the crystalline arrangements within the polymer chain, emphasizing the material's dense structure. This feature enables UHMWPE to be stronger and have higher impact resistance compared to other thermoplastic materials. Additionally, the effective transmission of the load carried by the molecular bonds on the polymer chains contributes to the strengthening of this characteristic (Beşergil, 2022).

Similar methods to the Ziegler Natta catalyst used for traditional HDPE are applied in the synthetic production of UHMWPE resins. The catalyst typically consists of organo-aluminum components such as titanium chloride, diethylaluminum, or triethylaluminum. Most of the processes described above are used in the production and shaping of UHMWPE in its liquid state. At the molecular level, the carbon backbone of UHMWPE has a flexible structure, allowing it to bend, twist, and fold in regular crystal regions. This chain folding enables the molecule to form locally organized leaf-like crystalline lamellar regions. These lamellae settle within amorphous regions and can connect with surrounding lamellae through bonding molecules. Figure 1 provides a schematic diagram at the molecular level illustrating these morphological features of UHMWPE (Beşergil, 2022; Han et al., 2023).

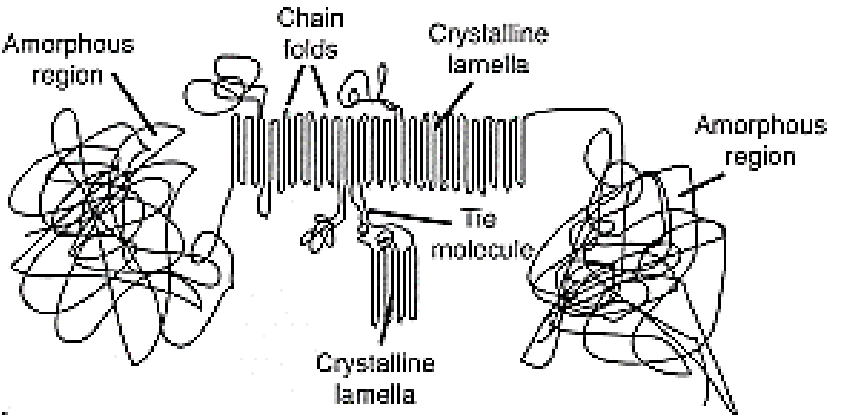

Figure 1. Schematic diagram of the morphological features of UHMWPE (Beşergil, 2022)

UHMWPE is a semi-crystalline polymer consisting of a crystalline and a non-crystalline amorphous phase. In the amorphous region, macromolecular chains are randomly arranged. In the crystalline region, orthorhombic unit cells covered with groups and twisted chains form a thin layer. These thin layers come together to form larger structures known as spherulites. The thin layers are assembled, and bonding molecules integrate into each layer structure. Crystal lamellae are microscopic and not visible to the naked eye. Lamellae refract visible light at room temperature, giving UHMWPE a white, opaque (matte) appearance. Above the melting temperature of the lamellae, UHMWPE becomes translucent. Lamellae are typically arranged in thicknesses of 10-15 nm and lengths of 10-50 μm (Kurtz et al., 1999; Edidin et al., 2000).

Production Methods of UHMWPE Materials

Numerous studies on the production of UHMWPE have highlighted deficiencies in the consolidation process, along with factors that lead to deformation and particle obstruction. Consequently, the properties of UHMWPE are dependent on both synthesis and manufacturing processes. The high molecular weight of UHMWPE complicates the integration of UHMWPE powder into

the free-flowing melt process. The long chain components of UHMWPE do not exhibit flow characteristics above the melting temperature; instead, they transition from a non-transparent to a semi-transparent structure, making the crystalline structure visible. Therefore, the UHMWPE production process has become a competitive field for manufacturers. There are four different production methods for UHMWPE: compression molding, ram extrusion, hot isostatic pressing (HIP), and direct compression molding (DCM). Compression molding and ram extrusion are two of the most commonly used processes for consolidating UHMWPE powders (Seok-Jo, 2003).

Compression Molding

In the compression molding process, UHMWPE powder is placed into a mold and then heated under pressure, transforming it into molds and sheets. The temperature of the process typically ranges between 200-250 °C, and a slow cooling process is employed to prevent potential fractures and cracks. The length of the semi-finished sheets usually varies from 1 to 2 meters up to 2-8 meters, while their thicknesses exhibit different values ranging from 1 mm to 200 mm. Finally, the mold and sheets undergo machining in a machine for the final product processing step. Figure 2 illustrates the compression molding production process of UHMWPE (Kurteri, 2008; Kellersohn, DIR., 1990; Li and Burstein, 1994).

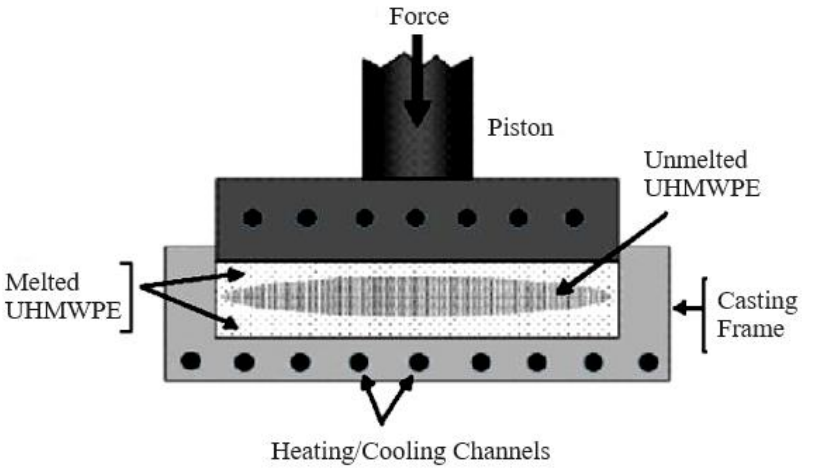

Figure 2. Compression molding production of UHMWPE (Kurteri, 2008)

Ram Extrusion

In the ram extrusion process, a motor rotates a screw enclosed in a heated chamber, allowing plastic granules to melt under temperature and pressure. The molten plastic takes shape along the mold, flowing into a long channel for cooling. The process temperature typically ranges from 160 to 220 °C. The shape of the mold also determines the form of the channel. After cooling, the plastic solidifies to assume its final shape. Products resulting from extrusion may include T-sections, U-sections, square sections, I-sections, L-sections, and circular sections. Figure 3 illustrates the ram extrusion production process of UHMWPE (Kurteri, 2008; Kellersohn, 1990; Li and Burstein, 1994).

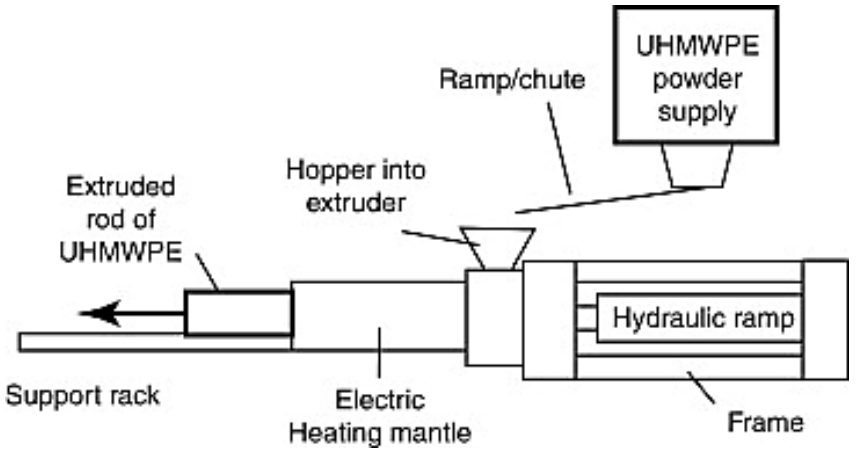

Figure 3. Ram Extrusion Production of UHMWPE (Li and Burstein, 1994)

Hot Isostatic Pressing (HIP)

This multi-stage transformation process begins with the cold isostatic pressing of a cylindrical component. During this cold isostatic pressing, a significant portion of the air is expelled. Subsequently, the compressed "green" bars are sintered in a HIP furnace. Inside the furnace, the oxygen level is kept low to prevent degradation of UHMWPE. The resulting rod-shaped billet material from this process is isotropic due to the hydrostatic sintering process and can be obtained using the resin's pressure casting method. The completed implants at the end of this process are manufactured using turning or milling processes (Kurteri, 2008).

Direct Compression Molding (DCM)

The polyethylene material used in the direct compression molding (DCM) process effectively transforms the resin into a fully processed or semi-processed piece. Separate casting molds are employed for each individual operation in this process. An advantage of DCM is achieving a completely smooth surface by eliminating processing marks on the joint surface. Additionally, it is

possible to reach high processing pressures when needed, as the casting surface area for each piece is smaller than the area used in expansive molds for pressure casting plates. The physical and chemical properties of the final product can be made more suitable through modifications that can be made in the DCM casting cycle (Han et al., 1981; Truss et al., 1980; Chen et al., 1981).

Properties of UHMWPE Materials

UHMWPE is a polymer with odorless, tasteless, and non-toxic properties. It exhibits high resistance to all corrosive chemicals except oxidizing acids. Due to the absence of polar groups in its molecules, it does not absorb water, making its moisture absorption very low. Additionally, it has a very low coefficient of friction, is self-lubricating, and highly resistant to wear. It has a slightly lower friction coefficient than Nylon and Acetal, similar to that of Teflon. Its resistance to wear is higher than Teflon, and it is 15 times more durable than carbon steel. The average mechanical properties of UHMWPE materials are provided in Table 1.

Table 1. Some mechanical and physical properties of UHMWPE material (Yılmaz, 2010)

PROPERTIES	UNIT	VALUE
Density	gr/cm^3	0,94
Molecular Weight	gr/mol	> 4.000.000
Water Absorption	%	0.01
Tensile Strength	MPa	25
Strain Failure	%	>300
Notched Impact Strength	kJ/m^2	unbreakable
Charpy Notched Impact Strength	kJ/m^2	>210
Coefficient of Friction	-	0,1-0,15
Hardness	Shore D	60-80
Melting Point	°C	130-138
Min. Operating Temperature	°C	-269
Maks. Operating Temperature	°C	90
Coefficient of Linear Expansion	$°C^{-1}$	$2x10^{-4}$
Dielectric Strength	KV/cm	900

Although the tensile mechanical behavior of UHMWPE is highly complex, it is possible to categorize its behavior into four distinct regions based on studies in the literature (Peterlin, 1971; Mortensen, 2007; Yang et al., 2010; Liang et al., 2014). The tensile curve of UHMWPE materials is presented in Figure 4.

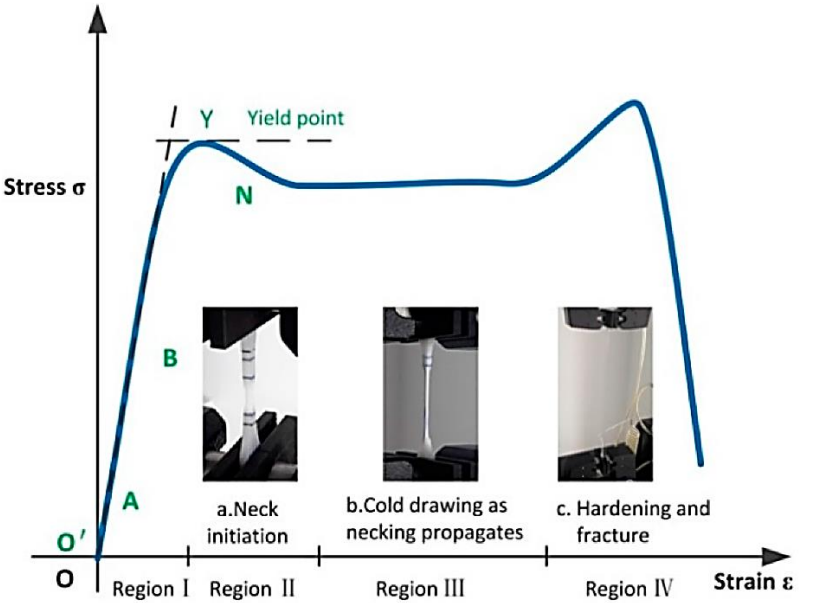

Figure 4. Typical engineering stress-strain curve of UHMWPE material under tension (Xu et al., 2016)

As shown in Figure 4, the tensile mechanical behavior of UHMWPE consists of sequentially linear elastic, strain softening or onset of necking, cold drawing hardening, and ultimately hardening-fracture regions. The first region is where UHMWPE undergoes linear elastic deformation and is typically very small. This region corresponds to the partial extension of the amorphous phase, limited somewhat parallel to the crystalline phase. The second region is characterized by the fragmentation of crystalline lamellae at spherical poles, resulting in the material exhibiting non-linear behavior (Peterlin, 1971; Defebvin et al., 2016).

At this stage, the yield point emerges along with the fragmentation of crystalline lamellae, leading to largely dispersed crystalline block structures connected by a limited amorphous phase. At the onset of this stage, the contribution of crystalline lamellae to stress is no longer effective; however, the stress in the crystalline network continues to increase with the contribution of the limited amorphous phase (Bartczak, 2018).

During the third stage, the crystalline lamellar blocks rotate to align in the direction of tension (Defebvin et al., 2016). Crystal blocks progress from the poles to the equatorial regions, undergoing a fibrillation process that involves extracting chains from crystalline lamellae (Peterlin, 1971). Therefore, chains that were previously part of crystalline lamellae become amorphous, increasing the length of the limited amorphous phase.

The decrease in the crystalline ratio is due to the fibrillation process, but this arises from the strong orientation within the chains. Fibrils in the loading direction result in the formation of new crystalline areas within the fibrils. Due to consecutive fibrillation-re-crystallization steps, chain unraveling is delayed. Finally, when the fibrils reach their maximum elongations corresponding to the last stage, a chain locking event occurs, significantly increasing the stress (Defebvin et al., 2016).

During the fibrillation process in the third stage and the combination of re-crystallization in the third and fourth stages, it is observed that the crystalline ratio remains almost constant throughout the entire deformation process (Wang et al., 2017). However, while the crystalline ratio undergoes a change, albeit not significantly, the role and size of crystalline regions change significantly throughout the entire deformation process.

Ultra-High Molecular Weight Polyethylene materials possess numerous significant properties, such as:

- Good insulating properties
- High corrosion resistance

- Excellent energy absorption
- Good dimensional stability
- Strong chemical resistance
- Water resistance
- Self-lubricating capability
- Highest abrasion resistance among all plastic materials
- Highest impact resistance among all plastic materials
- Lower coefficient of friction than PTFE
- Highest sliding abrasion and notched impact resistance among all commercial plastics

These properties make UHMWPE materials stand out in various applications (Harvey and Stein 1999).

Applications of UHMWPE Materials

UHMWPE is a unique polymer with exceptional mechanical and physical properties. These include the ability to create a smooth and slick surface, superior impact and abrasion resistance, and low intrinsic density. Consequently, UHMWPE is known for its capability to transform into various structures. These advantageous properties make it widely used in various fields today. UHMWPE is particularly prevalent in the field of ballistic protection. The popularity of this material in ballistic applications arises from its various advantages:

Lightweight: UHMWPE is significantly lighter compared to other ballistic materials. This enhances the mobility of individuals wearing armor and reduces overall load.

High Strength: The high molecular weight of UHMWPE equips the material with exceptional strength properties. This increases its capacity to absorb impacts and provides effective protection.

Flexibility: UHMWPE is a flexible material that, due to its ability to absorb impact energy, offers effective protection against various impact angles.

Durability: UHMWPE is resistant to chemicals and withstands various environmental conditions. These features enhance the material's long-term performance.

Excellent Energy Absorption: High energy absorption capacity enhances UHMWPE's ability to absorb ballistic impacts. This feature increases deformation by distributing impact energy.

These advantages popularize the use of UHMWPE in ballistic applications. This material is commonly employed in armored vehicles, military helmets, body armor, and ballistic plates. UHMWPE-based armor materials play a critical role in ensuring the protection of military and security personnel.

In their study, Fallah et al. (2014) investigated the dynamic responses of ultra-high molecular weight polyethylene (UHMWPE) fiber composites, which could be an alternative to steel in military applications, against explosive events. They analyzed the results of regional air-blast loading tests conducted on Dyneema HB26 panels. During these tests, various failure modes were observed, including permanent deformation, delamination, planar sliding, boundary buckling, regional melting, and matrix damage. The experimental results were compared with numerically simulated responses of soft steel and armor plates with the same areal density.

In an experimental study conducted by Hu et al. (2017), researchers examined the ballistic behavior of mosaic Silicon Carbide (SiC) ceramics bonded with Ultra-High Molecular Weight Polyethylene (UHMWPE) plates. Experiments against 7.62 mm x 51 mm Armor-Piercing (AP) bullets systematically investigated the effect of SiC ceramics on the ballistic performance of mosaic SiC/UHMWPE composite armor. The results indicated a direct correlation between the ballistic performance and the geometry of mosaic ceramics, revealing that an increase in the collapse amount in the UHMWPE plate consumed more kinetic energy of the bullet. The experiments encompassed various armor systems and detailed the role of the SiC ceramic front layer during the bullet penetration process. The findings demonstrated that the size of mosaic ceramics

enhanced bulletproof properties and highlighted the potential of the SiC ceramic and UHMWPE combination in lightweight armor design.

The study conducted by Liu et al. (2017) primarily focused on exploring the rational design of composite backing plates to create a high-performance armor system. In this study, a sandwich structure with a ceramic cylinder layer was chosen, consisting of a third layer of Ti6Al4V, a carbon fiber layer, and an aluminum alloy layer. The researchers created armor systems by combining these layers with Ti6Al4V as the first layer and UHMWPE as the middle layer, using alumina ceramic materials. They extensively examined the penetration process against a 12.7 mm armor-piercing bullet with a velocity of 818 m/s, discussing the ballistic mechanisms of each layer in composite backing plates experimentally and numerically in detail.

In his thesis project titled 'The Use of Composite Materials in the Manufacture of Ballistic Protective Equipment,' Bulut (2003) extensively examined the ballistic resistance values, mechanical properties, corrosion and chemical resistance properties, design criteria, manufacturing stages, and testing methods of Aramid and UHMWPE materials used in the manufacture of ballistic protective equipment. The results obtained showed that the ballistic performance of a material depends on its ability to absorb energy in a limited area and efficiently dissipate the absorbed energy. Tensile strength, elongation, and the speed of sound transmission in the fiber were identified as the most important parameters in fiber-based protectors.

Candan (2007), in his article titled 'Investigation of Terminal Ballistic Properties of Pressed and Unpressed Ultra-High Molecular Weight Polyethylene (UHMWPE) Armor Plates Against Small Arms,' investigated the general production stages, test methods, and results applied to armored vehicles in accordance with world standards, as well as the evaluation of the damage zone in terms of terminal ballistics for pressed and unpressed Ultra-High Molecular

Weight Polyethylene (UHMWPE) armor plates with the same areal density. According to the results obtained, the average collapse value obtained in pressed armor plates was determined to be 65% smaller than the average collapse value obtained in unpressed armor plates.

In the article 'The Effect Of Processing Conditions On The Performance Of UHMWPE-Fibre Reinforced Polymer Matrix Composites' written by Fejdyś et al. (2016), the performance of UHMWPE HB26 ballistic composite material was analyzed by altering the main pressing parameter, which is the temperature, in the manufacturing of ballistic composite materials. The results of this study provided insight into determining the most suitable pressing conditions for ballistic and personal protective applications. The optimum temperature for HB 26 was found to be T_press = 130 °C and T_packet = 115 °C. It was observed that exceeding the temperature of 130 °C negatively affected the material's properties.

In the article titled 'Design And Ballistic Performance Of Hybrid Composite Laminates' authored by Ćwik et al. (2016), the aim was to find the most cost-effective hybrid composite material as a replacement for expensive ballistic composites. In the initial stage of the study, 20 different hybrid composite materials were tested by firing bullets with a diameter of 20 millimeters at a speed of 1 km/s, using 100% HMWPE composite material as a reference. The hybrid composite materials with the best performance were then compared in the second stage with other hybrid composite materials containing STF. As a result, it was observed that lower-cost, improved hybrid composite materials could be used as alternatives to high-cost, high-performance composites. Among the examples, the best hybrid concept was selected with a configuration where fiber-reinforced polypropylene is in the front and UHMWPE is in the back.

In his study conducted in 2014, O'Masta investigated the structure, mechanical properties, dynamic deformation, and failure mechanisms of UHMWPE-reinforced [0/90] polymer matrix composites during ballistic impact. The primary mechanisms identified as a result of the analysis include penetration on

UHMWPE, occurring through the progressive fracture of fiber layers under the impact of the bullet. The number of fractured layers increased with the impact velocity. Bullet breakup by an intervening aluminum plate distributes interfacial forces between the bullet and laminate material over a broader area simultaneously in spatial and temporal dimensions. This reduces contact pressure, thereby increasing the ballistic limit of the laminate material.

In the study conducted by Nguyen (2015), the ballistic performance of thick UHMWPE composite material was examined, highlighting key penetration and fracture mechanisms. The analysis of the material under impact revealed that the penetration of thick targets occurred in two stages. After the formation of the initial cutting force, a significant global deformation occurred at the rear part where the target separated. In thin targets, only the swelling stage was identified. The comprehensive experiments in this study characterized for the first time the allowable ratios of sliding and swelling in the target at values close to the ballistic limit. It was observed that the stopping effect of cutting force increased with target thickness and impact velocity.

Various studies in the literature have focused on both failure mechanisms (B.G. Liu et al., 2019) and protective performances (Zhang et al., 2020; Zhang et al., 2019; Gemi et al., 2018). In a study by Attwood et al. (2015), the compressive behavior of the fiber material was investigated when loaded in the direction of reinforcing fibers. It was noted that the compressive strength of UHMWPE fiber-reinforced composite material was affected not by the fibers but by the micro-bending of the composite sheet. Duan et al. (2006) investigated the effect of frictional force between lead, fabric, and fabric yarn on the energy absorption of laminates. They suggested that there was a coupling effect between the two frictional forces, which could not only enhance energy absorption but also increase the tensile energy and kinetic energy of the fabric. In a comparison of stitched and unstitched fiber-reinforced composite materials for ballistic protection performance, Hosur et al. (2004) found that stitched fiber-reinforced composites had higher ballistic limits than

unstitched fiber materials, and this limit increased with thickness. In a study on the damage modes of fiber composite materials, Paul et al. (2007) found that the failure sequence of composite materials included matrix cracking, fiber breaking, delamination, and damage to the support material. Masta et al. (2015) investigated the impact response behavior of UHMWPE fiber-reinforced composite materials using high-speed cameras and X-ray scanning technology. They indicated that reinforcing fibers could significantly enhance the protective performance of composite materials when the total weight was similar.

CONCLUSION

There are many more studies in the literature on this subject. The research conducted indicates that UHMWPE materials exhibit high performance in terms of lightweight, high strength, flexibility, durability, and excellent energy absorption properties. Therefore, these materials can be comfortably used in armored vehicles, military helmets, body armor, and ballistic plates.

REFERENCES

Attwood, J. P., Fleck, N. A., & Waldley, H. N. G. (2015). The compressive response of ultra-high molecular weight polyethylene fibres and composites. Int. J. Solids. Struct., 71, 141-145.

Bartczak, Z. (2018). Evaluation of effective density of the molecular network and concentration of the stress transmitters in amorphous layers of semicrystalline polyethylene. Polymer Testing, 68(March), 261–269.

Beşergil, B. (2022, Şubat 2). Mühendislik Plastikleri; Ultra Yüksek Molekül Ağırlıklı Polietilen. Prof. Dr. Bilsen Beşergil. http://bilsenbesergil.blogspot.com/p/blog-page_719.html

Bulut, H. (2003). Balistik Koruyucu Teçhizatın İmalatında Kompozit Malzeme Kullanımı (Yüksek Lisans Tezi, İstanbul Teknik Üniversitesi Fen Bilimleri Enstitüsü, İstanbul).

Candan, C. (2007, Kasım). Hafif Silahlara Karşı Preslenerek ve Preslenmeden Üretilen Yüksek Yoğunluklu Polietilen (UHMWPE) Zırh Plakalarının Terminal Balistik Özelliklerinin İncelenmesi. 8. Uluslararası Kırılma Konferansı Bildiriler Kitabı, 7-9 Kasım 2007, İstanbul.

Chen, K. C., Ellis, E. J., & Crugnola, A. (1981). Effects of molding cycle on the molecular structure and abrasion resistance of ultra-high molecular weight polyethylene. ANTEC '81, 39, 270-272.

Cwik, T. K., Iannucci, L., Curtis, P., & Pope, D. (2016). Design And Ballistic Performance Of Hybrid Composite Laminates. Applied Composite Materials. DOI: 10.1007/s10443-016-9536-x

Defebvin, J., Barrau, S., Stoclet, G., Rochas, C., & Lefebvre, J. M. (2016). In situ SAXS/WAXS investigation of the structural evolution of poly(vinylidene fluoride) upon uniaxial stretching. Polymer, 84, 148–157.

Duan, Y., Keefe, M., Bogetti, T. A., et al. (2006). A numerical investigation of the influence of friction on energy absorption by a high-strength fabric subjected to ballistic impact. Int. J. Impact. Eng., 32, 1299-1312.

Edidin, A. A., & Kurtz, S. M. (2000). The influence of mechanical behavior on the wear of four clinically relevant polymeric biomaterials in a hip simulator. Journal of Arthroplasty, 15, 321-331.

Fallah, A. S., Micallef, K., Langdon, G. S., Lee, W. C., Curtis, P. T., & Louca, L. A. (2014). Dynamic response of Dyneema® HB26 plates to localised blast loading. International Journal of Impact Engineering, 73, 91-100.

Fejdyś, M., Łandwijt, M., Kucharska-Jastrząbek, A., & Struszczyk, M. H. (2016). The Effect of Processing Conditions on the Performance of UHMWPE-Fibre Reinforced Polymer Matrix Composites. FIBRES & TEXTILES in Eastern Europe, 24(4), 112-120. DOI: 10.5604/12303666.1201140

Gemi, L., Kayrici, M., & Uludag, M. (2018). Experimental and statistical analysis of low velocity impact response of filament wound composite pipes. Compos. B. Eng., 149, 38-48.

Han, K., Akin, Y., & Kesercioğlu, M.A. (2023, Mayıs 12). CNC freze ile işlenen ultra yüksek molekül ağırlıklı polietilen (UHMWPE) plakaların yüzey kalitesini etkileyen faktörlerin incelenmesi. 1. Bilsel International Harput Scientific Researches Congress, 25-26 Kasım, Elazığ/Türkiye, Cilt 1, 36-44.

Han, K. S., Wallace, J. F., Truss, R. W., & Geil, P. H. (1981). Powder compaction, sintering, and rolling of ultra-high molecular weight polyethylene and its composites. J. Macromol. Sci.-Phys., B19, 313-349.

Han, K., Tüylü, A., & Kesercioğlu, M. A. (2023). Investigating Surface Quality Parameters in CNC Milling of UHMW-PE Sheet. AS-Proceedings, 1(2), 383-388.

Harvey L. Stein, P.E. (1999). Ultrahigh Molecular Weight Polyethylene (UHMWPE). Ticona LLC.

Hu, D., Zhang, Y., Shen, Z., & Cai, Q. (2017). Investigation on the ballistic behavior of mosaic SiC/UHMWPE composite armor systems. Ceramics International, 43(13), 10368–10376.

Kellersohn, DIR. (1990). Processing of UHMW-PE (Hostalen GUR). In: Willert H, G.H.B, P. E, editors. Ultra-High Molecular Weight Polyethylene as Biomaterial in Orthopedic Surgery, vol. Lewiston, NY: Hogrefe & Huber Publishers; p 6-10.

Kurteri, R. (2008). Medikal Uhmwpe'nin Kuru ve Sulu Ortamlardaki Sürtünme ve Aşınma Davranışı (Yüksek Lisans Tezi, Sakarya Üniversitesi)

Kurtz, S. M., Muratoglu, O. K., Evans, M., & Edidin, A. A. (1999). Advances in the processing, sterilization, and crosslinking of ultra-high molecular weight polyethylene for total joint arthroplasty. Biomaterials.

Li, S., & Burstein, A. H. (1994). Ultra-High-Molecular-Weight Polyethylene – the Material and Its Use in Total Joint Implants. Journal of Bone and Joint Surgery-American Volume, 76A(7), 1080-1090.

Liang, X., Wu, X., Zeng, K., Xu, B., Wu, S., Zhao, H., Li, B., & Ruan, S. (2014). Micro ultrasonic powder molding for semi-crystalline polymers. Journal of Micromechanics and Microengineering, 24(4).

Liu, B. G., Wadley, H. N. G., & Deshpande, V. S. (2019). Failure mechanism maps for ultra-high molecular weight polyethylene fibre composite beams impacted by blunt projectiles. Int. J. Solids. Struct., 178, 180-198.

Liu, W., Chen, Z., Cheng, X., Wang, Y., Amankwa, A. R., & Xu, J. (2017). Design and ballistic penetration of the ceramic composite armor. Composites Part B: Engineering, 84, 33-40.

Mortensen, A. (2007). Concise Encyclopedia of Composite Materials Second Edition.

M.R. O'Masta, B.G. Compton, E.A. Gamble. (2015). Ballistic impact response of an UHMWPE fiber reinforced laminate encasing an aluminum-alumina hybrid panel. Int. J. Impact. Eng., 86, 131-144.

M.V. Hosur, U.K. Vaidya, C. Ulven, et al. (2004). Performance of stitched/unstitched woven carbon/epoxy composites under high-velocity impact loading. Compos. Struct., 64, 455-466.

Nguyen, L. H. (2015). The Ballistic Performance of Thick Ultra High Molecular Weight Polyethylene Composite (Doktora Tezi, RMIT University Mühendislik Fakültesi, Melbourne).

O'Masta, M. R. (2014). Mechanisms of Dynamic Deformation And Failure In Ultra-High Molecular Weight Polyethylene Fiber-Polymer Matrix Composites (Doktora Tezi, University of Virginia Mühendislik ve Uygulamalı Bilimler Fakültesi, Virginia).

Paul, W., Bart, V., Stepan, L., et al. (2007). The response of natural fibre composites to ballistic impact by fragment simulating projectiles. Compos. Struct., 77, 232-240.

Peterlin, A. (1971). Molecular model of drawing polyethylene and polypropylene. Journal of Materials Science, 6(6), 490–508.

Seok-Jo, Y. (2003). Development Of Wear-Enhanced All Polyethylene Acetabular Component In Total Hip Arthroplasty.

Truss, R. W., Han, K. S., Wallace, J. F., & Geil, P. H. (1980). Cold compaction molding and sintering of ultra-high molecular weight polyethylene. Poly. Engr. Sci., 20, 747-755.

Wang, F., Liu, L., Xue, P., & Jia, M. (2017). Crystal structure evolution of UHMWPE/HDPE blend fibers prepared by melt spinning. Polymers, 9(3).

Wei, H., & Benson, R. (2011). Polymeric Biomaterials. In Applied Plastics Engineering Handbook.

Xu, M. M., Huang, G. Y., Feng, S. S., McShane, G. J., & Stronge, W. J. (2016). Static and dynamic properties of semi-crystalline polyethylene. Polymers, 8(4).

Yang, Z., Peng, H., Wang, W., & Liu, T. (2010). Crystallization behavior of poly(ε-caprolactone)/layered double hydroxide nanocomposites. Journal of Applied Polymer Science, 116(5), 2658–2667.

Yılmaz, S. (2010). Çok Yüksek Molekül Ağırlıklı Polietilenin Hidrotermal Yaşlandırma Etkisi Altındaki Kırılma Davranışı (Yüksek Lisans Tezi, Kocaeli Üniversitesi).

Zhang, R., Qiang, L. S., & Han, B. (2020). Ballistic performance of UHMWPE laminated plates and UHMWPE encapsulated aluminum structures: Numerical simulation. Compos. Struct., 252, 1-12.

Zhang, Y., Liu, T., & Xu, Z. (2019). Dynamic response of hybrid carbon fibre laminate beams under ballistic impact. Compos. Struct., 210, 409-420.

CHAPTER IV

Free Vibratıon Analysis of Single And Multi-Stepped Tapered Beams with a Crack

Mehmet HASKUL[1]
Murat KISA[2]

1. Introduction

Beams are widely used in many engineering structures, and many studies on beams have been conducted in the literature and are still ongoing. Vibration analysis is a non-destructive testing method used to detect damage in a structure and its elements (beams, columns, rods, etc.). The ease of application and the fact that the method is more economical than the others have led to the frequent use of the vibration method, especially in the predictive maintenance. In this study, free vibration analysis of single and multi-stepped beams with varying cross-section was performed. For

[1] Doç. Dr., Şırnak Üniversitesi
[2] Prof.Dr., Harran Üniversitesi

free vibration analysis, first the stiffness and mass matrices of the variable cross-section beam were found. Then, the crack in the beam was modeled as a massless spring and the stiffness resulting from the crack was obtained using the principles of linear fracture mechanics. The element stifness, mass and crack-induced stiffness matrices obtained for the tapered cracked beam were integrated into a written finite element code and the free vibration analysis of the beam was performed. Finite element method was used in the calculations. Natural frequencies and mode shapes of the cracked beam were obtained depending on different crack depth ratios, crack locations and taper ratios. Changes in the natural frequencies and mode shapes are given with graphics. In the given graphs, the effects of crack locations, crack and taper ratios on the dynamic characteristics of the structure were clearly seen.

There are many studies in the literature on vibration analysis of beams, columns and frame structures with uniform and variable cross-sections containing single or multiple cracks (Salawu, 1997; Dimarogonas, 1996; Wauer, 1990; Gasch1993; Krawczuk & Ostachowicz, 1996; Jassim et al., 2013; Kisa 2011, 2012; Kisa and Gürel 2006, 2007; Kisa et al. 1998; Kisa and Brandon 2000). Du et al. (2021) used the transfer matrix method for the free vibration analysis of an axially loaded variable cross-section Euler-Bernoulli beam with many fixed members. Haskul and Kisa (2021a, 2021b) used the finite element and component mode synthesis methods to calculate the natural frequencies and mode shapes of varying cross-section cracked beams with a crack. Kisa and Brandon (2000) developed a finite element scheme to calculate the eigensystem of a cracked beam for different degrees of closure. Choi (2003) developed the finite element-transfer stiffness coefficient method to efficiently conduct free vibration analysis of 2D structures such as plate structures. Using the dynamic stiffness method, he formulated a free and forced vibration analysis algorithm for the frame structures. The method is based on the concept of transferring the dynamic stiffness coefficient associated with the force and displacement vector at each node from the left end to the right end

of the structure. Kisa (2004), investigated the effect of cracks on the dynamic properties of a cantilever composite beam made of graphite fiber reinforced polyamide using the finite element and component mode synthesis methods. Moon and Choi (2000) compared the numerical results obtained by the transfer dynamic stiffness method for a space frame structure with the results obtained by both the finite element method and experiment. Using the dynamic stiffness method, Boscolo and Banerjee (2011) investigated the in-plane free vibration behavior of plates. Mehmood (2015) used the finite element method and numerical time integration method (new signal method) in vibration analysis to understand the dynamic response of the frame subjected to moving point loads. Koohestani and Kaveh (2010) presented a method for the buckling and free vibration analysis of cyclically iterated space lattice structures. Ramu and Mohanty (2012) used Kirchhoff plate theory for finite element analysis to obtain the natural frequencies of a simply supported rectangular plate. Ranjbaran et al (2008) presented a mathematical formula for buckling analysis of a column and vibration analysis of a beam. The beam and column are assumed to be non-uniform and cracked. The problem is expressed as an optimization problem using variational method. An optimization technique is used for the analysis of the buckling load. Considering the similarity between the fundamental equation for buckling and free vibration, the beam's fundamental frequency and mode shape were calculated by the same method. Shabani and Cunedioglu (2020) performed a free vibration analysis of a non-uniform symmetrical beam with edge cracks made of functionally graded material. Timoshenko beam theory was used for the multilayer sandwich beam's finite element analysis, and the cantilever beam was modeled with 50 layers. Yendhe et al. (2016) investigated the vibration behavior of beams both experimentally and using the FEM software ANSYS. In this study, they analyzed the vibration of various cantilever beams with transverse cracks and different boundary conditions. Orhan (2007) investigated the free and forced vibration analysis of cracked beams using a finite element program to determine the crack in a cantilever beam. In the study,

single and double-sided crack conditions were evaluated. Ranjbaran (2014) investigated the effect of stiffeners on free vibration analysis of structural frames containing cracks. Saavedra and Cuitino (2001) presented the theoretical and experimental dynamic behavior of different multi-beam systems containing a transverse crack. Yoon et al. (2007) investigated the effect of two open cracks on the dynamic behavior of a double-cracked simply supported beam, both analytically and experimentally.

In this section, a method was developed for the free vibration analysis of single and multi-stepped fixed-free beams with variable cross-sections. Natural frequency and mode shape values were obtained for different crack depth ratios and various crack locations with different taper ratios.

2. Material and Method

In the study, the problem was solved by considering the beam shown in Figure 1. The beam was divided into elements by using the finite element method (see Figure 2). These elements, including the crack section, have two nodes and three degrees of freedom at each node. The stiffness and mass matrices of the beam with single and multi-stepped tapered cracked beams were obtained by taking these conditions into consideration.

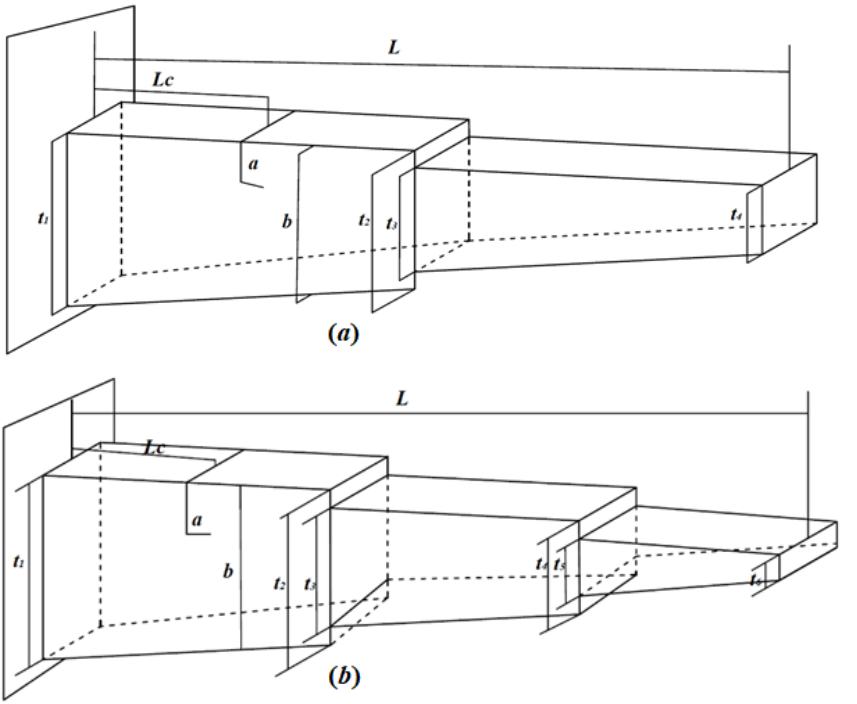

Figure 1. *Sketch of tapered cracked beam* ***(a)*** *single-stepped and,* ***(b)*** *multi-stepped*

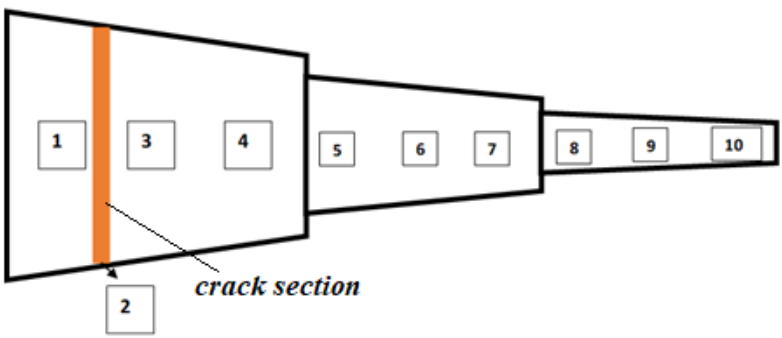

Figure 2. *Finite element modelling of the creacked beam*

The equations $EI_{zz}(x)$ and $EA(x)$ for the beam at distance x from the left end are given as:

$$EI_{zz}(x) = EI_{zz1}\left(1+\alpha\left(\frac{x}{L}\right)\right)^3 \quad (1)$$

$$EA(x) = EA_1\left(1+\alpha\left(\frac{x}{L}\right)\right) \quad (2)$$

where I_{zz1} and A_1 represent the area moment of inertia and cross-sectional area of the left end, respectively.

α for single and multi-stepped beam is given as following:

$$\alpha = \frac{t_2 - t_1}{t_1} = \frac{t_4 - t_3}{t_3} \quad (3)$$

$$\alpha = \frac{t_2 - t_1}{t_1} = \frac{t_4 - t_3}{t_3} = \frac{t_6 - t_5}{t_5} \quad (4)$$

The stiffness matrix of a variable cross-section beam element is given as (Haskul 2010):

$$K=\begin{bmatrix} \frac{1}{C} & 0 & 0 & \frac{-1}{C} & 0 & 0 \\ 0 & \frac{A_1}{D_1} & \frac{A_2}{D_1} & 0 & \frac{-A_1}{D_1} & \frac{A_1L-A_2}{D_1} \\ 0 & \frac{A_2}{D_1} & \frac{A_3}{D_1} & 0 & \frac{-A_2}{D_1} & \frac{A_2L-A_3}{D_1} \\ \frac{-1}{C} & 0 & 0 & \frac{1}{C} & 0 & 0 \\ 0 & \frac{-A_1}{D_1} & \frac{-A_2}{D_1} & 0 & \frac{A_1}{D_1} & \frac{A_2-A_1L}{D_1} \\ 0 & \frac{A_1L-A_2}{D_1} & \frac{A_2L-A_3}{D_1} & 0 & \frac{A_2-A_1L}{D_1} & \frac{A_1L^2-2A_2L+A_3}{D_1} \end{bmatrix} \quad (5)$$

where A_1, A_2, A_3, D_1 and C are:

$$A_i=\int_0^L \frac{x^{(i-1)}}{EI_{zz}(x)}dx, \quad i=1,2,3,$$

(6)

$$D_1 = A_1.A_3 - A_2^2 \quad (7)$$

$$\frac{1}{C}=\frac{EA_1}{L}\left[\frac{\alpha}{\ln(\alpha+1)}\right] \quad (8)$$

The mass matrix of a beam element with variable cross section is (Haskul 2010):

$$[M]=\begin{bmatrix} m_{11}^{A} & 0 & 0 & m_{12}^{A} & 0 & 0 \\ 0 & m_{11}^{B} & m_{12}^{B} & 0 & m_{13}^{B} & m_{14}^{B} \\ 0 & m_{21}^{B} & m_{22}^{B} & 0 & m_{23}^{B} & m_{24}^{B} \\ m_{21}^{A} & 0 & 0 & m_{22}^{A} & 0 & 0 \\ 0 & m_{31}^{B} & m_{32}^{B} & 0 & m_{33}^{B} & m_{34}^{B} \\ 0 & m_{41}^{B} & m_{42}^{B} & 0 & m_{43}^{B} & m_{44}^{B} \end{bmatrix}_{6x6} \qquad (9)$$

where m^{A}_{ij} and m^{B}_{ij} are:

$$[m]^{A}=\begin{bmatrix} \frac{1}{12}\rho A_1 L(4+\alpha) & \frac{1}{12}\rho A_1 L(2+\alpha) \\ \frac{1}{12}\rho A_1 L(2+\alpha) & \frac{1}{12}\rho A_1 L(4+3\alpha) \end{bmatrix} \qquad (10)$$

$$[m]^{B}=\begin{bmatrix} \frac{1}{35}\rho A_1 L(13+3\alpha) & \frac{1}{420}\rho A_1 L^2(22+7\alpha) & \frac{9}{140}\rho A_1 L(2+\alpha) & -\frac{1}{420}\rho A_1 L^2(13+6\alpha) \\ & \frac{1}{840}\rho A_1 L^3(8+3\alpha) & \frac{1}{420}\rho A_1 L^2(13+7\alpha) & -\frac{1}{280}\rho A_1 L^3(2+\alpha) \\ & & \frac{1}{35}\rho A_1 L(13+10\alpha) & -\frac{1}{420}\rho A_1 L^2(22+15\alpha) \\ \textit{Simetrik} & & & \frac{1}{840}\rho A_1 L^3(8+5\alpha) \end{bmatrix} \qquad (11)$$

The amount of energy required for the unit strain occurring in front of the crack, the strain energy release rate J for plane strain, is as follows (Tada et al. 1985):

$$J=\frac{1-\nu^2}{E}K_I^2+\frac{1-\nu^2}{E}K_{II}^2+\frac{1+\nu}{E}K_{III}^2 \qquad (12)$$

The strain energy release rate is always positive and includes three independent strain modes. If we restate *J* using the principle of superposition, we get:

$$J=\frac{1-\nu^2}{E}\left(K_{I1}+K_{I2}+....+K_{In}\right)^2+\frac{1-\nu^2}{E}\left(K_{II1}+K_{II2}+....+K_{IIn}\right)^2$$
$$+\frac{1+\nu}{E}\left(K_{III1}+K_{III2}+....+K_{III3}\right)^2 \qquad (13)$$

Flexibility coefficients resulting from cracks in the structure can be calculated using Castigliano's theorem and stress concentration factors. At the same time, if the amount of strain energy release is considered according to the Griffth-Irwin theory (Irwin, 1960), the flexibility coefficients are obtained as follows:

$$c_{ij}=\frac{\partial u_i}{\partial P_j}=\frac{\partial^2}{\partial P_i \partial P_j}\int_A J\left(P_i,A\right)dA \qquad \text{n} \qquad (14)$$

Flexibility coefficients c_{11}, c_{13}, c_{22} and c_{33} are stated as:

$$\left.\begin{aligned} c_{11}&=\frac{2\pi}{E^* b^2 d}\int_0^a \xi F_1^{\,2}\left(\frac{\xi}{b}\right)d\xi \\ c_{13}=c_{31}&=\frac{12\pi}{E^* b^3 d}\int_0^a \xi F_1\left(\frac{\xi}{b}\right)F_2\left(\frac{\xi}{b}\right)d\xi \\ c_{22}&=\frac{2\pi\kappa^2}{E^* b^2 d}\int_0^a \xi F_2^{\,2}\left(\frac{\xi}{b}\right)d\xi \\ c_{33}&=\frac{72\pi}{E^* b^4 d}\int_0^a \xi F_3^{\,2}\left(\frac{\xi}{b}\right)d\xi \end{aligned}\right\} \qquad (15)$$

for a node, the stiffness matrix for the crack is given by:

$$[C]^{-1} = \begin{bmatrix} \dfrac{c_{33}}{-c_{13}^{\,2} + c_{11}c_{33}} & 0 & \dfrac{c_{13}}{c_{13}^{\,2} - c_{11}c_{33}} \\ 0 & \dfrac{1}{c_{22}} & 0 \\ \dfrac{c_{13}}{c_{13}^{\,2} - c_{11}c_{33}} & 0 & \dfrac{c_{11}}{-c_{13}^{\,2} + c_{11}c_{33}} \end{bmatrix}_{3x3} \quad (16)$$

If the crack is considered as a massless spring element with two nodes and three degrees of freedom at each node, the stiffness matrix for this element is given as follows:

$$K_{cr} = \begin{bmatrix} [C]^{-1} & -[C]^{-1} \\ -[C]^{-1} & [C]^{-1} \end{bmatrix}_{(6x6)} \quad (17)$$

where K_{cr} indicates the stiffness matrix occured due to cracks in the beam.

It is known that cracks within the structure cause a decrease in stifftness. (Irwin, 1960). Stiffness matrix of cracked beam, $[K]_{wcr}$ is given as:

$$[K]_{wcr} = [K] - [K]_{cr} \quad (18)$$

The free vibration equation is given below in matrix format:

$$\left|[K]_{wcr} - \lambda[M]\right|\varphi = 0 \quad (19)$$

Using Equation 19, the dynamic properties of a single and multi-stepped variable cross-section beam with a crack were obtained.

3. Findings and Discussion

In this study, free vibration analysis was performed for cracked single and multi-step tapered beams, and the results were

obtained and interpreted. The results of these analyzes are given in the following part of the text.

3.1. Single-stepped tapered cracked beam with fixed-free ends

A free vibration analysis of a fixed-free single-stepped beam with varying cross-section and a crack was performed. A computer program was prepared using the finite element method for vibration analysis, and natural frequencies and mode shapes were determined for different crack location and crack depth ratios and taper ratio t_2/t_1=0.9 of the beam.

The geometric properties of the beam are taken as the length of the beam L=0.2m, the thickness of the beam t_1=0.025m and the width of the beam as 0.0078m, where the thickness ratio of the beam ($t_2/t_1 = t_4/t_3$) is assumed to vary linearly. The mechanical properties are taken as modulus of elasticity E=216GPa, Poisson ratio ν=0.3 and density ρ=7850 kg/m^3.

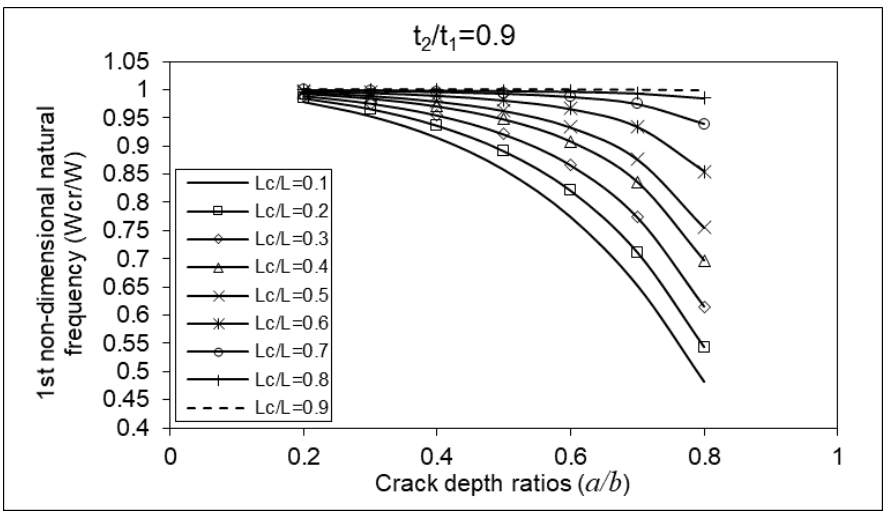

Şekil 3. *First non-dimensional natural frequencies of single-stepped cracked beam with fixed–free ends for crack locations (Lc/L=0.1–0.9) and taper ratio t_2/t_1=0.9 depending on crack depth ratios (a/b=0.2–0.8)*

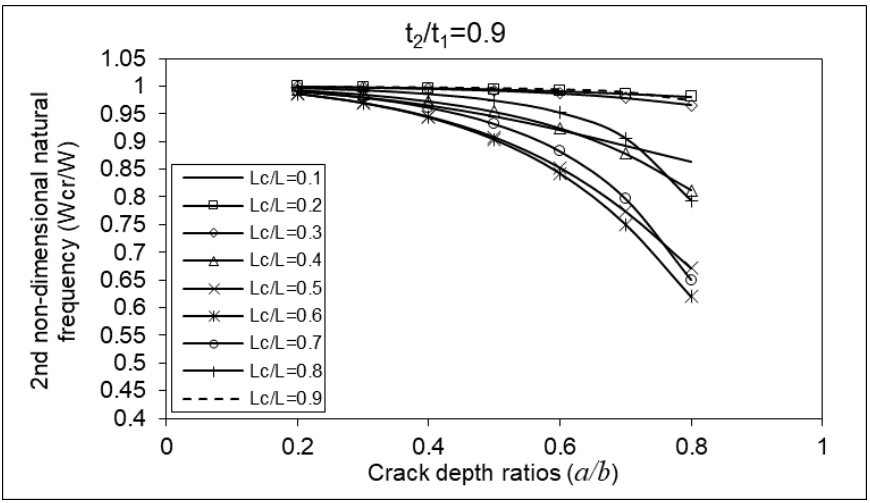

Şekil 4. *Second non-dimensional natural frequencies of single-stepped cracked beam with fixed–free ends for crack locations (Lc/L=0.1–0.9) and taper ratio t_2/t_1=0.9 depending on crack depth ratios (a/b=0.2–0.8)*

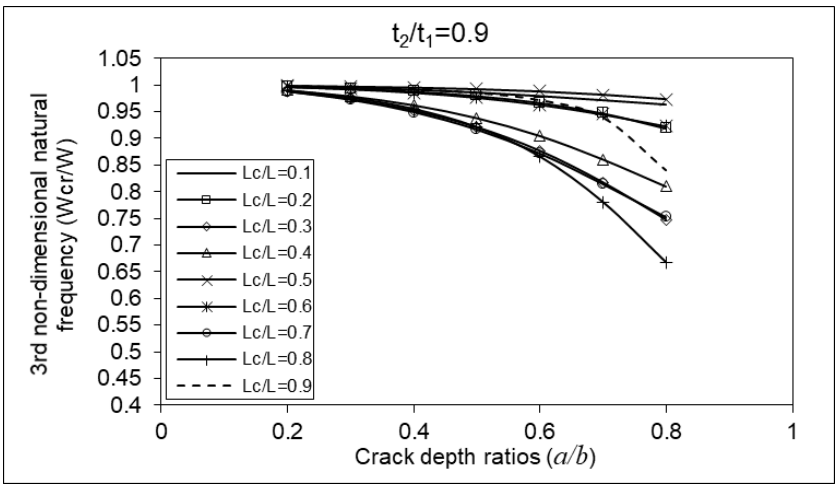

Şekil 5. *Third non-dimensional natural frequencies of single-stepped cracked beam with fixed–free ends for crack locations (Lc/L=0.1–0.9) and taper ratio t_2/t_1=0.9 depending on crack depth ratios (a/b=0.2–0.8)*

Figures 3, 4, and 5 show the first, second, and third dimensionless natural frequencies of the fixed-free single-stepped beam with a taper ratio $t_2/t_1=0.9$ and various of crack locations ($Lc/L=0.1–0.9$) according to the crack depth ratios ($a/b=0.2–0.8$). As seen in the figure, the maximum decrease in the first natural frequenciy occurred when the crack was located close to the fixed end ($Lc/L=0.1$). The maximum drops in the second and third natural frequencies occurred when the crack was at $Lc/L=0.6$ and $Lc/L=0.7$, 0.8, respectively. These frequency drops in the beam occur due to large energy losses in the crack section.

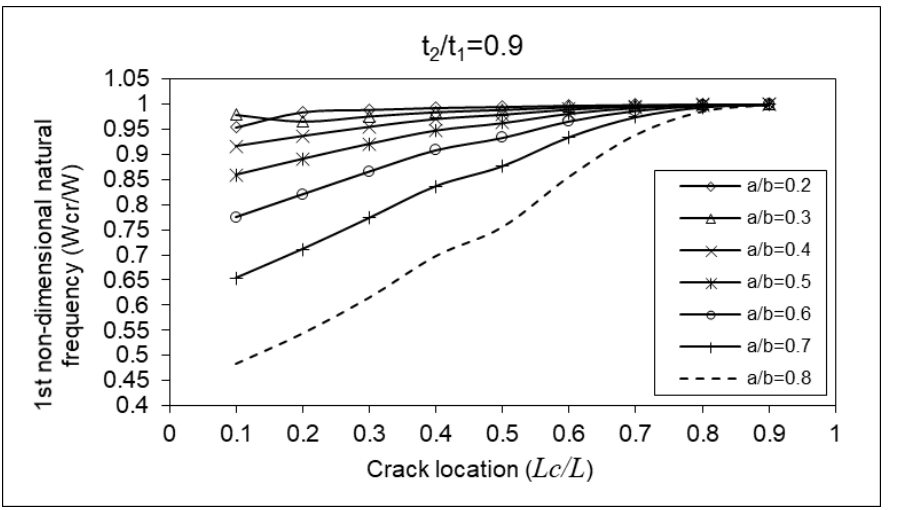

Şekil 6. *First non-dimensional natural frequencies of single-stepped cracked beam with fixed–free ends for crack depth ratios (a/b=0.2–0.8) and taper ratio $t_2/t_1=0.9$ depending on crack locations (Lc/L=0.1–0.9)*

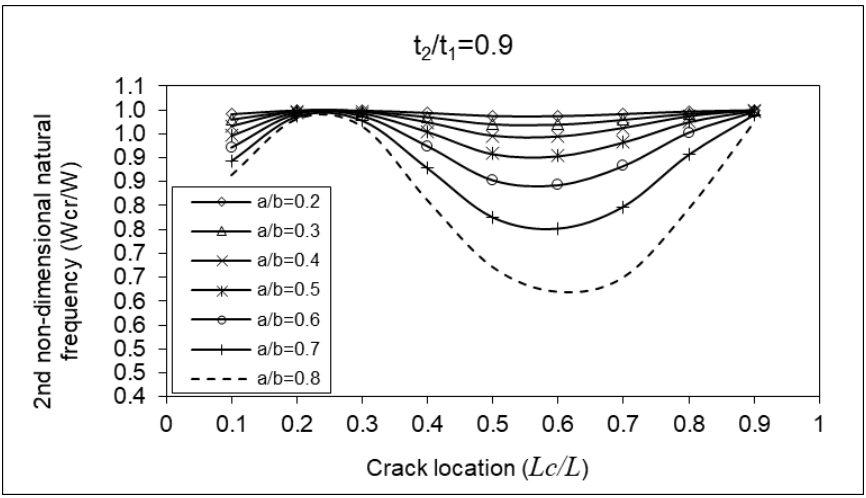

Şekil 7. *Second non-dimensional natural frequencies of single-stepped cracked beam with fixed–free ends for crack depth ratios (a/b=0.2–0.8) and taper ratio t_2/t_1=0.9 depending on crack locations (Lc/L=0.1–0.9)*

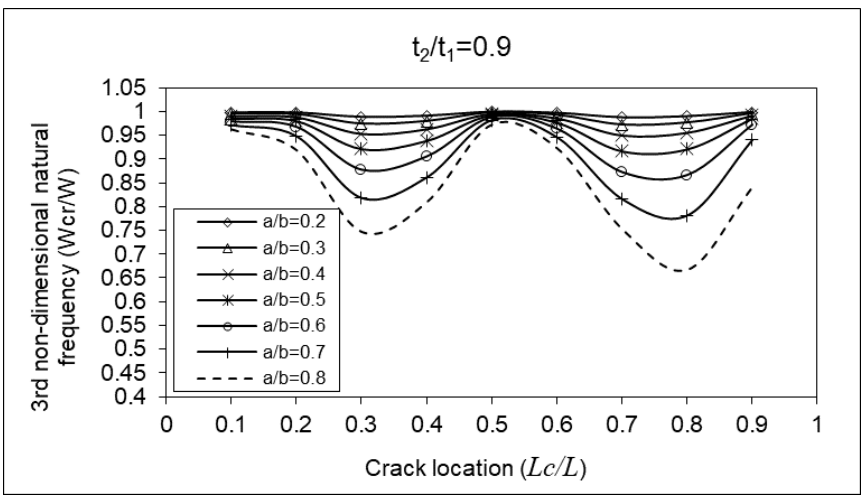

Şekil 8. *Third non-dimensional natural frequencies of single-stepped cracked beam with fixed–free ends for crack depth ratios (a/b=0.2–0.8) and taper ratio t_2/t_1=0.9 depending on crack locations (Lc/L=0.1–0.9)*

Figures 6, 7, and 8 present the non-dimensional natural frequencies of the fixed-free single-stepped beam according to taper ratio $t_2/t_1 = 0.9$. In these figures, variation of non-dimensional natural frequencies shows various crack locations ($Lc/L = 0.1–0.9$) according to the crack depth ratios ($a/b = 0.2–0.8$). The non-dimensional natural frequencies variation in Figures 6, 7, and 8 are the same and parallel to the changes in Figures 3, 4, and 5.

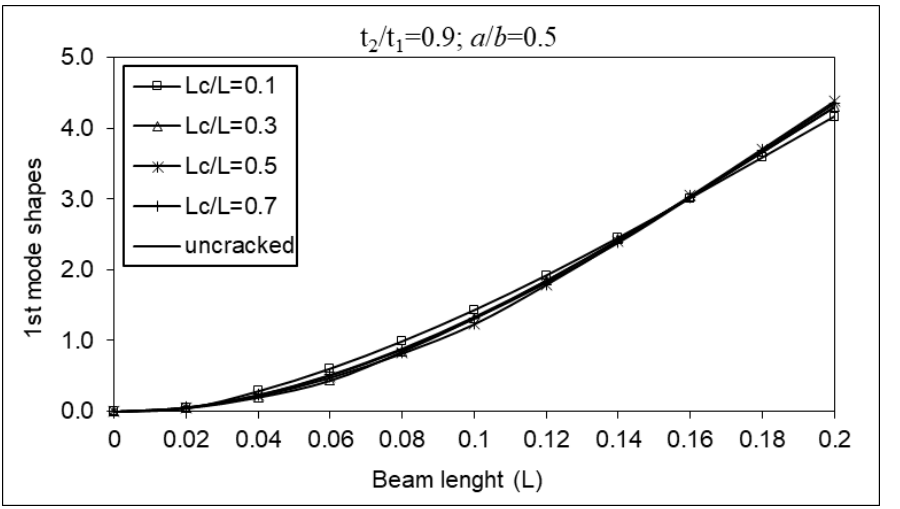

Figure 9. *First mode shapes of fixed-free cracked single-stepped beam for crack depth ratio a/b = 0.5 and taper ratio $t_2/t_1 = 0.9$*

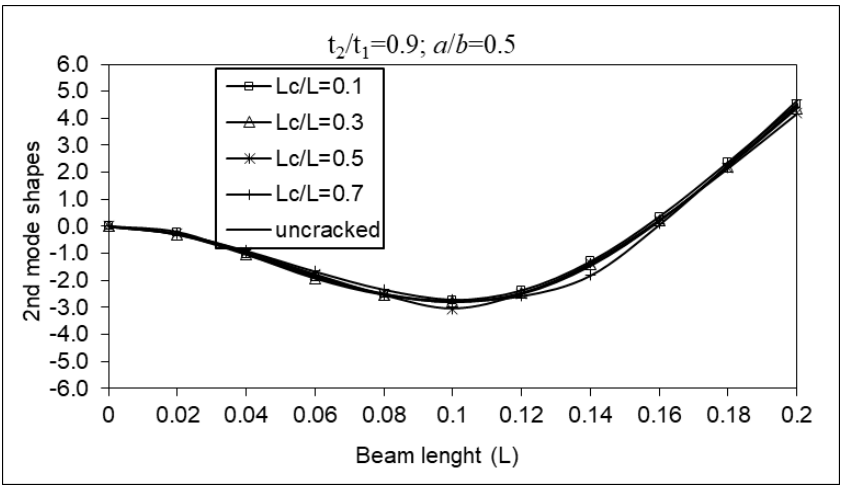

Figure 10. *Second mode shapes of fixed-free cracked single-stepped beam for crack depth ratio a/b = 0.5 and taper ratio t_2/t_1 = 0.9*

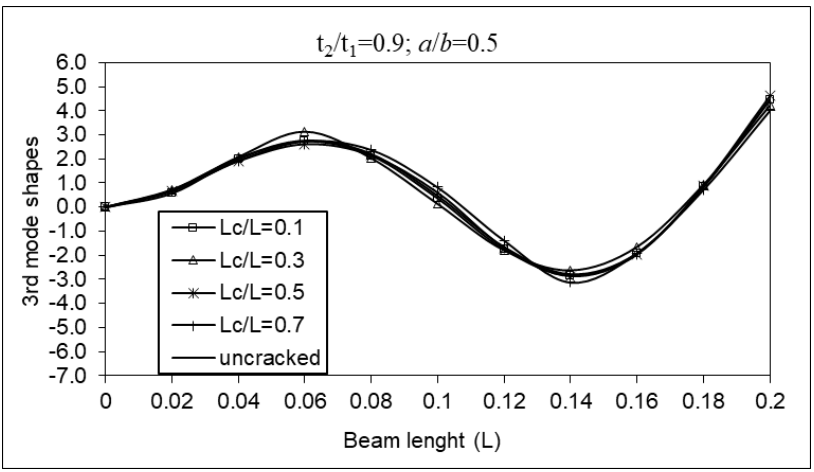

Figure 11. *Third mode shapes of fixed-free cracked single-stepped beam for crack depth ratio a/b = 0.5 and taper ratio t_2/t_1 = 0.9*

Figures 9, 10, and 11 show the first, second and third mode shape variations depending on the crack locations for the taper ratio $t_2/t_1=0.9$ and the crack depth ratio $a/b=0.5$. As seen in the figure,

when the crack position is *Lc/L=0.1*, the first mode shape, when *Lc/L=0.5* then the second mode shape and if *Lc/L=0.7* the third mode shape is most affected.

3.2. Multi-stepped tapered cracked beam with fixed-free ends

A free vibration analysis of a fixed-free multi-stepped beam with varying cross-section and a crack was performed. A computer program was prepared using the finite element method for vibration analysis, and natural frequencies and mode shapes were determined for different crack location and crack depth ratios and taper ratio t_2/t_1=0.85 of the beam.

The geometric properties of the beam are taken as the length of the beam L=0.18m the thickness of the beam t_1=0.025m and the width of the beam as 0.0078m where the thickness ratio of the beam ($t_2/t_1 = t_4/t_3 = t_6/t_5$) is assumed to vary linearly. The mechanical properties are taken as modulus of elasticity E=216GPa, Poisson ratio v=0.3 and density ρ=7850 kg/m^3.

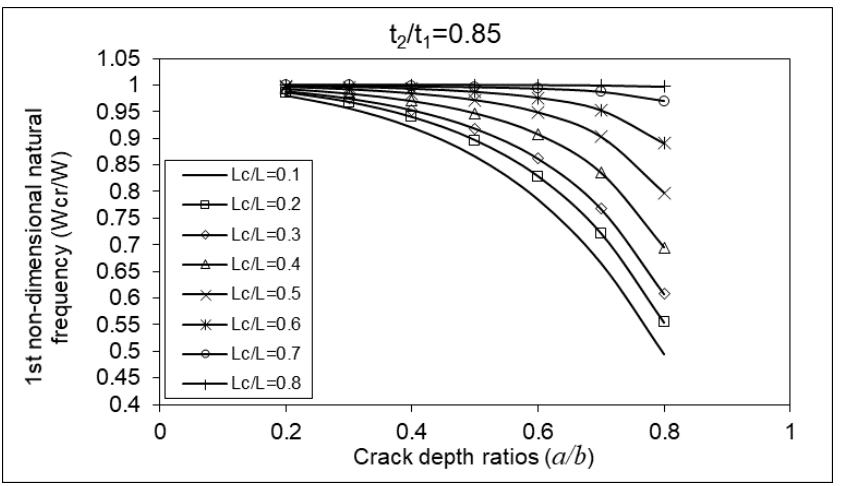

Figure 12. *First non-dimensional natural frequencies of multi-stepped cracked beam with fixed–free ends for crack locations (Lc/L=0.1–0.9) and taper ratio t_2/t_1=0.85 depending on crack depth ratios (a/b=0.2–0.8)*

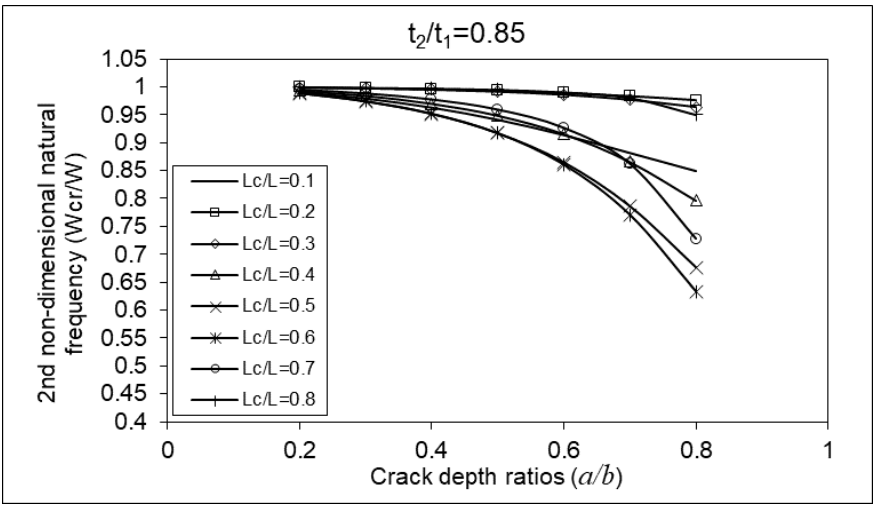

Figure 13. *Second non-dimensional natural frequencies of multi-stepped cracked beam with fixed–free ends for crack locations (Lc/L=0.1–0.9) and taper ratio t_2/t_1=0.85 depending on crack depth ratios (a/b=0.2–0.8)*

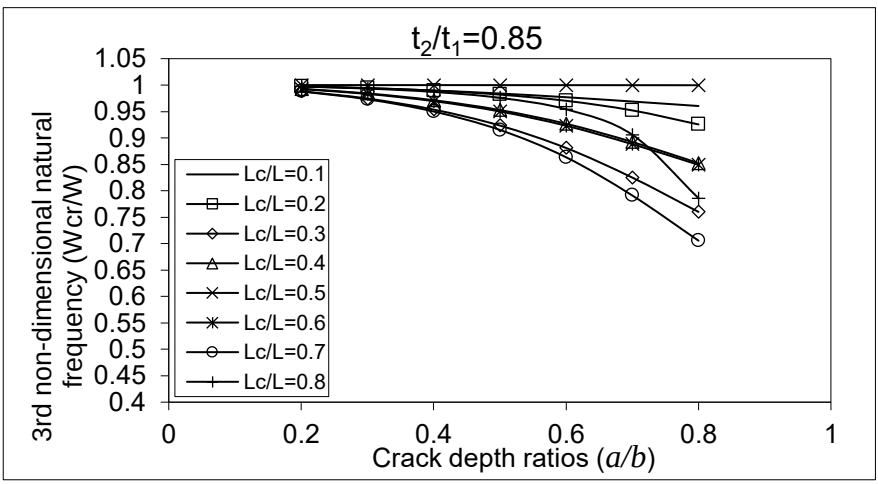

Figure 14. *Third non-dimensional natural frequencies of multi-stepped cracked beam with fixed–free ends for crack locations (Lc/L=0.1–0.9) and taper ratio t_2/t_1=0.85 depending on crack depth ratios (a/b=0.2–0.8)*

Figures 12, 13, and 14 show the first, second, and third dimensionless natural frequencies of the fixed-free multi-stepped beam with taper ratio $t_2/t_1 = 0.85$ and the various crack location ($Lc/L=0.1–0.9$) depending on crack depth ratios (a/b=0.2–0.8). As seen in the figure, the maximum decrease in the first natural frequency occurred when the crack was close to the fixed end ($Lc/L=0.1$). The maximum decreases in the second and third natural frequencies occurred as a result of the crack being located at $Lc/L = 0.6$ and $Lc/L = 0.7$, respectively.

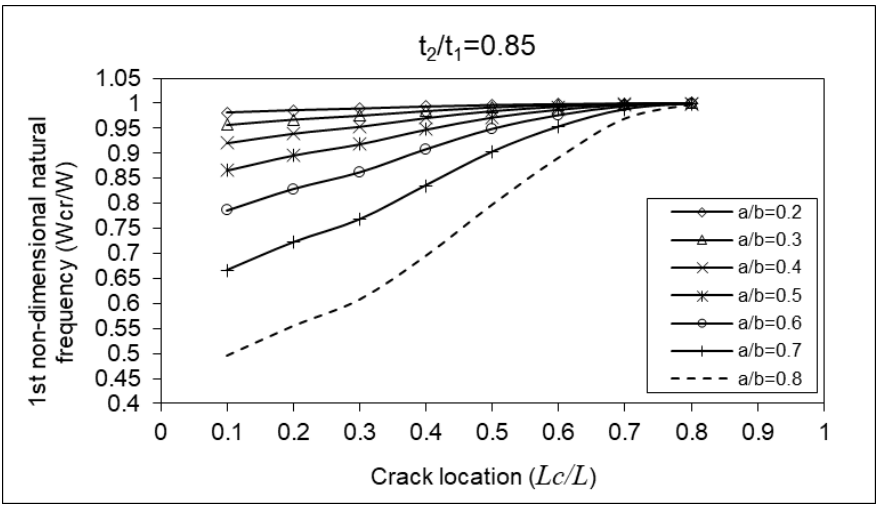

Figure 15. *First non-dimensional natural frequencies of multi-stepped cracked beam with fixed–free ends for crack depth ratios (a/b=0.2–0.8) and taper ratio t_2/t_1=0.85 depending on crack locations (Lc/L=0.1–0.9)*

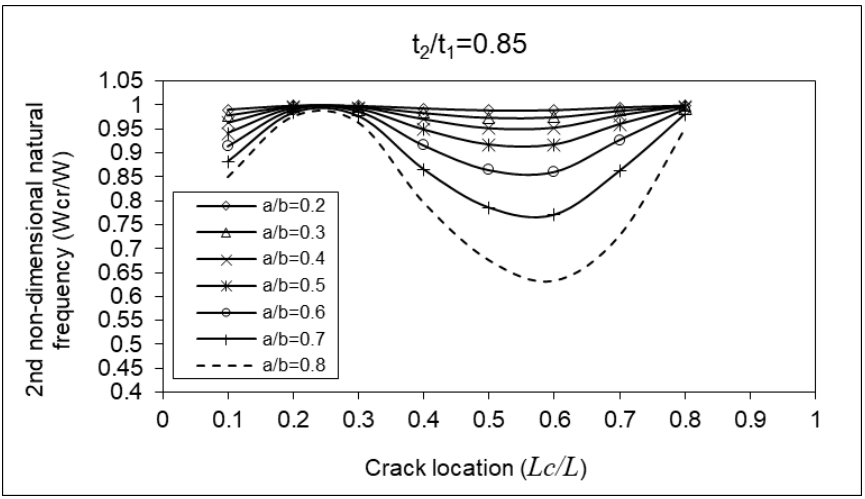

Figure 16. *Second non-dimensional natural frequencies of multi-stepped cracked beam with fixed–free ends for crack depth ratios (a/b=0.2–0.8) and taper ratio t_2/t_1=0.85 depending on crack locations (Lc/L=0.1–0.9)*

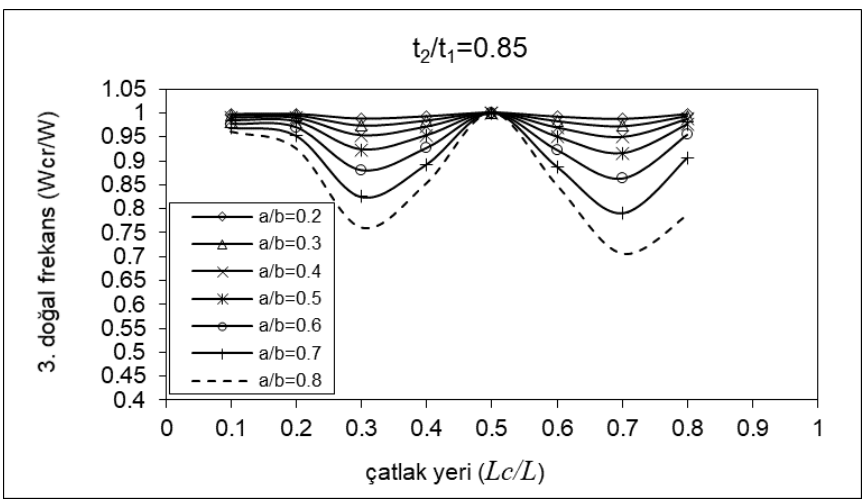

Figure 17. *Third non-dimensional natural frequencies of multi-stepped cracked beam with fixed–free ends for crack depth ratios (a/b=0.2–0.8) and taper ratio t_2/t_1=0.85 depending on crack locations (Lc/L=0.1–0.9)*

Figures 15, 16, and 17 present the non-dimensional natural frequencies of the fixed-free multi-stepped beam according to taper ratio $t_2/t_1 = 0.85$. In these figures, variation of non-dimensional natural frequencies were shown for various crack locations ($Lc/L = 0.1–0.9$) according to the crack depth ratios ($a/b = 0.2–0.8$). The non-dimensional natural frequencies variation in Figures 15,16, and 17 are the same and parallel to the changes in Figures 13, 14, and 15.

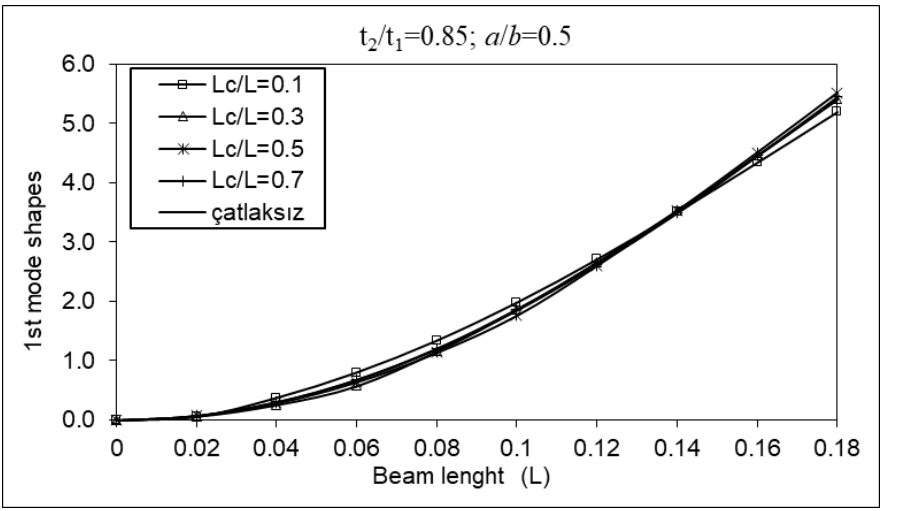

Figure 18. *First mode shapes of fixed-free cracked multi-stepped beam for crack depth ratio a/b = 0.5 and taper ratio $t_2/t_1 = 0.85$*

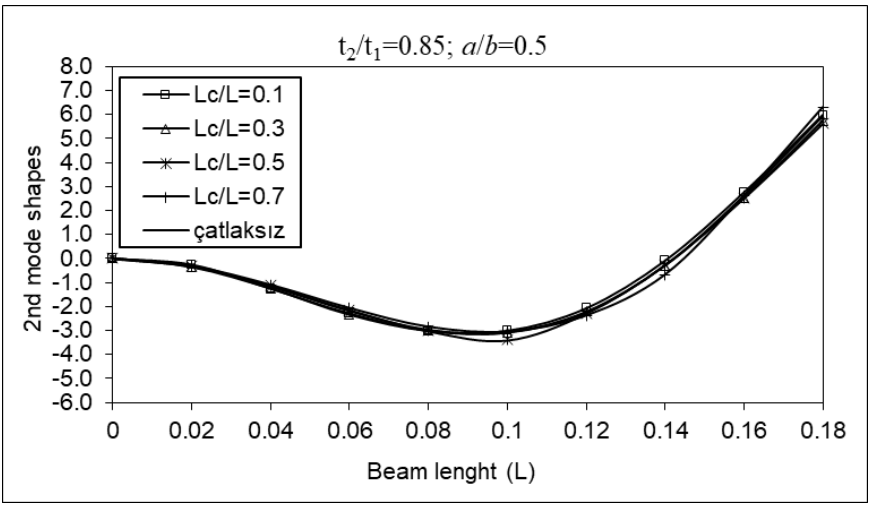

Figure 19. *Second mode shapes of fixed-free cracked multi-stepped beam for crack depth ratio a/b = 0.5 and taper ratio t_2/t_1 = 0.85*

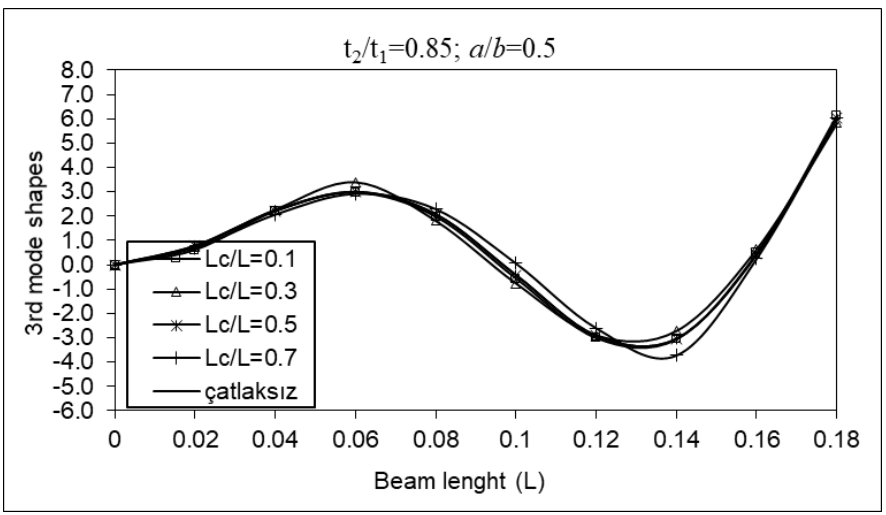

Figure 20. *Third mode shapes of fixed-free cracked multi-stepped beam for crack depth ratio a/b = 0.5 and taper ratio t_2/t_1 = 0.85*

Figures 18, 19, and 20 show the first, second and third mode shapes variations depending on crack locations for the taper ratio $t_2/t_1=0.85$ and the crack depth ratio $a/b=0.5$. The effect of crack

locations on mode shapes is clearly seen in the figures. If a crack is in the region of the maximum bending moment of the relevant mode, it will cause larger energy losses and cause larger changes in the relevant mode shapes.

4. Conclusion

In this study, free vibration analysis was examined for single and multi-stepped cracked beams with fixed-free ends and varying cross-section. A computer program was written using the finite element method. The crack in the beam is modeled as a massless spring. The element stifness, mass and crack-induced stiffness matrices obtained for the tapered cracked beam were integrated into a written finite element code and the free vibration analysis of the beam was performed. Using the written code, natural frequencies and mode shapes were calculated for different crack depth ratios, crack locations and taper ratios. Changes in natural frequency and mode shapes provide important information about the location and depth of the crack, making important contributions to non-destructive predictive maintenance.

As can be seen from the figures, the maximum decreases and changes in the first natural frequencies and mode shapes occurred when the crack was located close to the fixed end (*Lc/L=0.1*). The maximum drops and variations in the second and third natural frequencies and mode shapes occurred when the crack was at *Lc/L=0.6, Lc/L=0.7, 0.8*, respectively.

Crack sizes and locations are important regarding the magnitude of energy loss it will cause. The bending moment occurring in the beam section varies depending on the boundary and loading conditions along the beam. A crack located in a section where there is maximum bending moment will cause a large amount of energy loss and will also affect the dynamic behavior of the beam. All these results are clearly shown in this study.

References

Salawu, O. S. (1997). Detection of structural damage through changes in frequency: a review. *Engineering structures*, *19*(9), 718-723.

Dimarogonas, A. D. (1996). Vibration of cracked structures: a state of the art review. *Engineering fracture mechanics*, *55*(5), 831-857.

Wauer, J. R. (1990). On the dynamics of cracked rotors: a literature survey. *Applied Mechanics Reviews* 43 (1) 13–17.

Gasch, R. (1993). A survey of the dynamic behaviour of a simple rotating shaft with a transverse crack. *Journal of sound and vibration*, *160*(2), 313-332.

Krawczuk, M., & Ostachowicz, W. (1996). Damage indicators for diagnostic of fatigue cracks in structures by vibration measurements–a survey. *Journal of Theoretical and Applied Mechanics*, *34*(2), 307-326.

Jassim, Z. A., Ali, N. N., Mustapha, F., & Jalil, N. A. (2013). A review on the vibration analysis for a damage occurrence of a cantilever beam. *Engineering Failure Analysis*, *31*, 442-461.

Kisa, M. (2011). Vibration and stability of multi-cracked beams under compressive axial loading. *International Journal of the Physical Sciences*, *6*(11), 2681-2696.

Kisa, M. (2012). Vibration and stability of axially loaded cracked beams. *Structural engineering and mechanics: An international journal*, *44*(3), 305-323.

Kisa, M., & Gurel, M. A. (2006). Modal analysis of multi-cracked beams with circular cross section. *Engineering Fracture Mechanics*, *73*(8), 963-977.

Kisa, M., & Gurel, M. A. (2007). Free vibration analysis of uniform and stepped cracked beams with circular cross

sections. *International Journal of Engineering Science*, *45*(2-8), 364-380.

Kisa, M., Brandon, J., & Topçu, M. (1998). Free vibration analysis of cracked beams by a combination of finite elements and component mode synthesis methods. *Computers & structures*, *67*(4), 215-223.

Kisa, M., & Brandon, J. A. (2000). Free vibration analysis of multiple open-edge cracked beams by component mode synthesis. *Structural engineering and mechanics: An international journal*, *10*(1), 81-92.

Du, Y., Cheng, P., & Zhou, F. (2022). Free vibration analysis of axial-loaded beams with variable cross sections and multiple concentrated elements. *Journal of Vibration and Control*, *28*(17-18), 2197-2211.

Haskul, M., & Kisa, M. (2021). Free vibration of the double tapered cracked beam. *Inverse Problems in Science and Engineering*, *29*(11), 1537-1564.

Haskul, M., & Kisa, M. (2021). Free-vibration analysis of cracked beam with constant width and linearly varying thickness. *Emerging Materials Research*, *11*(1), 125-137.

Kisa, M., & Brandon, J. (2000). The effects of closure of cracks on the dynamics of a cracked cantilever beam. *Journal of sound and vibration*, *238*(1), 1-18.

Choi, M. S. (2003). Free vibration analysis of plate structures using finite element-transfer stiffness coefficient method. *KSME International Journal*, *17*, 805-815.

Kisa, M. (2004). Free vibration analysis of a cantilever composite beam with multiple cracks. *Composites Science and Technology*, *64*(9), 1391-1402.

Moon, D. H., & Choi, M. S. (2000). Vibration analysis for frame structures using transfer of dynamic stiffness coefficient. *Journal of Sound and Vibration*, *234*(5), 725-736.

Boscolo, M., & Banerjee, J. R. (2011). Dynamic stiffness method for exact inplane free vibration analysis of plates and plate assemblies. *Journal of Sound and Vibration*, *330*(12), 2928-2936.

Mehmood, A. (2015). Using finite element method vibration analysis of frame structure subjected to moving loads. *International Journal of Mechanical Engineering and Robotics Research*, *4*(1), 50-65.

Koohestani, K., & Kaveh, A. (2010). Efficient buckling and free vibration analysis of cyclically repeated space truss structures. *Finite Elements in Analysis and Design*, *46*(10), 943-948.

Ramu, I., & Mohanty, S. C. (2012). Study on free vibration analysis of rectangular plate structures using finite element method. *Procedia engineering*, *38*, 2758-2766.

Ranjbaran, A., Hashemi, S., & Ghafarıan, A. (2008). A new approach for buckling and vibration analysis of cracked column.

Shabani, S., & Cunedioglu, Y. (2020). Free vibration analysis of cracked functionally graded non-uniform beams. *Materials Research Express*, *7*(1), 015707.

Yendhe, V. S., Kadlag, P. V. L., & Shelke, P. R. S. (2016). Vibration analysis of cracked cantilever beam for varying crack size and location. *International Research Journal of Engineering and Technology*, *3*(8), 1913-1919.

Orhan, S. (2007). Analysis of free and forced vibration of a cracked cantilever beam. *Ndt & E International*, *40*(6), 443-450.

Ranjbaran, A. (2014). Free-vibration analysis of stiffened frames. *Journal of Engineering Mechanics*, *140*(9), 04014071.

Saavedra, P. N., & Cuitino, L. A. (2001). Crack detection and vibration behavior of cracked beams. *Computers & Structures*, *79*(16), 1451-1459.

Yoon, H. I., Son, I. S., & Ahn, S. J. (2007). Free vibration analysis of Euler-Bernoulli beam with double cracks. *Journal of mechanical science and technology*, *21*, 476-485.

Haskul, M. (2010). *Çatlak içeren değişken kesitli kirişlerde titreşim problem*inin sonlu elemanlar metoduyla *modellenmesi/Finite element method for the vibration of cracked beams with varying cross section (Harran Üniversitesi, Fen bilimleri Enstitüsü).*

Tada, H., Paris, P. C., & Irwin, G. R. (1973). The stress analysis of cracks. *Handbook, Del Research Corporation*, *34*(1973).

Irwın, G. (1960). Fracture Mechanics, Editors JN Goodier and NJ Hoff.

CHAPTER V

Materials and Manufacture Processes of Assault Rifle Barrels

Musa DEMİR
Faruk GÜNER

Introduction

The day humanity set foot on planet Earth, the demand for weaponry was born. At the beginning of human history, the gun was just a stone used for hunting, but as time went on, it evolved into the most advanced technological innovation created to safeguard and increase human sovereignty. After the wood was processed to create the spear, metal was processed to create swords and shields, and chemistry discoveries led to the creation of gunpowder, which subsequently, in turn, led to the development of firearms and, more recently, electronically powered weapons (Güner and Sofuoğlu 2018). In short, a substantial portion of this field's technological advancements also pertain to weaponry. While it is challenging to categorize them precisely, they can be looked at under the following

two headings: weapons that don't shoot back and weapons that are employed for attack and defense.

Additionally, there are numerous subclassifications for firearms. Considerations including caliber, intended use, and range are essential standards for these divisions. Light weapons are typically operated by one person, have a barrel diameter of less than 20 mm, can be fired from the hand or with shoulder support, can be loaded manually, can be semi-automatic or automatic and can shoot a flat trajectory at the target. They can also be fired manually, automatically, or in rapid fire. It qualifies as a weapon. Today, both military and civilian users commonly employ handguns made for personal use. Different guns utilize projectiles with varying geometric shapes and qualities. The general components of a pistol made in Turkey by the Tisaş company are seen in Figure 1. Light weapons also include rifles designed to fire more quickly across larger distances, even though the fundamental operating principle is the same.

Figure 1. *General parts of a firearm (Guner 2019)*

Rifles are usually classified as either military or hunting. Usually, both kinds are made to be used with both hands. The stock, barrel, bolt mechanism, and the stock including shoulder support constitute the rifle's basic components. Guns made for hunting share operational principles with army sniper rifles because hunting guns need to hit targets with great accuracy. Automatic infantry rifles are armed forces with a higher rate of fire but a lesser accuracy and range on targets. The barrel is one of the main distinctions between hunting and military rifles. Military rifle barrels are formed with grooves. The bullet's rotational motion is intended to be added to its forward motion with this form. Heavy machine guns, which typically operate with ground support, are weapons with significantly greater strength characteristics used in automatic infantry rifles.

Although there are different forms of automatic infantry rifles, they are generally based on two functional principles. The Cold War, which escalated after the Second World War, led to the emergence of a new generation of infantry rifles. The functional principle of the automatic infantry rifles of the two countries, which were the two poles of the Cold War, inspired many infantry rifles that are still produced untill today.

Automatic infantry rifles are usually manufactured in 5.52–7.65 mm caliber with a rifled barrel and magazines for 20–30 cartridges that can fire 600–800 rounds per minute. Fire control is usually done via a metal latch, and the gun can be operated individually, in threes, or continuously. The ability to fire three shots at once is an important feature. Especially during an infantry attack, it fires three bullets when the soldier pulls the trigger and stops. When the trigger is pulled again, the gun is ready to fire three bullets. Once the magazine is inserted and the crown is pulled, no further action is required until the magazine is empty. It is possible to install additional equipment such as grenade launchers, binoculars, or laser pointers.

Automatic infantry rifles, which are light firearms with long barrels, function through the pressure of the gunpowder that is released when the projectile is fired. Gunpowder is a compound that burns at very high speeds. During combustion, it expands around 600 times and forms gas. The gas released in the cartridge case propels the bullet forward and also provides the energy for the processes required to eject the empty cartridge and insert the new bullet into the chamber. The kinetic energy stored by the recoiling spring in the breech mechanism propels the new bullet from the magazine into the chamber and allows successive shots to be fired as long as the trigger is pulled. In all automatic infantry rifles, the main purpose is to prevent the cartridge case from flying backwards when the bullet is fired and to ensure that the pressure in the barrel drops to a safe level. This ensures safe and consistent shooting. The weapon shown in Figure 2 is the best-known automatic rifle in the world. The AK-47 from licensed Russian production has been the weapon in the hands of one side in every war since its manufacture in 1947. Apart from its low accuracy, it is the most important infantry rifle in many countries due to its simple manufacture and operation, as well as its resistance to adverse climatic and environmental conditions.

Figure 2. *AK-47 Assault Rifle (Güneş 2009)*

The AK-47 has a mechanism above the barrel that pushes the mechanism back and ensures rapid operation thanks to the pressure that enters the cylinder through a hole in the barrel where this piston is located. In the MPT-76, a Turkish design that emerged as a competitor to this operating principle, the mechanism retracts and

then returns to its place thanks to the pressure in the chamber, which acts directly on the bolt mechanism. Both types of rifles have different barrel lengths and calibers. Figure 3 shows the image of the Modern Infantry Rifle-76 (MPT-76).

Figure 3 General view of MPT-76 assault rifle (Guner 2019)

Apart from the mechanism that constitutes the working system, the most important part, when considered as a whole, is the barrel. If the pressure in the fired chamber moves backwards away from the barrel before it drops to a safe level, the cartridge material cannot withstand the high pressure and may rupture, and as a result, there is a risk of the gun barrel rupturing or even deforming due to an explosion. To avoid such situations, the mechanism head and bucket must be properly supported in the chamber until the pressure in the bucket drops to a safe level. This step, which is important for the safety and use of the gun, is usually provided with a locking mechanism.

The barrel can be defined as a long, perforated metal tube, with or without grooves, that houses the projectile or bullets to be sent to the target, the gunpowder, and the cartridge, which consists of the primer that ignites the gunpowder and which guides the projectile or bullets to the target through the primer. It is the most expensive part to manufacture. Although they are manufactured

using many production methods, the effective range can increase from 300 meters to 1300 meters depending on how sensitive the chosen method is, and it is quite normal for this sensitivity to be more expensive.

In the literature, positive results are often given for hot work steel alloys such as C60, heat-treatable steels, and 4340 or 4140 as barrel materials in terms of wear and service life.(Güner 2020, Hussain et al. 2021). One of the details that should be emphasized at this point is the way in which this material is produced and its contribution to quality. Steel, as we know, is produced by smelting ore or scrap steel. It is very important for the quality of the final product to maintain the desired ratio of alloying elements in the correct proportion and to reduce the proportion of undesirable elements. Since one-third of the world's steel production is made from scrap and the element composition in the scrap is not fully known, this can lead to problems with precision.

The most important step in producing a barrel is to create the groove-set shape that allows the bullet to return to the target. Machining is usually done to transfer technical details, such as the calculated spiral angle and groove depth, to the barrel. In addition to machining, barrels are manufactured using methods such as forging, electrochemical processes, and electric arcs. Among these methods, the most preferred is forging.

A further difficulty in the manufacture of barrels, apart from the rifling-set form, is the requirement for different wall thicknesses resulting from the different pressure values along the barrel. Since there is high pressure, especially in the area of the chamber in particular, a greater wall thickness in this area is required for strength. For this purpose, the groove-set shape is first produced on the inside of the barrel, and then the required outer shape is given by machining. The internal pressure curves in Figure 4 below show the pressure distribution along the barrel as a result of firing a 7.62 mm caliber infantry rifle at different temperatures. As can be seen from the curves, the first 150 mm of the barrel is subjected to extreme

pressure. Similarly, the changing temperature across the wall thickness of the barrel creates a pressure gradient from the inner surface, which comes into contact with the gunpowder gas, to the outside. For these reasons, internal pressure curves are used when developing the material and barrel geometries of gun barrels.

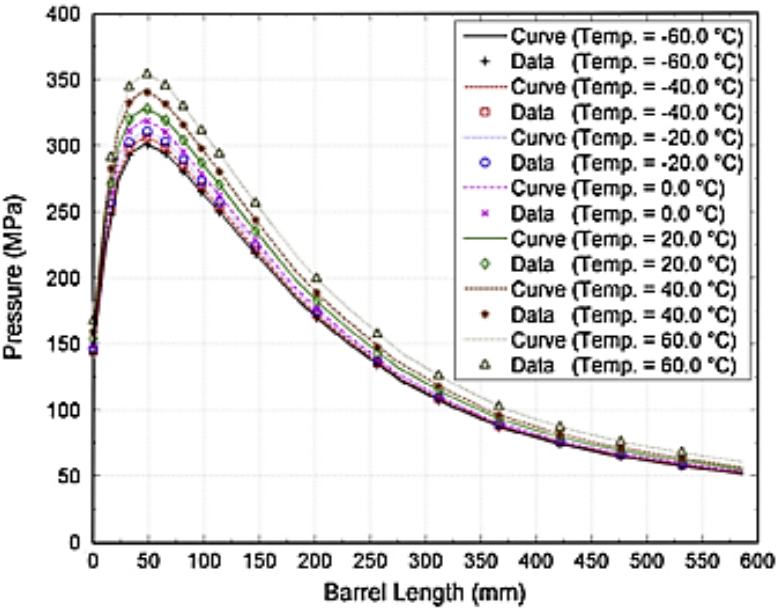

Figure 4. Internal ballistic curves of the 7.62 mm caliber assault rifle (Degirmenci 2015)

There are three stress factors that must be taken into account when designing barrels. The first of these is temperature, the second is pressure, and the third is friction. Although the effects of pressure and temperature have been mentioned so far in this section, friction is an effect that is generally not considered. In infantry rifles, the bullet seats itself into the groove-set in the barrel with a certain tightness. If it is too tight, the bullet cannot advance; if it is too loose, it wobbles. In forensic ballistic examinations, the correspondence between the groove and the seating shape of the bullet is examined in order to determine the firing barrel. The friction effect, which increases with the effect of temperature and pressure, is caused by

the guidance of the bullet through the groove shape. From this perspective, it becomes clear that the shape tolerance during production lies within a very narrow range. However, it becomes clear how difficult it is to develop a material with which the barrel, cartridge case and bullet made of different materials function smoothly in the temperature range from 40°C to -50°C.

1.Barrel Production Methods

When the first rifles appeared on the stage of history, their barrels were made of bronze or cast iron. Various alloying elements were added to reduce the hardness of the cast iron. The only way to increase the strength of the barrel was to increase its wall thickness. Although the strength did not increase significantly above a certain wall thickness, the weight of the system did. For this reason, barrels began to be forged from special alloy steels. Cold-forged barrels have been proven to have a 30% longer service life.

A decisive factor for the quality of barrel production is the application of spiral grooves-sets, usually 4-6 pieces, with a depth of 0.1 mm. In addition, holes are drilled in the barrel, or the outer surface is shaped by machining with classic lathes and milling machines. Another difficulty is the production of the short and narrow connecting cone that allows the bullet to fit into the rifling set between the chamber and the barrel, which is usually opened by honing. When machining these surfaces, a roughness value of R_a = 0.4 µm must be achieved so that the inner surface of the gun barrels appears very shiny when viewed.

An important point to consider in achieving the targeted sensitivities is compliance with standards. Especially when you consider that the NATO STANAG AEP-97 specifies a service life of 25,000 rounds for an infantry rifle, the difficulties of concepts such as precision, service life, and accuracy become even clearer (2020).

Figure 5 Image of the rifle-set structure of a standard pistol (2023c)

1.1.Broach Rifling Method:

There are two different application methods: single gravel or multi-gravel. Here, the grooves are opened individually by running the cutting tool on the rotating mandrel along the length of the barrel, the so-called rifling hook, through the barrel several times in the form of a single groove, either manually or with the aid of a machine. The process is repeated until the desired groove depth is reached. Assuming that each groove is opened at once, the process must be repeated as often as the number of grooves. The quality of the production depends directly on the skills of the technician. Since a single cutting tool is used, the tool costs are relatively low compared to other methods.

It is the oldest and slowest method of barrel production. It is a relatively expensive method, as it can sometimes take a technician a day to make a barrel. On the other hand, it is a production method

that offers very good shot distribution, as the mechanical and physical stresses remain very low. When the process of grooving, which was repeated by hand, was carried out by hydraulic machines, the button method was born. Figure 6 below shows the application of the single groove method and the parts of the cutting pin used in this method.

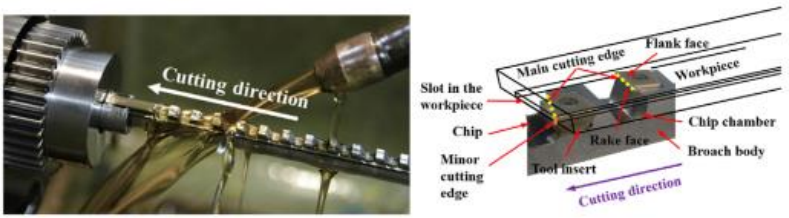

Figure 6 Application of the Single Broach method and pen sections (Huang et al. 2023)

In the multiple broaching method, the cutting tool has as many cutting edges as there are grooves. A cutting blade specially made for the barrel to be produced is passed once through the barrel and the groove shape is specified. Compared to the single stone method, the cost of the cutting tool increases slightly, but it is a faster method as the desired groove depth is achieved in one pass. Although this speed gives the method a considerable cost advantage, it also reduces the technician's influence on quality.

1.2.Button Rifling Method:

When opening rifling with the button method, a hole is first drilled in the billet where the barrel is to be made that is smaller than the minimum inside diameter of the rifling, and this hole is usually honed first. After honing, the cutting tool, the so-called button, which is generally made of very hard materials such as tungsten carbide and has a geometry opposite to the groove shape, is passed through the opened hole. The situation that one tries to express as the opposite of the groove shape is that the groove and the set have the same dimensions, but the groove in the cutting tool creates a set in the barrel. While the mandrel on which the cutting tool is located is

rotated by an electric stepper motor, the bench to which the motor is attached is pulled by a piston, creating a spiral groove- set. To prevent the barrel from heating up during shaping and to avoid residual stresses, the inside of the barrel and the mandrel are lubricated during the process. Since part of the plastic deformation energy acting on the steel is returned by elastic deformation, in many cases it is necessary to perform a second button press. As this is a fast method, it is often preferred in mass production.

As the machining is carried out in a single pass, stresses occur in the barrel. Slight preheating of the barrel facilitates shaping, and it is also possible to absorb the rebound caused by elastic deformation. The heated and shaped barrel is passed through the button several times until it has cooled down and the resulting changes in shape and surface roughness have been eliminated. The recrystallization temperature of the barrel material can be regarded as the upper limit for determining the heating temperature.

The method can be considered the most suitable processing method for mass production in terms of cost and speed. It is a method that enables low-cost, fast and medium-precision production of drums without the need for high technology. Although the notch effect remains on the surface, it is also an important advantage that thermal residual stresses are eliminated.

Figure 7 Cutting tool used in the button method (Guner 2019)

1.3.Forging Rifling Method:

This is a method that was developed in Germany before the Second World War. It was developed to extend the life of the barrel of the MG-42 machine gun used by Germany in the war. Although it can be applied hot, cold forging is more efficient as it does not affect the internal structure of the material. With this method, the barrel is produced in a different shape to its final dimensions. The barrel is made 30% shorter than the desired final length and the diameter of the barrel is 20% larger. Following a similar logic to the mandrel in the button method, the mandrel of harder material is inserted into the barrel with the opposite profile to the groove set. The outside of the barrel is hammered from four directions on a machine capable of 1500 hammer blows per minute. This process increases the length of the barrel. In the same way, the inner diameter of the barrel, which is squeezed and pressed, narrows and as it narrows, it takes on the shape of the mandrel inside. During forging, an attempt is made to achieve a compressive stress in the range of 45-130 bar with a hammer force of 700 kN.

In the button method, the mandrel holding the cutting tool is turned and pulled, whereas the forging method requires neither turning nor pulling, as the grooves on the mandrel are spiral-shaped. Forging the barrel of an infantry rifle takes about five minutes with today's technology. As the grain diameters in the inner structure of the forged barrel decrease, the strength values increase. Production benches are expensive, but are often preferred due to the quality they offer. In terms of mass production, cost and speed aspects are the main reasons for the focus of manufacturers.

The fact that the material is forged means that residual stresses remain in the internal structure. Heat treatments such as carbunitration are used to reduce the internal stresses and increase the hardness of the inner surface of the barrel. Steels such as 2340, which have a very high hardness, are difficult to shape using the forging method. The choice of button or electrochemical processes for barrels made of such materials leads to better results. Figure 8

shows a schematic diagram of the forging machine used to obtain a barrel by shaping metal powders by forging.

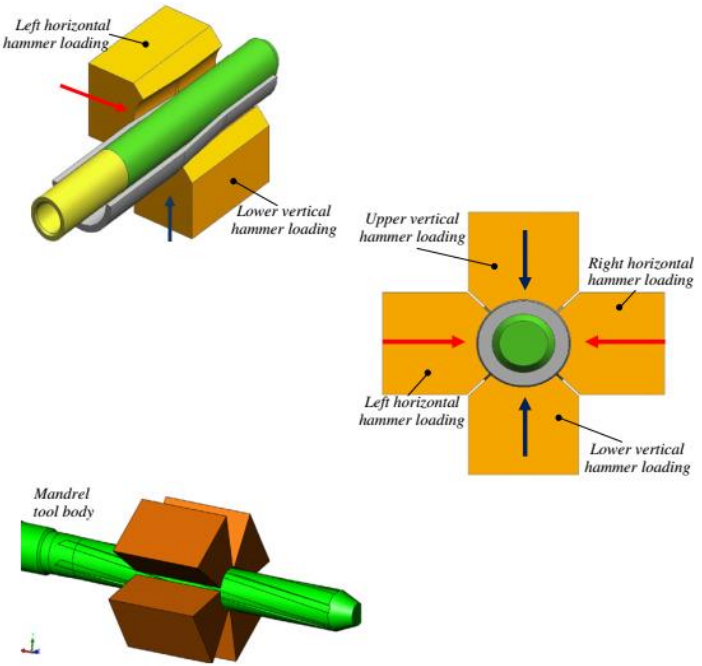

Figure 8 Shematic view of barrel forging

1.4.Electro-Chemical and Electro-Erosion Methods:

The most important advantage of the methods is that they can process any material. Very hard barrels in particular are processed using the electric arc method. Although they are slower and therefore more expensive than other methods, they enable production with high quality and precise tolerances.

In the electrochemical method, anode current is fed into the barrel. The drum charged with anode current is immersed in the corrosive medium. NaCl, NaOH, $NaNO_3$ are used as abrasives. The calculation of the time required for the amount of material that the chemical abrasive removes from the surface affects the precision of

production. While the production process should be carried out much more carefully, the chemical process and the cost of this process can be presented as the negative aspects of the electrochemical barrel production method.

In barrel production with an electric arc, an electric arc is brought into contact with the metal surface and the material is removed from the surface. The arc is the driving force of the method and no external force is required. This method is too slow and too costly to be suitable for mass production.

With both the arc and electrochemical methods, it is not possible for residual stresses to remain in the internal structure of the barrel. The initial investment costs for the arc method are very high and the electrochemical method, especially the chemicals and their disposal, are expensive.

1.5.Plastering or Flowing Plastering Method:

It is a method that is mainly used in the 21st century. It is a method similar to the forging method. It involves creating a set of grooves inside the barrel by crushing and expanding it from the outside of the barrel using three cleaning heads. As the extent of the cold forming is greater, the hardening effect of the material is also greater. In this way, hardening heat treatments such as nitriding, which is carried out with the forging method, are not required. As the deformation is greater in one direction, an elongated grain structure is formed in this direction, which increases the tensile strength. It is a method that offers the possibility of producing final barrel sizes in terms of surface quality and dimensional accuracy. The main advantage of this method is the reduction in labor costs due to production that does not require additional steps such as finishing.

2.Barrel Materials

The carbon ratio is an important hardness parameter in the definition of steel. While the carbon content increases the hardness,

it reduces the toughness. Since hardness and a certain toughness are desired simultaneously in the production of barrels, it is inevitable to use alloyed steels. In general, steels used for the production of barrels contain between 0.02% and 2% carbon. Above this value, the carbon content passes into the class of cast iron. Cast iron is not used in the manufacture of drums. 2 % carbon provides the required strength in terms of corrosion and heat resistance. Figure 9 shows the section of the iron-carbon diagram where barrel materials are preferred.

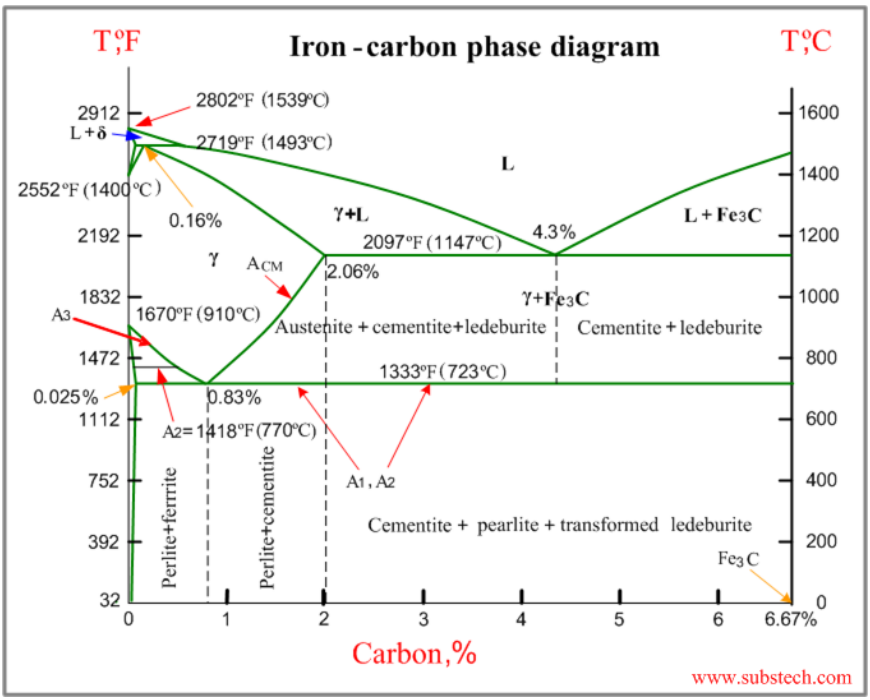

Figure 9 Iron-carbon phase diagram (2023a)

AISI4340 is a steel alloy that is often used in the manufacture of barrels. Looking at its components, we know that it contains approximately 1.7% C, 1% Mn, 0.5% Si and less than 0.05% P and S. Another steel alloy commonly used on the market is AISI 4140 steel and 416 stainless steel, which is easy to machine due to its high sulfur content and resistant to corrosion thanks to the 10% Cr content

in the alloys. The balance between hardness and machinability is very important for barrel steel. Machining extremely hard materials significantly increases tooling costs and causes many problems. As hardness increases, toughness and impact strength decrease and brittleness increases. Steels with a Rockwell hardness of 25-32 and a yield strength of over 700 MPa are considered suitable for the manufacture of barrels. To achieve the hardness, the entire barrel can be subjected to surface or heat treatment. Material optimization plays an important role when it comes to making the gun lighter by reducing the wall thickness of the barrel.

As mentioned in the previous sections, a significant proportion of steel production comes from scrap. In this case, the uncontrolled element ratio in its composition poses a risk to production quality. Secondary metallurgical processes such as vacuum arc remelting (VAR) are used to ensure that the steel has a high degree of purity and homogeneity. Apart from this, the question of whether the pipe material to be used is suitable for heat treatment is also an important criterion for selection.

The characteristic properties of steel are directly related to its chemical composition. As each alloying element added makes a positive or negative contribution, each alloying element is used in certain proportions. Apart from its functionality, steel is also named according to the amount of alloying elements it contains. If the weight percentage of the alloying element added to the steel is more than 5%, the steel is called alloyed steel. Alloying elements have positive and negative properties.

Basically, we can list the reasons for adding alloying elements as increasing heat treatment ability, increasing strength, increasing corrosion resistance, increasing high temperature resistance, ductility, wear and fatigue resistance . At this point, it would be appropriate to remind the effect of alloying elements on steel;

Carbon (C): Carbon, which is the basic alloying element of steel alloys, increases the hardness and strength significantly with

the increase in its amount in the structure. While the tensile and yield strength increases up to 0.8% carbon by weight, brittleness occurs after this value. For this reason, with the increase in the amount of carbon, it causes a loss of properties such as malleability and weldability. The increase in steel production in the modern sense by reducing the percentage of carbon has been a groundbreaking development in the advancement of barrel technology.

Manganese (Mn): In order to improve mechanical properties, the addition of manganese other than that from the ore is in question in steel production. It provides an effective strength plus in the steel structure of manganese up to 3% by weight. It gives the alloy an effect that increases hardenability and malleability .

Chromium (Cr): Chromium is the most added alloying element to steel with its properties such as increasing oxidation and corrosion resistance, laying the groundwork for carbide formation, improving hardenability by heat treatment , increasing tensile strength and wear resistance. In cases where K rom is insufficient, these properties are brought to the desired level by adding Nikel (Ni) and Molib (Mo) to the alloy.

Nickel (Ni): It is frequently used to increase strength and toughness in steel alloys with its grain thinning feature. When combined with chromium, it provides improvements in fatigue resistance, hardenability and ductility parameters.

Molybdenum (Mo): When used together with molybdenum, nickel and chromium, it significantly increases impact toughness, yield and tensile strength.

Silicon (Si): It is found in trace amounts in many alloys, as it is used to increase the fluidity of liquid metal and as a deoxidizer, whether in the production of steel from ore or scrap. Silicon, which is preferred to increase temperature resistance and hardness, has a negative effect on grain size.

Phosphorus (P): The presence of phosphorus in the steel structure increases the strength and hardness and reduces the

toughness, impact strength and ductility of the material. In order to increase corrosion resistance, it is added to steel alloys in low amounts.

Sulfur (S): Sulfur, which is generally encountered as an undesirable alloying element, is used to increase the machining capability, especially in free-cutting steels. With the increase in the amount of sulfur, impact strength and ductility decrease, which adversely affects the hardenability.

Titanium (Ti): It is used in steel alloys with its grain thinner, hardness enhancing, strong carbide forming properties.

Copper (Cu): Copper, which is used to increase corrosion resistance and hardness, greatly reduces ductility and creates brittleness.

Cobalt (Co): Cobalt, which is used for speed steels and high temperature resistant steels, reduces grain coarsening at high temperatures.

Aluminum (Al): It contributes to steel alloys as it is a grain thinner and a strong deoxidant.

Boron (B): It is used to contribute to the hardenability of low and medium carbon steels in very low quantities.

Wolfram (W): Wolfram, which is especially encountered in tool steels and high-speed steels, increases the strength of the steel. It is used in steels that are expected to withstand high temperatures with high temperature properties.

Niobium (Nb): It is used in steel alloys with its grain thinner, increasing yield strength, strong carbide forming properties.

Vanadium (V): Vanadium is an element that increases strengthening, high temperature resistance and hardenability depth.

Nitrogen (N): Nitrogen, nitride and nitride compounds, which are mainly used to increase hardness, also provide an increase in mechanical strength and resistance to corrosion.

Other alloying elements such as Ti, Mn, Zn etc. can also be used, but these are only used to a very limited extent in the manufacture of barrels (Sadeler and Atasoy 2016, 2011, Tan and Savaşkan 2020, Savaşkan, Tan, and Maleki 2015).

Quenched and tempered steels are one of the basic steel groups used as barrel material. These are unalloyed and alloyed machining steels that have a high toughness at a certain tensile strength and are suitable for hardening, particularly with regard to their chemical composition, especially the carbon content. In general, quenched and tempered steels are required to have high strength and ductility and are tempered at high temperatures after hardening. Quenched and tempered steels contain a high carbon content (0.25-0.60 C) in order to achieve sufficient martensite hardness.

Recultivation process; it is described as the entire process in which the workpiece is first hardened and then tempered, which ultimately gives it high toughness properties. The good results of the recultivation process, i.e. achieving the desired toughness or hardness value, are closely related to the cleanliness of the internal structure of the steel used. When cleaning the internal structure, gases such as hydrogen, oxygen and nitrogen are removed from the liquid steel and residues such as oxide and sulphur are removed. Improved steels according to international standards; they are divided into four main groups: unalloyed, manganese-alloyed, chromium-alloyed and chromium-molybdenum-alloyed quenched and tempered steels. (Standards). In unalloyed and manganese steels, the hot forming temperature is between 850-1100°C, in other steels; it ranges from 850-1050°C.

Hot-work tool steels can be used as an additional barrel material. When selecting these steels, criteria such as the production parameters, the suitability of the steel for heat treatment and the process conditions are taken into account. The selection of the hot work steel to be used during the process should be made taking into account the conditions to which the steel will be exposed, i.e. in a

direction that provides the necessary resistance to the primary damage mechanism that limits the life of the mold. In processes where thermal fatigue is observed, ESR (sub-slag remelting) steels are preferred.

Hot-work tool steels are steels designed for high-temperature applications above 200°C. The most fundamental property of these steels is that they can maintain sufficient strength during repeated hot forming processes, and this is ensured by the appropriate chemical composition. These steels must maintain their mechanical properties at high temperatures due to their areas of application. Therefore, hot-work tool steels contain special alloying elements that ensure hot hardness.

Hot-work tool steels are a preferred steel group in industrial applications as they are wear and fracture resistant at high temperatures, have high toughness values and are also impact resistant at high temperatures. Hot-work tool steels are designated with the letter H according to the AISI standards. These steels are divided into three groups depending on their alloying elements: They can be divided into chromium hot-work tool steels, tungsten hot-work tool steels and molybdenum hot-work tool steels.

The design of barrels is about determining the material that has the lowest weight, i.e. the smallest radial diameter, and the structural strength that allows the ammunition to be fired safely. For this reason, when designing the barrel, it is necessary to know the highest pressure that will produce a stress distribution at any point along the ammunition path in the barrel. These pressures are referred to as maximum station pressures and generally occur in the range of the heaviest bullets and most gunpowder. The fatigue that occurs when these pressures are repeatedly applied in the barrel is the most important design parameter. As the weight of the gun and developments in finite element software codes have become an important issue, the use of finite element software in barrel simulations has become widespread (Ilhak and Güner 2022).

Another problem in the construction of barrels is the decrease in the material strength of the barrel material when the temperature changes. Repeated firing of the gun releases a lot of heat as the gunpowder burns in the chamber. The temperatures that can occur in artillery and armour barrels can reach values that negatively affect the material properties. With light and rapid-firing weapons, this becomes even more important and appears to be a factor that has a negative effect on the material properties of the barrel and chamber and must be given greater account in the stress analysis. When calculating barrel designs, studies are carried out that take into account that the part is subject to thermomechanical stresses. The pressure curve in the figure shows the pressure curve that the bullet generates within the barrel geometry after firing. Along the barrel, there is a difference between the rear pressure value of the gun and the rear pressure value of the ammunition. This difference is related to the pressure values that occur when the bullet explodes, and the designed barrel was designed with the ammunition in mind.

When designing barrels, it is necessary to know the stress state of the barrel and to decide whether the material strength is insufficient in the event of stresses. The Von Misses (equivalent) stress value is calculated by substituting the stresses calculated for the loading condition, and the strength condition is evaluated by comparing whether the yield point of the material is below or above the Von Misses yield criterion. As can be seen in the figure, the geometry of the drum flute was developed taking the standards into account.

Tool steels, which are often preferred in industry, are high-quality steels that are used in machining or non-cutting production and can form hot or cold-worked parts by methods such as cutting, forging and pressing.

The carbon concentration and other alloying elements in steel have a direct effect on the structure and phase transformations that occur during metallurgical processes, plastic deformation and heat treatment. We can list the properties that are sought when hot work

tool steels are preferred as pipe materials: Resistance to deformation at application temperatures, resistance to mechanical and thermal shocks, resistance to wear at high temperatures, resistance to deformation due to heat treatment, machinability and resistance to hot cracking.

The variety of materials used in the manufacture of rifled barrels is greater than that of smoothbore barrels. With the development of production methods and alloy research, studies on the modification of existing materials are carried out on a daily basis.

32CrMoV12-10 steel is a low-carbon, high-alloy steel used in the manufacture of gun barrels, particularly in the heavy weapons industry. Most areas where this steel, which contains 3% Cr, 2% Mo and 1% V vanadium by weight, is used are in the defense industry. the 32CrMoV12-10 steel, whose wear and corrosion properties are improved by surface treatments such as etching and carburizing, is preferred in weapons such as the MP5 as a durable barrel material. Steel alloys are developed by using the alloying elements Cr, Mo and V, which are frequently found in the weapons industry due to their properties, in varying proportions. The barrel materials vary depending on the area of application of the weapon and the production method. This change occurs when alloying elements are added to the material. The addition of V can be found, for example, in 32CrMoV1210 steel, which is used in the heavy weapons industry. The V used here makes it possible to manufacture the barrel by forging and at the same time ensures high strength and durability.

Stainless steels are often used in the defense industry. Stainless steels such as AISI 340L/416/420 have good corrosion and wear resistance due to the high proportion of Ni and Cr in their structure and are easy to process due to their high S content. While austenitic stainless steels with low carbon content stand out in the defense industry due to their weldability, martensitic stainless steels are more popular in the manufacture of gun barrels due to their formability, shape, corrosion resistance and hardness properties.

Martensitic steels are another type of steel that was widely preferred in the past for the manufacture of gun barrels. Maraging steels are steels with very low carbon content that are known for their high strength and toughness without losing their ductility. These steels are a special class of ultra-high-strength steels with a very low carbon content that obtain their strength not from carbon but from the precipitation of intermetallic compounds. The most important alloying element is 15 to 25 % nickel by weight. Secondary alloying elements such as cobalt, molybdenum and titanium are added to produce intermetallic precipitates (2023b).

References

2020. AEP-97 Multi-Calibre Manual Of Proof And Inspection (M-Cmopi) For Nato Small Arms Ammunition. NATO STANDARDIZATION OFFICE (NSO).

2023a. "Iron-carbon phase diagram." SubsTech Substance &Technologies, accessed 04.12.2023. https://www.substech.com/dokuwiki/doku.php?id=iron-carbon_phase_diagram.

2023b. "Maraging steel." Wikipedia The Free Encyclopedia accessed 04.12.2023. https://en.wikipedia.org/wiki/Maraging_steel.

2023c. "Rifling." Wikipedia, accessed 04.12. https://en.wikipedia.org/wiki/Rifling.

Degirmenci, Ercan. 2015. "Effects of grain size and temperature of double base solid propellants on internal ballistics performance." *Fuel* 146:95-102. doi: 10.1016/j.fuel.2015.01.027.

Guner, Faruk. 2019. *Hafif Silahlar ve Balistik*. Ankara: Nobel Akademİk Yayincilik Eğİtİm Danişmanlik Tİc. Ltd. Ştİ. SertİfİKa No.: 40340.

Güner, F., and H. Sofuoğlu. 2018. "Effects of Process Parameters on Copper Powder Compaction Process Using Multi-Particle Finite Element Method." *IOP Conference Series: Materials Science and Engineering* 295. doi: 10.1088/1757-899x/295/1/012027.

Güner, Faruk. 2020. "Numerical Investigation of AISI 4140 Powder High Relative Density Compaction In Terms of Compaction Velocity." *Mechanics* 26 (1):5-11. doi: 10.5755/j01.mech.26.1.22862.

Güneş, Serkan. 2009. "Silah, Tasarım ve Kalashnikov Ak-47." *Sanat ve Tasarım Dergisi* 1 (4):35-52. doi: 10.18603/std.69780.

Huang, Shizhan, Tao Zhang, Zhibin Wang, Lin Cheng, Xuming Zha, Bicheng Guo, Decheng Zheng, Hong Xie, Zhiyang Xiang, Youliang Chen, and Feng Jiang. 2023. "Asymmetrical cutting-edge design of broaching tool based on FEM simulation." *Journal of Materials Research and Technology* 25:68-82. doi: 10.1016/j.jmrt.2023.05.181.

Hussain, Naveed, Faisal Qayyum, Riffat Asim Pasha, and Masood Shah. 2021. "Development of multi-physics numerical simulation model to investigate thermo-mechanical fatigue crack propagation in an autofrettaged gun barrel." *Defence Technology* 17 (5):1579-1591. doi: 10.1016/j.dt.2020.09.005.

Ilhak, Burak, and Faruk Güner. 2022. "Failure Analysis of Boron Carbide-Reinforced Rolled Homogeneous Armour Against Kinetic Energy Ammunition." *Transactions of the Indian Institute of Metals* 75 (7):1831-1841. doi: 10.1007/s12666-022-02545-1.

Sadeler, R., and S. Atasoy. 2011. "Fretting fatigue behaviour of hard anodizing coated 2014-T6 aluminium alloy with dissimilar mating materials under plane bending loading." *Fatigue & Fracture of Engineering Materials & Structures* 34 (6):383-388. doi: 10.1111/j.1460-2695.2010.01527.x.

Sadeler, R., and S. Atasoy. 2016. "The effect of contact pad hardness on the fretting fatigue behaviour of AZ61 magnesium alloy." *Fatigue & Fracture of Engineering Materials & Structures* 39 (4):502-510. doi: 10.1111/ffe.12387.

Savaşkan, Temel, Hasan Onur Tan, and Reza Anvari Maleki. 2015. "Effects of contact pressure and sliding distance on the lubricated friction and wear properties of Zn-25Al-3Cu alloy: A comparative study with SAE 65 bronze." *International Journal of Materials Research* 106 (10):1060-1066. doi: 10.3139/146.111282.

Standards, Turkish Institute of. Quenched and Tempered Steels Part 2: Technical Delivery Conditions For Unalloyed Quality Steels.

Tan, Hasan Onur, and Temel Savaşkan. 2020. "Determination of Dry Wear Properties of Zn-30Al-Cu Bearing Alloys in Terms of Their Copper Content and Working Conditions Including Pressure and Sliding Velocity." *Journal of Materials Engineering and Performance* 29 (7):4794-4803. doi: 10.1007/s11665-020-04976-7.

CHAPTER VI

The Impact of Biodiesel Utilization as an Alternative Fuel in Diesel Engines on Engine Performance and Emissions

Adem TÜYLÜ[1]
Yasin AKIN[2]
Muhammed Asım KESERCİOĞLU[3]

Introduction

The use of petroleum-derived fuels in internal combustion engines results in the release of toxic gases, emissions, negatively impacting both the environment and human health. Despite the introduction of electric and hybrid vehicles in today's market, gasoline and diesel engines are still heavily utilized from passenger

[1] Research assistant, Sakarya University of Applied Sciences
[2] Research assistant, Sakarya University of Applied Sciences
[3] Research assistant, Sakarya University of Applied Sciences

cars to heavy-duty vehicles. Especially due to the low fuel consumption and high torque outputs of diesel engines, they are expected to remain a primary energy source for vehicles in the automotive sector for an extended period. However, the diminishing petroleum reserves are leading researchers to focus on R&D initiatives for diesel engines. In the automotive sector, manufacturers and university research centers are actively conducting numerous experimental and theoretical studies to enhance diesel engine performance and reduce emissions, including nitrogen oxides (NOx) and particulate matter (PM). Emission reduction strategies involve structural modifications in engine geometry, improvements in fuel quality, optimization of engine operating parameters such as fuel injection timing and injection pressure, and the implementation of post-treatment systems like Diesel Oxidation Catalysts (DOC), Diesel Particulate Filters (DPF), and Selective Catalytic Reduction (SCR) systems. Furthermore, despite the introduction of electric and hybrid vehicles, gasoline and diesel engines continue to be intensively used in various vehicle categories within the automotive sector. The high fuel efficiency and substantial torque outputs of diesel engines are expected to maintain their status as primary energy sources for vehicles for an extended period. Nevertheless, the decreasing petroleum reserves are directing researchers towards extensive R&D efforts focused on diesel engines. In the automotive sector, manufacturers and university research centers are actively conducting numerous experimental and theoretical studies to enhance diesel engine performance and reduce emissions, including nitrogen oxides (NOx) and particulate matter (PM). Emission reduction strategies involve structural modifications in engine geometry, improvements in fuel quality, optimization of engine operating parameters such as fuel injection timing and injection pressure, and the implementation of post-treatment systems like Diesel Oxidation Catalysts (DOC), Diesel Particulate Filters (DPF), and Selective Catalytic Reduction (SCR) systems. The emissions in diesel engines are reduced through structural modifications in engine geometry, improvements in fuel quality, optimization of engine

operating parameters such as fuel injection timing and injection pressure, and the implementation of post-treatment systems like DOC, DPF, and SCR installed on the exhaust line. One notable improvement in diesel engines involves the integration of renewable, environmentally friendly alternative fuels with diesel, as highlighted by studies conducted by (Haşimoğlu et al., 2008; Ge et al., 2019; and Tüylü, 2021).

Biodiesel stands out as a prominent renewable alternative fuel for diesel engines. It is a fuel produced through various chemical processes involving animal or vegetable oils, exhibiting physicochemical properties similar to conventional diesel fuel. In the early 1900s, Rudolf Diesel himself utilized peanut oil as fuel for diesel engines. However, the high viscosity, poor volatility, and cold-flow characteristics of oils hinder their direct use in diesel engines. The use of untreated vegetable oils in diesel engines can lead to various problems over time, including injector clogging, carbon accumulation in segments, and degradation of lubricating oil. To overcome such challenges, vegetable oils undergo various chemical processes, transforming them into biodiesel fuels that can be seamlessly used in diesel engines without requiring any modifications. The historical application of biodiesel dates back to 1938 when palm oil ethyl ester was first used as fuel in a city bus. In diesel engines, biodiesel is often encountered as diesel-biodiesel fuel blends. The utilization of biodiesel in diesel engines has demonstrated the capability to reduce harmful emissions to the environment and human health, along with mitigating the performance decline typically associated with alternative fuels. The first instances of biodiesel use in diesel engines were observed in 1938 when palm oil ethyl ester was utilized as fuel in a city bus. In diesel engines, biodiesel is often utilized in the form of diesel-biodiesel fuel blends. The use of biodiesel in diesel engines has been shown to decrease harmful emissions to the environment and human health while mitigating the usual performance declines associated with alternative fuels (Alptekin and Çanakçı, 2006; Işık et al., 2016; Çoban, 2021; Selvan et al., 2022).

Biodiesel fuel is primarily produced from vegetable oils using various chemical methods. In this study, biodiesel fuels produced through the transesterification method, one of the biodiesel production techniques, have been predominantly examined. Additionally, information about other production methods is also provided. By reviewing existing literature, the effects of biodiesel fuel utilization in diesel engines on engine performance and emissions have been elucidated.

Biodiesel Production Methods

The utilization of oils as a viable fuel source in diesel engines necessitates a reduction in their viscosity. This objective can be pursued through the application of both thermal and chemical methodologies. The thermal approach entails a concerted effort to diminish the viscosity of oils by means of preheating. Nevertheless, owing to potential complications inherent in its implementation within the confines of vehicular engines, chemical methodologies are predominantly favored. These chemical methodologies are systematically classified into four principal categories, namely thinning, micro-emulsion formation, pyrolysis, and transesterification (Aksoy, 2010). Furthermore, the production efficiency in biodiesel production methods is expressed by the following equation (Abdullahi vd., 2023).

$$\text{Yield} = \frac{\text{mass of biodiesel}}{mass\ of\ oil} \times 100$$

Dilution Method

The dilution process refers to the procedure of attenuating vegetable and waste oils by blending them with a specific proportion of either a solvent or a diesel fuel. Among these procedures, the most prevalent involves the amalgamation of oils with diesel fuel. Consequently, the viscosity of the oil is mitigated, concurrently reducing the consumption ratio of diesel fuel (Özdemir ve Mutlubaş, 2016).

Microemulsion Method

Microemulsion is defined as a spontaneously formed balanced colloidal dispersion of immiscible liquids, either ionic or nonionic organic mixtures, with dimensions ranging from 1 to 150 nm. Microemulsion typically arises from the coalescence of one or more amphiphiles in the presence of two immiscible liquids. In the microemulsion process, the organic substance employed is alcohol, with short-chain aliphatic alcohols such as methanol and ethanol being commonly utilized (Aksoy, 2010).

Pyrolysis Method

Pyrolysis, defined as the process in which high-molecular-weight compounds undergo transformation into lower-level molecules at elevated temperatures, is generally executed through two primary methods. In the first method, vegetable oils are subjected to thermal decomposition within a closed container. The second method involves the thermal breakdown of vegetable and waste oils through distillation using conventionally prepared substances. Biodiesel obtained through the second method exhibits characteristics more closely resembling conventional diesel fuels (Özdemir ve Mutlubaş, 2016).

Transesterification Method

The transesterification method is the most commonly used technique in biodiesel production. In this method, oil and alcohol are reacted in the presence of a catalyst to produce biodiesel and glycerol. Short-chain alcohols, particularly methanol and ethanol, are used in the transesterification reaction due to their low cost compared to other alcohols. Methanol is the most widely used alcohol in biodiesel production. Biodiesel is expressed as fatty acid methyl esters obtained through the transesterification of triglycerides in vegetable oils with methanol (Figure 1).

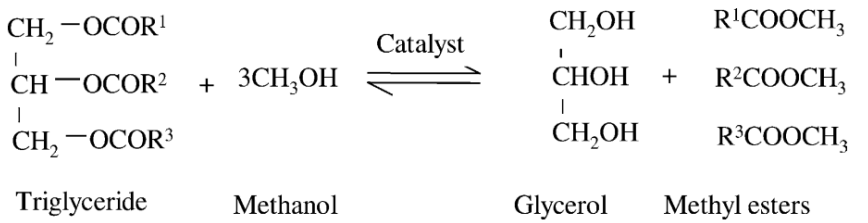

Figure 1. *General equation for transesterification of triglycerides (Meher et al., 2006)*

The transesterification method allows for the production of biodiesel from vegetable, animal, and waste oils. Across all biodiesel production methods, the largest share of the total production cost is attributed to the procurement of oil feedstock. Therefore, biodiesel production from waste oils, despite requiring various purification processes initially, is a more economical process. The process of biodiesel and glycerol production from waste oils is illustrated in Figure 2.

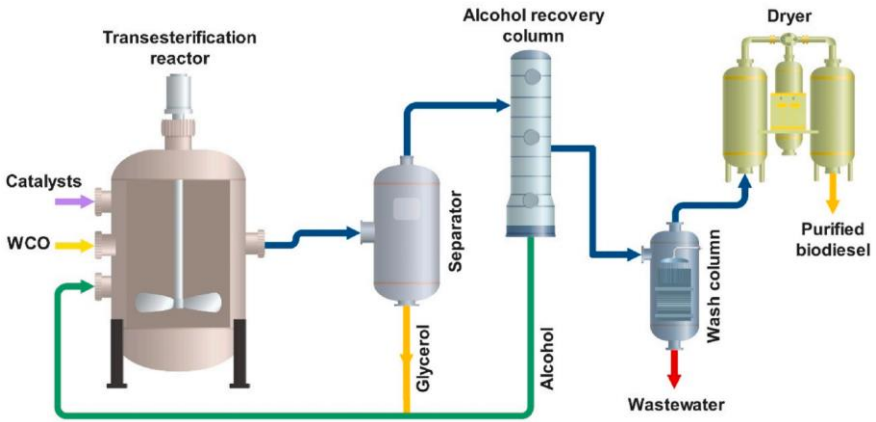

Figure 2. *Transesterification process of WCO (Hosseinzadeh-Bandbafha et al., 2022)*

Various parameters, including reaction time, reaction temperature, and the catalyst used, influence the quality of biodiesel fuel produced through the transesterification method. The efficiency

and duration of biodiesel production vary, particularly based on the catalyst employed in the reaction. Catalysts used in biodiesel production are categorized into two groups: homogeneous and heterogeneous catalysts. Within each group, catalysts are further classified as acidic, basic, or enzymatic based on their characteristics (Figure 3). In this classification based on the catalyst type, the most commonly used catalysts in the biodiesel production industry are homogeneous basic catalysts. Homoogeneous basic catalysts, such as sodium hydroxide (NaOH) and potassium hydroxide (KOH), are widely used in the biodiesel industry to achieve high-efficiency production with short reaction times (Mandari and Devarai, 2022; Nayab et al., 2022).

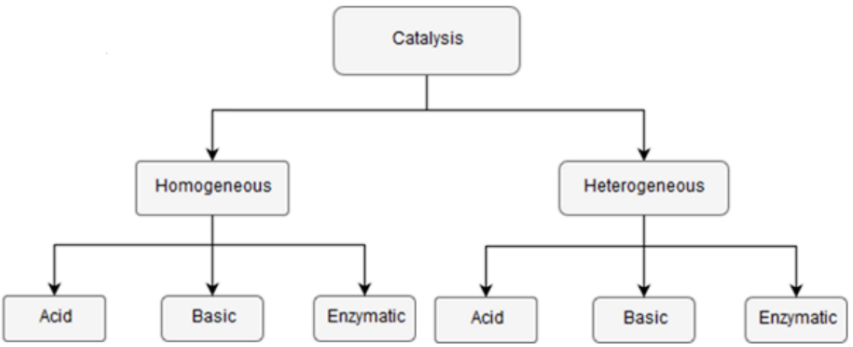

Figure 3. *Classification of catalysts used in biodiesel production*

The production processes of biodiesel through the transesterification method vary depending on factors such as raw material accessibility, economic viability, and geographical characteristics. According to Maheshwari et al. (2022), biodiesel can be produced from a variety of raw materials, including canola, soy, corn, cotton, and sunflower vegetable oils. The choice of catalyst type is determined based on the characteristics of the raw material, such as water content and free fatty acid levels. Additionally, through pretreatment before the reaction, the properties of the oil can be adjusted to meet the desired limit values. If the free fatty acid content exceeds 2.5% by weight, oil pretreatment is carried out. The

process steps of biodiesel production with alkaline catalysts are illustrated in Figure 4.

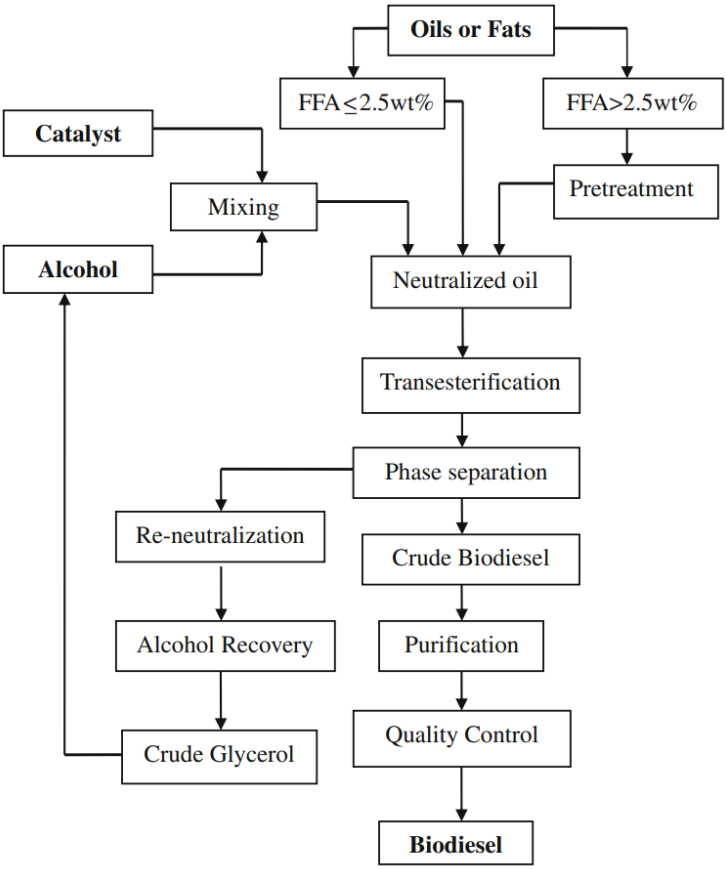

Figure 4. *Biodiesel production process with alkaline catalyst (Leung et al., 2010)*

The physicochemical properties of biodiesel fuels produced through the transesterification method are quite similar to those of diesel fuel. This allows biodiesel fuels to be used in diesel engines without any structural modifications. Basic properties of biodiesel and diesel fuel have been extracted from publications in the literature (Aydın and Öğüt, 2017; Hasan and Rahman, 2017; Krishna et al.,

2019; Vignesh et al., 2021; Elgharbawy et al., 2021; Zhang et al., 2022), as presented in Table 1. In Table 1, it can be observed that the calorific value of biodiesel fuel is lower than that of diesel fuel. Additionally, the higher oxygen content of biodiesel fuel compared to diesel fuel has significant effects on combustion, performance, and emissions in diesel engines.

Table 1. *Specifications of Biodiesel and Diesel Fuels*

Specifications	Units	Biodiesel	Diesel
Cetane number	-	47 - 67	43 - 65
Oxygen content	wt%	10 - 11.6	0 - 0.3
Kinematic viscosity	mm^2/s @40℃	1.9 - 12	2 – 4.2
Calorific value	MJ/kg	37.3 - 39.5	42.7 - 45
Flash point	℃	100 - 180	54 - 148
Cloud point	℃	-2 - 20	-9 - -5
Pour point	℃	-7.5	-20
Density	kg/m^3	835 - 896	816 - 840

The Impact of Biodiesel Fuel on Diesel Engine Performance and Emissions

Renewable, sustainable alternative fuels, with biodiesel being a prominent example, are widely used in diesel engines and extensively researched as fuel in experimental studies. The lower calorific value of biodiesel compared to diesel fuel often leads to a deterioration in engine performance when used in diesel engines. However, there are studies indicating improvements in engine performance with the use of biodiesel in diesel engines (Singh et al., 2020). Regarding emissions, the use of biodiesel generally results in reductions in CO, HC, and particulate matter emissions, but increases in NOx emissions are often observed. The effects of biodiesel usage on diesel engine performance and emissions can vary based on factors such as the quality of the fuel used in experimental studies, the capacity of the test engine, and operating conditions (Roy et al., 2013; Palani et al., 2022).

Şimşek and Çolak (2019) conducted experimental studies on a single-cylinder, 12 HP diesel engine, where they used biodiesel and propanol as alternative fuels. In their research, they utilized fuels obtained by adding 10%, 20% propanol to diesel, biodiesel, and a blend of biodiesel with 10%, 20% propanol. The engine was operated under full-load conditions. The best engine performance values were achieved with diesel fuel. They observed improvements in engine performance when propanol was added to biodiesel fuel. In comparison to diesel fuel, using biodiesel fuel resulted in decreases in CO, HC, and particulate matter emissions, along with an increase in NOx emissions. The addition of propanol to biodiesel led to a decrease in CO, particulate matter, and NOx emissions, while an increase in HC emissions was noted. They explained these changes in emissions by the structure of alcohol and biodiesel, where there are fewer carbon atoms and more oxygen atoms compared to diesel fuel.

Yeşilyurt et al. (2020) conducted experiments on a naturally aspirated, direct-injection diesel engine under four different load conditions and constant engine speed of 3000 rpm, testing biodiesel-diesel dual fuel blends and biodiesel-diesel-pentanol triple fuel blends. The biodiesel used in their study was methyl ester of hazelnut oil. They tested a total of 6 different fuels by adding pentanol to diesel, B20 (20% biodiesel, 80% diesel), and B20 fuels at volumetric ratios of 5%, 10%, 15%, and 20%. The highest thermal efficiency values in terms of brake thermal efficiency were obtained with diesel fuel. The increased NOx emissions due to biodiesel use were reduced to levels below those of diesel fuel by adding pentanol at ratios of 10% and above. Maximum values for HC, CO, and particulate matter emissions were observed when using diesel fuel. As the amount of pentanol added to biodiesel increased, greater reductions were achieved in these three emissions. The increase in the CO2 content in exhaust gases from diesel fuel to B20P20 fuel is noteworthy. They attributed these trends in emissions to the increase in oxygen levels in the combustion chamber and the improvement in

combustion efficiency resulting from the use of biodiesel and pentanol blends.

Radhakrishnan et al. (2019) tested diesel, orange peel oil biodiesel (BD100), BD94W4S2 (94% volume of biodiesel + 4% volume of water + 2% volume of surfactant), and BD90W8S2 (90% volume of biodiesel + 8% volume of water + 2% volume of surfactant) fuels in four-stroke, 2-cylinder, naturally aspirated, direct-injection experimental engines. They used Span80 as a surfactant to create a biodiesel-diesel emulsified fuel mixture. Maximum brake thermal efficiencies under different engine loading conditions were all obtained with diesel fuel. As the amount of water added to the biodiesel emulsified fuel mixture increased, the brake thermal efficiency values approached those obtained with diesel fuel. The reductions in CO, HC, and smoke opacity emissions due to biodiesel use further decreased with the addition of water to the biodiesel fuel. On the other hand, the increase in NOx emissions compared to diesel fuel due to biodiesel use was reduced as the amount of water in the emulsified fuel increased.

Sürer et al. (2023) investigated the effects of blending biodiesel produced from waste frying oils through the transesterification method with diesel fuel, and the addition of 25, 50, 75, and 100 ppm multi-walled carbon nanotubes (MWCNT) to B20 (80% diesel + 20% biodiesel) on the performance and emissions of a diesel engine. The MWCNT used in their study had an outer diameter of 4-16 nm, inner diameter of 2-6 nm, length of 15-35 μm, and specific surface area of 240 m2/g. They achieved the homogenous mixture of MWCNT and B20 fuel through a 30-minute mixing process in an ultrasonic bath (homogenizer). The experimental studies were conducted under full load conditions and varying engine speeds from 1600 rpm to 2600 rpm. As the amount of MWCNT added to B20 fuel increased, they observed increases in effective efficiency and effective power values. Additionally, they noted reductions in CO, HC, and particulate matter emissions, while NOx emissions increased with the increasing amount of MWCNT in the mixture.

Gad et al. (2021) investigated the impact of adding 25, 50, and 100 ppm of carbon nanotubes and graphene nanoplatelets to waste oil methyl ester on the performance and emissions of a diesel engine. It was observed that the addition of graphene nanoplatelets was more effective than the addition of carbon nanotubes in influencing engine performance and emission values. For instance, the increased NOx emissions compared to B20 and diesel fuels were more significantly reduced with the addition of graphene nanoplatelets to B20 fuel compared to the addition of carbon nanotubes. They achieved lower emissions for all pollutants, including CO, HC, particulate matter (is), and NOx, with the addition of nanoparticle blends compared to B20 fuel.

Öztürk et al. (2020) conducted research on the engine performance and emissions of triple fuel blends containing varying proportions of isobutanol, biodiesel, and diesel fuels in a common rail DI, 4-cylinder experimental engine. The fuels used in their study included mixtures of biodiesel and isobutanol at 20% and 15%, respectively (B20 and I15), as well as triple blends created with increasing proportions of isobutanol (I15B20, I25B20, and I35B20). They conducted their experiments at a constant engine speed of 1800 rpm under four different loads. The specific fuel consumption values for fuel blends containing biodiesel and isobutanol were found to be higher than those for diesel fuel. Under all operating conditions, they achieved the minimum HC emissions with the B20 fuel. When considering brake thermal efficiency and emission parameters together, they found that at low engine loads, B20 fuel provided the best results, while at high loads, the I35B20 fuel blend yielded the optimal outcomes.

Teoh et al. (2022) evaluated the engine performance and emission data obtained from a turbocharged, common rail DI, 4-cylinder diesel engine using diesel, B10 (10% biodiesel, 90% diesel), and P10 (10% tire pyrolysis oil (TPO), 90% diesel) fuels. They produced the P10 fuel by blending oil derived from waste tires through the pyrolysis process with diesel fuel. The maximum values for engine effective power and brake thermal efficiency were

achieved with the P10 fuel. Under full load conditions and at all engine speeds, P10 fuel resulted in the minimum values for NOx and CO emissions compared to the other two fuels.

Advantages and Disadvantages of Biodiesel Fuel

The advantages and disadvantages of using biodiesel in diesel engines are listed below in bullet points (Knothe et al., 2015; Knothe and Razon, 2017; Sadaf et al., 2018; Gebremariam and Marchetti, 2018; Yıldırım, 2019):

Advantages of Biodiesel

- Renewable fuel.
- Production from a wide variety of feedstocks.
- Production feasibility through various methods.
- Biodegradability.
- Reduction of most exhaust emissions (except nitrogen oxides, NOx).
- Higher flash point leading to safer handling and storage.
- Higher lubricating properties compared to diesel fuel.
- Absence of sulfur and aromatic content.
- Compatibility with diesel fuel in varying proportions.
- Compatibility with existing fuel distribution station infrastructure.
- Carbon-neutral nature.

Disadvantages of Biodiesel

- High production cost.
- Cold flow properties.
- Oxidative stability.
- High NOx emissions.

• While the biodegradability of biodiesel is often highlighted as an advantage, it also implies bacterial biomass, which can grow during the fuel storage process. Accumulations in the fuel lines may lead to blockages.

Conclusions

Renewable and eco-friendly biodiesel fuels rank first among alternative fuels used in diesel engines. Biodiesel fuel can be produced from various plant, animal, and waste oils using different methods. Biodiesel fuel produced from various vegetable oil feedstocks through the transesterification method is widely used in diesel engines. The use of biodiesel fuel in diesel engines does not require any structural modifications to the engine.

The use of biodiesel fuel in diesel engines generally results in a decrease in motor performance parameters compared to diesel fuel usage. Diesel engine CO, HC, and particulate matter emissions are significantly reduced with diesel-biodiesel fuel blends. However, NOx emissions tend to be higher in diesel-biodiesel fuel blends compared to diesel fuel.

REFERENCES

Abdullahi, K., Ojonugwa, S. S., Yusuff, A. S., Umaru, M., Mohammed, I. A., Olutoye, M. A., & Aberuagba, F. (2023). Optimization of biodiesel production from Allamanda Seed Oil using design of experiment. *Fuel Communications*, *14*, 100081.

Aydın, F., & Öğüt, H. (2017). Effects of using ethanol-biodiesel-diesel fuel in single cylinder diesel engine to engine performance and emissions. *Renewable energy*, *103*, 688-694.

Elgharbawy, A. S., Sadik, W., Sadek, O. M., & Kasaby, M. A. (2021). A review on biodiesel feedstocks and production technologies. *Journal of the Chilean Chemical Society*, *66*(1), 5098-5109.

Hosseinzadeh-Bandbafha, H., Nizami, A. S., Kalogirou, S. A., Gupta, V. K., Park, Y. K., Fallahi, A., ... & Tabatabaei, M. (2022). Environmental life cycle assessment of biodiesel production from waste cooking oil: A systematic review. *Renewable and Sustainable Energy Reviews*, *161*, 112411.

Krishna, S. M., Salam, P. A., Tongroon, M., & Chollacoop, N. (2019). Performance and emission assessment of optimally blended biodiesel-diesel-ethanol in diesel engine generator. *Applied Thermal Engineering*, *155*, 525-533.

Maheshwari, P., Haider, M. B., Yusuf, M., Klemeš, J. J., Bokhari, A., Beg, M., ... & Jaiswal, A. K. (2022). A review on latest trends in cleaner biodiesel production: Role of feedstock, production methods, and catalysts. *Journal of Cleaner Production*, *355*, 131588.

Mehmet, I. Ş. I. K., Aydın, H., Yücel, H., Budak, N., Oktay, H., & Bayındır, H. (2016). Aspir Ve Kanola Biyodizeli Kullanımının Egzoz Emisyonu Ve Motor Performansına Etkilerinin İncelenmesi. *Küresel Mühendislik Çalışmaları Dergisi*, *3*(1), 1-11.

Nayab, R., Imran, M., Ramzan, M., Tariq, M., Taj, M. B., Akhtar, M. N., & Iqbal, H. M. (2022). Sustainable biodiesel

production via catalytic and non-catalytic transesterification of feedstock materials–A review. *Fuel*, *328*, 125254.

Radhakrishnan, S., Munuswamy, D. B., Devarajan, Y., & Mahalingam, A. (2019). Performance, emission and combustion study on neat biodiesel and water blends fuelled research diesel engine. *Heat and Mass Transfer*, *55*, 1229-1237.

Ramos, M., Dias, A. P. S., Puna, J. F., Gomes, J., & Bordado, J. C. (2019). Biodiesel production processes and sustainable raw materials. Energies, 12(23), 4408.

Sadaf, S., Iqbal, J., Ullah, I., Bhatti, H. N., Nouren, S., Nisar, J., & Iqbal, M. (2018). Biodiesel production from waste cooking oil: an efficient technique to convert waste into biodiesel. *Sustainable cities and society*, *41*, 220-226.

Selvan, B. K., Das, S., Chandrasekar, M., Girija, R., Vennison, S. J., Jaya, N., ... & Rajamohan, N. (2022). Utilization of biodiesel blended fuel in a diesel engine–Combustion engine performance and emission characteristics study. *Fuel*, *311*, 122621.

Singh, D., Sharma, D., Soni, S. L., Sharma, S., Sharma, P. K., & Jhalani, A. (2020). A review on feedstocks, production processes, and yield for different generations of biodiesel. *Fuel*, *262*, 116553.

Sürer, E., Solmaz, H., Yılmaz, E., Calam, A. L. P. E. R., & İpci, D. U. Y. G. U. (2023). Dizel-biyodizel karışımına karbon nanotüp katkısının motor performansı ve egzoz emisyonlarına etkisinin incelenmesi. *Journal of the Faculty of Engineering and Architecture of Gazi University*, *38*(2).

Teoh, Y. H., Yaqoob, H., How, H. G., Le, T. D., & Nguyen, H. T. (2022). Comparative assessment of performance, emissions and combustion characteristics of tire pyrolysis oil-diesel and biodiesel-diesel blends in a common-rail direct injection engine. *Fuel*, *313*, 123058.

Vignesh, P., Kumar, A. P., Ganesh, N. S., Jayaseelan, V., & Sudhakar, K. (2021). A review of conventional and renewable biodiesel production. *Chinese journal of chemical engineering*, *40*, 1-17.

Zhang, Z., Lv, J., Li, W., Long, J., Wang, S., Tan, D., & Yin, Z. (2022). Performance and emission evaluation of a marine diesel engine fueled with natural gas ignited by biodiesel-diesel blended fuel. *Energy*, *256*, 124662.

Mandari, V., & Devarai, S. K. (2022). Biodiesel production using homogeneous, heterogeneous, and enzyme catalysts via transesterification and esterification reactions: A critical review. *BioEnergy Research*, *15*(2), 935-961.

Palani, Y., Devarajan, C., Manickam, D., & Thanikodi, S. (2022). Performance and emission characteristics of biodiesel-blend in diesel engine: A review. *Environmental Engineering Research*, *27*(1).

Çoban, A. (2021). Biyodizel karışımları ile çalışan bir dizel motorunda performans, NO ve is emisyonlarını etkileyen faktör seviyelerinin taguchi yöntemi ile belirlenmesi. *Academic Platform-Journal of Engineering and Science*, *9*(2), 229-237.

Gad, M. S., Kamel, B. M., & Badruddin, I. A. (2021). Improving the diesel engine performance, emissions and combustion characteristics using biodiesel with carbon nanomaterials. *Fuel*, *288*, 119665.

Tüylü, A. (2021). *Kısmi homojen dolgulu direkt enjeksiyonlu bir dizel motorunun deneysel ve numerik olarak incelenmesi* (Master's thesis, Sakarya Uygulamalı Bilimler Üniversitesi).

Öztürk, Y. E., Altınkurt, M. D., & Türkcan, A. (2020). Dizel-Biyodizel-İzobütanol Üçlü Karışımları Kullanılan Bir Dizel Motorda Performans Ve Emisyon Karakteristiklerinin Deneysel

Olarak İncelenmesi. *Uluslararası Yakıtlar Yanma Ve Yangın Dergisi*, (8), 56-66.

Yesilyurt, M. K., Yilbasi, Z., & Aydin, M. (2020). The performance, emissions, and combustion characteristics of an unmodified diesel engine running on the ternary blends of pentanol/safflower oil biodiesel/diesel fuel. *Journal of Thermal Analysis and Calorimetry*, *140*, 2903-2942.

Şimşek, D., & Çolak, N. Y. (2019). Biyodizel/Propanol yakıt karışımlarının dizel motor emisyonlarına etkisinin incelenmesi. *El-Cezeri*, *6*(1), 166-174.

Yıldırım, B. (2019). *Aşırı doldurmalı kısmi yalıtımlı bir dizel motorunda biyodizel ve EGR kullanımının performans ve emisyonlara etkilerinin incelenmesi* (Master's thesis, Sakarya Uygulamalı Bilimler Üniversitesi).

Gebremariam, S. N., & Marchetti, J. M. (2018). Economics of biodiesel production. *Energy Conversion and Management*, *168*, 74-84.

Ge, J. C., Yoon, S. K., & Choi, N. J. (2017). Using canola oil biodiesel as an alternative fuel in diesel engines: A review. *Applied Sciences*, *7*(9), 881.

Hasan, M. M., & Rahman, M. M. (2017). Performance and emission characteristics of biodiesel–diesel blend and environmental and economic impacts of biodiesel production: A review. *Renewable and Sustainable Energy Reviews*, *74*, 938-948.

Knothe, G., & Razon, L. F. (2017). Biodiesel fuels. *Progress in Energy and Combustion Science*, *58*, 36-59.

Özdemir, Z. Ö., & Mutlubaş, H. (2016). Biyodizel üretim yöntemleri ve çevresel etkileri. *Kırklareli Üniversitesi Mühendislik ve Fen Bilimleri Dergisi*, *2*(2), 129-143.

Knothe, G., Krahl, J., & Van Gerpen, J. (Eds.). (2015). *The biodiesel handbook*. Elsevier.

Roy, M. M., Wang, W., & Bujold, J. (2013). Biodiesel production and comparison of emissions of a DI diesel engine fueled by biodiesel–diesel and canola oil–diesel blends at high idling operations. *Applied Energy*, *106*, 198-208.

Aksoy, L. (2010). Alternatif enerji kaynağı olarak biyodizel ve üretim prosesleri. *Taşıt Teknolojileri Elektronik Dergisi*, *2*(3), 45-52.

Leung, D. Y., Wu, X., & Leung, M. K. H. (2010). A review on biodiesel production using catalyzed transesterification. Applied energy, 87(4), 1083-1095.

Haşimoğlu, C., İçingür, Y., & Özsert, İ. (2008). Turbo Şarjlı Bir Dizel Motorda Yakıt Olarak Biyodizel Kullanılmasının Motor Performans Ve Egzoz Emisyonlarına Etkisi. *Gazi Üniversitesi Mühendislik Mimarlık Fakültesi Dergisi*, *23*(1).

Alptekin, E., & Çanakçı, M. (2006). Biyodizel ve Türkiye'deki durumu. *Mühendis ve Makine*, *47*(561), 57-64.

Meher, L. C., Sagar, D. V., & Naik, S. N. (2006). Technical aspects of biodiesel production by transesterification—a review. Renewable and sustainable energy reviews, 10(3), 248-268.

CHAPTER VII

Numerical study of heat transfer and flow in partially heated fittings using nanofluid

Ali Abdulqader MAAROOF [1]
Nevin ÇELİK[2]
Celal KISTAK[3]
Ali TAŞKIRAN[4]
İhsan DAĞTEKİN[5]

Introduction

Nanofluid is a combination of the base fluid and nanoparticle size. Generally, nanoparticles consisted of carbides, oxides, and

[1] Salahaddin University, Erbil, Iraq Faculty of Engineering, Mechanical Engineering Department
[2] Fırat University, Elazığ, Turkiye Faculty of Engineering, Mechanical Engineering Department
[3] Fırat University, Elazığ, Turkiye Faculty of Engineering, Mechanical Engineering Depart Fırat University, Elazığ, Turkiye Faculty of Engineering, Mechanical Engineering Department ment
[4] Fırat University, Elazığ, Turkiye Faculty of Engineering, Mechanical Engineering Department
[5] Fırat University, Elazığ, Turkiye Faculty of Engineering, Mechanical Engineering Department

metals, whereas water, oil or ethylene glycol may be base fluids. Commonly, to increase the heat distribution capacity, nanofluids are now utilized. The nanofluid heat transfer improvement relies primarily on nanoparticles, the nanoparticles' scale, and nanoparticles' density in the base fluid. Opposition to the flow of fluid improves due to nanofluid use, which improves the friction factor and decreases the flow amount. An analysis is being carried out in this paper to evaluate the impact of different amounts of Cu nano-dispersion combined as an essential fluid in the water. The volume concentrations of Cu nanofluid worked on are 1%, 2%, 3%, and 4%. The thermal conductivity of Cu has been shown in Table 1.1. with advancements in thermal technology and thermal engineering, the production of microscale liquid flow structures, which have solidity and a solid ratio of surface to volume relative to traditional flow systems, is of great importance to increase heat shift through many sectors, including shipping, aerospace, and processing, microelectronics, chemical engineering [1].

As one of the most critical heat transfer methods, the control of thermal convection has also been extensively researched. Thermal conductivity in heat transfer fluids is the principal element in evaluating the efficacy of thermal convection heat transfer. The major downside to treating intermediate heat delivery fluids for energy-efficient heat transfer is the low thermal conductivity of natural fluids along with ethylene glycol, gasoline, and water. The preservation of tiny particles in fluids to increase the material's mobility characteristics, motion, and heat transfer characteristics is an essential strategy to growing. It is well understood that the substance's thermal conductivity can be improved by tiny particles of a micrometer or millimeter scale added to a base liquid. While these strong additives will increase the fluid's heat transfer coefficient, the realistic requesting is constrained by massive particle sedimentation, flow channel blocking, pipeline rust, and pressure drops [1].

Nanofluids, solid-liquid hybrid compounds composed of nanometer-sized rigid crystals, fibers, rods, or tubes immersed in

dissimilar base fluids, in addition to unnaturally high thermal conductivity, offer a persuasive technological spectrum to allow heat transfer as a consequence of their many advantages. Nanofluids display enhanced stability due to the scale effect and Brownian displacement of nanoparticles in liquids compared to traditional fluids made with rigid particles of a micrometer or millimeter size. Nanofluids will flow rapidly through a microchannel without cluttering these ultrafine nanoparticles, and the size of the heat transfer device could be decreased by using nanofluids with strong heat transfer capacity [1].

Table 0-1. Solid particles and base fluid thermal conductivity [1]

Matters	**Chemical symbols**	**Thermal conductivity (W/m.K)**
Solid metallic	Cu	401
	Al	237
	Ag	428
	Au	318
	Fe	83.5
Nonmetallic solids	Al_2O_3	40
	CuO	76.5
	Si	148
	SiC	270
	CNTs	~3000 (MWCNTs~6000 (SWCNTs)
	BNNTs	260-600
Base fluids	H_2O	0.613
	Ethylene glycol (EG)	0.253
	Engine oil	0.145

Fittings

The flow into the tubes or pipes with rapid enlargement or reduction in diameter occurs in a wide variety of construction processes, such as contacts between pipelines and piping's of

varying lengths and diameters, when fluid is extruded from a giant pipe or tank into a smaller diameter or making a branch in pipelines in order to the accumulation of sediments, of refolding geometries of nuclear protection inquiries. Many theoretical and experimental experiments on suddenly enlargement flows were performed by using different solution methods. Research has carried out a theoretical and analytical investigation on the diffusion of various liquid content by extending the axisymmetric pipe [2].

In pipe systems, a fitting or adapter is used to connect straight pipe or tube parts, conform to different sizes or to change the direction of flow and for other purposes, such as measuring and regulating fluid flow styles of pipe fittings in fluid flow system [3]

- Flange
- Eccentric
- Equal Tee
- Nipples
- Cross
- Elbow 90^{o}
- Plug
- Weldolet
- Valve
- Pipes

Reducer is a fitting feature that reduces fluid flow by reducing pipe size from larger to smaller. There are typically two forms of reducing agents available. This is a concentric reducer that is like a cone-shaped with a steady decrease across the tubing, except, in this case, it is possible to absorb air and cavitate. Moreover, the second is an eccentric, which is also a type of reducer that has one edge is parallel to the assembled shaft since it is not possible to absorb air [4].

CFD (Computational Fluid Dynamics)

In recent years, engineers have performed critical numerical computations with fast computers' assistance to forecast engineering spectacles and develop their design processes. Via numerical statistics, the resolution of a problem that has not yet been taken into an empirical phase could be unveiled, or the actual experimental findings can be enhanced. Computational fluid dynamics was a normal implementation required to formulate and evaluate the connected theoretical issues surrounding multi-physics phenomena. Several experiments have been carried out to tackle fluid dynamics and heat transfer problems in typical fluids that conform with the basic rules set out in the relevant existing literature, including those that correlate with the same subject's empirical findings. Although a new path, together with its advantages and difficulties, has been developed to introduce nanofluids in fluid dynamics and heat transfer. The same techniques used in traditional computational approaches may be implemented to support the engineering industry concerned with nanofluids. This current generation of coolants is a base fluid with nano-sized particle (1-100) units suspended. Chemistry, tribology, surfactants and covering, medicinal, and clinical uses are environmental. [1] in superconducting microprocessors, magnets, jacket water cooling in automobiles or fuel cells, or more precisely [5].

Like any other fluid, Computational fluid dynamics (CFD) may improve the feature role of nanofluids. The algorithm will be comparable to normal fluids, but when discussing the conservation equations for those fluids, nanoparticles' presence maintains variations in the computational mechanism and often dilemmas, like treating the fluid as a single or two-phase. In principle, this can influence the pacing of the solution and sometimes convergence [5].

Literature Review

Conventional thermal fluids like gas, ethylene glycol, and oil play a significant role in many technological areas, including power

generation, electrical systems, air conditioning, chemical processing, cooling and heating procedures, cooling of the atomic device, defense, and space, transport and microelectronics. Compared with solids, these fluids have low thermal characteristics. Using extended-surface (fins and microphones) to enhance heat flow channels), surface pressure, fluid suction/injection, and the application of electrical/magnetic fields have reached a standstill. Advanced developments with the potential to advance the thermo-physical attributes of modern fluids are thus a field of considerable interest investigation [2].

There is an excellent thermal conductivity of the solid particles. Many experiments have been interested in the thermal effects of conventional fluids of holding these solid elements. Adding such scattered elements of a micrometer or millimeter size [2, 3] into the water base fluid outcomes in a variation of the base fluids' flow and thermal characteristic, eventually leading to an improvement in heat transfer. Nevertheless, these particles measured in millimeters or micrometers cause poor balance, low stabilization, and close channels. Recent technological developments have enabled new materials to emerge, Compared with the conventional materials, with better efficiency and properties. Nanomaterials have drawn interest from many researchers that used different nanoparticle content in nanofluid throughout the past period. The advance of nanomaterials has facilitated the creation of a new nanoparticle content to the base fluid. Specific combination techniques for processing the nanomaterials are implemented (less than 100 nm normally). To see their influence on the resulting nanofluids' thermal and fluid characteristics relative to other fluids, certain forms of nanoparticles are then suspended. The term nanofluid was first identified by Choi [4] in 1995 at the Argonne National Laboratory, USA. Compared to other particles sized in milli/micrometers, those nanofluids have more resilience, lower pressure fall, and higher thermal conductivity. Scientists used other sorts of materials to make nanoparticles including ceramic oxide, nitrides, metal carbides, metals (Au, Cu, Al, etc.), and nonmetals, but

we used Cu in our research nanofluid because of higher thermal conductivity in relation to other nanoparticles. The thermal conductivity rises with both temperature and particle content using Cu nanoparticles with water [6].

Adnan M, et al. [7] The thermal features of three forms of nanoparticles (TiO_2, SiO_2, and Al_2O_3) distributed in water as base fluid were empirically tested in this research. Heat transfer analyzed numerically for turbulent flow by forced convection flow inside heated flat tube, the flat tube increases heat transfer by 6% and declines pressure by -4% within an increase of nanoparticle concentration. Cu nanoparticle is used with different d base fluid Xuan, and Li [8] used Cu nanofluid content from 2.5% to 7.5% thermal conductivity ratio varied from 1.24% to 1.78%. Cu was utilized as nanoparticles of ethylene glycol base fluid and Eastman et al. [9] observed that by dispersing 0.3 per cent of Cu nanoparticles, the efficient thermal conductivity of ethylene glycol nanofluid was improved by up to 40 percent Priya et al.[10] used Cu with an aqueous solution of cetyltrimethylammonium sodium salicylate. It has been showing that thermal conductivity has proportional relation with temperature and nanoparticle content. D. Badekas and D. D. Knight [11] solve Navier-Stokes equations numerically for the full axisymmetric incompressible flow, the working range was between $200 < Re < 400$ it showed that $\beta \leq 4$ have established that within Reynolds number the eddy length differs linearly. According to the nonlinear nature of the Navier-Stokes formulas, this would seem to be somewhat uncommon because of the broad expansion ratio, the eddy produced at the phase expands a great distance downwards (especially compared to the inlet size). The eddy is substantially extended downstream as the Reynolds amount is raised. Dagtekin and Unsal [12] solved numerically the Navier–Stokes equations for duct and circular cross-section area for suddenly expanded flows. The flow was considered stable thermally and laminar, and the fluid was incompressible. Working ratios of expansion , ranging between $1.5 \leq \beta \leq 10$, and Reynolds numbers ranging between $0.1 \leq Re \leq 500$. The investigation observed that the reattachment length Lr and the

eddy center which they are nondimensionalized within larger Reynold number, expansion Red > 500 and β > 10 vary linearly and, for a constant value, the eddy reattachment length Lr is improved with growing Reynolds number and a linear pattern is also identified for Red > 200. And if the flow is erratic, Re_d > 200. A two-dimensional backward-facing contracting stream for water/functional multi-walled carbon nanotube nanofluid for laminar flow and thermal transport was theoretically tested by Alrashed Abdullah AAA et al. [13], and the results of differing proportions of weight and volumes of Reynolds were studied in the presumed geometry. The findings on the decrease in friction coefficient pressure, Nusselt number, velocity contours, and static temperature were addressed. This analysis demonstrates that the increase in the percentage of weight or the amount of Reynolds nanoparticles induces a decrease in surface temperature and an increase in heat transfer coefficient. The axial velocity increases by growing the amount of Reynolds, allowing the momentum to increase. The axial velocity decreases by growing fluid momentum at the start of the channel, particularly in areas near the upper wall, and the probability of vortex production improves. Hsien-Hung et al. examined the heat transfer and flow characteristics of water-based forced convection nanofluids in the laminar flow regime within a horizontal circular tube under the boundary condition of continuous wall temperature [13] they found that water-based nanofluid heat transfer coefficient with 2 vol. is increased by 32 percent relative to that of pure water. An increase in the concentration of particle volume causes the pressure drop to increase. The pressure drop at 2 vol. percent of particle concentration approaches a limit that is almost 5.7 times relative to pure water [13].

Nanofluids and Thermophysical Properties

Nanofluid formation is created by dispersing solid nano-size particles into standard base fluids, like ethylene glycol, water, transformer oil, etc. Accumulation is a major concern and the main problem in the processing of nanofluids [14].

Figure 2.1 shows the amalgamation of nanoparticles within the fluid-based, which changes within the thermo-physical characteristics such as density, viscosity, heat capacity, and thermal conductivity using various nanoparticle material parameters to a different range [14].

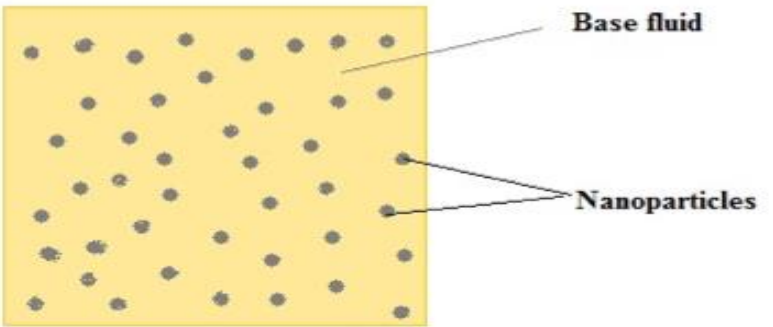

Figure 0.1. Formation of nanofluid [14]

To analyze the rise in thermal conductivity of nanofluids, numerous studies and theoretical research were carried out. In a typical solution, the introduction of nanoparticles rises thermal conductivity. This is due to the Brownian motion, which regulates nanoparticles – fluid suspension thermal behavior. The second explanation for this is the interfacial [15].

Layered structures form the surface of particles as it can be seen in Figure 2.3. These layered structures serve as a thermal bridge amongst nanoparticles and the bulk material, enhancing the gas's conductivity. No relation exists between the thermal properties of the nanolayer and the solid/liquid suspension. These coated molecules are located between the bulk liquid and a solid substance in an alternate physical state [15].

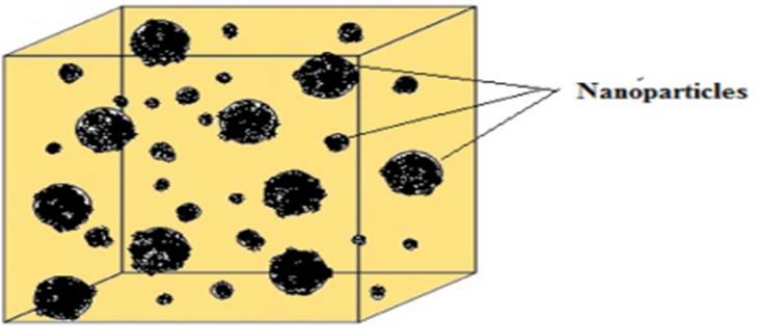

Figure 0.2. Nanoparticles Brownian motion [14]

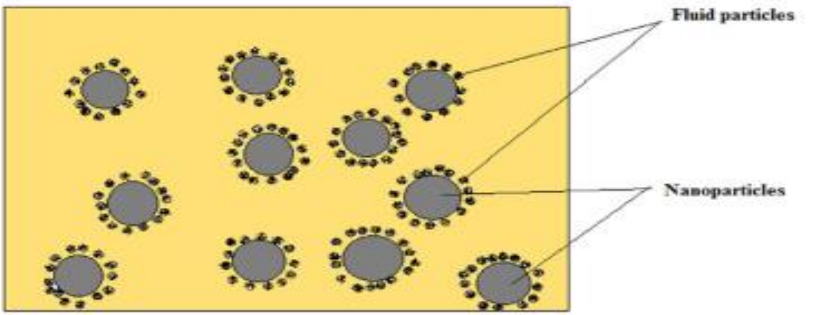

Figure 0.3. A solid/liquid connection nanofluid structure composed of nanoparticles, bulk liquid, and nanolayers [14]

Thermal Conductivity

To examine the increase in nanofluid thermal conductivity, various studies and theoretical work, have been carried out. The application of nanoparticles enhances the thermal conductivity in a standard solution. This is due to the Brownian motion Figure 2.2. as a key mechanism for controlling nanoparticles' thermal behavior–fluid suspensions [14].

It is possible to infer from the comprehensive analysis that the thermal conductivity of nanofluids is based on aspects like particles

(size, type, and substance), the material of the base fluid, and temperature, as shown in Figure 2.4

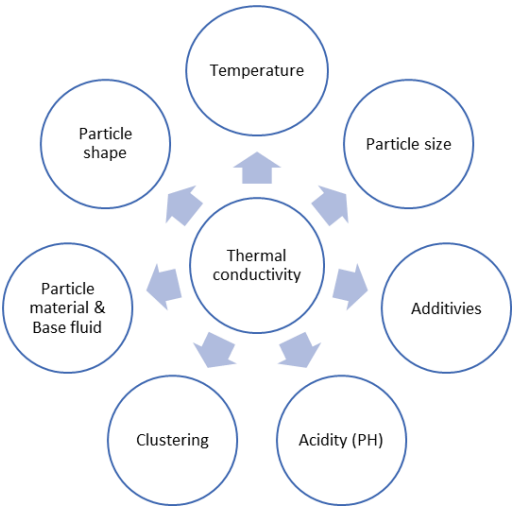

Figure 0.4. The element influencing nanofluid thermal conductivity [14]

The frontier layer (nanolayer), the liquid molecules near a solid particle surface that forms layers, is the second reason for this. Such layers' act and improve thermal conductivity as a thermal bridge across nanoparticles and a bulk liquid. There is no relationship between the nanolayer's thermal properties and the solid/liquid suspension. These coated components are present between a bulk liquid and a solid substance in an intermediary physical state. The solid-like nanolayer of liquid molecules is expected to improve thermal conductivity over conventional fluids in bulk. [15]. Study indicates that nanofluids have higher thermal conductivity than base fluids [16-18]. The investigators conducted tests with several base fluids (ethylene glycol, propylene glycol, methanol, glycerol, gear oil, fuel oil, paraffin, etc.). They used several techniques i.e. transient hot-wire instruments, persistent hot-disk thermal detector, nanofluid thermal conductivity can be measured with nanoscale materials [14].

Single-Phase and Two-Phase Modeling

In the heat transfer and hydrodynamic action method of algebraic reproduction (numerical simulation), two research findings are present in the literature. One solution is to imply that the suspended solid particles are in thermal equilibrium with the fluid phase and that there is a comparable zero velocity between the solid and fluid segments, meaning that the particles travel at the same velocity as the base fluid. Due to its ultra-small particle size, the researchers believe that a nanofluid consists of a fluidized solid phase and can thus be viewed as a single-phase fluid [8]. Although for a nanofluid, this statement can not necessarily stay consistent, according to Ding and Wen [19] findings. They studied the particle movement for a pipe flow in a nanofluid and reported that the distribution of particles at Peclet numbers greater than 10 is substantially non-uniform. Illustration. 3 this relationship between the concentration and the Peclet number for a pipe for a fraction of 0.05 particle volume indicates the homogeneous flow expectation is conditional [5].

Application of Nanofluids

Nanofluids' potential in heat transfer applications has drawn more and more interest since the initiation of nanofluids' principle around a decade ago. Numerous study papers provide surveys of various facets of nanofluids, namely preparation and characterization, strategies of calculating thermal conductivity, theory and model, thermal physical characteristics, convective heat transfer, and nanofluids, which attract heat transfer features in comparison to traditional heat transfer fluids. It could be identified from the current study that nanoparticles are used to strengthen the thermal conductivity of the base fluids. A crucial interpretation for optimizing the heat transfer of conventional fluids is the development in effective thermal conductivity. In thermal control systems for vehicles, the latest generation of coolants [20, 21] as cooling fluids [22] in medical sectors [23], antibacterial activities [24, 25], in power generation [26, 27] in new sensor technology [28,

29], in transmission system [30], in reactors [6]. The use of nanofluids in solar collectors and refrigerants in automotive heat exchangers is this segment's subject. This would transform nano-fluid technologies from laboratory to industrial claims in the automotive and solar collector industries [14].

Nanoparticles Used in Direct Absorption of Solar Collectors (DASC)

As working fluids for DASCs, nanofluids have drawn significant attention, concentrating primarily on the theoretical measurement and experimental analysis of the efficiencies of nanofluid-based DASCs [32-34] and observations of nanofluid radiative properties.[31-35]. Scientists from Arizona state university, Tyagi et al. [36] and Taylor et al. [37] reported that DASCs based on nanofluids in conjunction with surface-based collectors could achieve a theoretical enhancement in efficiency of up to 10 per cent. On the receiver hand, Lenert et al. [38] prophesied efficiencies exceeding 35 percent when nanofluid-based DASCs are attached to a power loop and increased concerning optical and solar thickness Time to show. Taylor et al. [38] estimated that nanoparticles by lower particle loads could absorb more than 95 per cent of incoming sunlight. They also retrieved the nanofluid extinction coefficient, both through model simulations and by spectroscopic quantities. The scientific community is very interested in nanofluids because of their high thermal conductivity and possible use as heat transfer fluids. The notion of explicitly absorbing nanofluids has recently demonstrated that suspension of liquid-nanoparticles is an important method for capturing solar thermal energy numerically and experimentally. Notable improvements in the absorption of solar radiation and the collector's efficiency render the nanofluids a strong heat transfer fluid for solar thermal requests. This can be employed in solar collectors for the effective absorption and conversion of thermal energy. The base fluid's modified thermophysical characteristics result from the application to the base fluid of very limited volume fractions of nanoparticles, including

reduced specific heat, better thermal conductivity and a higher heat transfer coefficient, and is appropriate for improved performance. The general tendency for migration of nanoparticles is why nanofluids optimize heat transfer [14].

By dispersing quite tiny volume percentages of nanoparticles in the base fluid, this improves absorptivity; nanofluid's extinguishing coefficient is greater than plain water (optical characteristics). This has improved heat transfer efficiency and greater absorption capability due to the relatively limited particle size relative to the spreading capacity. All in all, it improves the effectiveness of DASCs, and the findings well support this described earlier. According to the above experiments, it is established that nanofluids' optical properties are sensitive to nanoparticles' frameworks, scale, shape and volume fractions, and the host medium. Many fluids show strongly temperature-dependent refractive indices, leading to suspended nanoparticles, often exhibiting temperature-related optical features. Analysis technique, reveals that nanofluids ought to be chosen purposefully to see improvements in their process. All received solar radiation is consumed at a very high fraction of density into a thin layer of the surface where the thermal energy is quickly released to the atmosphere. The nanofluids may not absorb all the light energy at a fraction of the lower-intensity [36].

As a result, it is important to correctly monitor nanofluids' optical characteristics or result in detrimental solar collectors. The exceptional radiative attributes of ionic liquid-based nanofluids get them fine for direct absorption absorbers for solar collectors at medium to high temperatures. Their desirable optical and thermal characteristics and the resilience desired to make them ideal for solar collectors' ultimate performance with low-temperature direct absorption. There are already a few experiments that can also be investigated further in this field of ionic liquid nanofluids. In the field of DASCs and volumetric solar collectors, carbon nanotubes (CNTs) and graphene with high thermal conductivity, peculiar optical attributes, reasonable mechanical strength, and wide surface

area are also stated to have promise. That is why, there is a need for further research to be done on this subject [14].

Nanofluids in Automotive Cooling

Vehicle thermal management is a cross-cutting technology since engine performance, fuel efficiency, performance and comfort, aerodynamics, driver/passenger convenience, availability of materials, pollution, repair, and device longevity are explicitly or implicitly influenced. Correspondingly, the construction and operation of fuel-efficient over-road trucks that follow rigorous emission requirements are crucial to an efficient and responsive thermal management system [39].

Choi et al. [4] shows that because of their considerably higher thermal conductivity than base fluids, nanofluids' ability is known as a new class of coolants for the thermal activity of vehicles. Thanks to innovations shifting to more power output, cars and trucks' heat-rejection requirements are increasingly rising. Numerically, Ollivier et al. [40] studied the potential use of nanofluids in a gas spark ignition engine as a jacket water refrigerant. The authors executed numerical simulations of unregulated heat transfer through the flask and the coolant flow from inside. Researchers stated that differences in the thermal signal for knock detection improved by 15 percent because of nanofluid's higher thermal conductivity over those expected to use water. Thermal engine and service systems management for heavy-duty vehicles is a technique that tackles energy consumption reduction by increasing the thermal efficiency of engines and reducing the use and leakage of parasitic energy. The most commonly employed coolant for automobiles is a comparatively weak heat transfer agent, opposed to only wind, ethylene glycol, and a water mixture. Engine oils do much worse as a tool for heat transfer. The addition of nanoparticles to the normal engine coolant can increase cooling speeds for vehicles and heavy-duty engines. What can be associated with an expansion with a decreased size coolant system to eliminate engine heat. Smaller coolant systems lead to smaller and lightweight radiators and

represent nearly every part of the vehicle industry and economy. If the drag coefficient is raised and the fuel consumption is also elevated, this can happen. Similarly, better cooling ratios can be used with car and truck engines to extract extra heat from low horsepower engines on the same size as the coolant system. A strong coolant for nanofluids in the engine is pure ethylene glycol with nanoparticles. Compared to an ethylene glycol and water mixture of 50/50, pure ethylene glycol is a weak heat transfer agent, but nanoparticles' application would boost the situation. A strong coolant for nanofluids in the engine is pure ethylene glycol with nanoparticles. In contrast to an ethylene-glycol and water combination of 50/50, pure ethylene glycol is a weak heat transfer agent, although nanoparticles' application will boost the situation. There is also a high boiling point for this nanofluid that is suitable for sustaining coolant flow in a single phase. Additionally, to increase the coolant's normal working temperature and eliminate excess heat using the new coolant method, a higher boiling point coolant usage may be rendered. Further heat-rejection makes for a range of system changes for higher-powered engines [41] Tzeng, et al. nanoparticles of CuO and Al_2O_3 dispersed into engine transmission gasoline four-wheel-drive engine transmission was the measuring unit. Four engine operating speeds of the rotary blade coupling transmission were tested for the inside temperature spread. At four-engine running speeds (400, 800, 1200 and 1600 rpm), the temperature distribution outside the rotary blade coupling system was measured and the optimal heat transfer capacity composition of nanofluids was examined. The authors reported that the lowest transmission temperatures were given by CuO nanofluids at both high and small rotational velocities. Furthermore, from a thermal performance point of view, nanofluids in transmission have a strong advantage. Nevertheless, such concerns as particle formation, particle assemblage, and surface degradation must be kept in mind, as with other nanofluids' implementations. Surface-modified nanoparticles efficiently dispersed in mineral oils are documented to effectively wear reduction and load-bearing power enhancement in automotive

lubrication applications. The results of a research project involving manufacturing sector and universities refer to the use of lubricant nanoparticles to enhance tribological features such as load carrying efficiency, wear resistance, and govern of friction between mechanical parts that move. These results are promising for the development in the level of heat transfer in automotive structures [42].

Ollivier et al. [40] reported that nanofluids' use contributes to increased thermal signal changes by about 15% relative to those expected using just water. The authors used the CFD numerical simulation method to assess the importance of engine cooling for nanofluid use. The simulation results showed that nanofluids could raise the dissipating efficiency of the engine heat and that Cu-water nanofluids had enhanced heat transfer capacity. It has also been It was observed that the more concentrations of nanoparticles, the greater the dissipation potential of the engine oil. The heat-dissipating power rose by 44.1% as the concentration reached 5%. Despite a tremendous boost in heat transfer efficiency, the engine cooling system pump's workload just increased by 6%, which should be acceptable [43].

Those are other applications that nanofluid used in different fields [44-46]:

- Engine transmission oil.
- Regeneration of boiler waste flue gas.
- Cooling of electronics.
- In transformer cooling oil nanofluids.
- Applications in biomedicine. Heating and air conditioning of residences.
- Cooling Nuclear Systems.
- Solar water heating.
- Engine cooling.

- Nanofluids in drilling.
- High power lasers, tubes for microwaves.
- Drilling.
- Cooling of welding.
- Lubrications.
- Thermal storage.
- Cooling (household fridge, chillers).
- Coolant for cooling system in diesel electric generator as jacket water.

Advantages of Nanofluids

In the past few decades, rapid advancements over nanotechnology have contributed to developing a new class of coolants called "nanofluids". Nanofluids are refined suspensions created around a decade ago for functionalized carbon nanoparticles to improve heat transfer fluids' thermal conductivity, which has now also become a popular nanotechnology area. These thermal nanofluids reflect a class of their distinction from traditional colloids for other applications in heat transfer applications. Nanofluids have the following benefits as opposed to traditional solid – liquid heat transfer intensification suspensions [44]:

- High specific surface area and hence greater transfer of surface heat between particles and fluids. High dispersal steadiness, with prevailing Brownian particle motion.

Reduced particle clogging relative to traditional slurries, allowing miniaturization of the device. Elastic properties involve thermal conductivity and the surface's wettability by distributions of irregular particles to match several demands.

Limitation

Implementations of nanofluids in industries such as heat exchanger processes sound incredible with these features. However many justifications, like lengthy consistency, increased pumping capacity and pressure loss, thermal efficiency of nanofluids in turbulent flow and mature areas, lower actual nanofluid heat, and higher production costs for nanofluids, can hinder the production and integration of nanofluids [47].

High Cost of Nanofluids

The higher production cost of nanofluids is one factor that could discourage the use of nanofluids in the industrial sector. Either one-step or two-step methods may generate nanofluids. However, advanced and advanced equipment is needed for both strategies. Lee and Mudawar [48] and Pantzali et al. He emphasized that nanofluids' high cost is one of the disadvantages of nanofluids' implementation.

Increasing surfactant concentrations will increase nanofluids' viscosity and create more significant decreases in pressure in the collector scheme. Although the larger pressure decreases result in greater demands for the circulation of the operating fluid for pumping capacity. Also, considerations such as temperature variations in thermo-physical properties, the difference in particle size, shift in particle volume fraction, and photo-thermal deprivation all require further investigation [49].

The equations of Nanofluid

The nanofluid density is given as in Equation 2.1.

$$\rho_{nf} = (1 - \varphi)\rho_f + \varphi\rho_s \tag{0.1}$$

The heat capacitance of the nanofluid is expressed as ([50], [51]) as shown in Equation 2.2.

$$(\rho C_p)_{nf} = (1 - \varphi)(\rho C_p)_f + \varphi(\rho C_p)_s \tag{0.2}$$

The efficient nanofluid thermal conductivity is computed by the method of Maxwell-Garnetts as follows Equation 2.3.

$$\frac{k_{nf}}{k_f} = \frac{k_s + 2k_f - 2\varphi(k_f - k_s)}{k_s + 2k_f + \varphi(k_f - k_s)} \quad (0.3)$$

This formula is limited to spherical nanoparticles where other nanoparticle forms are not taken into consideration. This model is ideally suited for researching the improvement of nanofluid heat transfer [51-54]. When possessing a dilute suspension of fine spherical particles, the nanofluid's viscosity could be estimated as the viscosity of a base fluid. and is given in [59] investigation as shown below in Equation 2.4.

$$\mu_{nf} = \frac{\mu_f}{(1-\varphi)^{2.5}}$$

Volume fraction is expressed as following Equation 2.5.

$$\varphi = \left(\frac{\mathrm{m_s}}{\left(\mathrm{m_p} + \mathrm{m}_f\right)}\right) \times 100 \quad (0.5)$$

Table 0-2. Thermo-physical properties of water and Cu nanofluid (At 25^{0}C) [55]

Volume fraction φ	**Density (kg/m^3)**	**Cp (J/kg K)**	**Thermal Conductivity (W/m.K)**	**Dynamic viscosity (kg/m.s)**
Water	997	4179	0.60	8.91x10^{-4}
Cu	8954	383	400	-
1%	1076	3863	0.618	9.13x10^{-4}
2%	1156	3591	0.636	9.37x10^{-4}
3%	1235	3353	0.655	9.61x10^{-4}
4%	1315	3145	0.674	9.86x10^{-4}

Material and Method

We start this chapter with a description of the theory of convection within their differential equations following a discussion of boundary conditions. This chapter deal with numerical programming and calculation of problem, also the numerical step of solution explained and model of investigation with meshing size, thermal and fluid flow boundary condition

Convection Heat Transfer

So far, we have found a solid or quiescent fluid to be transported. We now assume that heat transfer through a fluid in conduction involvement, which is the heat convection process, is categorized as normal (or free) and forced convection via bulk fluid motion, based on how the fluid movement is introduced as in Figure 3.1. In forced convection, by peripheral means, including a pump or a fan, the fluid is forced to flow over a surface or through a vessel. Every fluid displacement in natural convection is explained by natural causes, like the buoyancy effect, which increases the warmer fluid and the decline of the cooler fluid. Based on which the fluid is required to move over a surface or a vessel, convection is often known internally and externally [56]. Think of the cooling of a hot block over the top surface with a fan circulating air. We recognize that heat is transmitted to the ambient colder air from the hot block, and the block cools gradually. People do understand that the block cools faster if the fan is shifted to a higher rpm. The replacement of air by water further enhances the flow of convection heat. Experience has taught that convection heat transfer relies heavily on the fluid properties of dynamic viscosity m, thermal conductivity k, density x, and real heat Cp, as well as fluid velocity V. Regarding the form of fluid flow (including being flowing or turbulent), it also varies depending on the geometry and harshness of the solid surface. Therefore, due to the extreme dependency of convection on several factors, we consider the convection heat transfer relationships very complicated.

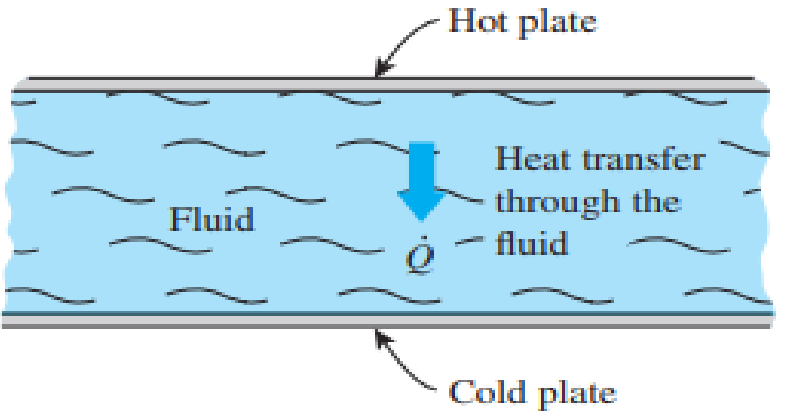

Figure 0.5. Transmission of heat by a fluid moving between two adjacent plates [57]

It is not strange because the most complicated heat transfer mechanism is convection [63]. The convection heat transfer level is considered equal to the temperature differential and is easily represented by Newton's cooling law, considering the complexities of convection as shown as,

$$Q_{conv} = hA_s(T_s - T_\infty) \tag{3.6}$$

Solid surfaces always constrain fluid flow, and it is essential to remember how solid surfaces influence fluid flow. Deem the fluid's flow not porous (i.e. impermeable to the fluid) in a stationary pipe or over a solid surface. Both experimental findings demonstrate that a fluid in motion brings to a full halt at the surface and expects a surface-related zero velocity. This is because of viscous impact, a liquid in close contact with a solid "sticks" to the surface, and no fall. This is referred to as the state of no-slip. Owing to viscous forces between the fluid layers, the layer that holds to the surface reduces the neighboring fluid layer, delays the next layer. The no-slip state is then accountable for the velocity profile's growth. The boundary layer is the flow area neighboring to the wall in which the viscous influences (and thus the velocity gradients) are important [57].

Derivation of Differential Convection Equations

The control formulas of fluid flow in the boundary layers are studied in this chapter. To keep the analysis at a realistic level, we also need flow to be steady and two-dimensional, and the fluid to be Newtonian with consistent characteristics (density, viscosity, thermal conductivity, etc. Assume a fluid's parallel movement along a surface. We select a differential volume element of length dx, height dy, and unit depth in the z-direction (normal to the paper) for analysis and take the flow line across the surface to be x and the normal orientation to the surface be y. For a uniform free velocity V, the fluid flows across the surface, but the velocity inside the boundary layer is two-dimensional: u is the velocity's x-component, and v is the component of y. It should be remembered that u = u(x, y) and v = v(x, y). In a continuous two-dimensional flow. Next to this fluid section, we add three fundamental laws, mass conservation, momentum conservation, and energy equations, in boundary layers [58].

The Continuity and Momentum Equations

The mass concept maintenance is essentially a declaration that mass should not be produced or lost within a system, and all the mass must be provided for throughout an analysis. The sum of mass within the controlling volume stays unchanged in stable flow, and thus mass preservation can be represented as in Equations 3.2 and 3.3.

Rate of mass flow into control volum
$$= \text{Rate of mass flow out of control volume}$$

$$\rho u(dy.1) + \rho v(dx.1) = \rho(u + \frac{\partial u}{\partial x}dx)(dy.1)\rho(v + \frac{\partial v}{\partial y}dy)(dx.1) \quad (0.7)$$

$$\frac{\partial u}{\partial x} + \frac{\partial v}{\partial y} = 0 \qquad (0.8)$$

Figure 3-2 is the maintenance of the mass relationship in differing structures, also recognized as the continuity equation or mass equilibrium of a stable density fluid's continuous two-dimensional flow [57].

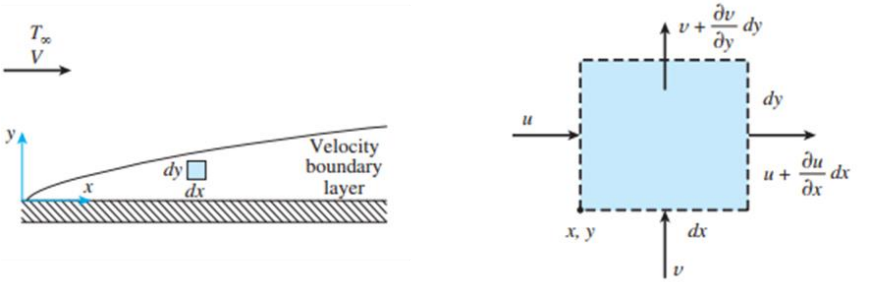

Figure 0.6. Schematic for differentia velocity analysis for two dimentional in control volume fluid element

The Momentum Equations

The equations of motion in the velocity boundary layer are established by introducing Newton's second law of motion to the boundary layer relative control volume. The second law of Newton is an example of the balance of momentum that can be explained as "The resultant force effecting the control volume is equal to mass multiply with acceleration of fluid element within control volume".

The forces that affect the control volume are body forces that operate in the body of the control volume (as magnetic, gravitational force) relative to the body's volume. Another force that is surface forces works on the control surface (such as friction forces relative to the surface due to hydro-static pressure and shear pressures caused by friction impacts). To analyze the control volume by isolating it from surroundings, the force at the surface appears, and force at the surface takes place by detached body according to Newton's second

law, the compressive force directed to the surface of a fluid element by the effect of surrounding fluid can be expressed by Newton's motion law expressed in [64] as shown in Equation 3.4

$$F_{surface,x} + F_{body,x} = \delta m * a_x \quad (3.9)$$

and fluid element mass in the control volume shown as in Equation 3.5.

$$\delta m = \rho(dx.\,dy.\,1) \quad (0.10)$$

Where flow is two dimension and steady and velocity parallel to flow u = u(x, y), the differential of u velocity is written as in Equations (0.11) and (0.12.)

$$du = \frac{\partial u}{\partial x}dx + \frac{\partial u}{\partial y}dy$$

$$a_x = \frac{du}{dt} = \frac{\partial u}{\partial x}\frac{\partial u}{\partial t} + \frac{\partial u}{\partial y}\frac{\partial y}{\partial t} = u\frac{\partial u}{\partial x} + v\frac{\partial u}{\partial y}$$

You may well be curious in assuming that since flow is constant, the acceleration is zero since acceleration is the level of velocity transition over time, and there is no variation at steady over time. However, according to the garden hose nozzle, this interpretation is not right. Steady essentially means no difference in time at a given point ($\partial u/\partial t = 0$), but the only thing that can be changed from one location to another is the value of a quantity ($\partial u/\partial x$ and $\partial u/\partial y$). Pressure and viscous are the forces which are affecting on flow element in the control volume. The viscous stress can be exported into two distinct perpendicular elements of two-dimensional flow at the imaginary surface inside the fluid. The first is normal to the surface. The second is shear stress proportional to the wall side. and the velocity gradient that related to the normal stress is $\partial u/\partial x$ and $\partial v/\partial y$, are below $\partial u/\partial y$, to that is shear stress-related. For simplicity, neglect the normal stresses, the forces effecting on surface forces in the control volume for the x-direction

explained schematically at Figure 3.3. And the net surface force effecting on x-direction become

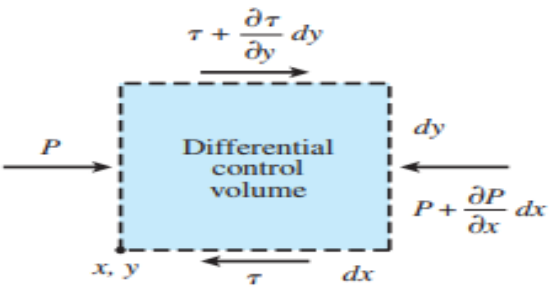

Figure 0.7. x-momentum derivation equation in differential control volume two- dimensional flow [57]

$$F_{surface,x} = \left(\frac{\partial \tau}{\partial y} dy\right)(dx.1) - \left(\frac{\partial P}{\partial x} dx\right)(dy.1)$$

$$= \frac{\partial \tau}{\partial y} - \frac{\partial P}{\partial x}(dx.dy.1) \qquad (0.13)$$

$$= \left(\mu \frac{\partial^2 u}{\partial y^2} - \frac{\partial P}{\partial x}\right)(dx.dy.1)$$

Since $\tau = (\mu \frac{\partial u}{\partial y})$ Substituting Equation 3.7, 3.8 in to Equation 3.3 and divide by dx·dy·1 it give

$$\rho_{nf}\left(u\frac{\partial u}{\partial x} + v\frac{\partial u}{\partial y}\right) = -\frac{\partial P}{\partial x} + \mu_{nf}\left(\frac{\partial^2 u}{\partial x^2} + \frac{\partial^2 u}{\partial y^2}\right) \qquad (3.14)$$

The relation in Equation 3.9 is for momentum at x-direction. That was when a body effected by force acted in x-direction, the term can be added to the right side of the equation explained that it is expressed per volume of the fluid at a boundary layer. Equation 3.10 shows momentum balance about y-direction is represented in [57].

$$\rho_{nf}\left(u\frac{\partial v}{\partial x}+v\frac{\partial v}{\partial y}\right) = -\frac{\partial P}{\partial x}+\mu_{nf}\left(\frac{\partial^2 v}{\partial x^2}+\frac{\partial^2 v}{\partial y^2}\right) + (\beta\rho)_{nf}g(T_H-T_C) \quad (3.15)$$

The Equation of Energy

To balance any system that involves the mechanism, energy input and output are equal to the change in a system's energy content throughout a process that specifies energy balance. Throughout the steady-flow unit, the total energy content of the control volume stays unchanged, and the energy that reaches the control volume in some manner must therefore be equal to the amount of energy that exits it. The first law of thermodynamics embodied the physical principle of energy, which states that "Energy cannot be created nor destroyed only can be changed" even with time. Then the total energy equation form developed to ($E_{in} - E_{out} = 0$) for a flow in the steady system as it was explained in energy equation that energy could only be transported by mass, heat, and work, the following Equation 3.11 is for energy balance in control volume at steady-flow can be expressly written as [57].

$$u\frac{\partial T}{\partial x}+v\frac{\partial T}{\partial y}=\alpha_{nf}\left(\frac{\partial^2 T}{\partial x^2}+\frac{\partial^2 T}{\partial y^2}\right) \quad (3.16)$$

The Boundary Layer of Velocity

Consider flow over the flat plate of Figure 3.4. To incorporate a boundary layer's definition, fluid particles coming into interaction with the surface they accept to have zero velocity. These particles then hold back the particles' motion in the adjacent fluid layer, which slows the particles' motion in the next layer until the

influence converts to insignificantly at a distance y = δ from the surface. the relation of fluid motions is explained below [59].

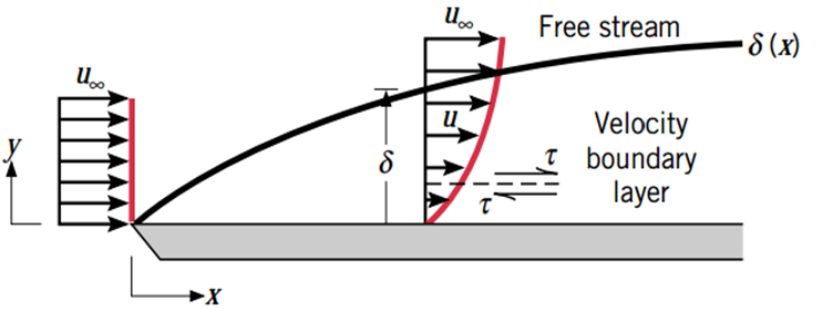

Figure 0.8. Velocity boundary layer creation on a flat board [60]

Associated with shear stresses in parallel fluid speed aircraft. With rising distance y from the surface, the variable x velocity of the fluid, u, must then be increased before the free stream value u_∞ etc., is reached. The ∞ subscript is used to define conditions beyond the boundary layer in the free stream. The quantity δ is known as the thickness of the boundary layer, and is usually defined as the y value for which $u = 0.99u_\infty$. The profile of limit layer velocity refers to the way u differs through the boundary layer by y. Thus, fluid flow is considered by two different sections [56].

The Thermal and Heat Boundary Layer

Just as a limiting layer of velocity forms when there is fluid movement over a surface, where the fluid-free stream and surface temperatures establish thermal boundary layer differ.

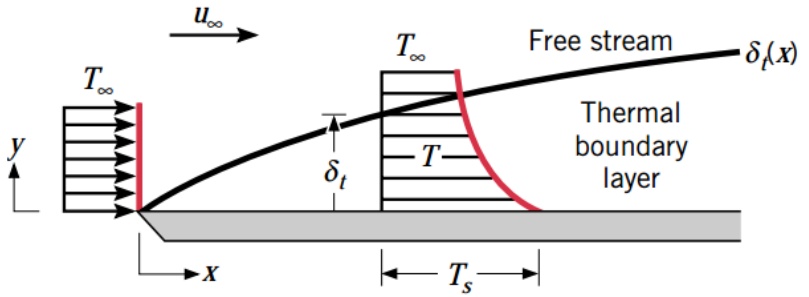

Figure 0.9. Isothemal flat plate thermal boundary layer [60]

Consider flows over a flat, isothermal plate Figure 3.5. At the vanguard it has a uniform temperature profile with T(y) = T_∞. However, at the metal's surface temperature, fluid particles that interface with the plate reach thermal equilibrium. [61]. Those particles share energy with those in the neighboring fluid. The fluid forms structure and temperature gradients. The Fluid area in which the temperature gradients are the thermal boundary layer and the thickness of the thermal boundary layer is δ_t usually defined as the value of y corresponding to the ratio [(Ts-T_∞)/(Ts-T_∞)] = 0.99 with the impact steadily far from the leading edge [60].

Laminar and Turbulent Modeling

Studies such as from Kalteh et al. [62], and Mahmoudi et al. [63] calculate using the laminar flow scheme to demonstrate the Improve in Nanofluid heat transfer efficiency. Talebi et al. [64] modeling a laminar flow of nanofluid Cu/water to demonstrate a positive effect on heat transfer efficiency by aggregating solid particles. Akbari et al. [65] have carried out more statistical work. This showed the negligible impact of particle concentration. In both the primary and secondary flow models. In their paper, Specific tube tilts were tested to determine the impact of suspension. The transmission rate of heat was stated to be maximal under these

conditions, value at an angle of 45°. For multiple geometries, the laminar simulation was carried out. Shaykhzad et al. [66] conducted a CFD investigation into Cu/water nanofluid convection, which assumed laminar flow in a square cavity. We tested the influence of two heat sources flowing through the walls to determine the optimum location concerning heat transfer efficiency. They also reported a rise in the quantity of Nusselt with an increasing concentration of nanoparticles. Feng and Kleinstreuer [67]. Analyzed a laminar for a radially refrigerated network. The writers applied a particular dimension to the usage of nanofluids as refrigerants as a result of their study, nanofluid reduces the total entropy provided by the disc system by increasing the hydraulic capacity substantially. For the best possible author's details, the literature on entropy number calculations usage is limited to nanofluid. In this area, this will lead to further future studies. In a homogeneously heated tube and 2 disks across the radial geometry, a laminar flow was described by Maïga et al. [56]. In this study, the Reynolds number change on the growth in the heat transfer coefficient was discussed. While the increase in the number of Reynolds lowered the coefficient of heat transfer for the conduit, the other flow was largely negligible.

Physical Model

The schematic diagram of the considered model and related characteristic parameters are shown in Figure 3.6 with coordinates in two-dimensional it is suddenly expanded fitting shape with two different entrance cross-section view. The same geometry dimension has been used for concentric shape with reversing interface for both circular and rectangular cross-section area the inlet length L_i = 2d and for outlet length L_o = 3D was used to avoid impacting the flow at the expansion by the inlet boundary circumstances. In contrast, the length of the outlet Lo was adequate to obtain a fully defined flow proportion for operating expansion., partially heated location L_H coordinated from L_i to (L_i + D). the investigation working was at β = 1.5 for fitting size and hydraulic diameter Equation 3.13 used for

noncircular which has been created by ANSYS Mechanical APDL. The fluid flow and heat transfer simulation in nanofluid were applied to expand fittings suddenly. The purpose of this investigation the physical comparison and benefit will be exposed at results [11] investigated that at sudden expansion location (at start of larger diameter) the eddy reattachment length and eddy center is considered at streamline solution which has is an important effect on the fluid flow that is affected by inner velocity and kinematic viscosity and β (expansion ratio). The same dimension is used for concentric shape, but the inlet flow condition is interred at a bigger diameter for both axisymmetric and planar geometry.

$$\beta = \frac{D}{d}$$

$$D_h = \frac{4ab}{2 \times (a+b)} \tag{0.18}$$

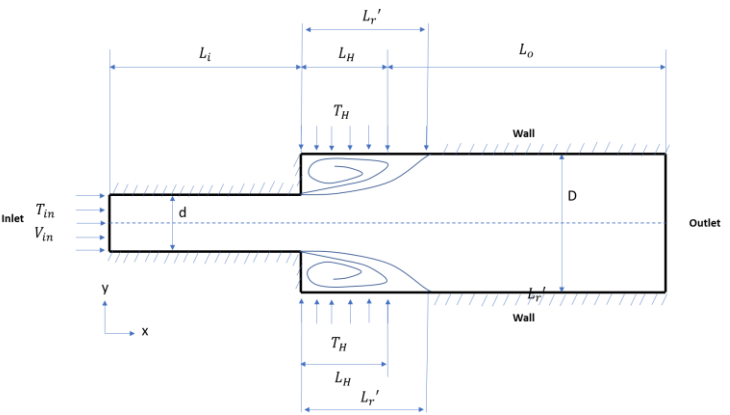

Figure 0.10. Schematic illustration of physical sudden expansion geometry (axysimmetric or planar)

Working Range and Calculations

The ANSYS solver utilizes the finite volume method to transform the regulating partial differential equations into a framework of distinct algebraic equations, and then it addresses them depending on the provided boundary conditions. For the disorderly layers adjacent to the wall, a realizable k-model was implemented, and the Basic scheme was selected for pressure velocity pairing to minimize error in computing the maximal residual values for all numerical parameters is taken as 1e-4. To obtain both momentum and energy equation and simulating flow and heat properties by CFD-Posting by changing Reynold number for both laminar-turbulent range between $200 \leq Re \leq 5000$. Flow patterns and limitation for laminar and turbulent is depended on diameter for circular diameter laminar region is always $Re < 2100$ and for the turbulent region, $Re > 4000$, and for laminar duct region $Re < 2300$ also turbulent is $Re > 4000$.

The inlet velocity which has been used in the Equation 3.14 changed by Reynolds number and volume fraction of nanofluid applied to inlet boundary condition, the dynamic viscosity of the fluid is changed, whereas other parameters are kept constant for an expansion ratio by Equation 3.12 for Re, and volume fraction of Cu nanoparticles $0\% \leq \varphi \leq 4\%$ has been taken for circular and rectangular cross section area, as shown in Table 3.1. Equation (3.15) is used to find Nusselt number for various flow patterns and pressure losses between inlet and outlet. The characteristic of solid metal C_u nanoparticle and pure water base fluid has been taken from [68] at $T = 25^oC$ which is listed in Table 2.1 for simulating various volume fraction material property Equations 2.1 – 3.5 are used to obtain in the Table 3.1.

$$V_{in} = \frac{\mu_{nf} \times Re}{\rho_{nf} \times D_h} \tag{3.19}$$

$$Nu_x = \frac{h \times D_h}{k_f} \tag{3.20}$$

$$\Delta P = P_{out} - P_{in} \quad (3.21)$$

Table 0-3. Nanofluid properties for different volume fractions

φ	ρ (kg/m3)	Cp (J/kg.K)	K (w/m2.K)	μ (kg/m.s)
0	997	4180	0.6	8.91E-4
1%	1076.57	3864.19	0.618	9.14E-4
2%	1156.14	3591.86	0.636	9.37E-4
3%	1235.71	3354.60	0.655	9.61E-4
4%	1315.28	3146.05	0.674	9.87E-4

Grid Size and Meshing

The grid size or several nodes affect results, which can be changed by setting various mesh sizes. They have a relation with each other for both investigated sudden expansion shape 51×51 for circular cross-section and 48×48 for rectangular cross-sectional and 48×48 for circular concentric shape. The thickness has been ignored because of exporting the shape into CFX, which only internal and external flow allowed to be simulated our present investigation is internal flow shape. The computing realm was translated to a hierarchical, non-uniform, orthogonal finite-volume chart. In the streamwise (x) and cross-stream (y) directions, the cells are non-uniformly distributed to position a larger number of cells near the fully turbulent area for concentration on the wanted area. The geometry and the grid of both 3D fittings are shown in Figure 3.7 and Figure 3.8, respectively. Both tubes were treated as a solid tube with a standardized constant temperature in the modeling procedure, and the heat was radially passed to the fluid that was partly heated in the flow direction. In ANSYS CFX program, the computational meshes of the circular and square models were built by meshing method, and the grid was finer almost instantly altered walls in both cases because there are sharp differences in the boundary layers in this zone.

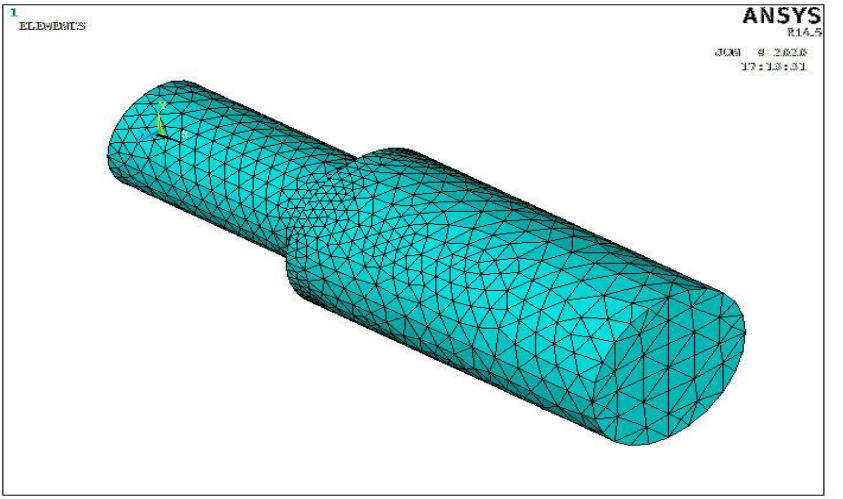

Figure 0.11. Circular cross section meshed shape

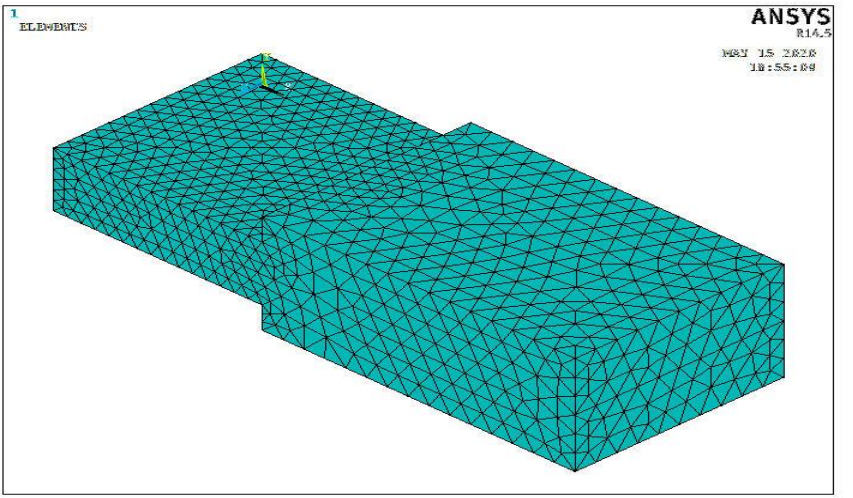

Figure 0.12. Rectangular cross section meshed shape

Grid Independence Test

Three different grid sizes (51× 51, 44 × 72, 75 × 81) were chosen for 4 percent circular nanofluid cross-sectional, and (51 x 51) grid points were considered for solution effects in the measurements in order to verify the grid independent of the current research. This grid-scale has demonstrated an insignificant deviation in the center of both reattachment lengths and temperature. In terms of the normalized reattachment length Lr' (Lr'= Lr/d) and temperature at the exit of geometry, Table 3.2 introduces the grid dependence studies for β = 1.5 for and Re = 200, 500 and 1100.

	51×51		44×72		75×81	
Re	**Lr'**	**T (°C)**	**Lr'**	**T (°C)**	**Lr'**	**T (°C)**
200	1.5	27.30	1.5	27.3	1.5	27.3
500	1.62	25.98	1.6	25.98	1.61	25.93
1100	1.71	25.62	1.71	25.62	1.64	25.62

Table 3 2. Reattachment lengths and temperature values at center of exit for different grid size for β = 1.5

Boundary Conditions

Cold flow is known as the physical boundary conditions for the geometry T_{in} (inlet), beginning of suddenly enlarged wall located at L_H applied to T_H (partially heated), and inter L_i and remaining of L_o walls are adiabatic (isolation). The flow has two different patterns at L_i low- temperature inlet flow, and from L_o to end, flow is effected by sudden expansion and partially heated temperature. The mesh file and shape size were created by Ansys APDL further exported to CFX. It has been presumed that the outer side surfaces of partially heated locations are applied to T_H temperature without considering convection with the surrounding air. Simultaneously, the two flow pattern configurations' assessment as per the thermal concert will be determined at the same boundary conditions. The heat extracted from each conduit wall should then be the same as the heat withdrawn from the wall [69]. Distributed temperatures have been applied to all considered surfaces are

Inlet cold wall T_{in} = 25°C

Outlet with relative pressure = 0 Pa

Partially heated wall with $T_H = 70^oC$

Walls at L_i and L_o - L_H surrounding length are isolation (adiabatic)

The Reattachment Length

The eddy produced at the step outspreads to a large distance because of the large expansion ratio. These research in the laminar and turbulent regime at $200 \leq Re \leq 5000$ Reynold number and expansion ratio between $1.5 \leq \beta \leq 7$ have confirmed that the relation between the eddy's length with Reynolds number is proportional and varies linearly. The reattachment length appeared at streamline for both axisymmetric (circular) and planar (duct) geometries for the dimensionless reattachment length as functions of Reynolds number and expansion ratios [12].

Assumptions

It is easy to fluidize the nanoparticles in the base fluid, so the nanofluid mixture is called a single stage, and the slip motion between modes is assumed insignificant. [70]. The nanoparticles and the base fluid are both considered to be in thermal equilibrium with each other and the relative velocity is either small or close to zero. Efficient thermo-physical characteristics rely on nanoparticles' concentration in terms of temperature and volume and both base fluid and suspended particles' conditions. Therefore the well-known single-phase flow equation (i.e., mass, momentum, and energy conservation equations) could be easily generalized and used for nanofluids. Throughout the research, it is possible to model and simulate nanoparticle and base fluid with single-phase or two-phase methods. In realism, the movement between the solid particles and liquid is not considered zero at the two-phase method due to some reasons such as gravitation, the conflict between the C_u particles and water [8]. The issue was believed to be three-dimensional, solid,

incompressible and Newtonian laminar and turbulent fluid flow, constant nanofluid thermophysical characteristics, no gravitational effect, forced convection the axial direction and the wall thickness of the tubes was ignored

Result and Discussion

In this chapter we focused more on suddenly expansion than contraction for both axisymmetric and planar geometry for forced convection, the result discussed for thermal and fluid property compared with other results at various locations

Using nanofluid in the cooling process has benefit can be applied at both locations at a hot location when nanofluid is caring heat and at a cooling location which heat is scattered to the surrounding. our investigation that is partially heated at beginning of suddenly enlarged has been studied for caring heat effected by heated location and condition. The detail and result have been taken at the center for both (r = 0, 0, 0) and (0, y/2, z/2) alone x-axis for pressure, temperature, velocity curves, and convection heat transfer coefficient has been taken at the surface for both D and (L_H, y, z) along the x-axis.

Results for Sudden Expansion Fittings

Streamline Analysis

Figure 4.1 (a, b) present streamline for water at Re =1100 it shows the result of suddenly enlarged diameter the amount of nanoparticle in a base fluid which Re has a large effect on stretching on sudden axisymmetric location the investigation is also confirmed in [11, 12, 71]. This research in the laminar and turbulent regime at an expansion ratio of β =1.5 have demonstrated that the length of the eddy varies linearly with Reynolds number Figure 4.2 and Figure 4.3 present comparison for various streamlines situation for both shapes Figure 4.2 (a, b) at Re =1100 shows that for ϕ = 4% reattachment length reduces compared with water because of reducing of inlet

velocity of 4% nanofluid. The same can be appeared in Figure 4.2 (c, d) due to the increase of Reynolds number to Re = 5000 turbulent flow enhancing of reattachment length and eddy center is more stretched down compared to Re = 1100 streamlines with benefit to 4% nanofluid.

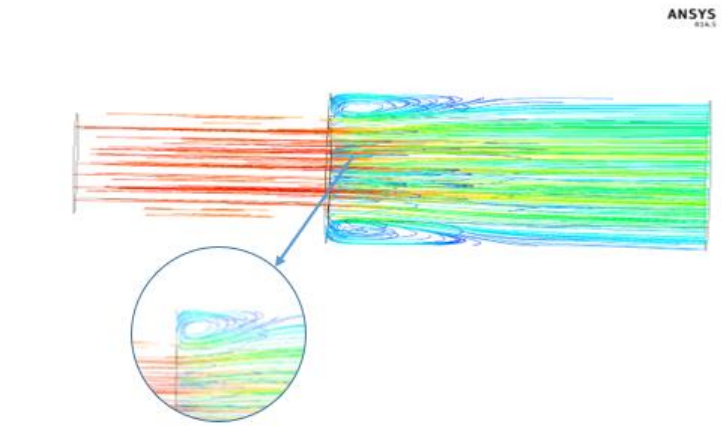

(a) 2D

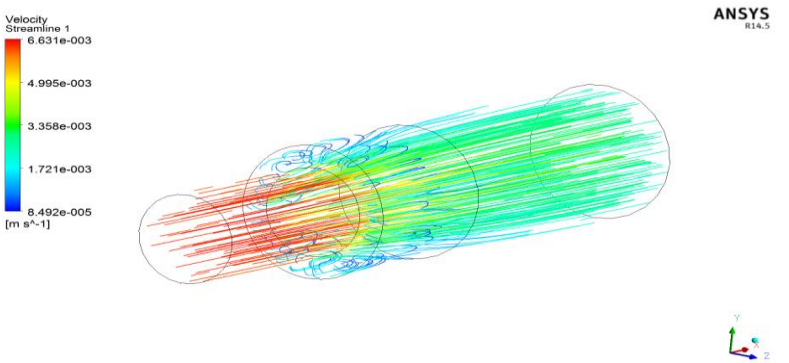

(b) 3D

Figure 0.13. Streamlines of circular cross section for water at Re = 1100

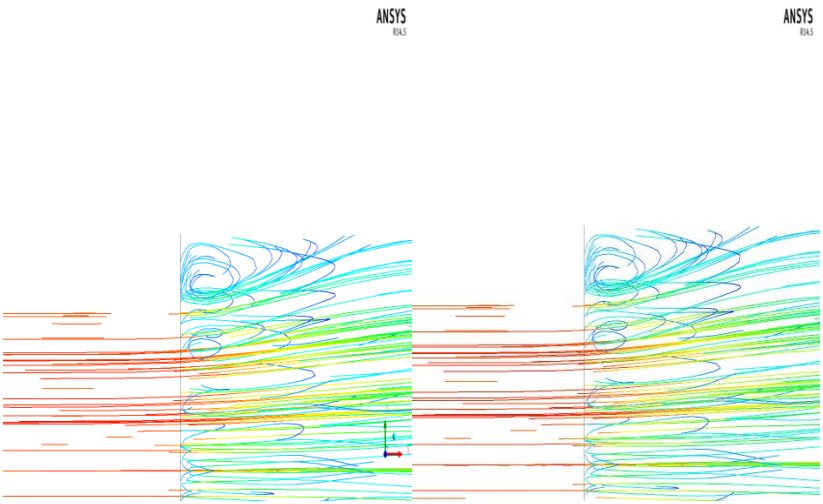

a) Water at Re =1100 *b) 4% nanofluid at Re=1100*

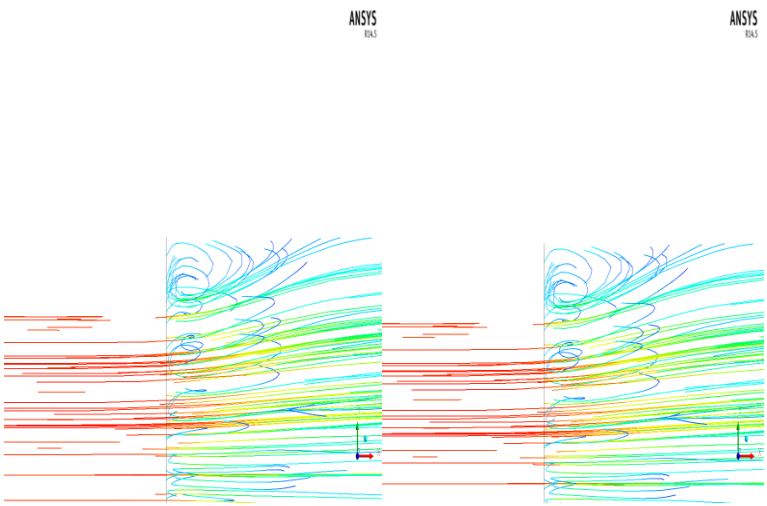

c) Water at Re = 5000 *d) 4% nanofluid at Re = 5000*

Figure 0.14. The streamlines for axisymmetric (β = 1.5)

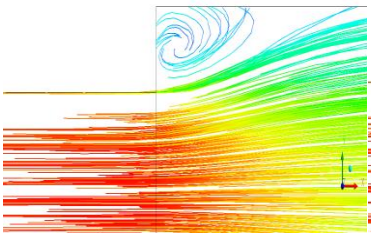

a) Water Re = 1100

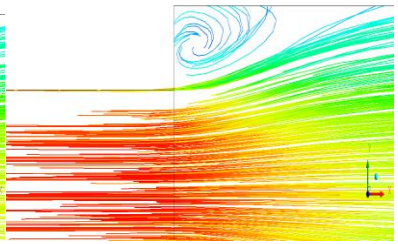

b) 4% nanofluid Re = 1100

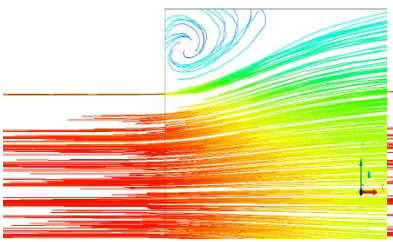

c) Water Re = 5000

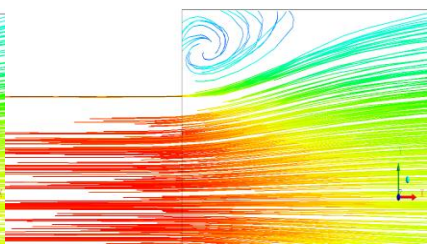

d) 4% nanofluid Re = 5000

Figure 0.15. The streamlines for planar geommetry (β =1.5)

Pressure and Velocity Analysis

The velocity relation with flow characteristic in Figure 4.4 shows numerical inlet velocity that has been calculated by Equation 3.14 reduction at inlet velocity appeared as volume fraction is increased due to rise nanofluid weight percentage that has effects on flow pressure drop.

Figure 4.5 shows the velocity of momentum equation that has been solved by CFD velocity percentage decrease between the inlet and outlet velocity for $\varphi = 0.04$ at Re = 500 is 41.3% within enhancing of Reynold number to Re = 5000 percentage decrease become 46.3% for circular and the same was noticed at Figure 4.6 and percentage decrease for duct at $\varphi = 0.04$ flow at Re=500 is 37.7% & Re = 5000 is 41.8% because of throttling at the enlarged section the pressure at smaller section is going down near to vacuum effect as it appears in Figure 4.7 and Figure 4.8 higher pressure drop appeared for duct shape compared to the circular-cross section area. Figure 4.9 and Figure 4.10 chart shows the pressure drop vs Reynolds number for three types of flow patterns nanofluid contents the result shows that within enhancing Reynolds number, the amount of pressure drop becomes higher due to enhancement in inlet velocity and suddenly expanding in fitting geommety. Within the increasing weight percentage of nanoparticles, pressure drop becomes more noticeable which is the result of higher viscosity and density of working fluid. Consequently, by enhancing the amount of fluid depletion along the suddenly enlarged path or fluid velocity in the indirect paths, this behavior causes the reduction of momentum and the increase of pressure drop.

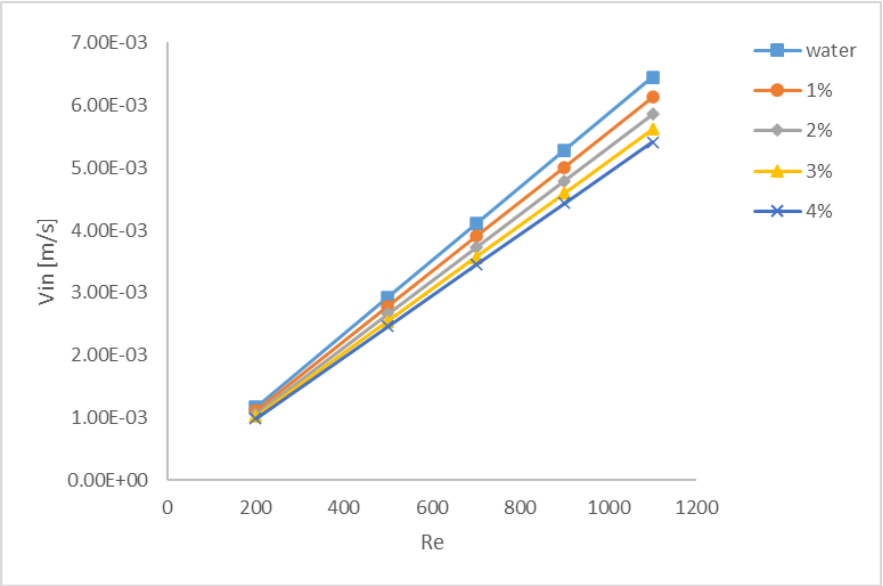

Figure 0.16. Reynolds number with inlet velocity for various amount of nanofluids

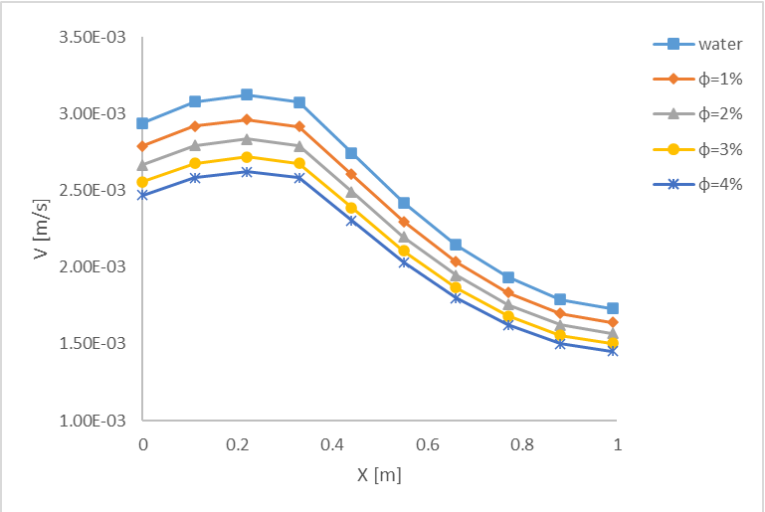

(a) Re = 500

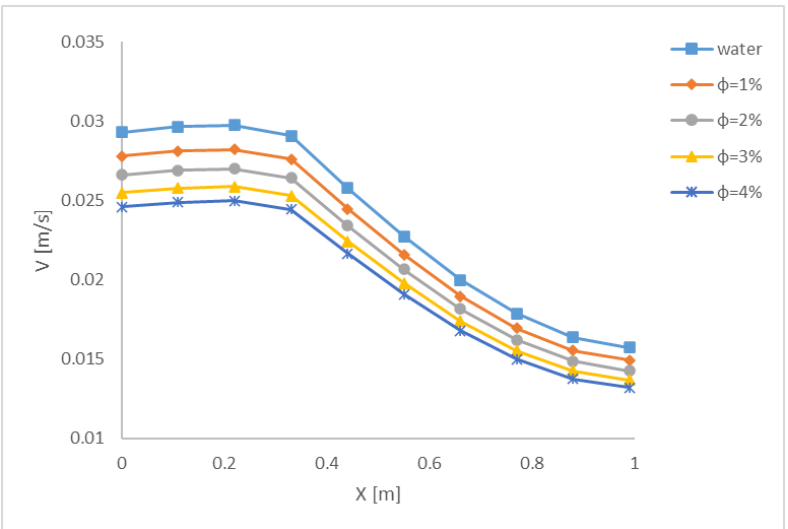

(b) Re = 5000

Figure 0.17. The centerline velocities variation for axisymmetric flow (β = 1.5)

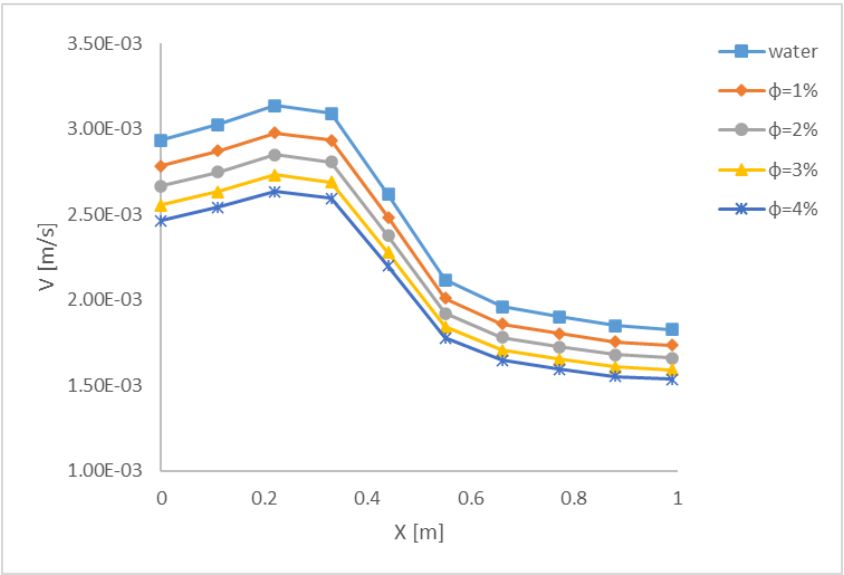

(a) Re = 500

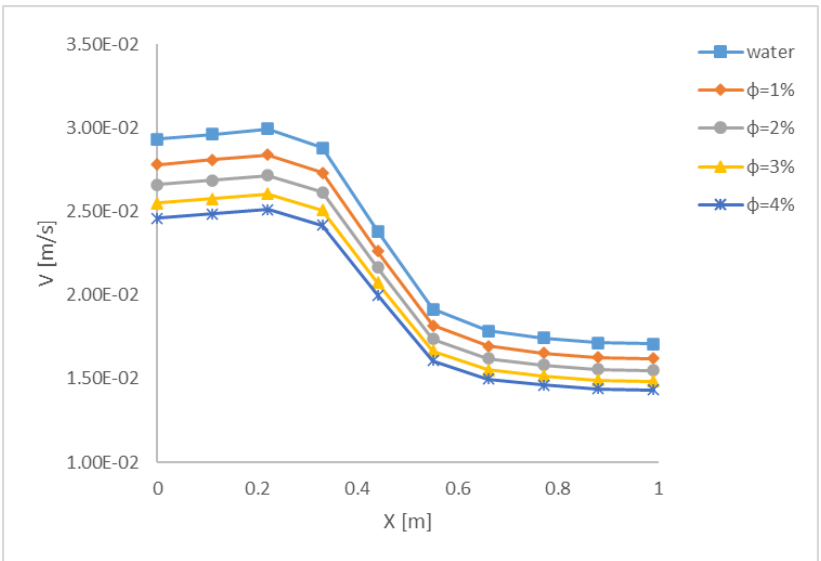

(b) Re = 5000

Figure 0.18. The centerline velocities variation for planar flow

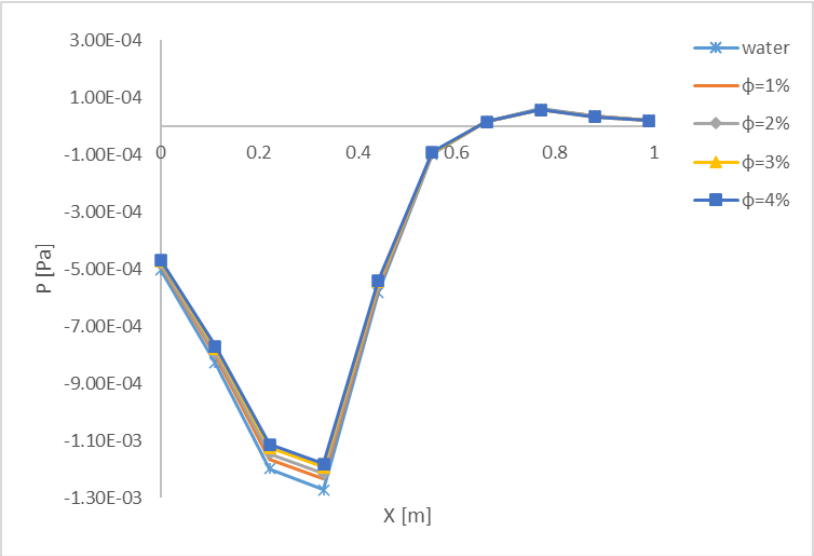

(a) Re = 500

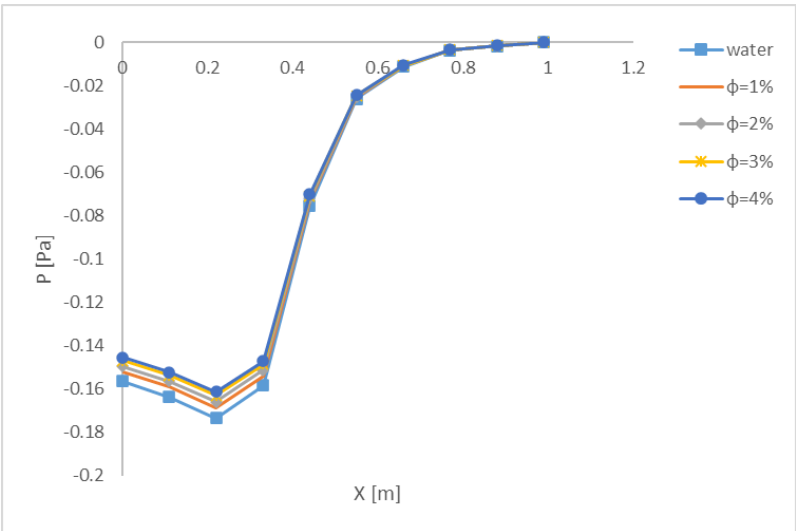

(b) Re = 5000

Figure 0.19. Pressure variation along sudden expansion (circular)

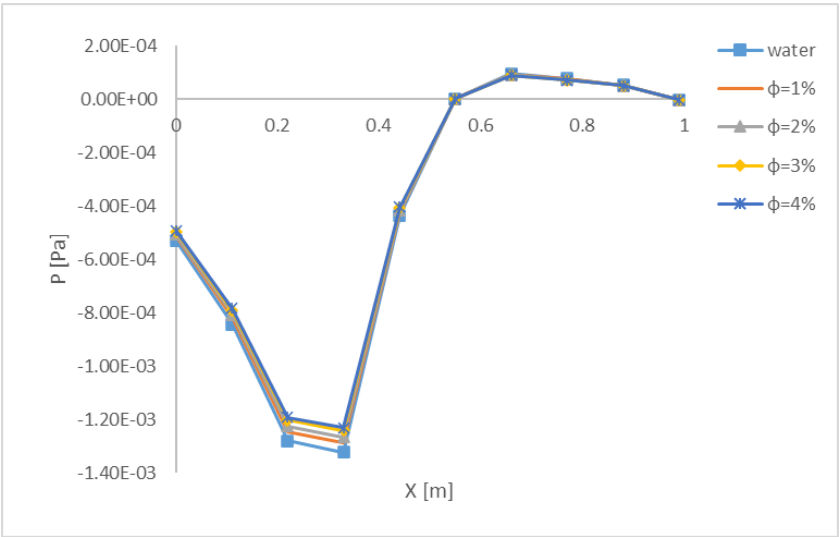

(a) Re = 500

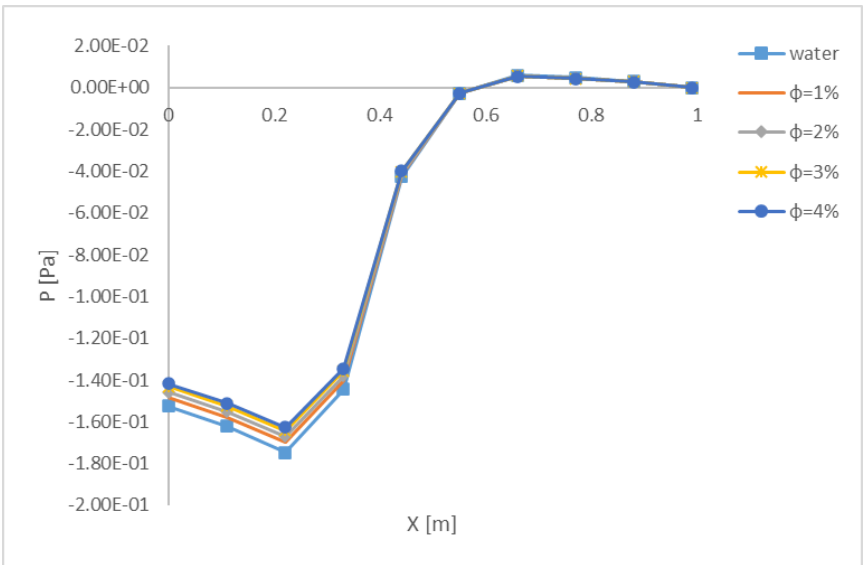

(b) Re =5000

Figure 0.20. Pressure variation along duct (planar)

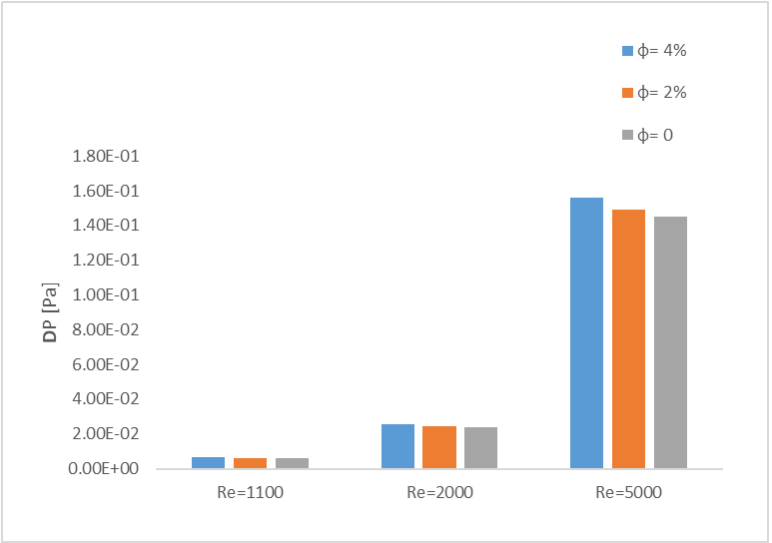

Figure 0.21. Pressure drop in different Reynolds numbers for axisymmetric sudden expansion geometry

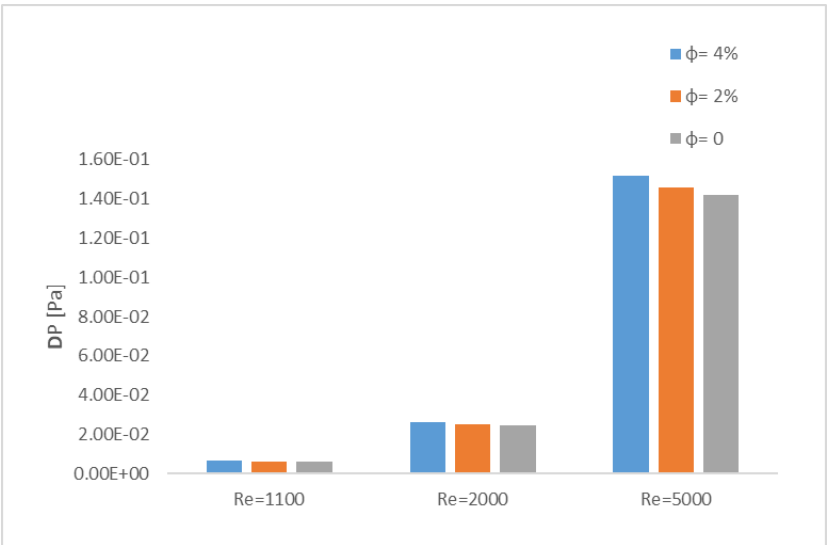

Figure 0.22. Pressure drop in different Reynolds numbers for planar geometry

Reattachment Length Analysis (Lr')

The relation between Reynolds number with reattachment length (Lr' = Lr/d) has been found for various expansion ratio for both axisymmetric and planar at Figure 4.11 and Figure 4.12 respectively for water and there is good agreement between this study with literature Dagtekin and Unsal [12]. As it is found that as Re number increases reattachment length Lr' also is increasing. It seen that the values of reattachment lengths of axisymmetric Table 4.1 are lower than that of planar geometry Table 4.2.

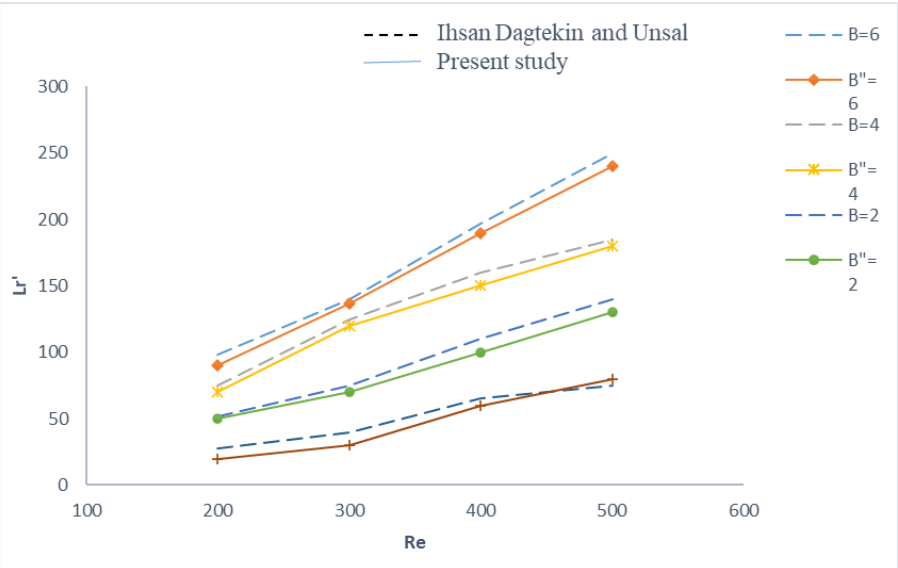

Figure 0.23. Variation of reattachment length with Reynolds numbers at different expansion ratio for axis- symmetric geometry for the comparison with available literature [12].

Table 4 1 Reattachment length for various Reynolds number at β (axisymmetric).

Axisymmetric geometry								
Re	β = 6	β" = 6	β = 4	β" = 4	β = 2	β" = 2	β =1.5	β"=1.5
200	98	90	75	70	52	50	28	20
300	140	137	125	120	75	70	40	30
400	197	190	160	150	110	100	65	60
500	250	240	185	180	140	130	75	80

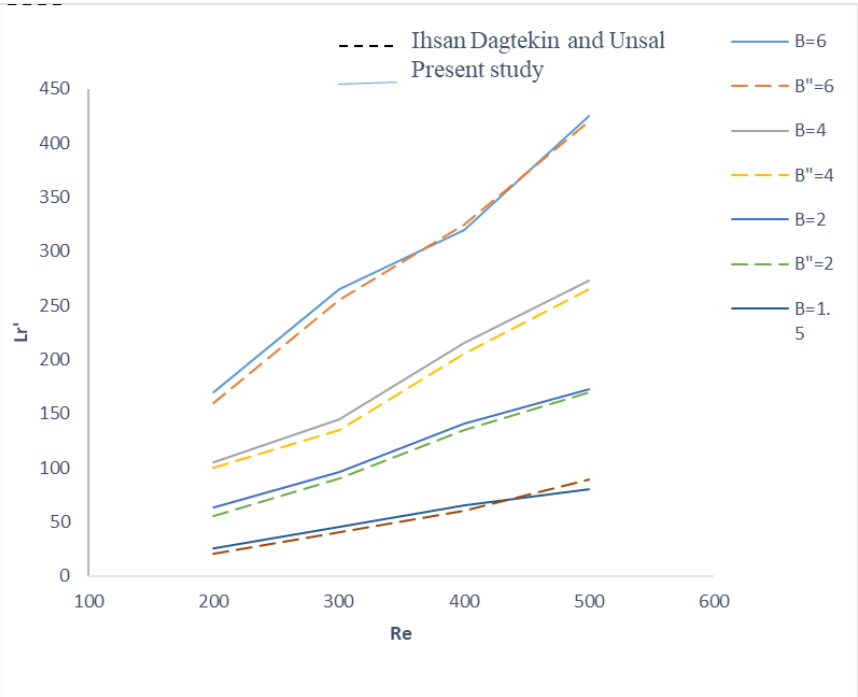

Figure 0.24. Variation of reattachment length with Reynolds number at different expansion ratio for planar geometry for the comparison with available literature [12].

Table 0-4. Reattachment length for various Reynold number at β (planar).

Planar geometry								
Re	β = 6	β"=6	β=4	β"=4	β=2	β"=2	β=1.5	β"=1.5
200	170	160	105	100	63	55	25	20
300	265	255	145	135	96	90	45	40
400	320	325	215	205	141	135	65	60
500	425	420	273	265	173	170	80	89

Temperature Effect

Advantage of using nanofluid in the cooling process this investigation the boundary condition studying was for carrying heat partially during fluid flow the temperature variation along shape have been found at Figure 4.14 and Figure 4.15 outlet temperature is enhanced significantly during flow and volume fraction and temperature of partially heated location T_H, and heated length L_H those properties were had a strong effect on heat- carrying and outlet temperature the relation is proportional. Thermal properties of nanofluid are calculated for different nanoparticle content It has been showing that within the increasing of Reynolds the temperature difference decreases between inlet and outlet since the momentum of cooling fluid is strengthened [72].

The relationship between velocity and temperature fields determines the amount of heat transfer. Any factor that can enhance fluid velocity eliminates the temperature variation and reduce the heat transfer from partially heated to the fluid. On the other hand, by enhancing the volume fraction the temperature difference was raised. And enhance heat transfer from partially heated location to fluid flow and increase the temperature at outlet this relation appeared in Figure 4.13 the detail has been taken at the center of the shape.

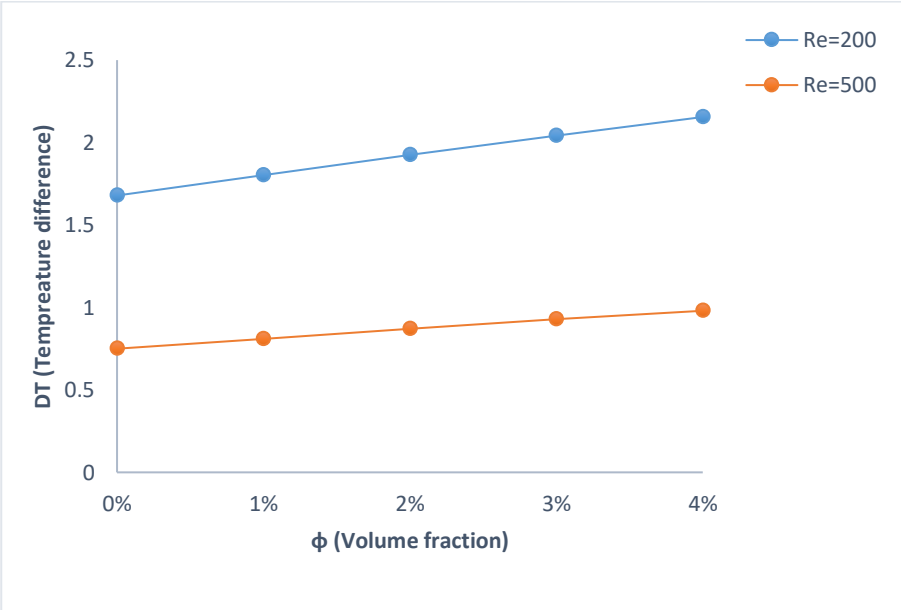

Figure 0.25. Relation between □T (T_{in} - T_{out}) and volume fraction for circular geommetry at (β=1.5)

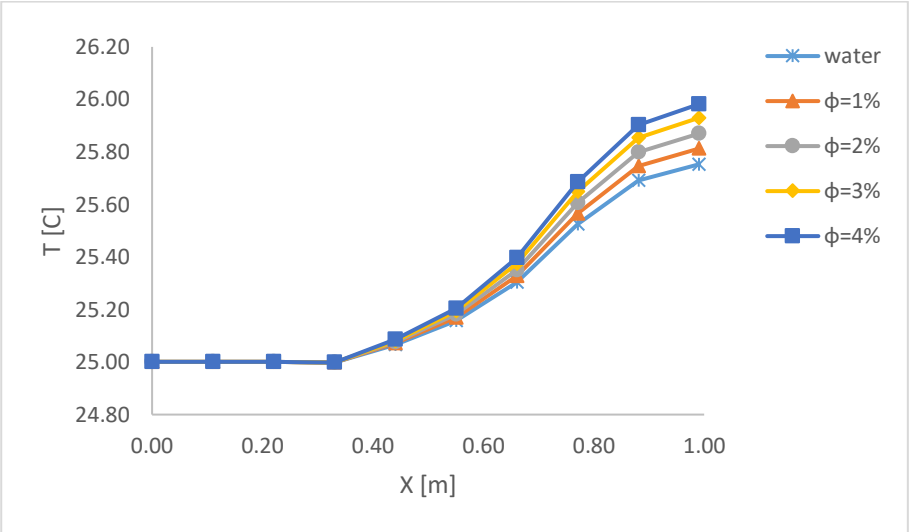

(a) Re = 500

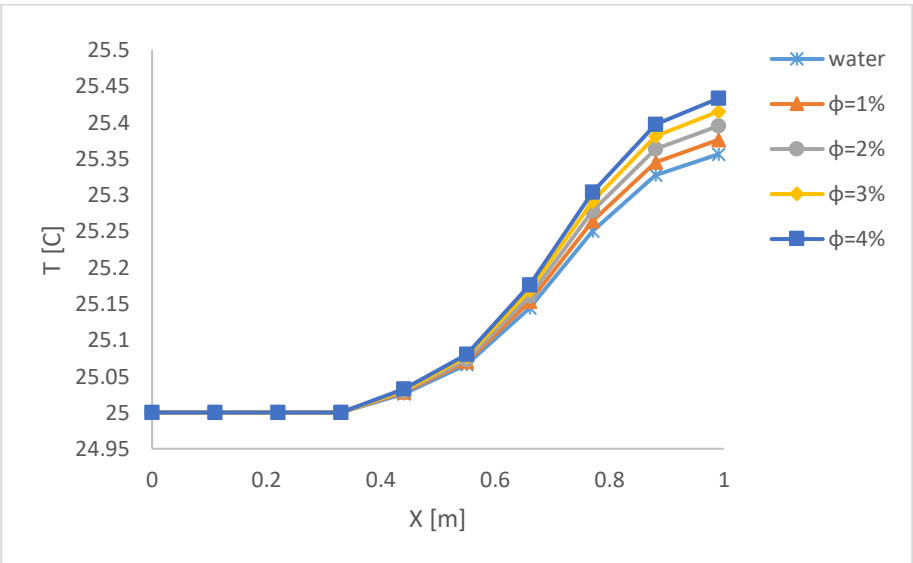

(b) Re = 5000

Figure 0.26. Temperature rise along the centerline for circular geommetry at (β=1.5)

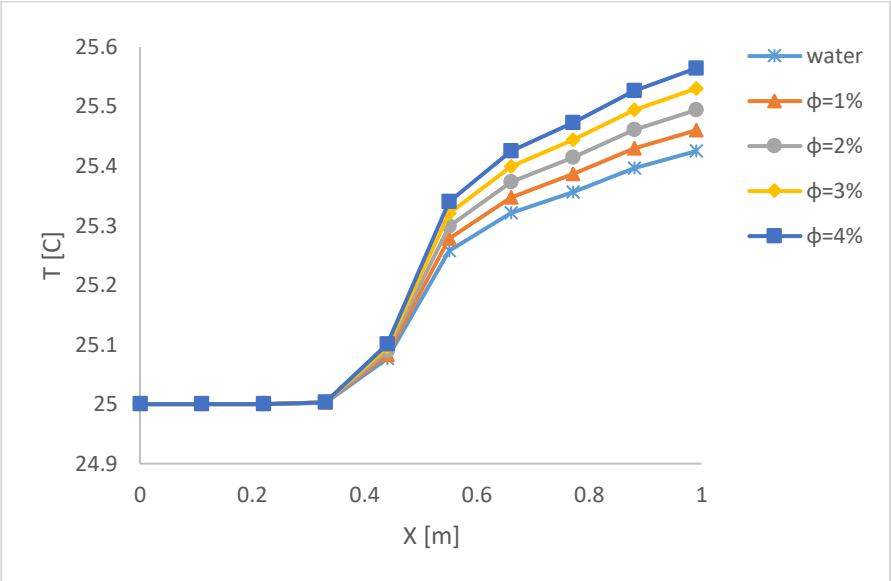

(a) Re = 500

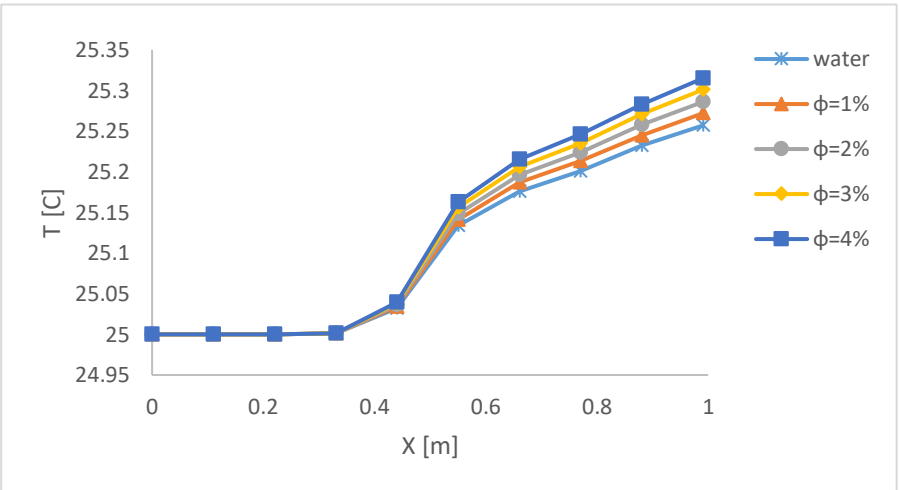

(b) Re = 5000

Figure 0.27. Temperature rise along the centerline for planar geommetry at (β=1.5)

Evaluation of Nusselt Number

Evaluating the heat transfer coefficient at the surface of larger diameter at a heated location for calculating local Nusselt number that has been given by Equation 3.15 is going to be reduced alone x-axis as shown in Figure 4.16 and Figure 4.17 for water and 4% nanoparticle content for different Reynold number. Despite an increase of Reynolds number augmented heat transfer coefficient but the effect of high thermal conductivity of nanofluid reduce Nusselt number, and same appeared for duct shape in Figure 4.18 and Figure 4.19, this reduction was expected and explained in Figure 4.20 because of enhancing in thermal conductivity, and reduce in specific heat capacity Figure 4.21, but during increasing in volume fraction the local Nusselt number of 4% nanofluid have a higher value than pure water this relation explain that the variation in local Nusselt number with volume fraction is proportional and that is an improvement that nanofluid with higher volume fraction gives better cooling fluid than water.

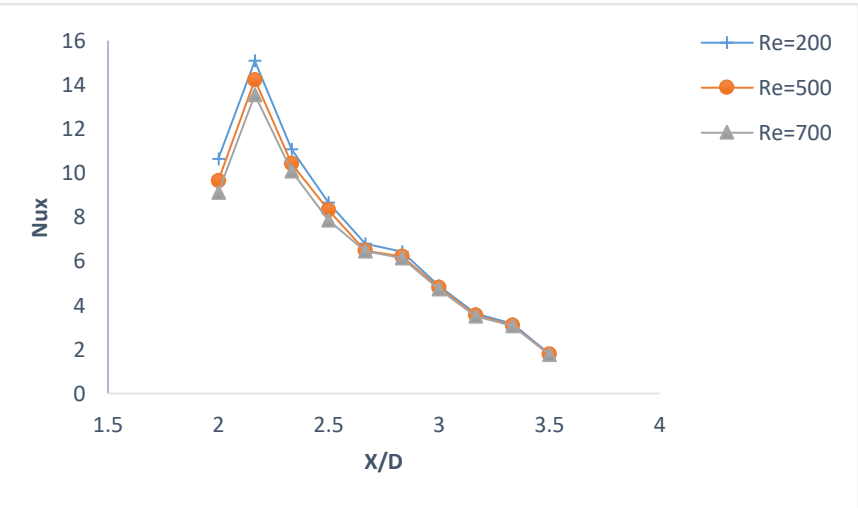

Figure 0.28. Local Nusselt number variation along the surface of heated part for different Reynolds numbers in the axisymmetric geometry (water).

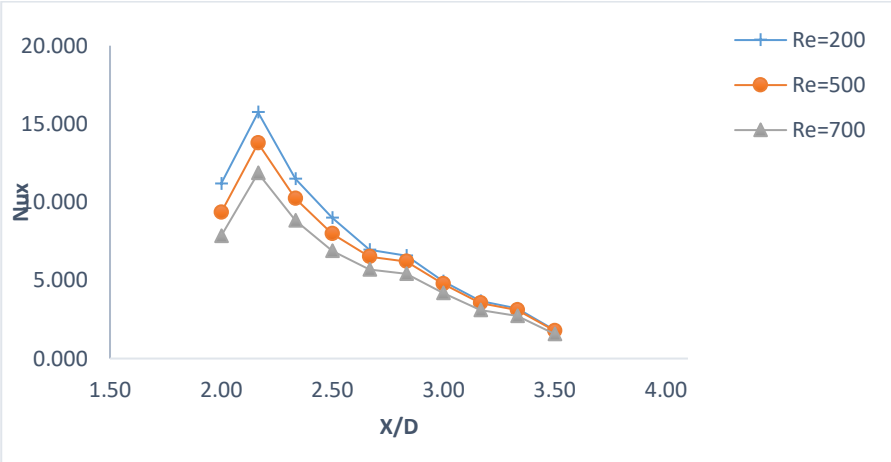

Figure 0.29. Local Nusselt number variation along the surface of heated part for different Reynolds numbers in a circular geometry for (4% nanofluid) at (β=1.5).

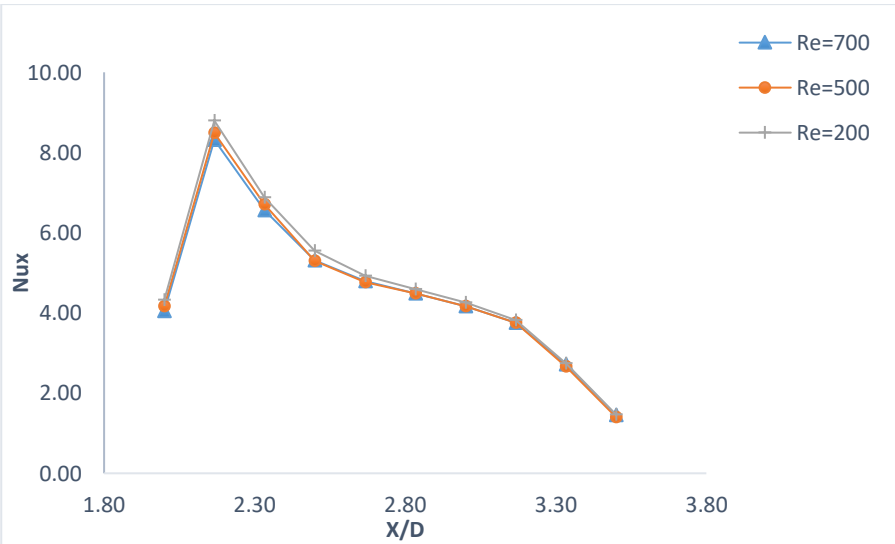

Figure 0.30. Local Nusselt number variation along the surface of heated part for different Reynolds numbers in a duct shape for (water) at (β=1.5).

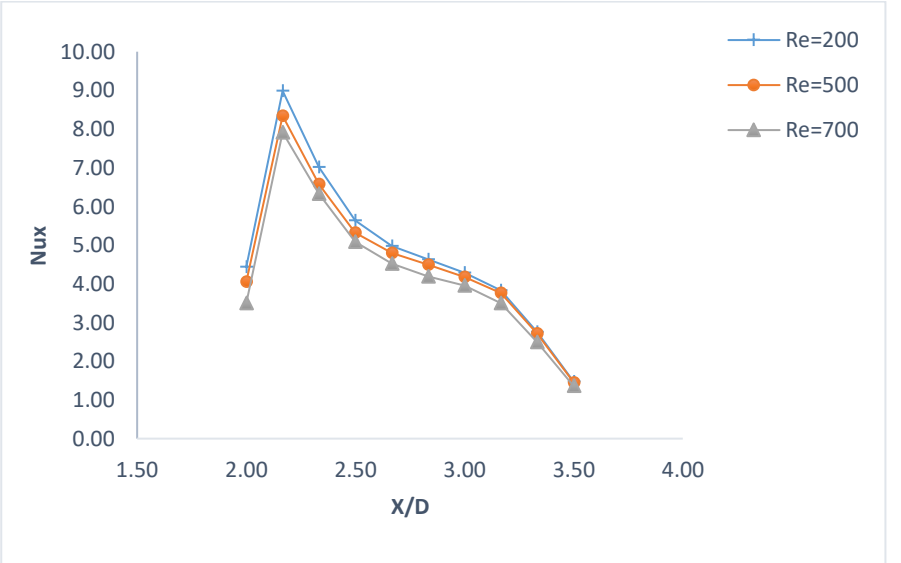

Figure 0.31. Local Nusselt number variation along the surface of heated part for different Reynolds numbers in a duct shape for (4% nanofluid) at (β=1.5).

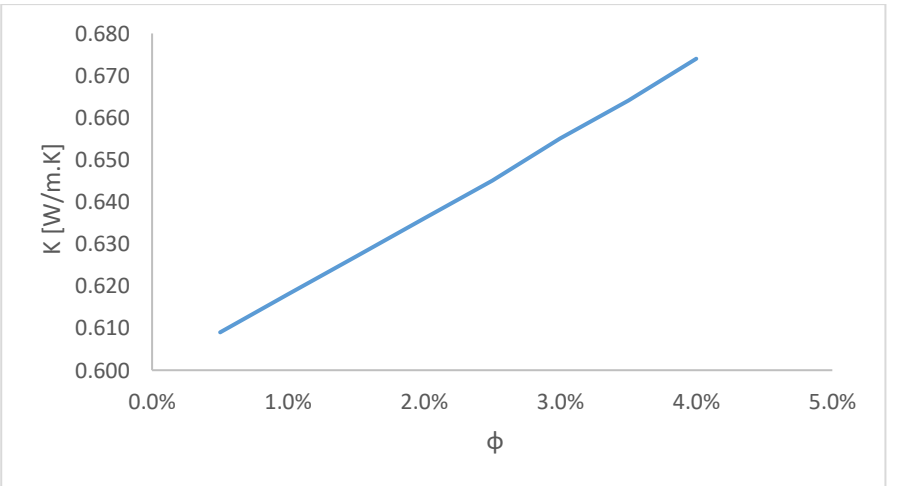

Figure 0.32. Variation of thermal conductivity with volume fraction.

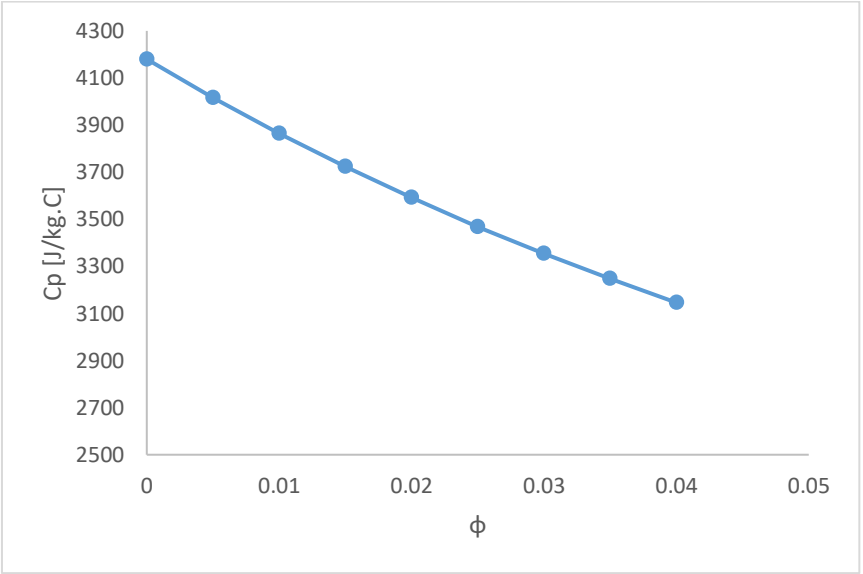

Figure 0.33. Variation of C_p with volume fraction

Contours

Figure 4.22 shows the effect off temperature contours for all entire body. According to the contours of Figure 4.23 and Figure 4.24 (a, b) for circular cross sectional are and duct respectively by enhancing Reynolds number, the thermal boundary layer thickness of the hot areas adjacent to the circumstance of geometry significantly reduced and consequently because of reducing in outlet temperature of fluid, heat transfer reducing, thermal boundary layer has been discussed before in Chapter 3. Figure 4.25 and Figure 4.26 shows velocity boundary layer which express that as Reynold number enhancement the distance y from the surface increase, due to increase in inlet velocity the same think can be noticed in Figure 4.27 for planar geometry.

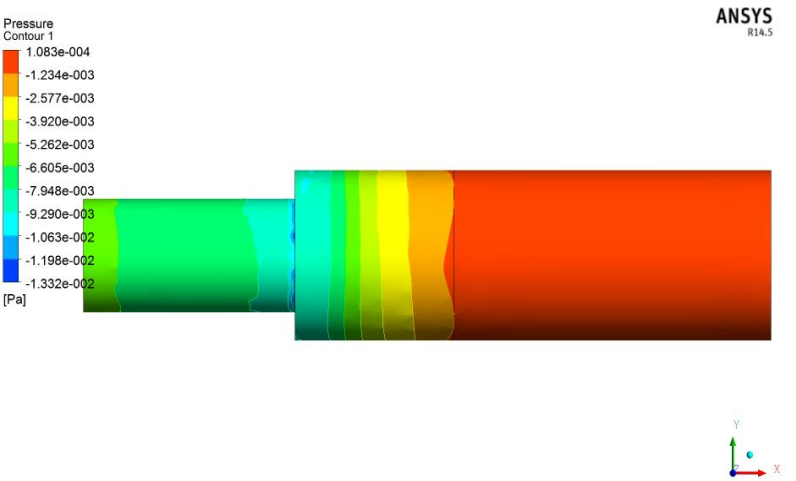

(a) Water

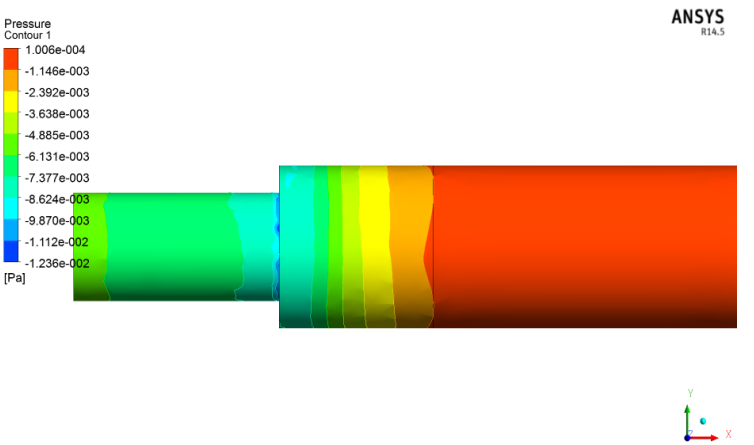

(b) 4% Nanofluid

Figure 0.34. Pressure contour at Re = 1100 for circular duct

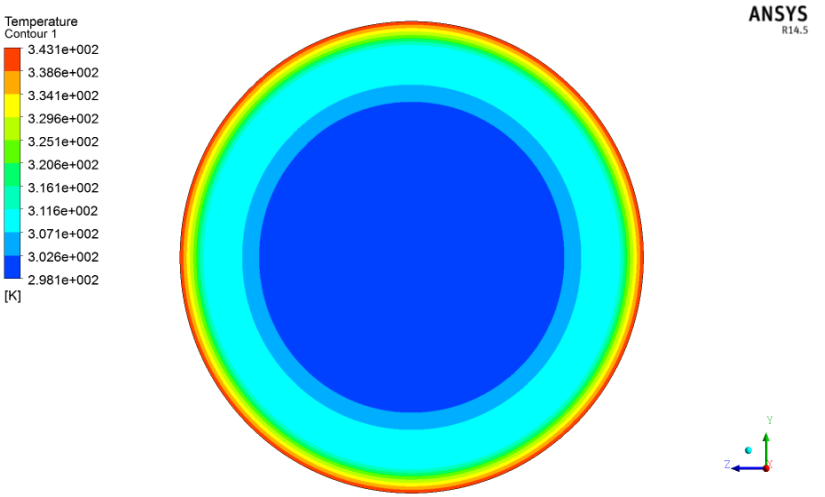

(a) Re = 1100

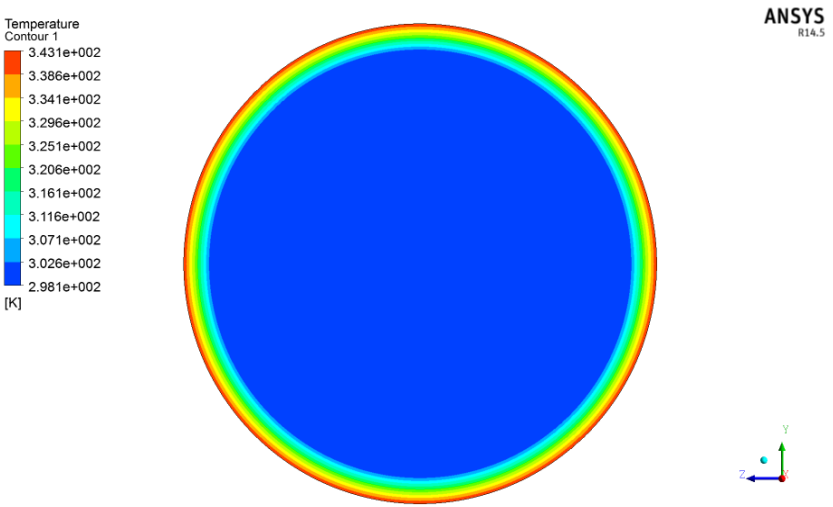

(b) Re = 5000

Figure 0.35. Temperature contours at x = 0.5 m partialy heated location for φ = 4% nanofluid (circular)

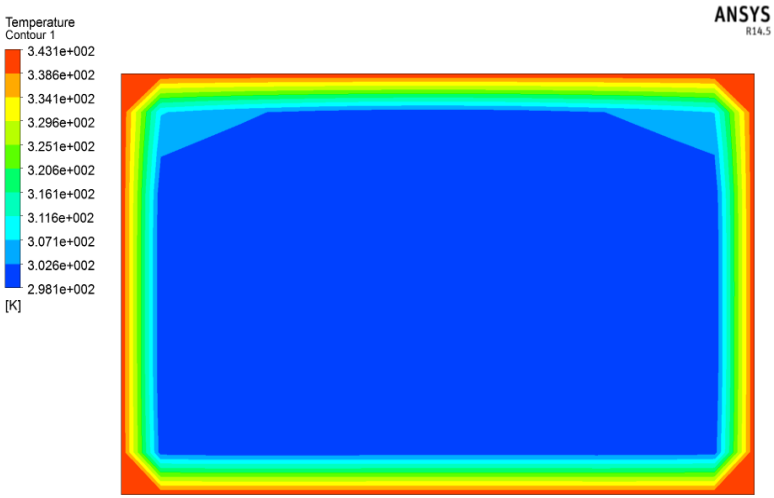

(a) Water

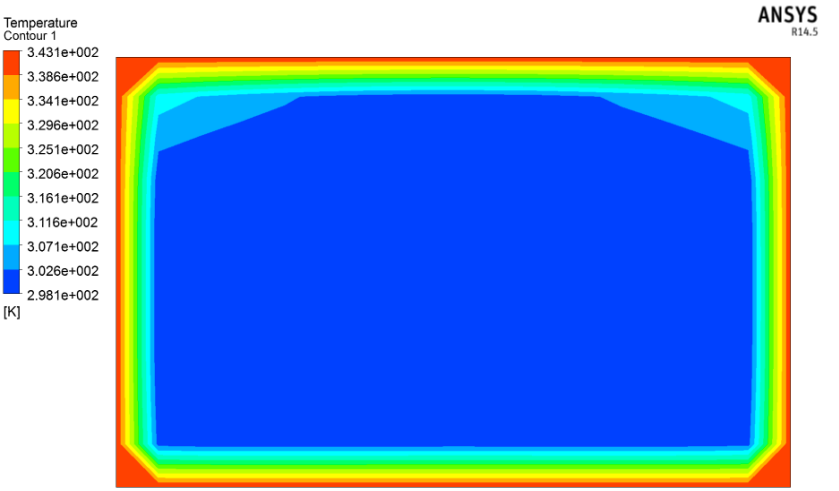

(b) 4% Nanofluid

Figure 0.36. Temperature contours at outlet at Re =1100 (planar)

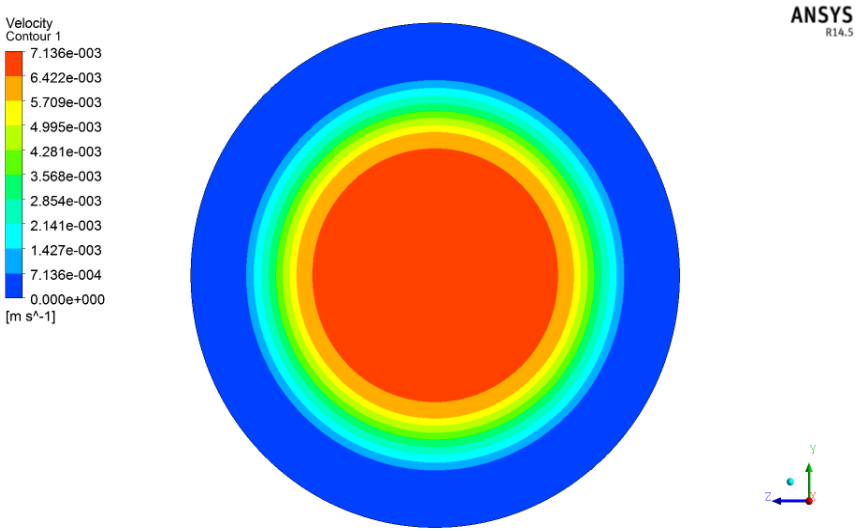

(a) Re = 1100

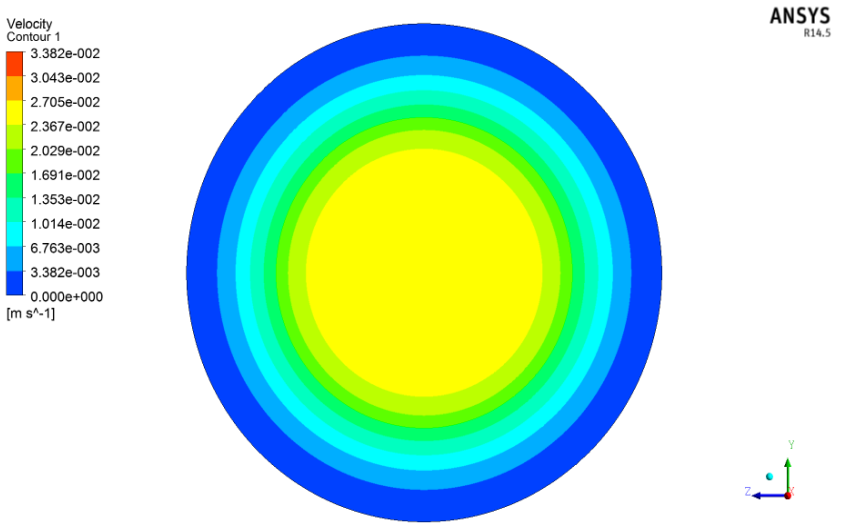

(b) Re = 5000

Figure 0.37. Velocity contours at x = 0.5 m for water at (β=1.5)

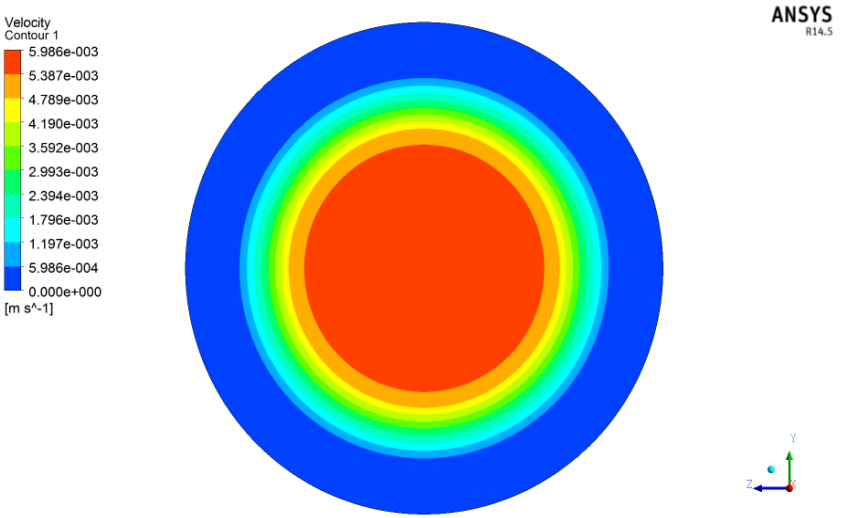

(a) Re = 1100

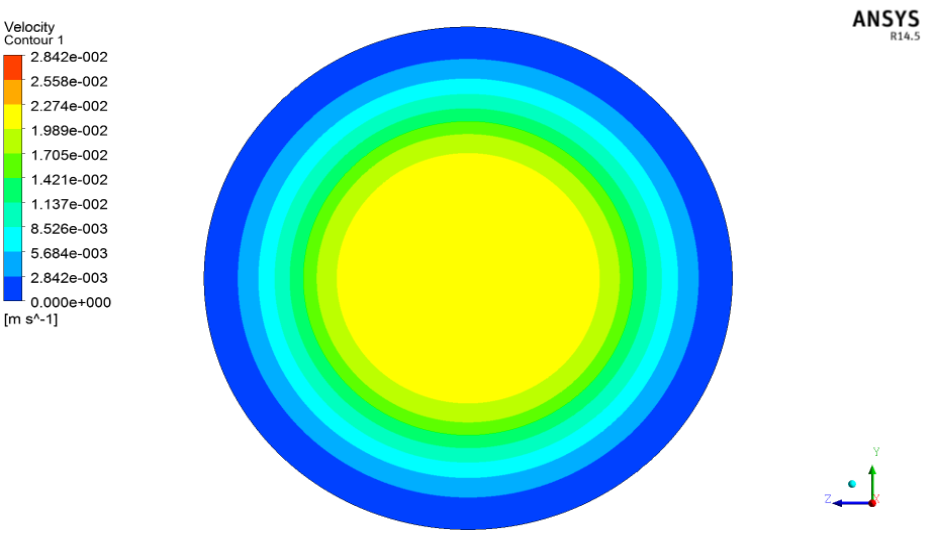

(b) Re = 5000

Figure 0.38. Velocity contours at x = 0.5 m for φ = 4% nanofluid circular grommetry at (β=1.5)

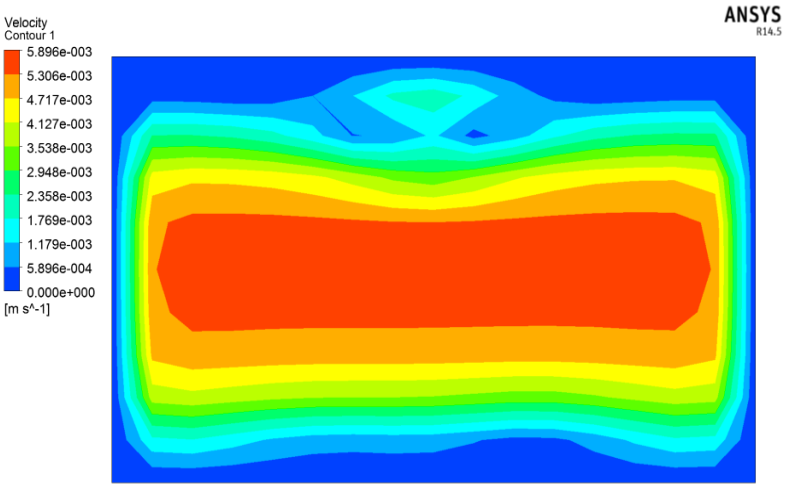

(a) Re = 1100

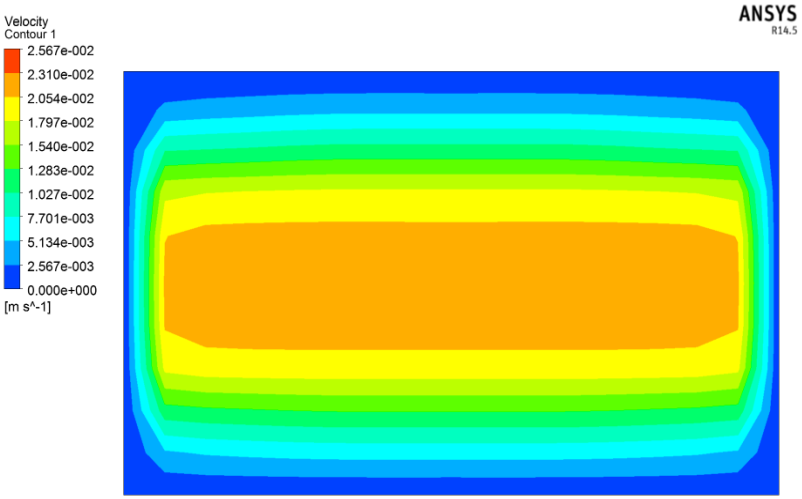

(b) Re = 5000

Figure 0.39. Velocity countours for φ = 4% nanofluid planar geommetry at (β=1.5)

Results for Sudden Contraction Fittings

The solution of suddenly contraction geometric flow was analyzed the same size, expansion ratio and boundary condition applied for it .expected the pressure reduced at suddenly contraction area due to reduction of cross-section area as appeared in Figure 4.28, besides that velocity along the flow is enhanced Figure 4.32 shows the relation for axisymmetric geometry for ϕ = 4% at Re = 500, also the geometry has an effect on temperature curve along with flow Figure 4.29 explains that outlet temperature is higher because of the duration of stay compared to that which was in suddenly expansion at Figure 4.10, streamline reattachment effect is not noticeable at suddenly changed diameter for suddenly contraction geometry as appeared at Figure 4.33 also Figure 4.30 and Figure 4.31 shows the relation of local Nusselt number .

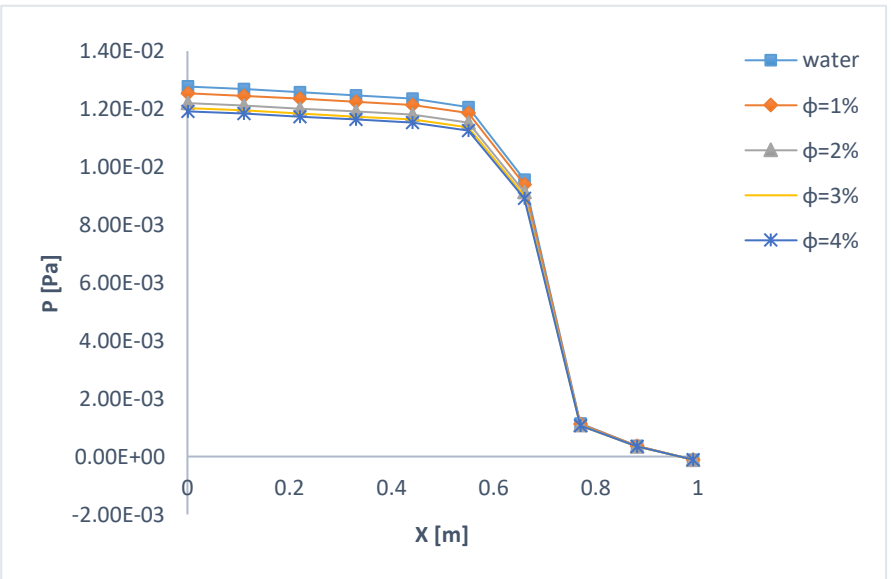

Figure 0.40. Pressure variation along x-axis at Re = 500 for concentric circular shape

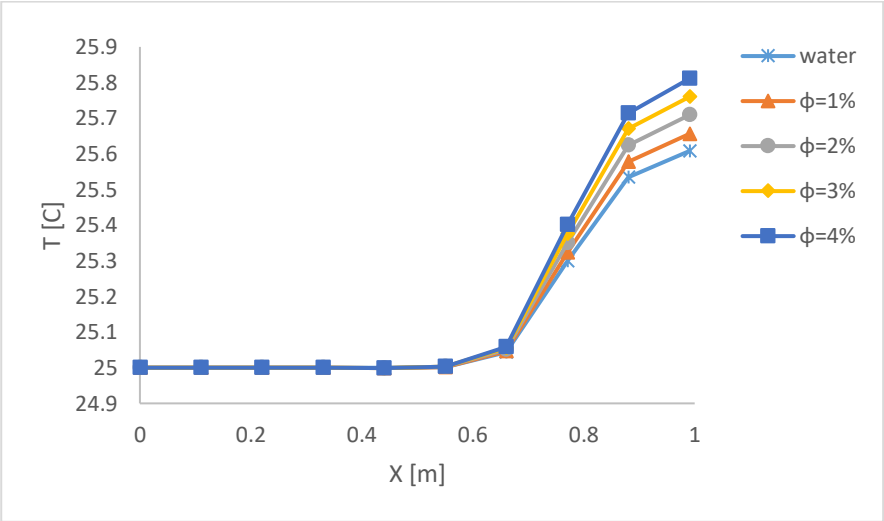

Figure 0.41. Temperature variation along x-axis at Re = 500 for suddenly contraction circular duct

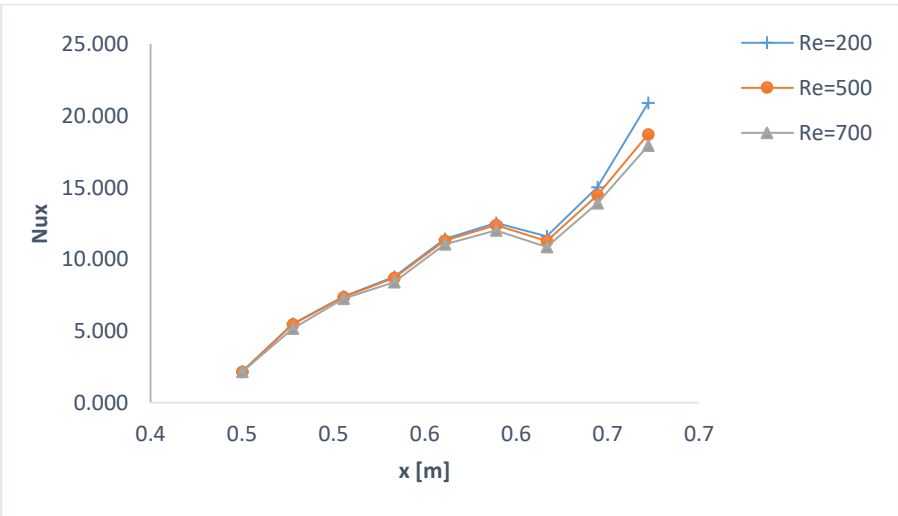

Figure 0.42. Local Nusselt number variation along the surface of heated part for different Reynolds numbers in a circular shape for (water).

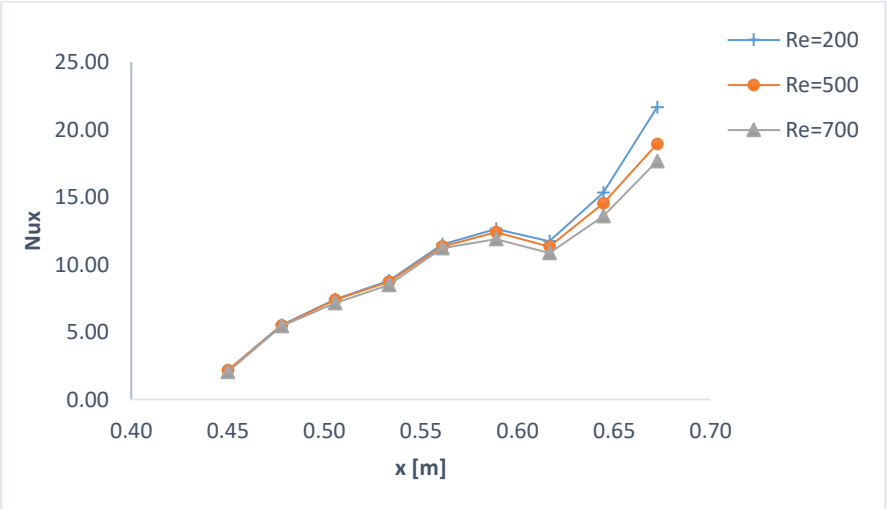

Figure 0.43. Local Nusselt number variation along the surface of heated part for different Reynolds numbers in a circular shape for (4% nanofluid).

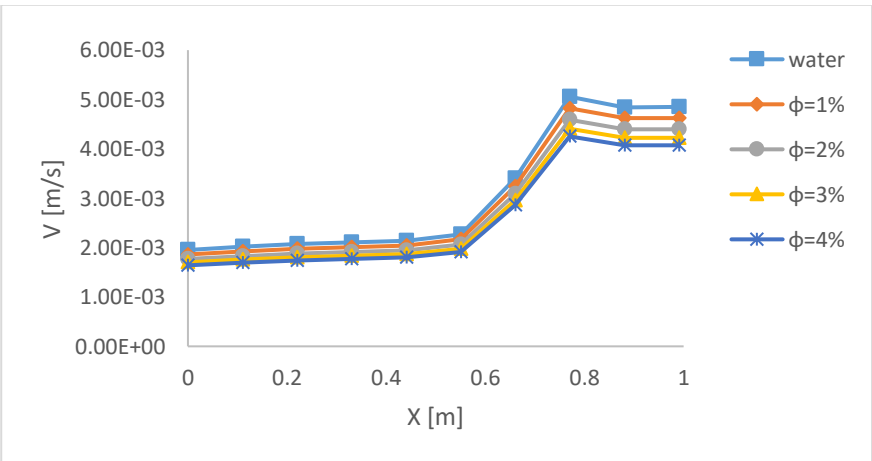

Figure 0.44. Velocity variation along x-axis at Re = 500 for circular duct

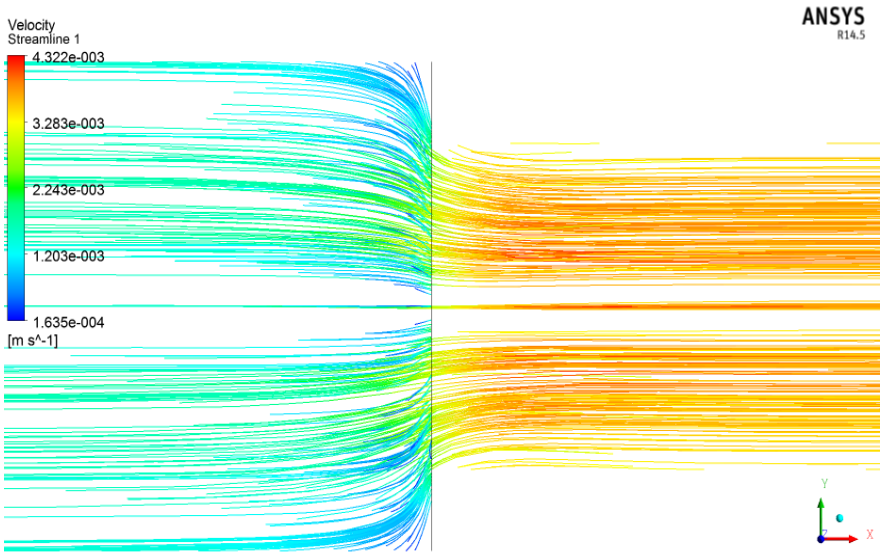

Figure 0.45. Streamlines of sudden contraction circular duct (ϕ = 0.04 for Re = 500)

Conclusions

Heat transfer and fluid flow were analyzed using CFD in a partially heated concentric reducer (suddenly expansion and contraction) fittings in circular and rectangular coordinates by using Cu nanofluids that contained with water base fluid. Some findings can be extracted as follows:

- With increase of ϕ inner velocity decreases and streamlines more stretched down and reattachment length reduced at the same Reynolds number.
- Using nanofluids at cooling process in higher temperature location is better than water as it was shown in our research at **D**T & Nu relation.

- The results show that working at lower Re and higher volume fraction gives better coolant fluid because it gives nanofluid chance to carry more heat.
- The pressure drop is higher at planar geometry compared with axisymmetric duct.
- The pressure drop has strong relation with nanofluid contents in base fluid such that with increasing of nanofluid contents in base fluid pressure drop decreases.
- Reattachment length is higher at planar geometry compared with axisymmetric at same ϕ for various Re numbers.
- Due to increase in nanofluid contents ϕ temperature difference increases for both planar and axisymmetric cases.
- The investigation showed that with increase of nanoparticle in base fluid the flow will behavior due to higher density and at same time velocity will be decrease alone x-axis density difference showed in Table 2.1

References

[1] R. Saidur, K. Leong, H.A. Mohammed, A review on applications and challenges of nanofluids, Renewable and sustainable energy reviews, 15 (2011) 1646-1668.

[2] E.O. Macagno, T.-K. Hung, Computational and experimental study of a captive annular eddy, Journal of fluid Mechanics, 28 (1967) 43-64.

[3] A. Phocaides, Handbook on pressurized irrigation techniques, Food & Agriculture Org., 2007.

[4] C. Choi, H. Yoo, J. Oh, Preparation and heat transfer properties of nanoparticle-in-transformer oil dispersions as advanced energy-efficient coolants, Current Applied Physics, 8 (2008) 710-712.

[5] A. Kamyar, R. Saidur, M. Hasanuzzaman, Application of computational fluid dynamics (CFD) for nanofluids, International Journal of Heat and Mass Transfer, 55 (2012) 4104-4115.

[6] O.A. Alawi, N.A.C. Sidik, Influence of particle concentration and temperature on the thermophysical properties of CuO/R134a nanorefrigerant, International Communications in Heat and Mass Transfer, 58 (2014) 79-84.

[7] A.M. Hussein, K. Sharma, R. Bakar, K. Kadirgama, The effect of nanofluid volume concentration on heat transfer and friction factor inside a horizontal tube, Journal of Nanomaterials, 2013 (2013).

[8] Y. Xuan, Q. Li, Heat transfer enhancement of nanofluids, International Journal of heat and fluid flow, 21 (2000) 58-64.

[9] J.A. Eastman, S. Choi, S. Li, W. Yu, L. Thompson, Anomalously increased effective thermal conductivities of ethylene glycol-based nanofluids containing copper nanoparticles, Applied physics letters, 78 (2001) 718-720.

[10] K.R. Priya, K. Suganthi, K. Rajan, Transport properties of ultra-low concentration CuO–water nanofluids containing non-spherical nanoparticles, International Journal of Heat and Mass Transfer, 55 (2012) 4734-4743.

[11] D. Badekas, D. Knight, Eddy correlations for laminar axisymmetric sudden expansion flows, (1992).

[12] İ. Dağtekin, M. Ünsal, Numerical analysis of axisymmetric and planar sudden expansion flows for laminar regime, International journal for numerical methods in fluids, 65 (2011) 1133-1144.

[13] H.-H. Ting, S.-S. Hou, Numerical study of laminar flow forced convection of water-Al2O3 nanofluids under constant wall temperature condition, Mathematical Problems in Engineering, 2015 (2015).

[14] M. Gupta, V. Singh, R. Kumar, Z. Said, A review on thermophysical properties of nanofluids and heat transfer applications, Renewable and Sustainable Energy Reviews, 74 (2017) 638-670.

[15] P. Keblinski, J.A. Eastman, D.G. Cahill, Nanofluids for thermal transport, Materials today, 8 (2005) 36-44.

[16] L. Chen, H. Xie, Silicon oil based multiwalled carbon nanotubes nanofluid with optimized thermal conductivity enhancement, Colloids and Surfaces A: Physicochemical and Engineering Aspects, 352 (2009) 136-140.

[17] X. Wei, H. Zhu, T. Kong, L. Wang, Synthesis and thermal conductivity of Cu2O nanofluids, International Journal of Heat and Mass Transfer, 52 (2009) 4371-4374.

[18] W. Yu, H. Xie, L. Chen, Y. Li, Enhancement of thermal conductivity of kerosene-based Fe3O4 nanofluids prepared via phase-transfer method, Colloids and surfaces A: Physicochemical and engineering aspects, 355 (2010) 109-113.

[19] Y. Ding, D. Wen, Particle migration in a flow of nanoparticle suspensions, Powder Technology, 149 (2005) 84-92.

[20] K. Suganthi, V.L. Vinodhan, K. Rajan, Heat transfer performance and transport properties of ZnO–ethylene glycol and ZnO–ethylene glycol–water nanofluid coolants, Applied energy, 135 (2014) 548-559.

[21] M. Elias, I. Mahbubul, R. Saidur, M. Sohel, I. Shahrul, S. Khaleduzzaman, S. Sadeghipour, Experimental investigation on the thermo-physical properties of Al2O3 nanoparticles suspended in car radiator coolant, International Communications in Heat and Mass Transfer, 54 (2014) 48-53.

[22] L.S. Sundar, E.V. Ramana, M.K. Singh, A.C. Sousa, Thermal conductivity and viscosity of stabilized ethylene glycol and water mixture Al2O3 nanofluids for heat transfer applications: An experimental study, International Communications in Heat and Mass Transfer, 56 (2014) 86-95.

[23] M. Kole, T. Dey, Role of interfacial layer and clustering on the effective thermal conductivity of CuO–gear oil nanofluids, Experimental thermal and fluid science, 35 (2011) 1490-1495.

[24] M. Saeedinia, M. Akhavan-Behabadi, P. Razi, Thermal and rheological characteristics of CuO–Base oil nanofluid flow inside a circular tube, International Communications in Heat and Mass Transfer, 39 (2012) 152-159.

[25] B. Wang, X. Wang, W. Lou, J. Hao, Thermal conductivity and rheological properties of graphite/oil nanofluids, Colloids and Surfaces A: Physicochemical and Engineering Aspects, 414 (2012) 125-131.

[26] Q. Zhang, G. Chen, S. Yoon, J. Ahn, S. Wang, Q. Zhou, Q. Wang, J. Li, Thermal conductivity of multiwalled carbon nanotubes, Physical Review B, 66 (2002) 165440.

[27] K. Borodianskiy, Effect of carbon nanotubes' addition on mechanical properties and thermal conductivity of copper, Journal of Materials Science, 54 (2019) 13767-13774.

[28] R.S. Khedkar, A.S. Kiran, S.S. Sonawane, K. Wasewar, S.S. Umre, Thermo–Physical Characterization of Paraffin based Fe3O4 Nanofluids, Procedia Engineering, 51 (2013) 342-346.

[29] I. Mahbubul, R. Saidur, M. Amalina, Thermal conductivity, viscosity and density of R141b refrigerant based nanofluid, Procedia Engineering, 56 (2013) 310-315.

[30] R. Mostafizur, M. Bhuiyan, R. Saidur, A.A. Aziz, Thermal conductivity variation for methanol based nanofluids, International Journal of Heat and Mass Transfer, 76 (2014) 350-356.

[31] Z. Luo, C. Wang, W. Wei, G. Xiao, M. Ni, Performance improvement of a nanofluid solar collector based on direct absorption collection (DAC) concepts, International Journal of Heat and Mass Transfer, 75 (2014) 262-271.

[32] T.P. Otanicar, P.E. Phelan, R.A. Taylor, H. Tyagi, Spatially varying extinction coefficient for direct absorption solar thermal collector optimization, Journal of Solar Energy Engineering, 133 (2011).

[33] S.-H. Lee, S.P. Jang, Extinction coefficient of aqueous nanofluids containing multi-walled carbon nanotubes, International Journal of Heat and Mass Transfer, 67 (2013) 930-935.

[34] M. Sohel, R. Saidur, M.F.M. Sabri, M. Kamalisarvestani, M. Elias, A. Ijam, Investigating the heat transfer performance and thermophysical properties of nanofluids in a circular micro-channel, International Communications in Heat and Mass Transfer, 42 (2013) 75-81.

[35] Y. Xuan, H. Duan, Q. Li, Enhancement of solar energy absorption using a plasmonic nanofluid based on TiO 2/Ag composite nanoparticles, Rsc Advances, 4 (2014) 16206-16213.

[36] H. Tyagi, P. Phelan, R. Prasher, Predicted efficiency of a low-temperature nanofluid-based direct absorption solar collector, Journal of solar energy engineering, 131 (2009).

[37] R.A. Taylor, P.E. Phelan, T.P. Otanicar, C.A. Walker, M. Nguyen, S. Trimble, R. Prasher, Applicability of nanofluids in high flux solar collectors, Journal of Renewable and Sustainable Energy, 3 (2011) 023104.

[38] A. Lenert, E.N. Wang, Optimization of nanofluid volumetric receivers for solar thermal energy conversion, Solar Energy, 86 (2012) 253-265.

[39] M.W. Wambsganss, Thermal management concepts for higher-efficiency heavy vehicles, SAE transactions, (1999) 41-47.

[40] E. Ollivier, J. Bellettre, M. Tazerout, G.C. Roy, Detection of knock occurrence in a gas SI engine from a heat transfer analysis, Energy Conversion and Management, 47 (2006) 879-893.

[41] S.-C. Tzeng, C.-W. Lin, K. Huang, Heat transfer enhancement of nanofluids in rotary blade coupling of four-wheel-drive vehicles, Acta Mechanica, 179 (2005) 11-23.

[42] X.-Q. Wang, A.S. Mujumdar, A review on nanofluids-part II: experiments and applications, Brazilian Journal of Chemical Engineering, 25 (2008) 631-648.

[43] M. Bai, Z. Xu, J. Lv, Application of nanofluids in engine cooling system, in, SAE Technical Paper, 2008.

[44] W. Yu, D.M. France, J.L. Routbort, S.U. Choi, Review and comparison of nanofluid thermal conductivity and heat transfer enhancements, Heat transfer engineering, 29 (2008) 432-460.

[45] D. Elcock, Potential impacts of nanotechnology on energy transmission applications and needs, in, Argonne National Lab.(ANL), Argonne, IL (United States), 2007.

[46] M. Muruganandam, P.M. Kumar, Performance Evaluation of Internal Combustion Engine by using MWCNT/Water

based Nanofluid as a Coolant, JOURNAL OF APPLIED FLUID MECHANICS, 11 (2018) 15-21.

[47] Y. Li, S. Tung, E. Schneider, S. Xi, A review on development of nanofluid preparation and characterization, Powder technology, 196 (2009) 89-101.

[48] R. Nazar, A. Noor, K. Jafar, I. Pop, Stability analysis of three-dimensional flow and heat transfer over a permeable shrinking surface in a Cu-water nanofluid, International Journal of Mathematical and Computational Sciences, 8 (2014) 782-788.

[49] D.P. Kulkarni, D.K. Das, R.S. Vajjha, Application of nanofluids in heating buildings and reducing pollution, Applied Energy, 86 (2009) 2566-2573.

[50] K. Khanafer, K. Vafai, M. Lightstone, Buoyancy-driven heat transfer enhancement in a two-dimensional enclosure utilizing nanofluids, International journal of heat and mass transfer, 46 (2003) 3639-3653.

[51] E. Abu-Nada, Application of nanofluids for heat transfer enhancement of separated flows encountered in a backward facing step, International Journal of Heat and Fluid Flow, 29 (2008) 242-249.

[52] S.E.B. Maiga, S.J. Palm, C.T. Nguyen, G. Roy, N. Galanis, Heat transfer enhancement by using nanofluids in forced convection flows, International journal of heat and fluid flow, 26 (2005) 530-546.

[53] S.J. Palm, G. Roy, C.T. Nguyen, Heat transfer enhancement with the use of nanofluids in radial flow cooling systems considering temperature-dependent properties, Applied thermal engineering, 26 (2006) 2209-2218.

[54] S. Mirmasoumi, A. Behzadmehr, Numerical study of laminar mixed convection of a nanofluid in a horizontal tube using two-phase mixture model, Applied Thermal Engineering, 28 (2008) 717-727.

[55] H.F. Oztop, E. Abu-Nada, Numerical study of natural convection in partially heated rectangular enclosures filled with nanofluids, International journal of heat and fluid flow, 29 (2008) 1326-1336.

[56] A. Bejan, Convection heat transfer, John wiley & sons, 2013.

[57] Y. Cengel, Heat and mass transfer: fundamentals and applications, McGraw-Hill Higher Education, 2014.

[58] S. Whitaker, Forced convection heat transfer correlations for flow in pipes, past flat plates, single cylinders, single spheres, and for flow in packed beds and tube bundles, AIChE Journal, 18 (1972) 361-371.

[59] D.C. Wilcox, Turbulence modeling for CFD, DCW industries La Canada, CA, 1998.

[60] T.L. Bergman, F.P. Incropera, D.P. DeWitt, A.S. Lavine, Fundamentals of heat and mass transfer, John Wiley & Sons, 2011.

[61] J. Hinze, Turbulence 2'nd edition, MacGraw Hill, New-York, (1975).

[62] M. Kalteh, A. Abbassi, M. Saffar-Avval, J. Harting, Eulerian–Eulerian two-phase numerical simulation of nanofluid laminar forced convection in a microchannel, International journal of heat and fluid flow, 32 (2011) 107-116.

[63] A.H. Mahmoudi, M. Shahi, A.H. Raouf, A. Ghasemian, Numerical study of natural convection cooling of horizontal heat source mounted in a square cavity filled with nanofluid, International Communications in Heat and Mass Transfer, 37 (2010) 1135-1141.

[64] F. Talebi, A.H. Mahmoudi, M. Shahi, Numerical study of mixed convection flows in a square lid-driven cavity utilizing nanofluid, International Communications in Heat and Mass Transfer, 37 (2010) 79-90.

[65] M. Akbari, A. Behzadmehr, F. Shahraki, Fully developed mixed convection in horizontal and inclined tubes with uniform heat flux using nanofluid, International Journal of Heat and Fluid Flow, 29 (2008) 545-556.

[66] G. Sheikhzadeh, A. Arefmanesh, M. Kheirkhah, R. Abdollahi, Natural convection of Cu–water nanofluid in a cavity with partially active side walls, European Journal of Mechanics-B/Fluids, 30 (2011) 166-176.

[67] Y. Feng, C. Kleinstreuer, Nanofluid convective heat transfer in a parallel-disk system, International Journal of Heat and Mass Transfer, 53 (2010) 4619-4628.

[68] E. Abu-Nada, H.F. Oztop, Effects of inclination angle on natural convection in enclosures filled with Cu–water nanofluid, International Journal of Heat and Fluid Flow, 30 (2009) 669-678.

[69] A.H. Abdelrazek, S. Kazi, O.A. Alawi, N. Yusoff, C.S. Oon, H.M. Ali, Heat transfer and pressure drop investigation through pipe with different shapes using different types of nanofluids, Journal of Thermal Analysis and Calorimetry, 139 (2020) 1637-1653.

[70] Y. Xuan, W. Roetzel, Conceptions for heat transfer correlation of nanofluids, International Journal of heat and Mass transfer, 43 (2000) 3701-3707.

[71] P. Scott, F. Mirza, J. Vlachopoulos, A finite element analysis of laminar flows through planar and axisymmetric abrupt expansions, Computers & fluids, 14 (1986) 423-432.

[72] A.A. Alrashed, O.A. Akbari, A. Heydari, D. Toghraie, M. Zarringhalam, G.A.S. Shabani, A.R. Seifi, M. Goodarzi, The numerical modeling of water/FMWCNT nanofluid flow and heat transfer in a backward-facing contracting channel, Physica B: Condensed Matter, 537 (2018) 176-183.

CHAPTER VIII

Comparing the CR210&CR240 Materials' Numeric Analysis at the End of the Automotive Door Panel Stamping Process

Ceren PALACI
Mehmet Kaan BAGBAKAN
Alp Eren SAHIN

INTRODUCTION

Sheet metals are widely used in various industrial sectors, with the automotive industry being the most common application area. The unique properties of sheet metals make them indispensable as a primary material in the automotive industry. These properties

include high elasticity modulus, high yield strength, and a high level of formability [1].

Non-formed sheet metals be exposed from gravity. This might affect the form of the panel. They can undergo sagging due to their unstable microstructure before entering the press line, as shown in the. Figure 1 shows the free shape and gravity free shape of the sheet metals when entering the forming line. This is not a deformation but can easily be predicted through simulations. [2].

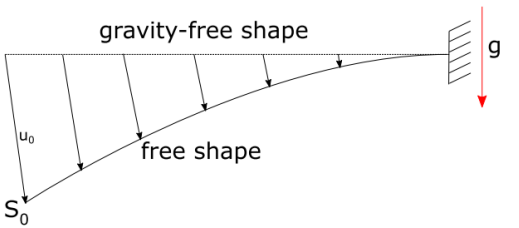

Figure 1. Sagging Caused by Gravity [2].

Sheet metals are used in the production of almost all commercial and passenger vehicles in the automotive sector. They are used in front door panels, rear door panels, floor and roof panels, fenders, trunk lids, and front hood panels, etc. They are lightweight, strong, and can take on complex shapes. The sheet metal stamping process is used widely in the automotive industry. They have low labor costs, but high equipment and tooling costs. Thus, this process is ideally suited for high-volume production [3].

Stamping, which is the most commonly used method for forming sheet metals, involves three main components, a female die and a male die and a blank holder. These components are produced by supplier companies through the casting method. The die design is then performed by the relevant department based on the desired form of the panel [3,5].

Typical deformations in sheet metal stamping are wrinkling (due to compressive stresses), tearing (due to tensile stresses) and springback (due to elasticity) [3, 10]. The tearing of sheet metal

usually occurs through local necking before actual fracture as shown in the Figure 2. During the tearing of sheet metal, one region may be separating while another region has just started necking or has not yet reached the necessary conditions for necking. These irregular deformations are typically caused by low plastic strains [7].

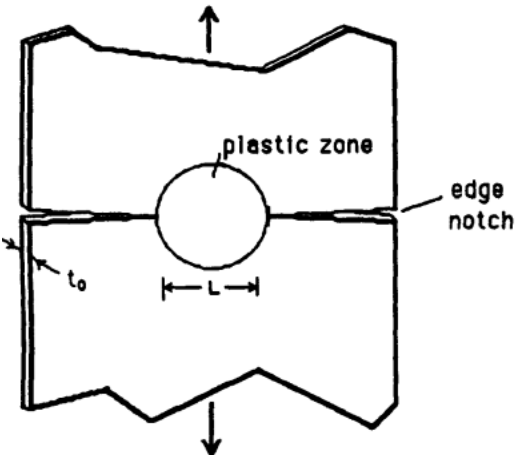

Figure 2. *How tearing causes fracturing on a sample [7]*

In this study, the panels will be under a force. The forces will cause our panel to deform. This deformations caused by force might be tearing or displacement. The main goal in our study is to see how different materials react to the same force under same conditions. The thinner panels are not very durable compared to thicker panels. They can be tear, even fracture under a force. On the other hand, softer alloys as Alluminium based steels, can tear earlier than the other materials [3,7]. This paper will show the main parameters which affects the most. The materials used in these analysis are two types of sheet metal materials in the industry. They have high durability, yield strength and formability. They are also both formable under cold forming operations. [4]

Transportation is an essential topic that encompasses a significant part of human life today. Therefore, it is crucial for transportation to be comfortable, safe, and cost-effective as much as

possible. Automotive companies carry out extensive studies in order to achieve these optimal conditions. A large portion of these studies covers the exterior structure, which is the most noticeable part of a vehicle. Besides aesthetic concerns, it is also one of the areas that require the utmost attention in terms of safety

1.MATERIALS AND METHOD

1.1.Materials

Table 1. Global Standards [4]

External Standards	
ASTM A568M	Standard Specification for Steel, Sheet, Carbon, and High-Strength
ASTM A635M	Low-Alloy, Hot-Rolled and Cold-Rolled, General Requirements for Standard Specification for Steel Sheet and Strip, Heavy-Thickness Coils, Carbon, Hot-Rolled
ASTM E8M	Test Methods for Tension Testing of Metallic Materials
ASTM E45	Test Methods for Determining the Inclusion Content of Steel
ASTM E112	Test Methods for Determining Average Grain Size
ASTM E517	Test Method for Plastic Strain Ratio r for Sheet Metal
ASTM E646	Test Method for Tensile Strain-Hardening Exponents (n-values) of Metallic Sheet Materials
EN 10051	Specification for Continuously Hot Rolled Uncoated Plate, Sheet and Strip of Non-Alloy and Alloy Steels – Tolerances on Dimensions and Shape
EN 10131	Cold Rolled Uncoated and Zinc or Zinc-Nickel Electrolytically Coated Low Carbon and High Yield Strength Steel Flat Products for Cold Forming – Tolerances on Dimension and Shape
EN 10143	Continuously Hot-Dip Coated Steel Sheet and Strip – Tolerances on Dimensions and Shape
ISO 4967	Steel – Determination of Content of Non-Metallic Inclusions –

	Micrographic Method
ISO 6892-1	Metallic Materials – Tensile Testing at Ambient Temperature
ISO 10113	Metallic Materials – Sheet and Strip – Determination of Plastic Strain Ratio
ISO 10275	Metallic Materials – Sheet and Strip – Determination of Tensile Strain Hardening Exponent
JFS A 1001	Hot Rolled Steel Sheet and Strip for Automobile Use
JFS A 2001	Cold Rolled Steel Sheet and Strip for Automobile Use
JIS G0320	Standard Test Methods for Heat Analysis of Sheet Products
JIS Z2241	Method of Tensile Test for Metallic Materials
JIS Z2254	Metallic Materials – Sheet and Strip – Determination of Plastic Strain Ratio
SEP 1240	Testing and Documentation Guideline for the Experimental Determination of Mechanical Properties of Steel Sheets for CAE Calculations

Two materials were analyzed and compared within the scope of this study. These materials are A22 CR210B2 and A23 CR240B2. Related global standards are given in Table 1. The mechanical properties and chemical composition of the analyzed materials are given in Table 2 and 3. [4]

Table 2. Alloys of the materials used [4]

Variant	**A22**	**A23**
Common Global Grade Name	CR210B2	CR240B2
Yield Strength, Mpa(min)	210	240
Yield Strength, Mpa(max)	270	300
Tensile Strength, Mpa(min)	320	340
Tensile Strength, Mpa(max)	400	440
ASTM Total Elongation, %(min)	33	30
EN Total Elongation, %(min)	31	28
JIS Total Elongation, %(min)	37	34
BHI, Mpa(min)	30	30

Table 3. *Composition of the materials used [4]*

Steel Grade	%C	%Si	%Mn	%P	%S	%Al	%Cu
CR210B2	0.06 >	0.5 >	0.7 >	0.085 >	0.025 >	0.015 >	0.2 >
CR240B2	0.1 >	0.5 >	1.0 >	0.1 >	0.03 >	0.015 >	0.2 >

Mechanical properties are valid in both the transverse and longitudinal directions. It is acceptable to certify material for shipment using only one test direction. For the determination of mechanical properties, the material cross sectional area shall be defined as that of the steel substrate only; contribution of any metallic and/or organic coating to the calculated cross-sectional area used for stress calculations is neglected. (i.e. Zn, e-coat and/or paint are not included). This method of determining the cross sectional area of the test bar will be used as the referee method in all cases where the mechanical properties of the incoming material are in dispute.[4]

Yield Strength is defined as lower yield stress or 0.2% proof stress (for materials without marked yield point). Plastic Strain Ratio (r-value) is defined for a specific test direction with respect to the rolling direction. It is measured at 20% total elongation (or maximum uniform elongation if less than 20%). Strain Hardening Exponent (n-value) is measured over the range 10-20% strain. Other test setups may be acceptable at the discretion of the regional Materials Engineering Mechanical properties are reported following standard rounding rules.[4]

1.2. Cad Modelling

All models have designed with CATIA 3D Design Program. Dimensions are similar but not the exact same as the original panels. Figure 3 shows the dimensions of the used door panel.

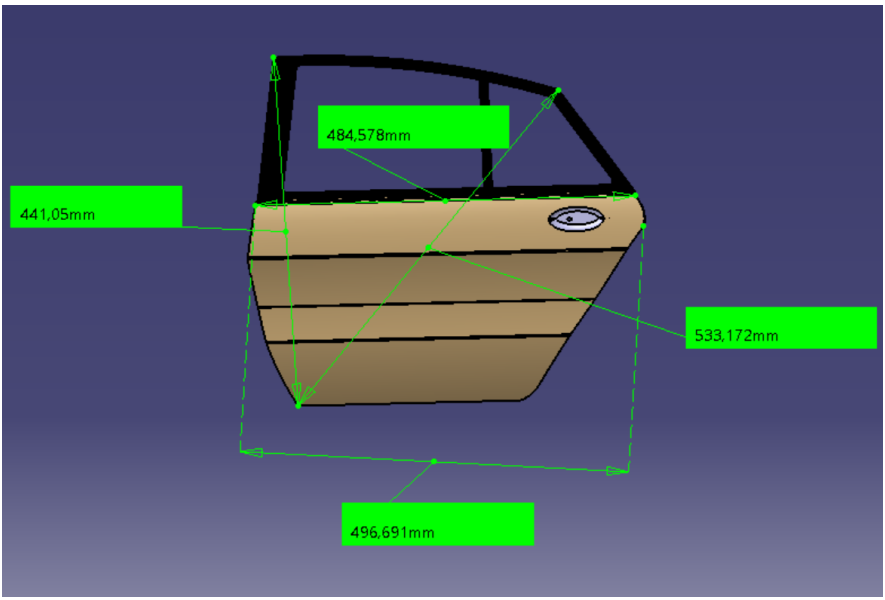

Figure 3. *Dimensions of the Door Panel*

The manufacturing of a door panel is also an important topic. Stamping is the most common process in the automative industry. In stamping operation, There are three main parts; Punch, Die, Blank Holder. Figure 4 is designed with the panel design in this study. There are two dies. They form the sheet metal to a panel. The panel designs used in this study, have formed by these dies. [9,10]

Stamping can be explained briefly as in the Fig. 4, when the die opens, only the plastic part of the deformation is preserved, and the relieved elastic deformation leads to the component reverting to a shape distinct from the die. In general, the progression of a die design and stamping process is as follows: part design, process model, die design, die manufacturing, die tryout, product. [11,12]

Red points show that this operation is not safe. There are deformations with the color red. This symbolyses that the deflections are tearing. The design must be updated until the simulation gives safe results.

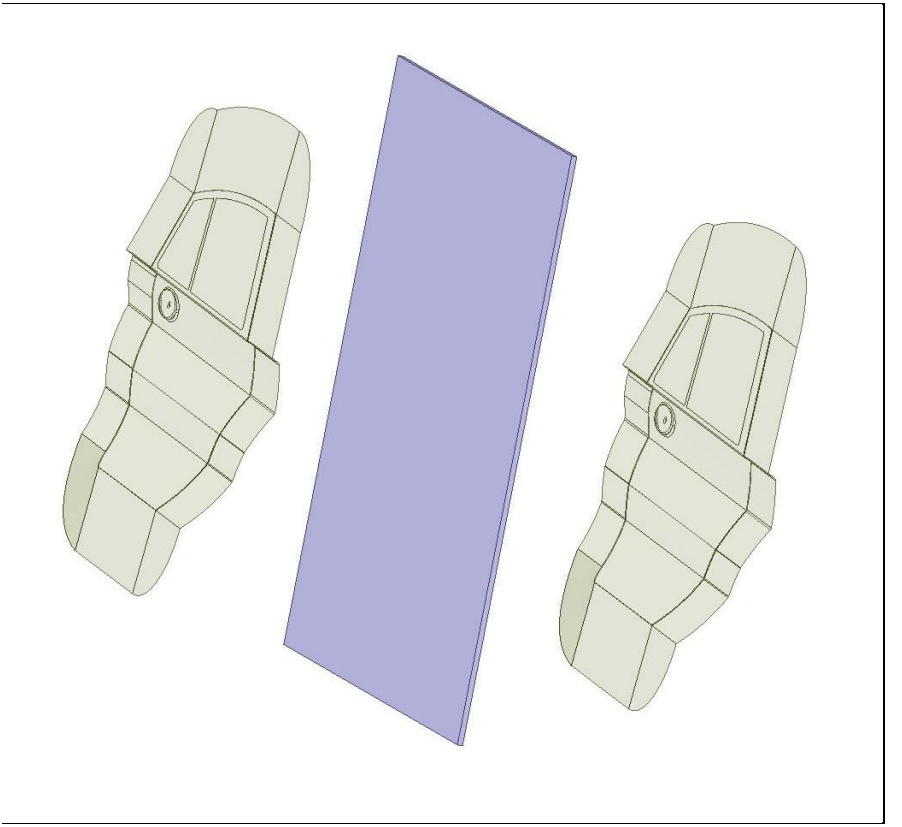

Figure 4. *Stamping Simulation of the Door Panel*

1.3. Methods

Analysed door panels have designed on CATIA. The dimensions do not reflect the real dimensions. Analysis have accomplished in ANSYS R5 Analysis Program.

The method used in the program is static structural analysis. The force is applied on a one specific point. The amount of force is 50 kN. Panels have already designed and formed. Therefore, the analysis process only completed with static structural analysis.

There are two analysis:

1. Personal Vehicles Door Panel [A22 CR210B2]
2. Personal Vehicles Door Panel [A23 CR240B2]

Forces are applied to whole surfaces. The amount of force is 50 kN. Analysis have applicated to each panel once. There are two materials, therefore there will be two results according to analysis. Forces are applied from the same direction. The surfaces under no force are fixed. The meshing distance is 5 mm as mentioned in the Table 4. Table 5 shows the unit system of the applicated analysis for both materials.

***Table 4**. Initial Conditions of Meshing*

State	Fully Defined
Scoping Methhod	Geometry Selection
Geometry	1 Body
Suppressed	No
Type	Element Size
Element Size	5 mm
Defeature Size	Default
Behavior	Soft

***Table 5.** Unit System*

Unit System	Metric (mm,kg,N,s,mV,mA)
Angle	Degrees
Rotational Velocity	Rad/s
Temperature	Celcius

2.RESULTS

Analysis of the Door Panel

Material 1: A22 CR210B2

In Figure 6, a static load of 50000 N is applied to the door panel with the given structural configuration in Fig. 5. The obtained amount of normal stress from the analysis is presented in Figure 7, the total deformation quantity is shown in Figure 8, and the amount of normal elastic strain is depicted in Figure 9, as observed.

Table 6, 7, 8, 9 and 10 show the values of deformation, Young Modulus, Poisson's Ratio, Bulk Modulus, Shear Modulus and density, Tensile Yield Strength and Tensile Ultimate Strength.

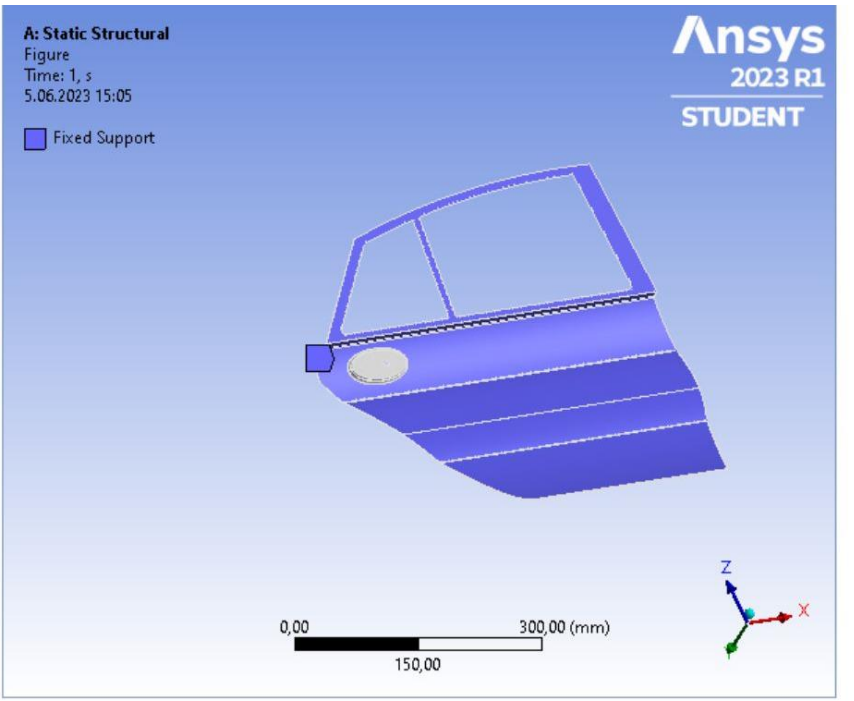

Figure 5. *Static Structure of the Panel*

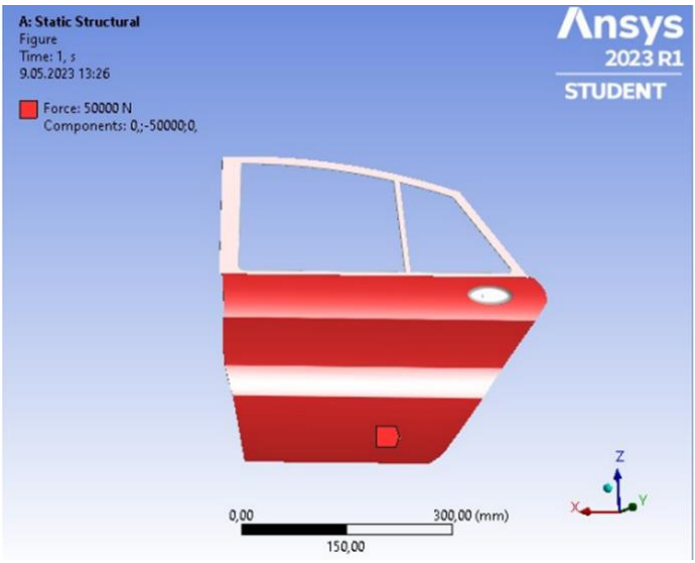

Figure 6. *Application of the Force*

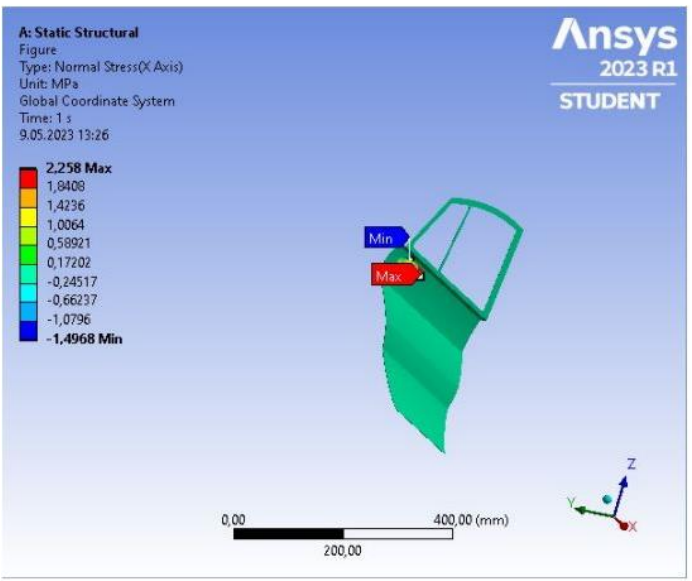

Figure 7. *Normal Stress*

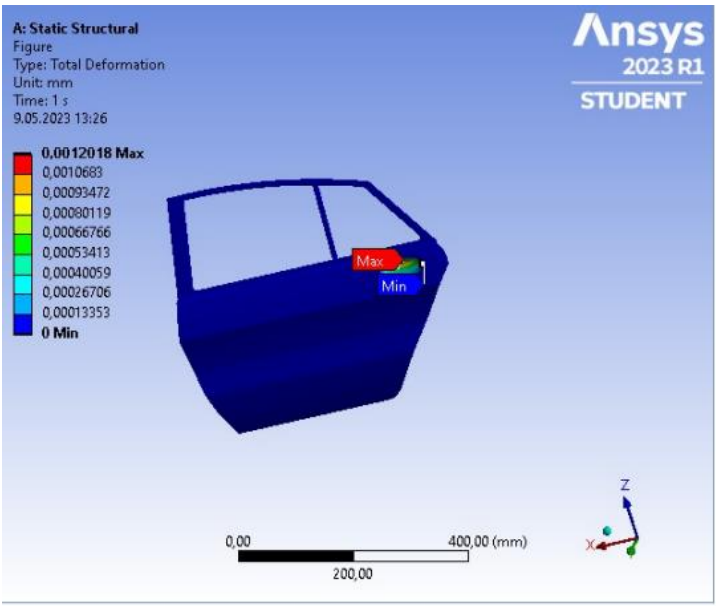

Figure 8. *Total Deformation*

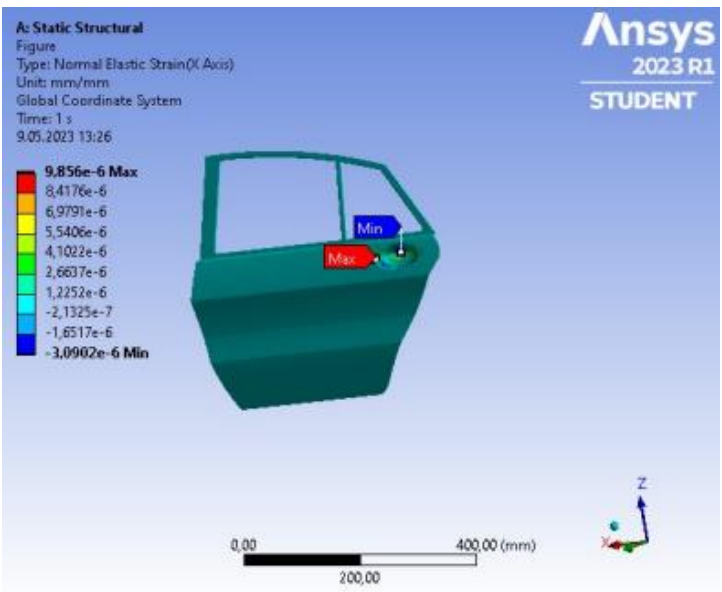

Figure 9. *Elastic Strain*

Table 6. *Amount of the Deformation*

Time (s)	Min (mm)	Max (mm)	Average (mm)
1,	0,	1,202e-003	1,1349e-005

Table 7. Parameters

Young Modulus MPa	Poisson's Ratio	Bulk Modulus MPa	Shear Modulus MPa
2,1e+005	0,3046	1,7912e+005	80484

Table 8. Density

Density kg mm^-3
7,85e-006

Table 9. *Yield Strength*

Tensile Yield Strength MPa
237,4

Table 10. *Ultimate Strength*

Tensile Ultimate Strength MPa
422,5

Material 2: A23 CR240B2

In Figure 10, a static load of 50000 N is applied to the door panel as in the first analysis. The obtained amount of normal stress from the analysis is presented in Figure 11, the total deformation quantity is shown in Figure 12, and the amount of normal elastic strain is depicted in Figure 13, as observed.

Table 11, 12, 13, 14 and 15 show the values of deformation, Young Modulus, Poisson's Ratio, Bulk Modulus, Shear Modulus and density, Tensile Yield Strength and Tensile Ultimate Strength.

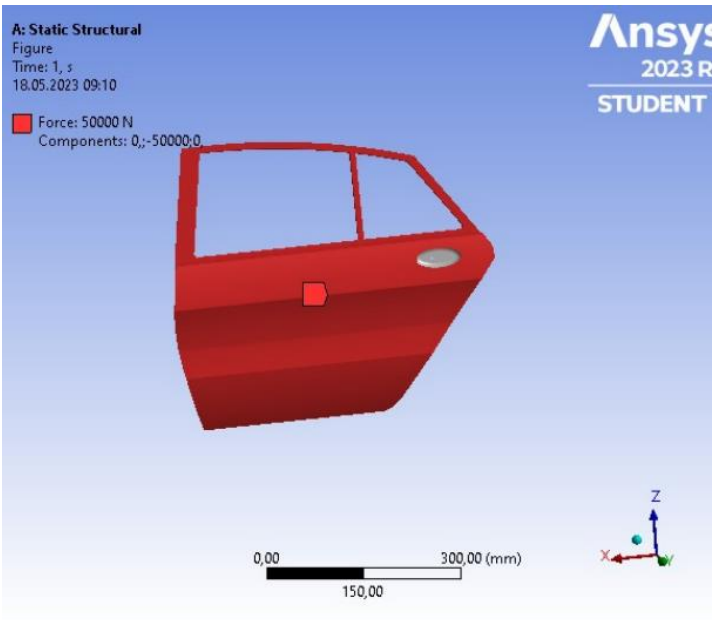

Figure 10. *Static Structure and the Application of the Force*

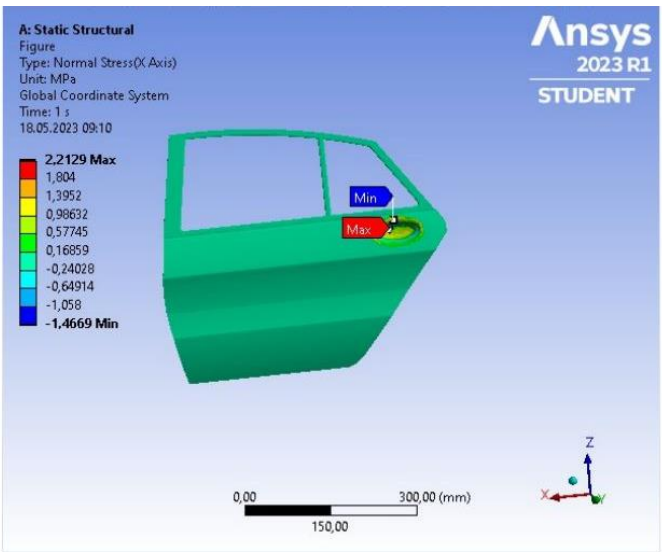

Figure 11. *Normal Stress*

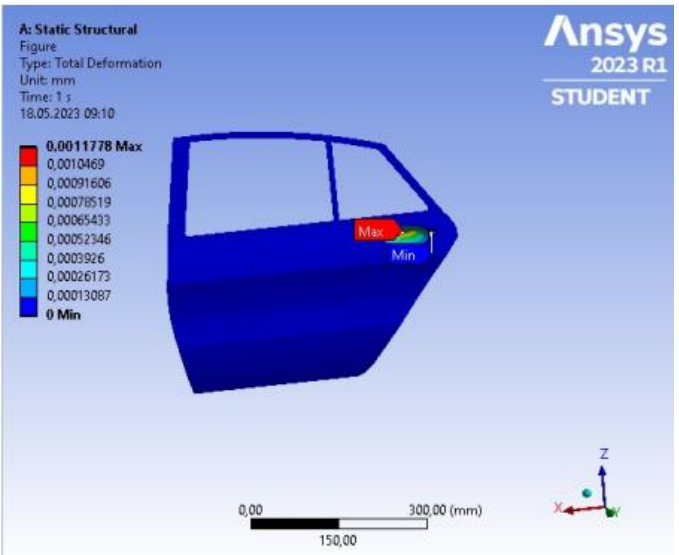

Figure 12. *Total Deformation*

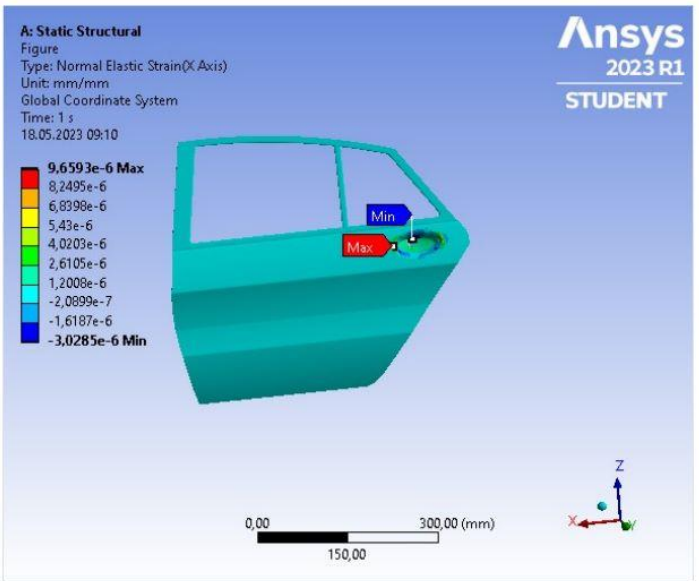

Figure 13. *Normal Stress*

Table 51. Amount of the Deformation

Time (s)	Min (mm)	Max (mm)	Average (mm)
1,	0,	1,778e-003	1,1349e-005

Table 12. Parameters

Young's Modulus Mpa	Poisson's Ratio	Bulk Modulus Mpa	Shear Modulus Mpa
2,1e+005	0,3046	1,7912e+005	80484

Table 13. Density

Density kg mm^-3
7,85e-006

Table 14. Yield Strength

Tensile Yield Strength Mpa
237,4

Table 15. *Ultimate Strength*

Tensile Ultimate Strength Mpa
422,5

CONCLUSION

There are two analysis. Door panel materials analysed are common sheet metal steels in the automotive industry, A22 CR210B2 and A23 CR240B2. 50 kN force is applied via a static force. Static Structural Analysis which is significantly similar to the stamping operation, have accomplished with given conditions.

The analysis results did not reveal a significant difference between the normal stress and normal elastic stress values of the two materials.The results we have show that total deformation is critically based on the material used. It can be clearly seen that planary surfaces are not deformated. Plastic strains are optimum on that surfaces. In the other hand, doorhandles have complex structure. Therefore, these areas have deformations that can cause problems even tearing.

If we compare the materials, A22 CR210B2 gave 0.0012018 mm deformation, second material A23 CR240B2 gave 0.0011778

mm deformation. The results show us that A23 CR240B2 gives less deformation on the door panel surface. Although there is a minimal difference between two materials' results, it can be clearly seen that A23 CR240B2 gives less deformation than A22 CR210B2.

Based on the results obtained, it is observed that when comparing A22 CR210B2 and A23 CR240B2 steels, utilizing A23 CR240B2 steel is more suitable and safe as the door panel material of an average private passenger vehicle.

ACKNOWLEDGMENTS

We would like to express our gratitude to the employees of FORD OTOSAN for their contributions to this study.

REFERENCES

1. Marciniak, Z., Duncan, J. L., & Hu, S. J. (2002). Mechanics of Sheet Metal Forming. Butterworth-Heinemann.
2. Claus, F., Hagen, H., & Hamann, B. (2021). Calculating the gravity-free shape of sheet metal parts. The International Journal of Advanced Manufacturing Technology, 113(11-12), 3401–3417. doi:10.1007/s00170-021-06702-6
3. Yongseob Lim , Ravinder Venugopal , A Galip Ulsoy (2013). Process Control for Sheet-Metal Stamping. Springer
4. Engineering Material Specification, Ford Global Technologies, LLC, 2017.
5. Makinouchi, A. (1996). Sheet metal forming simulation in industry. Journal of Materials Processing Technology, 60(1-4), 19–26. doi:10.1016/0924-0136(96)02303-5
6. Govik, A., Moshfegh, R., & Nilsson, L. (2013). *The effects of forming history on sheet metal assembly. International Journal of Material Forming, 7(3), 305–316.* doi:10.1007/s12289-013-1128-9
7. Hosford, W. F., & Atkins, A. G. (1990). *On fracture toughness in tearing of sheet metal. Journal of Materials Shaping Technology, 8(2), 107–110.* doi:10.1007/bf02833622
8. Vasilyev, A. A., Rudskoy, A. I., Glukhov, P. A., Sokolov, S. F., & Kolbasnikov, N. G. (2018). Estimation of the Degree of Recrystallization upon Annealing of Cold-Rolled Automobile Body Sheet Steels Using EBSD Analysis and Hardness Measurements. Russian Metallurgy (Metally), 2018(10), 973–979. doi:10.1134/s0036029518100191
9. Horton, P. M., & Allwood, J. M. (2017). Yield improvement opportunities for manufacturing automotive sheet metal components. Journal of Materials Processing Technology, 249, 78–88. doi:10.1016/j.jmatprotec.2017.05

10. Firat, M. (2008). A numerical analysis of sheet metal formability for automotive stamping applications. Computational Materials Science, 43(4), 802–811. doi:10.1016/j.commatsci.2008.01.

11. Liu, Y., Peng, X., & Qin, Y. (2004). FE simulation for concurrent design and manufacture of automotive sheet-metal parts. Journal of Materials Processing Technology, 150(1-2), 145–150. doi:10.1016/j.jmatprotec.2004.01

12. Spence, A. D., Chan, H.-L. (Harley), Mitchell, J. P., & Capson, D. W. (2005). Automotive Sheet Metal and Grid Digitizing Solutions. Computer-Aided Design and Applications, 2(1-4), 135–144. doi:10.1080/16864360.2005.107383

CHAPTER IX

Psychometric Diagram and Basic Definitions

Musa DEMİR[1]
Faruk GÜNER[2]

Introduction

The atmosphere around us is considered a binary mixture of dry air and water vapor, known as humid air. This mixture, crucial for the study and consideration of air conditioning technology, is a significant component of the air in our environment and a factor that impacts human life. The examination of this mixture takes into account the presence of dry air and water vapor, playing a role in technologies designed for climate control and affecting various aspects of human life. These effects should aim to enhance human life comfort. Conditions for comfort are sometimes achieved through processes like heating, cooling, humidification, and

[1] Ph.D., Giresun University
[2] Ph.D., Giresun University

dehumidification of air. Generally, people prefer relative humidity between 40% and 60% and temperatures ranging from 22°C to 27°C.

Humid Air: The air within the atmosphere contains a certain amount of water vapor and is therefore referred to as humid air (Çengel 2000).

Dry air: Dry air is a common mixture in the atmosphere, primarily composed of nitrogen, oxygen, argon, carbon dioxide, and some other gases. These components are the main building blocks of dry air, constituting the overall composition of the atmosphere. Air without water vapor is referred to as dry air(Çengel 2000).

Water vapor is considered a significant component of humid air. The proportion of water vapor in humid air can vary between 0.05% and 3% by mass. Being lighter than air, water vapor diminishes in density as it ascends through the atmosphere. Hence, altitude stands as a crucial factor affecting the amount of water vapor within humid air(Çengel 2000).

Ideal Gas Model and Calculations for Humid Air: Calculations involving humid air are often simplified using the ideal gas model. This model is employed to mathematically describe the behavior of humid air. The ideal gas model aids in understanding the relationship between pressure, temperature, and volume of humid air, utilizing the equation PV = RT, where P represents pressure, V denotes specific volume, R stands for the gas constant, and T signifies temperature. However, under real conditions, humid air may not perfectly adhere to the ideal gas model; hence, corrected models can be utilized for precise calculations(Çengel, Cimbala, & Engin 2008).

Definitions: Measurements utilized in climate technology generally involve temperature and humidity levels (Önen), (Zorkun &Ardıç 1980). These attributes are quantitative values obtained through experiments. Typically, all measurement systems consist of transducers that convert the perceived physical quantity into another more useful magnitude, intermediary stations that transform this

converted magnitude into desired output values, and terminals that record, control, and display the output values. However, before understanding how these measurements are carried out, it's important to define concepts such as accuracy, precision, and sensitivity.

Accuracy: It indicates how close a measurement is to the true value. It determines how precise and reliable a measurement is. Accuracy refers to the closeness of measurement results to the true value. Good accuracy implies that measured values are close to the true values.

Precision: It represents the repeatability and accuracy of a measurement. Precision indicates how closely results match each other when the same measurement is conducted repeatedly. Higher precision implies greater consistency in measurements. A precise measurement yields similar results under identical conditions.

Sensitivity: Sensitivity denotes how quickly and distinctly a sensor or measurement system responds to input changes. In other words, sensitivity specifies how a sensor perceives minor alterations and promptly reacts to these changes. High sensitivity indicates a measurement system that readily detects small changes and responds rapidly (Cengel, Boles, & Kanoğlu 2011).

These definitions are fundamental terms in understanding measurement and sensor technologies in engineering. They play a crucial role in making accurate and reliable measurements. Sensors are devices that detect physical, chemical, or biological changes and convert these changes into measurable signals. They are commonly used to gather environmental data, direct control systems, conduct measurements, and more. Here are some common types of sensors and their applications:

Temperature Sensors: They detect temperature changes and measure temperature. Used in many applications such as climate systems, industrial process control, and weather forecasting.

Pressure Sensors: They detect and measure pressure changes. Found in areas like tire pressure monitoring systems in vehicles and blood pressure measurement in medical devices.

Light Sensors: They measure ambient light levels. Applied in automatic lighting systems, cameras, and solar panels.

Humidity Sensors: They detect humidity levels. Used in climate control systems, soil moisture measurement, and water management applications (Demir, Omeroglu, & Özakın 2023).

Gas Sensors: They detect the presence of specific gases. Used in fields such as gas leak detection, air quality monitoring, and industrial safety (DEMİR &ADIGÜZEL 2023).

Motion Sensors: They detect motion. Applied in security systems, lighting controls, and automation systems.

Magnetic Sensors: They detect changes in magnetic fields. Used in devices like compasses, electric motors, and door locking systems.

Capacitive Sensors: They measure changes in capacitance. Applied in applications like touchscreens and monitoring fuel levels.

Current Sensors: They measure electric current. Used in electricity consumption monitoring, overcurrent protection, and industrial control systems.

Sensors play a critical role in many aspects of modern technology and are fundamental components of data collection and automation. These devices help us better understand the world around us and develop more efficient systems.

Temperature Measurements: Temperature is the measure of how hot or cold we perceive a substance to be physically. Scientifically, temperature represents the measure of kinetic energy possessed by a substance at the molecular and atomic levels. Temperature measurement systems typically consist of sensors, signal converters, and indicators. These systems can employ different methods depending on the intended application of

temperature measurement, the measurement range required, and the desired measurement precision (Didier Thevenard PhD &Shephard 2014). Temperature measurement devices can be classified based on various sensor types, as described below:

- Temperature scales are thermometers containing liquid within glass, operating based on liquid expansion.
- Bimetal thermometers rely on the bending of plates made of two different metals due to temperature changes.
- Thermocouples measure temperature using the thermoelectric effect resulting from the contact of two different metals.
- Resistance and thermistor-type temperature gauges utilize the change in material resistance due to temperature.
- Radiation thermometers are devices that measure temperature based on the radiation emitted by objects.

Signal Converters: These devices receive measurement signals of physical quantities detected by sensors (such as resistance values changing with temperature) and convert them into an output signal understandable by an indicator. This output signal is typically expressed in terms of voltage or similar magnitudes.

Indicators: Indicators are divided into two main categories: analog and digital. Analog indicators typically possess a coil system, while digital indicators operate by comparing signals from signal converters with a reference voltage and converting them through transistors (Güney, Kaygusuz, & Reviews 2010).

Liquid-in-Glass Thermometers: They operate by utilizing the rise of the liquid inside the thermometer tube in response to an increase in temperature. Typically, the measurement accuracy of these thermometers reaches up to one degree Celsius, making them

suitable for household and medical purposes (Çengel, Cimbala, & Engin 2008).

Bimetal Thermometers: Bimetal thermometers operate on the principle of metals expanding differently based on temperature. These thermometers are created by joining two different metal strips, where one end is fixed to a certain point while the other ends are joined in a manner that allows free expansion. Due to the different rates at which these metals expand with temperature, these bending rates are transformed into signals and conveyed to indicators. Such thermometers typically measure temperatures within the range of -100 to +500 °C. The measurement accuracy varies between 2 to 5 °C depending on the scales used. Bimetal thermometers find application in the manufacturing industry, medicine, the food industry, various industrial uses, and in many areas such as air conditioning technology (Güney 2010).

Thermocouples: Thermocouples are specialized measuring devices formed by connecting the ends of two different thin metal wires. Exposing these connections to varying temperatures causes an electric current to circulate within this system, known as the Seebeck effect, which relies on measuring temperature differences (Demir, Omeroglu, & Özakın 2023). The intensity of the electric current varies based on the temperature difference between the connected ends. While one end of a thermocouple serves as the measurement tip, the other functions as the reference tip. Thermocouples can be created using different combinations of metals and are generally standardized. The most commonly used types are E, J, K, R, S, and T. For instance, type E thermocouples are preferred in standard applications, type J is used for lower temperatures, and type K is suitable for outdoor atmospheric conditions. The measurement accuracies of thermocouples can range from 0.5% to 2.2% depending on the temperature range and type. This allows for a considerably wide range of usage temperatures based on the advantages offered by different types. Additionally, due to their durability and cost-effectiveness, thermocouples are among the most widely used devices for temperature measurements.

PRT (Platinum Resistance Thermometers): Platinum Resistance Thermometers (PRTs) are specialized temperature measurement devices containing platinum wire that responds sensitively to changes in temperature. The electrical resistance of this wire changes with temperature, and these variations are precisely measured to determine the temperature. Due to their high precision, PRTs are widely preferred in laboratory and industrial measurement applications. These devices are used in a range of fields such as scientific research, temperature calibration, and precise industrial process control.

Thermal Imaging Cameras: Thermal imaging cameras are devices used to visually display surface temperatures of objects. These devices present temperature differences in the form of colored images or thermal maps. Thermal imaging cameras find application across various domains. In industrial settings, they are used for a wide spectrum of purposes, ranging from detecting electrical and mechanical faults to inspecting building insulation. Additionally, firefighting teams utilize these cameras to identify fire sources and rescue individuals. In the medical field, thermal imaging cameras are employed for body temperature monitoring and medical diagnostics.

Radiation Thermometers: Radiation thermometers operate based on detecting thermal radiation emitted by an object, offering a non-contact method for temperature measurement. These thermometers are preferred in places where temperature measurement needs to be non-contact or where very high temperatures are measured. Some of these thermometers operate on the principle of detecting color changes and are known as optical pyrometers. Their measurement tolerances increase with rising temperatures and can range from 1°C starting up to 25°C. Another type, infrared thermometers, rely on capturing thermal radiation at specific wavelengths. These thermometers are used to measure temperatures of distant objects without contact and determine object surface temperatures in large areas.

Resistance and Thermistor Type Temperature Sensors: The operating principle of resistance and thermistor type temperature sensors is based on the change in electrical resistance with temperature. Positive Temperature Coefficient (PTC) resistors are of the type where electrical resistance increases as the temperature rises and are typically made from platinum or nickel-iron alloy fine wires. On the other hand, Negative Temperature Coefficient (NTC) sensors are thermistor resistors where electrical resistance decreases with increasing temperature and can be produced using semiconductor material technology. NTC sensors have a long lifespan and maintain measurement accuracy. Measurement tolerances can vary depending on the materials used and are generally usable up to 300°C. These types of temperature sensors are delicate instruments and may require careful storage and installation to ensure their continued accurate operation.

Psychrometric charts: Psychrometric charts developed by the American Society of Heating, Refrigerating and Air-Conditioning Engineers (ASHRAE) are used to determine the properties of moist air (Handbook 1997). Psychrometric charts are tools that graphically depict the properties of moist air under specific atmospheric pressure. These charts present the variation curves of moist air properties without scales, and it is recommended to refer to the original chart when making calculations (Didier Thevenard PhD &Shephard 2014).

In a psychrometric chart, the quantities that assist in determining the properties include: specific enthalpy, wet-bulb and dry-bulb temperatures, relative humidity, absolute humidity, specific volume (density), and dew point temperature. While some of these quantities can be directly read from the chart, others are determined through calculations.

Psychrometric charts are a significant tool in determining the properties of moist air, and there are equations and values available to calculate these properties.

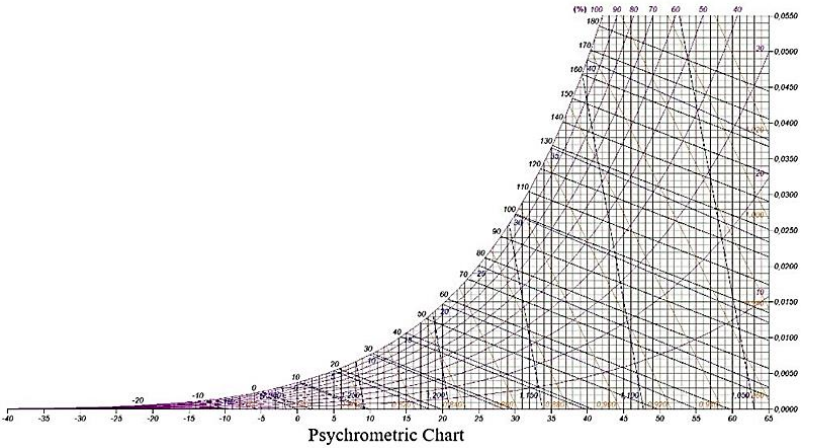

Figure 1. General view of the psychrometric diagram (Gatley 2004)

1. Dry Bulb Temperature:

Dry bulb temperature refers to the temperature measured by a traditional thermometer that measures the air temperature. This temperature is indicated on the horizontal axis in psychrometric charts (Cengel, Boles, & Kanoğlu 2011).

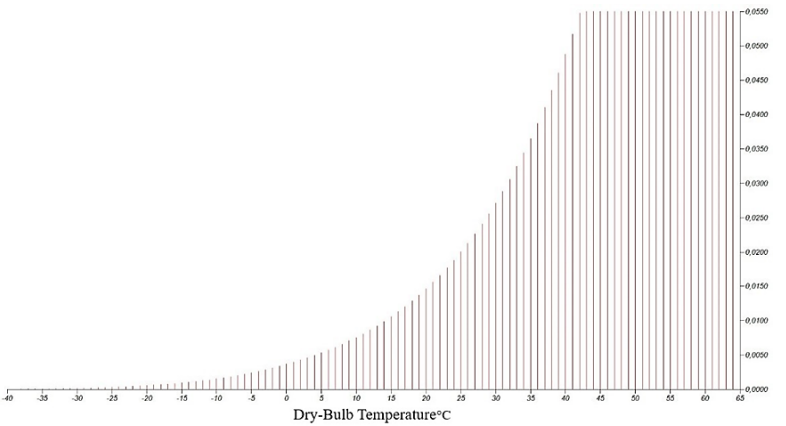

Figure. 2. View of the dry bulb temperature on the psychrometric diagram

2. Wet Bulb Temperature: Wet bulb temperature represents the temperature measured with a standard thermometer wrapped in a moist cloth. To determine this temperature, the temperature point on the horizontal axis is identified, and a vertical line is drawn from this point to intersect with the saturation curve. From this intersection point, an isenthalpic line is drawn, indicating the point where it intersects with the vertical line of the dry bulb temperature (Cengel, Boles, & Kanoğlu 2011).

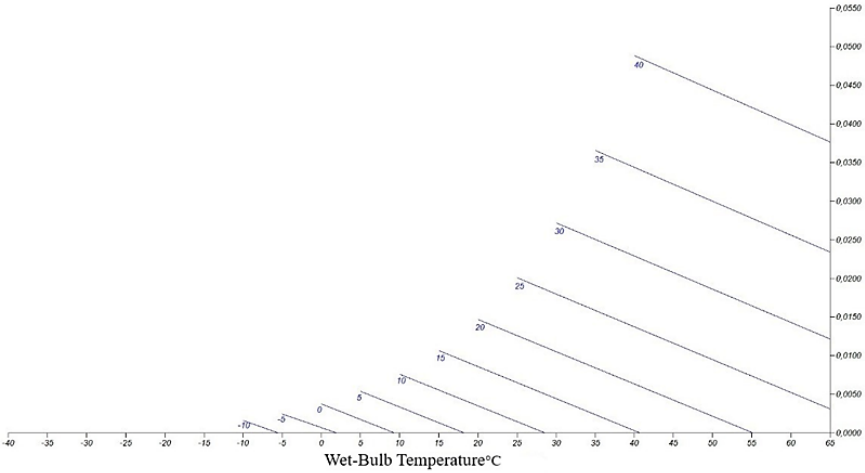

Figure. 3. View of wet-bulb temperature curves on psychrometric diagram

3. Relative Humidity: Relative humidity represents the ratio of the partial pressure of water vapor in moist air to the partial pressure of water vapor in saturated air at the same temperature and pressure. This is typically measured using an electronic hygrometer or a psychrometer(Çengel 2000).

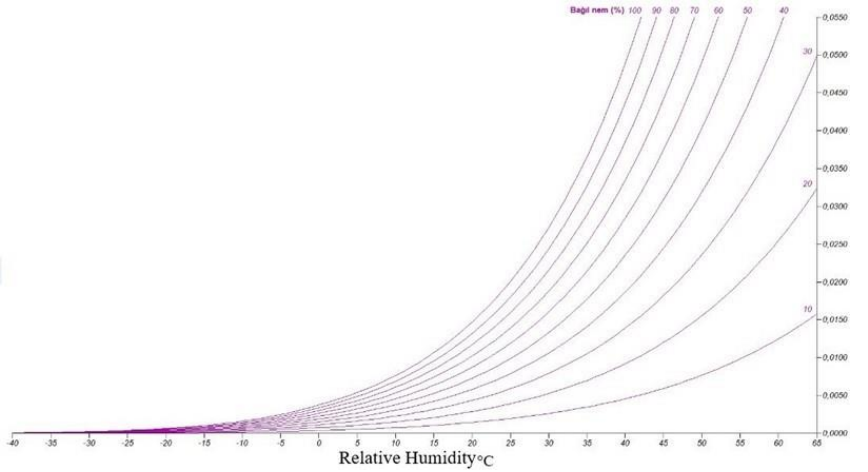

Figure. 4. View of relative humidity curves on psychrometric diagram

4. Absolute Humidity: Absolute humidity refers to the ratio of moisture content in a unit volume (typically cubic meter) of air to the mass of dry air. It is represented on the horizontal axis and is commonly expressed as kilograms per kilogram (Schramek 2003).

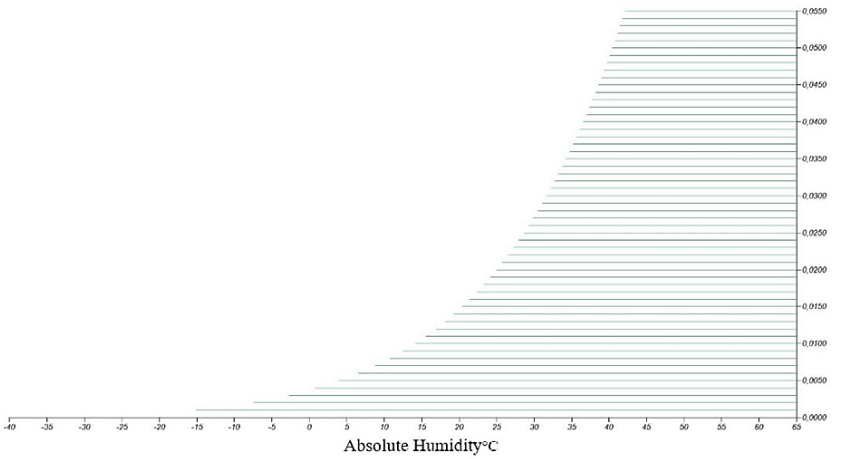

Figure.5. Appearance of absolute humidity curves on the psychrometric diagram

5. Specific Volume: Specific volume represents the volume occupied by one kilogram of dry air, with its unit being cubic meters per kilogram (Schramek 1999).

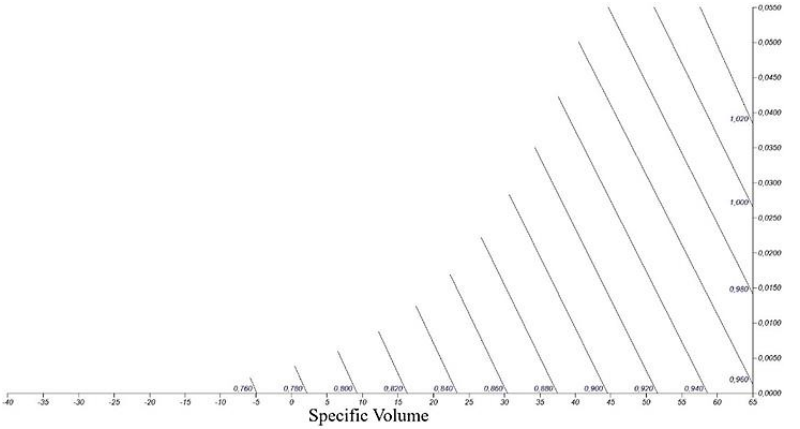

Figure. 6. Change of specific volume curves on the psychometric diagram depending on temperature

6. Specific Enthalpy: Specific enthalpy represents the amount of energy contained in one kilogram of air, with its unit being joules per kilogram (kJ/kg) (Wang &Wang 2000).

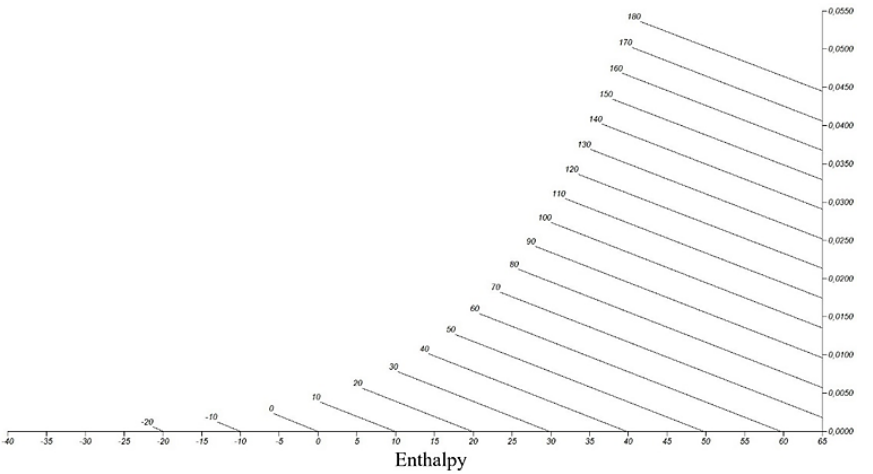

Figure. 7. Entalpi curves on a psychrometric diagram

5. Dew point temperature: Dew point temperature signifies the temperature at which water vapor in the air begins to condense while the absolute humidity remains constant.

HVAC (Heating, Ventilation, and Air Conditioning) Processes: HVAC (Heating, Ventilation, and Air Conditioning) involves a series of processes aimed at controlling the temperature and humidity levels in an environment. These processes typically encompass factors such as sensible heating, sensible cooling, humidification, and dehumidification. HVAC systems can combine these processes to achieve desired comfort conditions in a space (Wang &Wang 2000).

Simple Heating (Raising the Temperature): To increase the temperature of the environment, various tools such as electric heaters, radiators, or heat pumps are commonly used in this process (Schramek 1999).

Simple Cooling (Lowering the Temperature): To lower the temperature of the environment, various tools such as air conditioning systems, fans, or cooling systems can be preferred (Stoecker &Stoecker 1998).

Humidifying (Adding Humidure): This is the process of increasing the humidity level by adding water vapor to the environment. Humidifiers are preferred to address dryness issues in indoor spaces, especially during the winter months (Schramek 2003).

Dehumidifying (Removing Humidure): This process is carried out to remove excess moisture from the environment. Air conditioning systems usually cool the air, causing water vapor to condense and facilitating moisture removal (BULGURCU).

A psychrometric chart is a tool that graphically represents atmospheric conditions. By displaying temperature and humidity ratios together, it helps us understand environmental conditions at a specific point (DEVRESİ). Arrows on the psychrometric chart typically represent specific processes (heating, cooling,

humidification, dehumidification), and by following these arrows, necessary actions can be determined to achieve the desired air conditions (Özkol 1994), (Eisenwerke 1975).

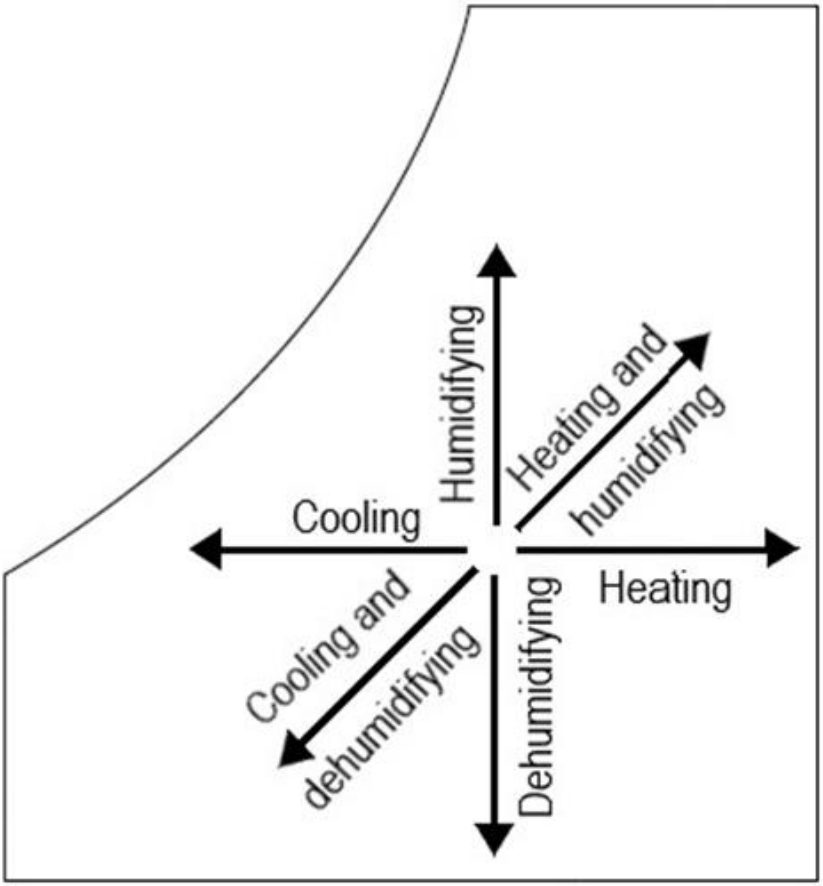

Figure. 8. The representation of heating, cooling, humidification, and dehumidification processes by moving arrows on the psychrometric diagram

Results:

Psychrometrics is a fundamental science used in various fields from agriculture to aviation, from HVAC systems to the

drying and storage of foodstuffs, spanning from the pharmaceutical industry to the textile sector. The studies in this field are grounded in the principles of ideal gas laws, Dalton's law of partial pressures, and the laws of energy and mass conservation. Psychrometrics was diagrammatically conceptualized by Willis Carrier in 1904 and has continually evolved to the present day. The diagram developed by Carrier and the i-x diagram prepared by Mollier are widely used, particularly by engineers and technicians working in the fields of HVAC and air conditioning.

This section aims to explain the fundamental principles in the fields of HVAC and air conditioning, as well as the intended purposes of psychrometric charts. It endeavors to provide a general understanding of how these processes can be combined to achieve specific air conditions and the steps to be followed.

References

BULGURCU, Hüseyin. "İKLİMLENDİRME SİSTEM TASARIMINDA BİLGİ TEKNOLOJİLERİNİN KULLANIMI."

Cengel, Yunus A, Michael A Boles, & Mehmet Kanoğlu. 2011. *Thermodynamics: an engineering approach*. Vol. 5: McGraw-hill New York.

Çengel, Yunus A. 2000. *Mühendislik yaklaşımıyla termodinamik*: Literatür.

Çengel, Yunus A, John M Cimbala, & Tahsin Engin. 2008. *Akışkanlar mekaniği: temelleri ve uygulamaları*: Güven Kitabevi.

DEMİR, Musa, & Nesrin %J Osmaniye Korkut Ata Üniversitesi Fen Bilimleri Enstitüsü Dergisi ADIGÜZEL. 2023. "R12, R22, R134A, R404A Soğutucu Gazlarının Evaporatör Performansının Belirli Bir Oranda Azaltılmasıyla Yıllık Enerji Ve Ekonomi Tasarrufu Kıyaslaması." 6 (1):416-426.

Demir, Musa, Gokhan Omeroglu, & Ahmet Numan %J Heat Transfer Research Özakın. 2023. "Experimental determination of the effect of fins of different cylindrical geometries on electrical and thermal efficiency in an air-cooled PVT system." 54 (3).

DEVRESİ, NO-FROST DOLABIN ELEKTRİK. "TESİSAT TEKNOLOJİSİ VE İKLİMLENDİRME."

Didier Thevenard PhD, PEng, & Mark W %J ASHRAE Transactions Shephard. 2014. "Temperature trends for locations listed in the tables of climatic design conditions in the 2013 ASHRAE Handbook-Fundamentals." 120:133.

Eisenwerke, Buderus' sche. 1975. *Handbuch für Heizungs- und Klimatechnik.(Stichworte Teil 1)*: VDI Verlag.

Gatley, Donald P %J Ashrae Journal. 2004. "Psychrometric chart celebrates 100th anniversary." 46 (11):16.

Güney, M. Ş. 2010. *Klima Tekniği* Vol. 1. ANKARA: Nobel Yayın.

Güney, Mukrimin Sevket, Kamil %J Renewable Kaygusuz, & Sustainable Energy Reviews. 2010. "Hydrokinetic energy conversion systems: A technology status review." 14 (9):2996-3004.

Handbook, ASHRAE Fundamentals. 1997. ASHRAE Fundamentals Handbook. Inc.

Önen, E %J Bayındırlık ve İskan Bakanlığı Teknik Yayınlar. "Havalandırma ve Klima Tekniği." (9).

Özkol, Nuri %J Küçük ve Orta Ölçekli Sanayi Geliştirme ve Destekleme İdaresi Başkanlığı. 1994. "Uygulamalı Klima Tekniği." (21).

Schramek, E %J Ttmd, Ankara. 1999. "Recknagel-Sprenger Schramek-Isıtma ve klima tekniği el kitabı."

Schramek, Recknagel-Sprenger. 2003. Isıtma+ Klima Tekniği. Kasım.

Stoecker, Wilbert F, & Wilbert F Stoecker. 1998. *Industrial refrigeration handbook*. Vol. 10: McGraw-Hill New York.

Wang, Shan Kuo, & Shan K Wang. 2000. *Handbook of air conditioning and refrigeration*. Vol. 49: McGraw-Hill New York.

Zorkun, Mehmet Emin, & Ali Rıza Ardıç. 1980. *Soğutma tekniği ve klima*: MEB.

CHAPTER X

Experimental investigation of water hammer phenomenon by image processing

Celal KISTAK[1]
Haydar EREN[2]

1. INTRODUCTION

The simplest pumping plant consists of a pump, a pipeline and a tank at a certain height. In such a system, in the event of a sudden interruption of electrical power, unless special precautions are taken, dangerous water hammer may occur at the pump outlet and at critical points of the pipeline.

Estimation of the maximum and minimum pressures that may be caused by water hammer at each point of the plant has been one of the main problems of the engineer designing the plant, as well as a classical field of endeavour for engineering science. Various

[1] Arş. Gör. Dr. , Fırat Üniversitesi
[2] Prof. Dr. , Fırat Üniversitesi

approaches have been tried to solve the problem and at the end of these endeavours, graphical, algebraic, semi-analytical methods have been developed and abbreviations have been prepared which can be used practically by engineers.

Characteristics and finite difference methods developed in the last 25 years have made it possible to calculate the pressure at any point of the plant at any time with the help of a computer. In addition, the simulation of many elements on the pipeline such as check valve, air boiler, control valve and balance shaft can be taken into account as appropriate boundary conditions.

Serious problems awaiting the operators arise in pumping systems, especially in cases where no precautions are taken against water hammer caused by momentum change during power outages and stops/starts.

In particular, water hammer, which causes consequences such as pipe bursting, compensator rupture, rupture of connections of concrete masses, should be considered at the design stage and a hydraulic analysis and water hammer control should be carried out after the design of each new pipeline.

In our country, in pipelines that have been completed in recent years and considered as new pipelines, damage/failure cases are encountered as a result of impact during the first commissioning.

The most commonly used methods for water hammer analysis and their shortcomings can be listed as follows:

The use of "Fingeryan" abaci should no longer be considered due to their inadequate limits [1],

The "Ruus" method[2] is too safe and not practical,

It is not practical to draw detailed boundary conditions with graphical analyses when computers are available,

- Regulating valves cannot be a solution in every geometry, especially in cases of negative pulse Water hammer in pipelines can occur as a result of many situations. For example, unavoidable

causes such as sudden de-energisation of the pump motor, closing / opening manoeuvres of the valves on the line and starting the pump can be listed. As a result of the water hammer event, overpressure (suppression) and underpressure (depression) conditions occur in the pipeline at certain periods. Under these pressures, the pipe or other elements on the line may be damaged. For these reasons, water hammer calculation must be made during the design of pipelines and anti-impact elements must be installed on the line.

Water hammer calculation can be done by solving the time-dependent equations of motion and continuity in the pipe. These equations can be solved by two methods. These are graphical solution method and numerical solution method.

Graphical methods have been used for a long time due to their simplicity and practicality. However, it is not possible to calculate the regions outside the graphical limits and to see the change of pressure along the pipeline according to time with this method. Thanks to the high memory capacity and processing speed of today's computers, much more detailed and precise calculations can be made with the numerical method. All kinds of hydraulic elements (pump, pressure regulating valve, check valve, air boiler, etc.) can be modelled mathematically and used as boundary conditions in the solution of water hammer equations [3].

The first studies of the water hammer phenomenon were carried out by Menabra [4]. In these studies, different flow parameters were evaluated.

Michaud [5] studied the use of air ducts and safety valves to ensure the controllability of water hammer phenomena.

In the early 19th century, Weston [6], Carpenter [7] and Fritzel [8] tried to develop the in-pipe velocity change-pressure relationship.

The basic theories of transition flow were proposed by Jukowski [9]. Later on, these equations also formed the basis of the water hammer phenomenon. Jukowski analysed different physical

conditions with parameter variations, and then he used advanced mathematical relations with the data equations he obtained.

In his water hammer experiments, Gibson [10] worked with pipeline equipment in downstream valves. With these studies, he made significant progress in revealing the gas release relations of low pressure waves. Through his work, he explained the relationship between gas release states and column separation processes.

In the mid-1960s, the development of mathematical and numerical models began with the general acceptance of reference works. The basis for these models was the work of Gibson [11], Schylinder [12], Angus [13] and Parmakian [14] who developed arithmetic procedures.

The first computer-proportional procedures involving water hammer analysis were developed by Thibessard [15], Li [16], Streeter and Li [17], Streeter [18,19], Vande Riet [20] and Contractor [21]. These arithmetic-based models have been compiled with different algorithms and used in many studies. Dagtekin used image processing method for fully developed turbulent method [22].

Chen et al [23] developed a high tolerance algorithm with the Super Propagative Viscosity Method. With the diffusive viscosity method, it is ensured that the computable efficiency can be obtained closer to the results in the application conditions in discontinuity conditions. Comparisons with the standard diffusive method are the basis of the study. While investigating the water hammer phenomenon, it will be an important factor to consider the fluid types. The study of systems transporting non newtonian fluids can be an important field of study [24].

In this study, image processing techniques were utilised in order to examine pressure changes more clearly and time-dependent.

Within the scope of the study, measurements were made with the help of an imaging system consisting of two cameras, an image capture card and a computer. Unlike previous studies in terms of measurement technique, in this study, more accurate and

comprehensive pressure values were obtained by obtaining simultaneous images by using two cameras simultaneously instead of a single camera. In addition, as an alternative to the existing methods, the time variations of the water level obtained from any selected point along the pipe were determined with the help of images taken from digital cameras.

In the study, the scenario in which the water hammer event occurs in the case of valve closure and the power failure situation were analysed and the valve closure was performed by means of a pneumatic actuator.

With a camera that captures up to 500 frames per second, pressure changes can be analysed at higher resolution.

2. IMAGE PROCESSING AND ANALYSIS

2.1 Imaging System

Image processing can be defined as the processing and analysis of digital images obtained from devices such as video cameras, cameras and scanners by means of computers and various software. Although there are different definitions in the literature, the combination of hardware units and software used to obtain and analyse images is defined as an image processing system (IS). In this system, optical properties such as colour, reflection and light transmittance, geometric properties such as width, depth, diameter, angle, perimeter and location properties such as position can be easily examined by computer. For this reason, as a result of the rapid developments in the field of electronics and software in recent years, these systems are used in many fields with the development of components that enable the economic and widespread use of image processing systems. These areas can be given as many examples such as medicine, aviation, fluid mechanics. Although it varies according to the need, an imaging system consists of basic components, each of which has an important function in obtaining a healthy image. When a digital camera system is considered, the necessary components are one or more digital cameras and lenses,

image capture (Figure 2.1), lighting and computer hardware and software. When capturing images to be processed using the camera and image capture card and finally using appropriate software, light and optical changes help to increase the efficiency of the image obtained and to obtain a more precise image.

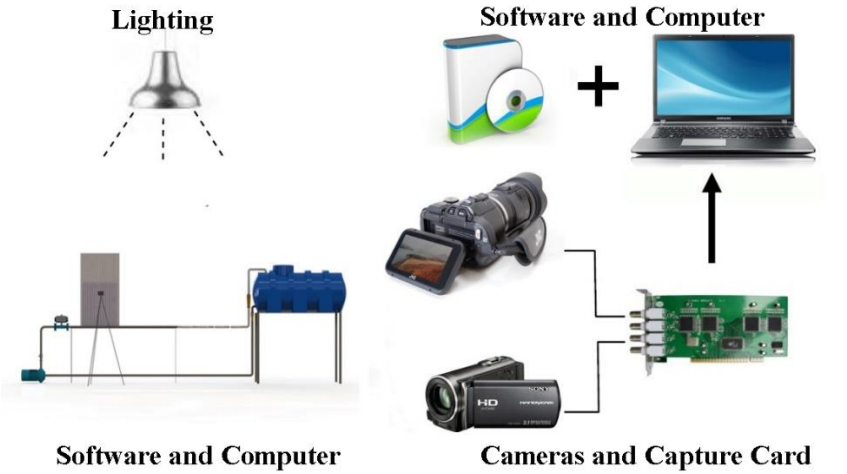

Figure 2.1. Components of the vision system

2.2 Image Identification and Modelling

Digital images can be formed by the combination of a matrix of small and many cells, each forming a different colour value.The cells, which are called the basis of the images, are called pixels and are usually square (Figure 2.1).If this matrix is considered, there are basically two properties of each pixel.One is its position in the matrix and the other is its light sensitivity.If the image is examined with these properties, it is seen that a two-dimensional function f (x,y) is defined (Figure 2.2). The pixel in the upper right corner of the screen is the default starting point of the coordinate system. This pixel is at coordinate (0.0).

If a camera with 1920x1080 resolution value is considered, the image obtained in this case can take values up to 1920 pixels in x value and 1080 pixels in y value.

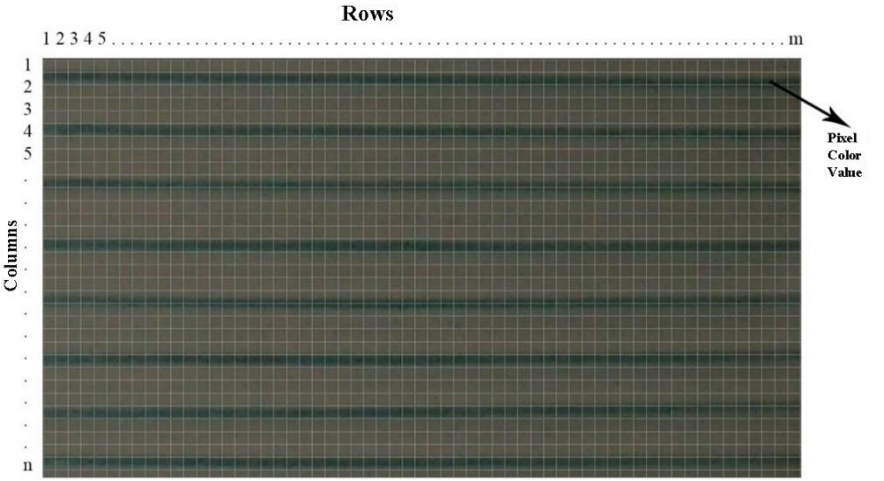

Figure 2.2. Image representation as a matrix

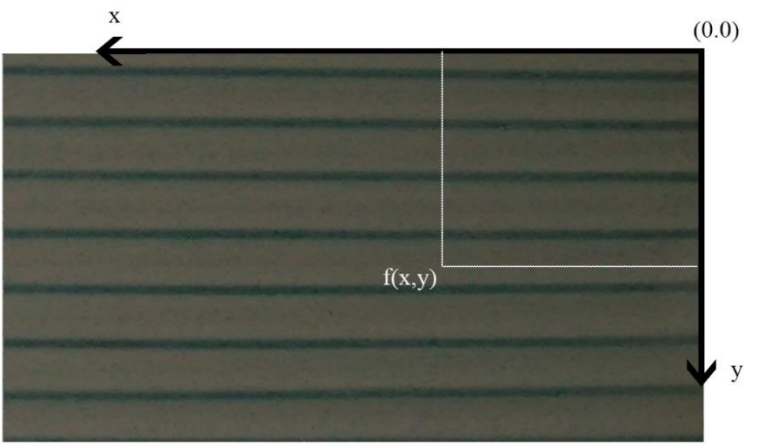

Figure 2.3. Representation of the image as a function of f

The range of grey values in images can be expressed as : G={0.1.2....255}.This means that a grey scale image can have 256

different values of grey scale values.255 grey values correspond to white colour and 0 grey values correspond to black.

According to the situations caused by hardware limitations, the grey level is generally determined as powers of two. To give an example of this situation, it is 8-bit (28).

Colour images are displayed as 24-bit data in computer environments. RGB, that is, the image is formed by superimposing three grey level images filtered as red, green and blue.

As a result, in order to change the colour in an image, the first parameter is the sequence number of the colour in the palette (RGB sequence) and the second parameter is the mixing ratio of R, G, B values to be used to create the colour.

Features that most affect the quality of a digital image,

- the number of colours in the image,
- is the number of pixels in the image, in other words its resolution.

The more the number of colours in an image, the more detail there is in the image, which means that the image contains more sensitive information. As the number of colours decreases, the number of details in the image decreases and accordingly the image quality decreases. The human eye perceives up to 256 different colour tones under the best conditions. For this reason, it is sufficient to use at most 256 colours in the image for the human gaze. However, computers can create and perceive 16 million and more colour tones. Therefore, more effective results can be obtained by using more colours in image processing [25].

2.2 Image Processing Techniques

The process of creating new images by changing the characteristics and appearance of the image by processing the images that have been converted into a digital image as a data, picture can be called image processing. In other words, to make a

more comprehensive definition, after the digital images are obtained, processes such as removing noise, removing reflections caused by the lighting system, improving image quality, image repair can be applied in the computer environment. All of these corrections made on digital images are generally called image processing. Image enhancement, image filtering and restoration, image compression, pattern recognition, feature extraction, edge detection, line tracing, etc. There are many other image processing applications [26].

With the thresholding technique, images with different grey levels are converted into binary number system, i.e. 1 and 0 values. The relevant pixel above this value is assigned a value of 1 and the others are assigned a value of 0.

With the segmentation process, the colours determined in the image can be visually extracted and then, if necessary, sharpening can be performed or separated from the whole image. With the segmentation technique, different objects or parts can be separated while they can be cleaned from the background image.

Contrast enhancement technique can be used to adjust the brightness and contrast of the image as well as the contrast of green and red colours. With the algorithms developed for image restoration, it is aimed to make corrections in the image damaged by known causes.

Filters are of great importance in image processing. Filtering techniques take place in frequency or spatial environment. Spatial environment refers to the collection of pixels and these methods define the operations performed directly on pixels.

With a low-pass filter, large and homogeneous areas are emphasised, while details are reduced and the image is simplified. On the contrary, the high-pass filter is used to sharpen and sharpen small details.

As a result, the pixels defining the image can be identified by their positions and grey levels. This image is shown in Figure 2.1 in matrix form. Filters and algorithms, which are actually mathematical

operations, also appear as mathematical expressions to perform various operations on the matrix on the image. After these operations, the desired new images are obtained.

2.3 Calibrations

The digital camera, which is an electronic imaging system with optical elements, is affected not only by low or high resolution, but also by a number of systematic distortions that affect the metric quality of images, such as lens distortion, sensor plane deformation and electronic transfer errors. Consequently, in order to make images metrically usable, these systematic errors need to be identified, modelled and corrected. This process is called calibration. Distortions in digital images obtained with digital cameras can be corrected with the help of computers with existing algorithms and software [27].

Optical distortions are caused by the physical structures of the imaging elements of the camera elements and consist of changes in the image point position in the image plane (Figure 2.3).

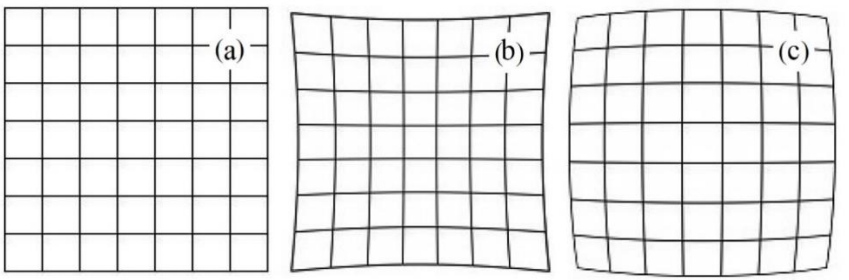

Figure 2.4. Incoming angular distortions in the images a) original image b) concave

In order to prevent unwanted image distortions, there are lenses that give a planar image and have very high prices. In addition to this situation, since it is not possible for the glass-based material used in the lens system to be processed perfectly and have a homogeneous distribution or for multiple lenses to be placed perfectly on the same axis, each lens system has more or less

distortion. In these cases, which can be corrected by various computationally demanding processes, it is sufficient to know the internal orientation parameters (skewness, correction coefficient, centre point).

2.3.1 Angular Calibration of the Image

In order to make dimensional readings on the images, lens-induced convex or concave situations must be eliminated and made planar. For this process, "Camera Calibration Toolbox" from Matlab toolboxes is a very common application. After the camera parameters are recorded precisely, they can be easily corrected by making the necessary calculations by the programme.

Once the camera parameters are obtained, they can be used to correct all images for that camera, provided that the lens focal length does not change.

2.3.2 Perspective Calibration

If the cameras are not perpendicular to the plane of the table, or at least not at right angles to all pipes, a perspective image is formed. In this case, even if the water level is the same everywhere, it looks different in the near parts and different in the far parts (Figure 2.5). For this situation, the grids and calibration settings on the camera itself (Figure 2.6) have been adjusted with the help of various adjustments between the camera and the object and the image has been made suitable for data acquisition.

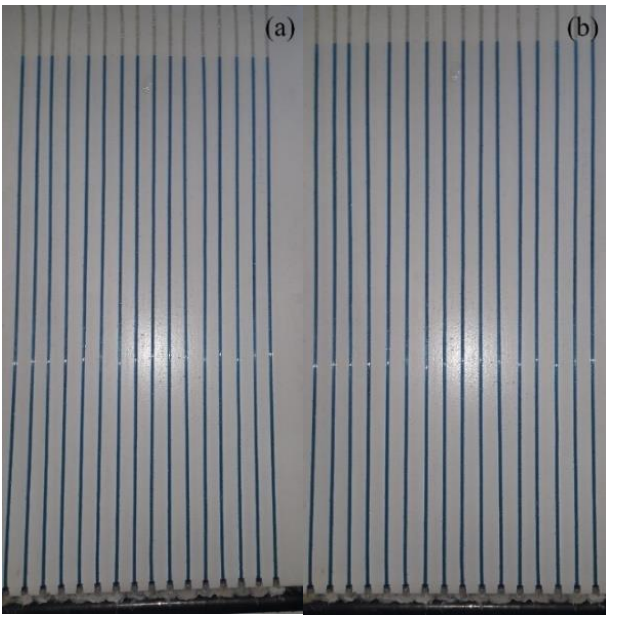

Figure 2.5. Image perspective calibration a) Uncalibrated image b) Image after calibration

Figure 2.6. Perspective calibration using grids

2.3.3 Metric Calibration

Digital images consist of images with the smallest cellular structures. While one of the two images with the same resolution is a microscope image, the other can be a map. In order to determine the actual metric expressions in images expressed in pixels, reference metric elements should be found in these pixel values and transformations based on them should be made. This process is actually nothing more than a simple direct proportion. For example, if there are 500 pixels between a 100 cm long reference, 100/500=0.2 cm/pixel. If this basic ratio in the image is known, measurement operations on the image can be easily performed with many image processing software.

In this study, a 132 cm long tape measure attached to the side of the table was used for referencing (Figure 2.7).

Figure 2. 7. *Tape measure used for referencing*

2.4 Measurement of Time Dependent Pressure Changes by Imaging Technique

For the first time, the variation of the water hammer event at different points along the pipe has been determined using digital video images. For this purpose, a code was developed by making use of the filter and various identification functions available in the Matlab programme used in the study. Basically, the region to be measured on the image is divided into 16, which is the number of pipes. In order to get rid of the background contamination in the image, the image was flipped horizontally depending on the lens condition and an offset was defined to make measurements at the input empty values.

The basic logic in the pressure measurement technique with the virtual level meter is based on the principle that the area within the determined 16 regions is divided into blue channels in each photograph depending on the number of frames of the video and the value of the last pixel to the left is determined and this is recorded in an excel spreadsheet depending on the number of frames and time, then multiplied by the pixel / real distance ratios and the time-dependent change is formed.

3. MATERIAL AND METHOD

In the experimental setup, the pump, various valves, fittings, pipes and tanks in the classical type water installation were used. In order to view the pressure change with the camera, food dyes of different colours were used and blue colour was preferred for the best image and experiments were carried out. In the experimental system, the simulation of a sudden power failure of the pump was tried by switching off the switch and switching off the power in the relevant socket. In addition, the ball valve in the system is opened and closed by a pneumatic actuator in order to ensure that the valve closure in the system is provided under the same conditions in each experiment.

3.1 Experimental Setup

In order to investigate the water hammer phenomenon by flow visualisation method, an experimental set-up was used in the fluid mechanics laboratory of Fırat University, Faculty of Engineering, Mechanical Engineering. The experimental setup consists of a pump, pipeline valves, pneumatic actuator, compressor, two video cameras and a rotameter to be used for flow measurement.

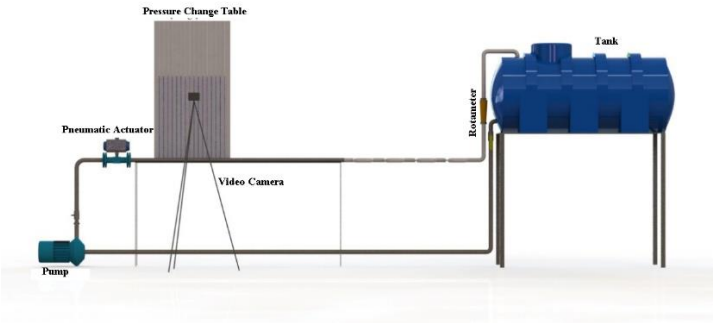

Figure 3.1. Solid model of the experimental setup

3.2 Conducting the Experiments

When the test process is basically analysed, it is seen that it consists of three main sections;

- Preparation and standard installation flow process
- Scenario-based flow intervention status
- It can be separated as the acquisition of images.

In the installation flow process, the water taken from the tank with the help of the pump moves in the main line of the installation through the pipes and is in a continuous rotation state.

3.3 Image Acquisition

While the scenarios foreseen to be observed in the system are realised in the desired parameters, the cameras, which are among the system elements, visually record the situations. Camera number one

is positioned in front of the pressure observation table and it is aimed to record the images in the clearest and most processable way with the help of a tripod. By changing the shooting modes of camera number one in the range of 25-500 frames/second, the pressure change ranges observed depending on time can be reduced and data sensitivity can be increased. Camera number two is used to determine the type of closure by recording the closing time of the flanged type valve during the first scenario.

Since the pressure line should be obtained as smooth columns in the images obtained, the curtains in the environment were closed to prevent light from shining from the opposite side of the pipes, which are transparent and very suitable for reflection.

Different light, filter and night mode shooting of camera number one in various time periods were tried and the most workable results were obtained in the daytime, night mode off and the environment was arranged in such a way that direct light was not received from the opposite side.

4. RESULTS

Through the image processing algorithm created in the Matlab programme;

- The video file is read in order to read the values obtained from the experimental setup,
- The video is saved as an object,
- The number of frames in the video is taken,
- Determine how many frames a value will be taken,
- The array in which the values will be written is determined,
- Each square is read as a matrix,
- The red, green, blue range of the colour to be extracted is determined,

- Dilatation and gap filling operations are performed to make the corners more prominent in the image and to combine the gaps,
- The image is divided into 16 regions on a pixel basis and the last pixel value of the desired colour in this region is read and the conversion based on the formula between the known real distance and the pixel is performed and the values are read.

The graphs of 0.3 m3/h flow rate value obtained as a result of these processes are given below.

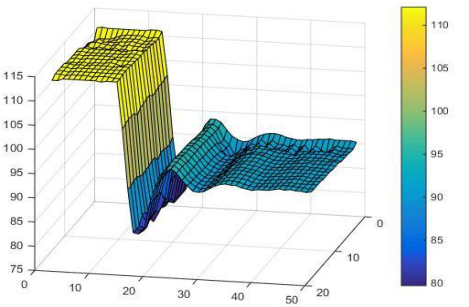

Figure 4.3. 3D pressure-time change graph for 0.3 m3/h valve closing scenario

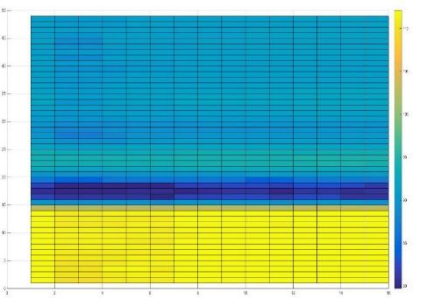

Figure 4.4. Pressure-time change graph for 0.3 m3/h valve closing scenario

The pressure change graphs obtained as a result of the power failure scenario for a flow rate of 0.7 m3/h in the experimental setup are given in Figures 4.9 and 4.10.

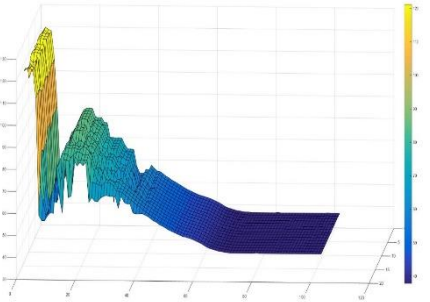

Figure 4.9. 3D pressure-time change graph for 0.7 m3/h power failure scenario

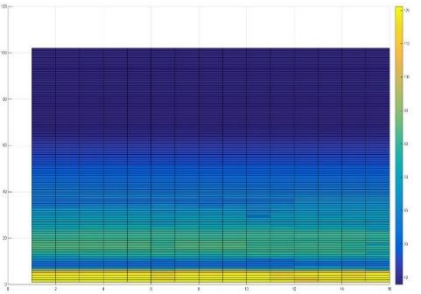

Figure 4.10. Pressure-time change graph for 0.7 m3/h power failure scenario

This paper examines how current image processing techniques and flow visualisation methods can be used in an experimental investigation on water hammer analysis. MATLAB and high-speed cameras, as well as image processing algorithms, have enabled the water hammer phenomenon to be analysed more effectively.

This study highlights the utility of current image processing techniques, particularly for visualising the time-dependent variations of flow and understanding the complexity of the water hammer event. Data acquired with high-speed cameras capture the behaviour of the fluid in detail and image processing algorithms can be used to analyse these data in a more accurate way.

Deep learning based image processing methods allow to obtain results in the field of water hammer analysis with a precision that was not possible before. The use of these techniques brings a new perspective to the academic literature and contributes to the development of more robust strategies in engineering projects on water hammer control.

In conclusion, this study demonstrates how image processing and flow visualisation techniques can be successfully integrated in experimental studies, revealing new developments and potential in this field.

REFERENCES

[1] Parmakian I, 1953. Waterhammer Analysis, Dover Publacitions

[2] Ruus E, 1977. Charts for Waterhammer in Pipelines with air Chambers, *CanadianJournal of Civil Eng*. , 4, 3, 293-313

[3] Kavurmacıoğlu L., 2009. Boru Hatlarında Su Darbesi Olayı Ve Önleme Çareleri, *9.Ulusal Tesisat Mühendisliği Kongresi*, İstanbul

[4] Menabrea, L. F1885, Note sur les effects de choc de l'eau dans les conduites, *C. R. Hebd.Seances Acad. Sci.* 47, July–Dec., . 221–224.

[5] Michaud, J, 1878. Coups de be´lier dans les conduites. E ´ tude des moyens employe´s pour en atteneur les effects, *Bull. Soc. Vaudoise Ing. Arch*. 4~3, . 56–64, 65–77.

[6] Weston, E. B, 1885. Description of Some Experiments Made on the Providence, RI Water Works to Ascertain the Force of Water Ram in Pipes, *Trans. Am. Soc. Civ. Eng*. 14, p. 238.

[7] Carpenter, R. C1893, Experiments on Waterhammer, *Trans.ASME*, 15.

[8] Frizell, J. P., 1898. Pressures Resulting from Changes of Velocity of Water in Pipes, *Trans. Am. Soc. Civ. Eng.* 39,1–18.

[9] Joukowski, N. E., 1898. Memoirs of the Imperial Academy Society of St. Petersburg, *9~5 ~Russian translated by O Simin 1904,Proc. Amer. Water Works Assoc.* 24, . 341–424.

[10] Gibson, A.H., 1908. Water Hammer in Hydraulic Pipelines. Archibald Constable and Co. Ltd., London.

[11] Gibson, N.R., 1919–1920. Pressures in penstocks caused by gradual closing of turbine gates. Transactions of ASME 83, 707–775.

[12] Schnyder, O., 1932. Uber Drucksto Xe in Rohrleitungen. (On water hammer in pipe lines.). *Wasserkraft und Wasserwirtschaft* 27 (5),49–54; 27(6), 64–70; 27(8), 96 (in German).

[13] Angus, R.W., 1935. Simple graphical solution for pressure rise in pipes and discharge lines. *Journal of the Engineering Institute of Canada* 18 (2), 72–81, 264–273.

[14] Parmakian, J., 1955. Waterhammer Analysis. Prentice-Hall, New York (Reprint in 1963, Dover Publications, New York)

[15] Thibessard, G., 1961. La simulation du coup de be´ lier sur calculateur nume´rique. (The simulation of water hammer on a numericalcalculator.). In: *Proceedings of the Ninth IAHR Convention, Dubrovnik*, Yugoslavia, pp. 881–890 (in French)

[16] Li, W.H., 1962. Mechanics of pipe flow following column separation. *ASCE Journal of the Engineering Mechanics Division*, 88 (4),97–118

[17] Streeter, V.L., 1963. Water hammer analysis with non-linear frictional resistance. *In: Proceedings of the First Australian Conferenceon Hydraulics and Fluid Mechanics*. Pergamon Press, New York

[18] Streeter, V.L., 1964. Water hammer analysis of pipelines. *ASCE Journal of the Hydraulics Division* 90 (HY4), 151–172

[19] Streeter, V.L., 1965. Computer solution of surge problems. *Proceedings of the Institution of Mechanical Engineers* 80 (3E), 62–82.

[20] Van De Riet, R.P., 1964. A computational method for the water hammer problem. Mathematisch Centrum, Report TW 95,Amsterdam, The Netherlands

[21] Contractor, D.N., 1965. The reflection of water hammer pressure waves from minor losses. *ASME Journal of Basic Engineering* 87,445–452.

[22] Demirpolat T, A.B., Dağtekin, İ., Eren, H., Düz, H., 2013."Determination of Darcy Friction Factor Using Image Processing Method in Fully Developed Turbulent Flow" *European Conference of Technology and Society*.

[23] H, Chen,H,Liu,J.Chen,L,Wu., 2013. Chebyshev super spectral viscosity method for water hammer analysis, *Propulsion and Power Research,* 2 3, 201-207

[24] Yanen, C., Solmaz, M.Y. & Aydoğmuş, E. (2021). Determination of Rheological Properties and Dispersion Quality of Shear Thickening Fluid. European Journal of Science and Technology, (28), 781-784.

[25] Doğan (Açıkgöz), R., Doğan , S. ve Banger, G., 1999. Raster Görüntüleri Yapısı, Görüntüleme Tekniklerininin Temelleri ve BITMAP Formatı, *Harita ve Kadastro Mühendisliği Dergisi*, 86: 61-80.

[26] Kocaman, S., 2013. Baraj Yıkılması Probleminin Deneysel ve Teorik Olarak İncelenmesi. *Doktora tezi*, Çukurova Üniversitesi, Adana, Türkiye

[27] Karslı, F. ve Ayhan E., 2005. Orta ve Yüksek Çözünürlüklü Dijital Kameraların Metrik Performanslarının Belirlenmesi TMMOB Harita ve Kadastro Müh. Odası, *10. Türkiye Harita Bilimsel ve Teknik Kurultayı*, Ankara.